N78-21442

COPY NO. ____

SYNTHESIS AND ANALYSIS OF PRECISE SPACEBORNE LASER RANGING SYSTEMS

AUGUST 1977 **MDC E1729**

VOLUME I FINAL REPORT

PREPARED BY E. A. PADDON

MCDONNELL DOUGLAS ASTRONAUTICS COMPANY-EAST
P. O. BOX 516
ST. LOUIS, MISSOURI 63166

PREPARED FOR: GODDARD SPACE FLIGHT CENTER
GREENBELT, MARYLAND 20771

MCDONNELL DOUGLAS ASTRONAUTICS COMPANY - EAST

Saint Louis, Missouri 63166 (314) 232-0232

MCDONNELL DOUGLAS CORPORATION

FOREWORD

Volume I of this report presents the results of a study effort conducted during the 1973-1975 time period. The initial study effort had a very broad scope and considered a number of different system approaches. As a result of this effort, a more detailed study was conducted to define a Shuttle borne laser ranging experiment. Volume II of this report presents the results of the second study effort.

TABLE OF CONTENTS

TABLE OF CONTENTS (Continued)

LIST OF FIGURES

LIST OF FIGURES (Continued)

LIST OF TABLES

LIST OF PAGES

1.0 INTRODUCTION AND SUMMARY

The purpose of the study was to synthesize and evaluate laser measurement systems which showed a capability to meet planned space-based earth physics investigations; to define critical system and component performance areas; and to develop optimum system approaches based on parametric evaluation of performance, cost, and risk.

The measurement accuracy goals were 2 cm rms range estimation error and 0.003 cm/sec rms range rate estimation error, with no more than 1 cm (range) static bias error. Further, each selected measurement concept was to be capable of meeting these objectives with any of the specified targets.

The specified links included links between a high altitude, transmit/receive satellite (HATRS), and one of three targets, (1) a low altitude target satellite, passive (LATS), (2) an active low altitude target, and (3) a ground-based target. The number of links was subsequently expanded to include operations with a primary transmit/receive terminal intended to be carried as a Shuttle payload, in conjunction with the Spacelab program. The primary emphasis of the Shuttle links was ranging to passive retro-reflectors on the ground, although ranging to other orbital satellites was a desired capability.

The early part of the study was oriented toward defining the constraints and parameters associated with these links. As with most radar links, the principle constraints on feasibility were the target signature, the minimum allowable beamwidths, and the required received signal energy to achieve the desired ranging accuracy. The most critical link is the link between the HATRS and the passive LATS, and we compared the various measurement concepts for this application. We investigated CW and pulse-burst mode-locked laser measurement concepts, to satisfy the range rate measurement goals. These measurement concepts were found to be significantly short of meeting either the range or range rate measurement accuracy goals for the HATRS to passive LATS link. The major problem for the CW mode-locked laser measurement concept was due to the large required signal energy to overcome the background from a sunlit earth. A pulse-burst, mode-locked laser measurement concept was evolved to reduce the duty cycle, and hence reduce the effect of background. This concept was initially considered feasible, even though significant development would be required. This concept, however, was found to be considerably inferior to the more conventional single pulse measurement concepts for range measurements. Since both range and range

rate (or range-sum-rate) measurements would be made on the same fundamental waveform, the pulse-burst, mode-locked measurement concept provided no fundamental measurement advantage and was, therefore, discarded.

A micro-wave frequency modulated, single frequency CW laser was considered as a remotely possible alternate technique for obtaining range-sum-rate measurements. However, since the passive LATS considered in this study was based on the LAGEOS, the dispersive effect of multiple cube-corners distributed on a spherical surface would preclude meaningful measurements at side-band frequencies materially greater than achievable with the single pulse, mode-locked laser measurement concept, thus this concept was considered inappropriate.

The remaining two measurement concepts were based on a presently available technique (a Q-switched, cavity dumped laser) and a reasonable extrapolation of this laser to add a mode-locker within the cavity to reduce the emitted pulse-width from the 4 to 6 ns range to values on the order of 0.2 ns. These two measurement concepts were retained throughout the balance of the study; no conclusion as to an optimum choice was reached. The Q-switched, cavity dumped laser, in ruggedized form, exists today. Although this measurement concept can only approach the accuracy goals, development of a space qualified system, using this technology, would be relatively straight forward. On the other hand, the Q-switched, mode-locked cavity dumped laser can readily meet the measurement accuracy goals (with suitable targets), but the laser does not exist, even in laboratory form at this time. An oscillator/amplifier combination to achieve equivalent performance has been built and is currently in operational evaluation, however this system is not readily adapted to a space environment. We concluded that the short pulse technique is decidedly superior, and has the long range potential to meet the science objectives; however, for more immediate applications, such as a Shuttle/Spacelab experiment, the readily available Q-switched, cavity dumped laser was a more reliable concept and has the potential to meet most, if not all, of the projected experiment goals.

Detailed evaluation of the target signature of the LAGEOS configuration revealed a number of problems which will limit the achievable measurement accuracy. The impulse response of the LAGEOS was found to vary significantly with optical frequency and velocity aberation, resulting in a varying mean response, which is also potentially thermally sensitive. In addition, when the short pulse technique is employed, coherent interference effects cause the detected return pulse to vary in shape and amplitude on a pulse to pulse basis. The effect of this variation

in detected pulse shape and amplitude is dependant on the measurement technique, but will certainly increase the rms measurement error. Although the variation in pulse shape for the longer pulse laser is less visible, the effect is similar, since the centroid of the effective return pulse will vary in a similar manner. For targets with smaller effective dimensions, such as planar arrays at a near normal incidence, the dispersive effect is virtually eliminated; the pulse-to-pulse mean amplitude variations will of course remain. These variations in signal amplitude can be countered by averaging or thresholding techniques.

When the target is active, i.e., equipped with a laser receiver and transmitter the signature problems are virtually eliminated, and viable, high margin links can be configured. The selected target terminal configuration employed an asynchronous receive/transmit system to simulate an ideal target. The key to the operation of the system is precise recording of the time-of-arrival of the received pulses and of the time-of-departure of the transmitted pulses. Subsequent processing can then extract the propagation time estimates, even though the clocks at the HATRS and LATS (or ground) terminals are not perfectly synchronized.

A major concern during the study was the accuracy with which the transmit beam and receiver fields-of-view could be oriented. For the link between the HATRS and the passive LATS, very narrow transmit beamwidths and small receiver fields-of-view will be required. The net pointing accuracy required will be on the order of one microradian. We determined that this accuracy is theoretically achievable, based on current and projected state-of-the-art in guidance and navigation technology, although many problems remain to be solved.

The pointing accuracy required for the Shuttle experiment is considerably less stringent, more on the order of 50 to 100 microradian. However, the navigation uncertainties and attitude reference errors in the Shuttle systems results in pointing uncertainties on the order of milliradians to degrees unless auxillary subsystems are added to improve the references. The acquisition and pointing control problem for a minimum cost experiment requires further study to ascertain feasibility and interface requirements.

The net conclusion is that both the Shuttle experiment and the long range earth physics mission objectives can be met with existing and projected technology; no extraordinary development problems are envisioned. The concepts are considered fundamentally sound, and reflect the application of current ground-based laser radar technology to space-borne system applications.

2.0 LINK ANALYSIS

2.1 SUMMARY. One of the early activities in the study was to select a link analysis summary format which would serve, with minor modification, to document both active and passive link margin summaries. The format shown in Table 1 evolved from this activity, and is similar to an optical communication type of link margin analysis format. For links with passive targets, all entries shown are used. When analyzing a link with an active target, lines 7, 8, and 9 are deleted.

The format shown in Table 1, for ranging with passive targets, is identical in content to the classical radar range equation, with a few $(4\pi/\lambda^2)$ factors added to convert from range to free space loss and from radar scattering cross-section to target receive/transmit antenna gain product. The classical radar range equation can be written,[1]

$$P_r = P_T G_T A_e \sigma S_T S_r / (4\pi)^2 R^4 \qquad (1)$$

P_r = received signal power (watts)

P_T = transmitted signal power (watts)

G_T = transmit antenna gain (relative to an isotropic antenna)

A_e = receiver effective antenna area (m^2)

σ = radar scattering cross-section of the target (m^2)

S_T, S_r = transmittance of the transmit and receive paths

R = range to the target (m).

The target radar scattering cross-section is defined as the product of the projected target area, the transmit antenna gain of the target, and the target reflectivity.

[1] Skolnik, M. I., "Introduction to Radar Systems," McGraw-Hill, New York (1962), pg 37-5.

TABLE 1

HAIRS TO LATS(PASSIVE)
CIRCUIT MARGIN SUMMARY
OPTICAL WAVELENGTH .53 MICROMETERS,RANGE 30000. KM
PULSEWIDTH= .20 NANOSECONDS

	PARAMETER	UNITS	VALUE	
1	TRANSMITTER POWER	DBW	-20.00	10.0 MILLIWATTS
2	TRANSMITTER LOSSES	DB	-.97	
3	TRANSMIT ANTENNA GAIN	DB	121.07	5. MICRORADIANS
4	POINTING LOSS	DB	-1.39	1. MICRORADIANS
5	FREE SPACE LOSS	DB	-297.04	
6	ATMOSPHERIC LOSS(DOWN)	DB	.00	
7	TARGET GAIN PRODUCT	DB	208.50	
8	ATMOSPHERIC LOSS(UP)	DB	.00	
9	FREE SPACE LOSS	DB	-297.04	
10	RECEIVE ANTENNA GAIN	DB	131.00	.61 METERS DIA.
11	RECEIVER LOSSES	DB	-3.98	
12	RECEIVED SIGNAL POWER	DBW	-159.85	
13	TRANSMIT PULSE RATE	DB/SEC	10.00	10. PULSES/SEC.
14	ENERGY PER PULSE	DBJ	-169.85	
15	ENERGY PER PHOTON	DBJ	-184.26	
16	RECEIVED PHOTONS/PULSE	DB	14.41	
17	QUANTUM EFFICIENCY	DB	-6.02	25.0 PERCENT
18	RECEIVED P-E/PULSE	DB	8.39	6.91 P-E
19	BACKGROUND RADIANCE	DBW	-17.70	.0170 WATTS/M2-A-ST
20	RECEIVER FOV(STERRAD.)	DB	-87.07	50. MICRORADIANS
21	OPTICAL FILTER BANDWIDTH	DB	6.99	
22	RECEIVE ANTENNA AREA	DBM2	-5.51	
23	RECEIVER LOSSES	DB	-3.98	
24	RECEIVED BACK. POWER	DBW	-107.26	
25	ENERGY PER PHOTON	DBJ	-184.26	
26	RECEIVED PHOTONS/SEC	DB/SEC	77.00	
27	QUANTUM EFFICIENCY	DB	-6.02	
28	BACKGROUND P-E/SEC	DB/SEC	70.98	
29	RECEIVER GATE WIDTH	DB-SEC	-86.99	2.00 NANOSECONDS
30	BACKGROUND P-E/GATE	DB	-16.01	.03 P-E
	LINK MARGIN			
18	RECEIVED P-E/PULSE	DB	8.39	6.91 P-E
31	REQUIRED P-E/PULSE	DB	.00	1.00 P-E
32	LINK MARGIN	DB	8.39	6.91

$$\sigma = r\, G_{TT}\, A_T \qquad (2)$$

r = target reflectivity (assumed = 1)

G_{TT} = target transmit gain = $4\pi/\Omega$

A_T = target projected area (m^2)

Ω = effective target transmit beamwidth (steradians)

The radar range equation can then be rearranged to the form shown in Equation (3).

$$P_r = P_T G_T G_R S_T S_r G_{TT} G_{TR} L_{FS}^2 \qquad (3)$$

$G_R = \left(\frac{4\pi}{\lambda^2}\right) A_e$ = radar receive antenna gain

$G_{TR} = \left(\frac{4\pi}{\lambda^2}\right) A_T$ = target receive antenna gain

$L_{FS} = (\lambda/4\pi R)^2$ = free space loss

λ = wavelength (m)

These terms are shown in the first twelve lines of Table 1. Provisions were made to divide the loss terms into significant components, and the $G_{TT} \cdot G_{TR}$ product was shown rather than the individual terms. The parameter values are shown in dB, thus line 12 is the sum of the first eleven lines. For easy reference, the major parameters are also printed in natural units.

Line 1 shows the transmit power, and is chosen to provide adequate signal margin within the constraints of feasibility for space-qualifiable hardware. The second line shows the optical transmittance of the transmit optics path. This term is a function of the optical design of the transmitter and the optical elements necessary to form and steer the transmit beam. These losses are discussed in Section 2.2.

The radar transmit antenna gain, relative to an isotropic (4π steradian) radiator, is shown in line 3, and is discussed in Section 2.3, as is the transmit antenna pointing loss term, shown on line 4.

The free space loss terms are computed for the range and wavelength shown in the heading, and appear (for passive target ranging) in lines 5 and 9. Atmospheric losses are also shown in two places, lines 6 and 8. These losses are discussed in Section 2.4.

The target gain product is shown in line 7, and discussed in Appendix F. The radar receive antenna gain, line 10, is discussed in Section 2.3., and the receiver optical losses, line 11, are discussed in Section 2.2.

The received signal power, line 12, in dBW, is simply the sum of the first eleven lines. Most of the systems considered in this study employed pulses of optical energy for ranging. Line 13 shows the pulse repetition rate, and line 12 minus line 13 defines the energy per pulse, shown in line 14.

The energy per photon, is defined as $h\nu$, where h is Plank's constant[2] (6.6256×10^{-34} Js) and ν is the optical frequency (c/λ). This is shown in line 15 (also line 25), and line 14 minus line 15 yields the mean number of received signal photons per pulse, line 16, delivered to the photodetector. Line 17 shows the detector quantum efficiency, and the sum of lines 16 and 17 yields the mean number of detected signal photoelectrons per pulse, shown on line 18.

Many of the potential laser ranging concepts are severely background limited, and all are affected to some extent. Lines 19 through 30 show the background level calculations. The background source, for most of the links, is the sunlit Earth. The background calculation is similar to the signal calculation. The background radiance, in watts/m^2-angstrom-steradian, is shown in line 19. This is documented in Section 2.4. The receiver field-of-view, steradians, is shown in line 20. Note that the field-of-view in steradians is approximately $\pi/4$ times the square of the full plane FOV (in radians). This approximation is virtually exact (within 0.001 dB) for fields-of-view less than 0.1 radians.

An optical filter is used to reduce background illumination, and the filter bandwidth, in Angstroms, is shown in line 21. The receiver antenna area (m^2) is shown in line 22, and the receiver optical losses in line 23 (same as line 11). The received background power, line 24, is simply the sum of lines 19 through 23.

[2] Abramowitz and Stegun, "Handbook of Mathematical Functions," Dover Publications, New York, 5th Edition, pg 7.

Conversion from background power to photoelectrons per pulse is accomplished by converting first to photons/sec (line 26), then, considering quantum efficiency (line 27), to detected photoelectrons per second (line 28). The detection techniques for the candidate laser measurement concepts all employ some form of time gating of the detector output. The effective receiver gate width (line 29), summed with the background rate yields the detected background photoelectrons per gate (or pulse), shown in line 30.

Following line 30, the final margin calculation is shown. Line 18 is repeated, for convenience, followed by the required photoelectrons per pulse, line 31, and the signal margin in line 32. The required signal photoelectrons per pulse are discussed in Appendix F, and are either input as a specified parameter or calculated based on the detection technique and observed background level.

Appendix D presents the link margin analysis summaries for the various links, the computer program used to perform the summary analyses, and the specific parameters used.

2.2 OPTICAL EFFICIENCIES. The transmittance of the receiving and transmitting optics is a function of the number and types of optical elements employed, and the coatings used. A conservative estimate of the number and type of elements for a typical optics system was made, and that figure was used for all terminals. Table 2 summarizes the element counts, the efficiency per device, and the total efficiency computation for the typical terminal receive and transmit optics. The most significant loss element is the narrow band optical filter. In the range of optical pass-bands from 1 to 100 Å, the filter efficiency is not grossly a function of bandwidth, or wavelength for that matter, but rather a strong function of the materials, techniques, and the supplier. The available data shows peak transmissibilities ranging from ∿40% to as high as 85% in the vicinity of 5Å bandwidths in the visible and near IR frequencies. Sixty percent transmittance is used as a reasonable compromise value.

2.3 ANTENNA GAIN AND POINTING LOSS CALCULATIONS

2.3.1 HATRS. The transmit antenna gains for the candidate HATRS laser radar systems are required to be relatively large, to permit operation with passive targets at long range. The receive antenna gains, similarly, are required to be relatively large. The receive antenna size varies from 0.6m to 1.0m dia-

TABLE 2
TYPICAL RADAR TERMINAL OPTICAL EFFICIENCIES

INTERFACE	TRANSMIT	RECEIVE
Reflecting Surfaces	9 @ 0.99	11 @ 0.99
Transmissive Elements	5 @ 0.98	5 @ 0.98
Bandpass Filter	NA	0.6
Beamsplitter	2 @ 0.98	2 @ 0.98
TOTAL	0.793	0.466
Allocated	0.80(-0.98 dB)	0.40(-3.98 dB)

meter, and is assumed to be a centrally obscured (Cassegrain) configuration. The receive antenna gain is simply,

$$G_R = (\pi/\lambda)^2 \, (D_P^2 - D_S^2) \tag{4}$$

D_P = primary diameter

D_S = secondary diameter

The transmit antenna gain is a function of the beam intensity profile, dimensions, and truncation. The nominal transmit beam has a Gaussian intensity distribution. We have assumed an offset feed arrangement is used, as shown in Figure 1, in order to use the same primary optics as the receiver. The transmit beam diameter is truncated by the beam combining mirror, and the beam diameter shown in the primary aperture is the truncation diameter expanded to final size. The far-field gain of a truncated Gaussian beam (on-axis) is given by Equation (5).

$$G_T = 2(\pi \, D_o/\lambda)^2 \left[1 - e^{-D_T^2/D_o^2}\right]^2 \tag{5}$$

D_T = truncation diameter (m)

D_o = $1/e^2$ power diameter of the beam (m)

OPTICS ARRANGEMENT

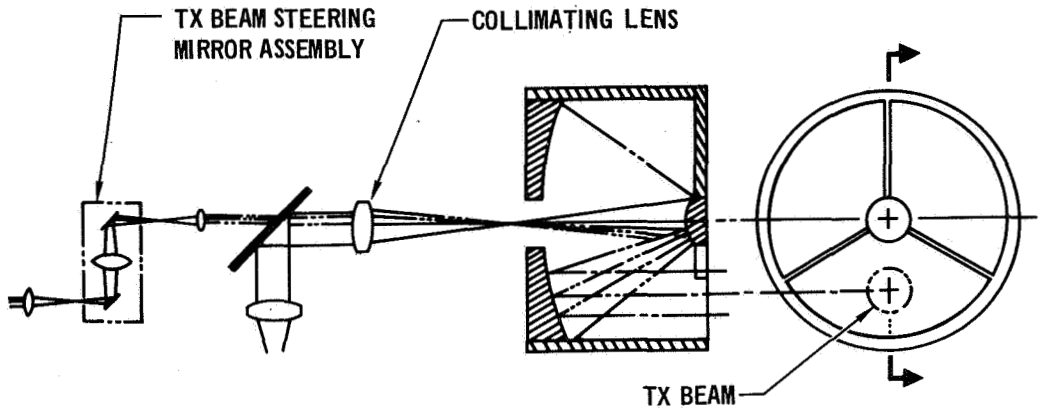

FIGURE 1

The truncation at the beam combining mirror also results in a loss of receive antenna gain. The significance of the losses to the transmit and receive gain is dependant on the desired transmit beamwidth (and gain). If the image of the transmit beam truncation aperture does not overlap the secondary or fall outside of the primary, then the product of the receive and transmit antenna gains is given in Equation (6).

$$G_R G_T = 2\left(\pi D_o/\lambda\right)^2\left(\pi D_p/\lambda\right)^2\left(1-D_S^2/D_P^2 - D_T^2/D_P^2\right)\left(1 - e^{-D_T^2/D_o^2}\right)^2 \qquad (6)$$

The two loss terms, on the right, can reduce the net signal significantly unless considerable care is used to choose the parameters. Since the transmit beam is truncated, the far field antenna pattern is no longer exactly Gaussian. For the systems considered here, the approximation is relatively good. This can be seen by computing the far field pattern of the truncated beam.[3]

[3] Buck, A. L., "The Radiation Pattern of a Truncated Gaussian Aperture Distribution," Proceedings of the IEEE, March 1967, pg 448.

$$E\{K\theta\} = \int_0^{r_T} e^{-r^2/r_o^2} J_o(K\theta r)\, r\, dr \tag{7}$$

$J_o(x)$ = Bessel function of the first kind

$K = 2\pi/\lambda$

θ = angle off boresight, radians

$r_o = e^{-2}$ power beam radius

r_T = truncation radius

Clearly,

$$E\{0\} = \frac{1}{2} r_o^2 \left(1 - e^{-r_T^2/r_o^2}\right) \tag{8}$$

Equation (7) can be reduced to a Bessel function series as shown in Appendix G. The result is,

$$E\{K\theta\} = \frac{1}{2} r_o^2 \sum_{n=1}^{\infty} \left(\frac{2r_T}{K\theta\, r_o^2}\right)^n J_n(K\theta r_T)\, e^{-r_T^2/r_o^2} \tag{9}$$

Thus,

$$\frac{G(\theta)}{G(o)} = \left[\frac{\sum_{n=1}^{\infty} \left(\frac{2r_T}{K\theta\, r_o^2}\right)^n J_n(K\theta r_T)\, e^{-r_T^2/r_o^2}}{\left(1 - e^{-r_T^2/r_o^2}\right)}\right]^2 \tag{10}$$

Equation (10) is thus the gain loss for the truncated Gaussian beam as a function of angle off boresight. Combining (10) and (5) results in Equation (11).

$$G_T(\theta) = 2(\pi D_o/\lambda)^2 \left[\sum_{n=1}^{\infty} \left(\frac{2r_T}{K\theta\, r_o^2}\right)^n J_n(K\theta r_T)\right]^2 e^{-2r_T^2/r_o^2} \tag{11}$$

By expanding the Bessel functions in series form, and rearranging terms, the expression in Equation (12) is obtained, and was used for the computation of the radiation pattern plotted in Figure 2.

where,

$$e_J(x) = \sum_{K=0}^{J} \frac{x^K}{K!} = \text{the incomplete exponential}$$

Figure 2 shows that the effect of truncation is to decrease the on axis gain, and slightly broaden the far field pattern. The pattern calculated for the truncated Gaussian beam can be approximated quite well for pointing errors to about 2.8 microradians as a nontruncated Gaussian beam with an on-axis gain equal to the gain of the truncated Gaussian beam.

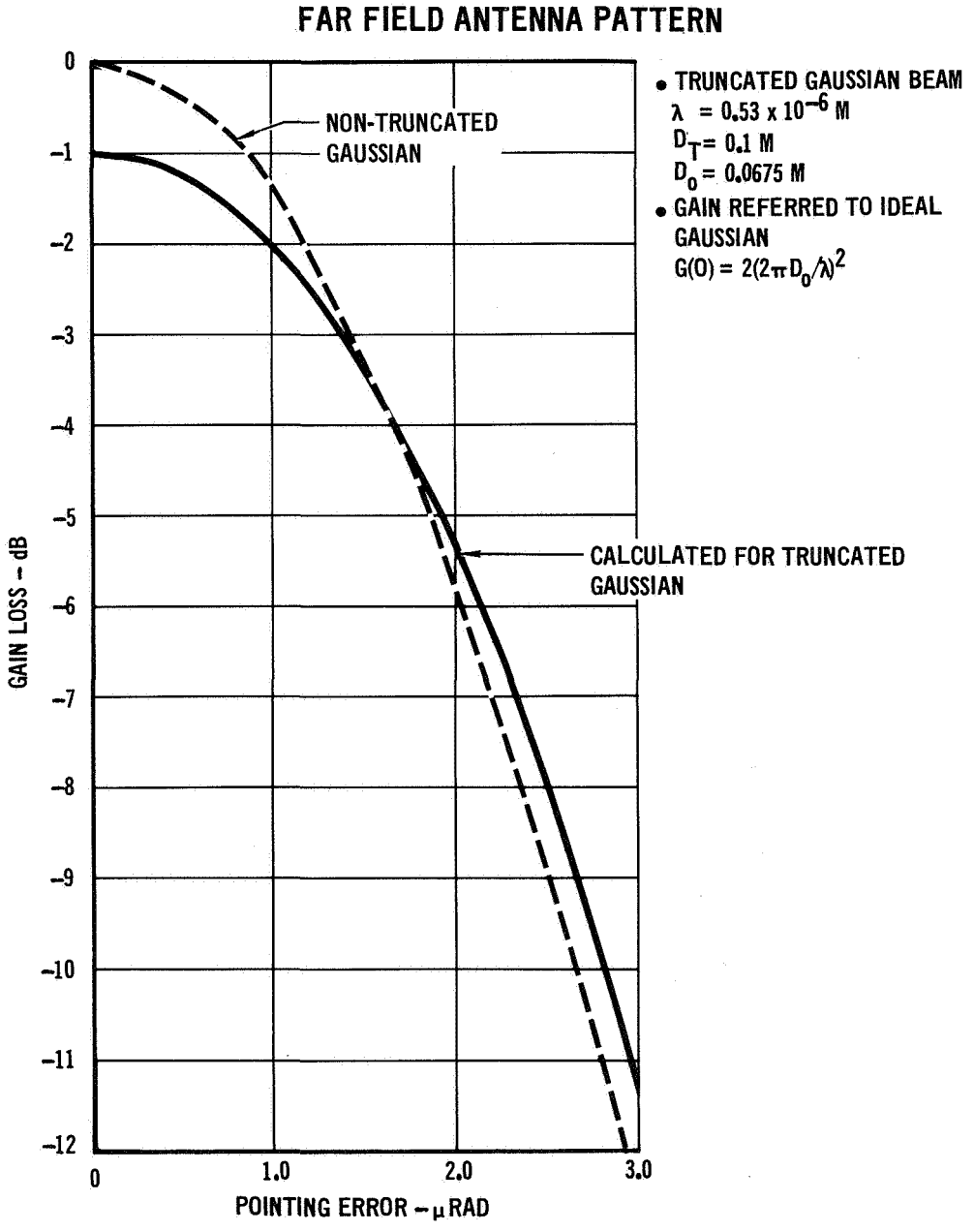

FIGURE 2

2.4 MISCELLANEOUS LINK PARAMETERS

2.4.1 Background Noise and Sources. Most of the links considered in this study operate predominantly with the Earth in the field-of-view of the receiver. The background radiance of the sunlit Earth, considering only diffuse reflection,[4] is ∿0.017 watts/m^2-Å-steradian at 0.53 μm wavelength, and 0.00875 watts/m^2-Å-steradian at 1.06 μm wavelength.

An active LATS receiver would normally view deep space, with a reasonably large field-of-view. The moon, under these conditions, is the brightest body in the sky other than the sun, and has a spectral radiance[4] of 4.7×10^{-3} W/m^2-Å-steradian at 0.53 μm and 1.6×10^{-3} W/m^2-Å-steradian at 1.06 μm.

An active ground-based terminal would see atmospheric scattered sunlight during daylight operation, which has a spectral radiance[4] of about 3.5×10^{-3} W/m^2-Å-steradian at 0.53 μm and 2.5×10^{-3} W/m^2-Å-steradian at 1.06 μm.

These values have been used in the link margin analyses. In all cases, operation with the sun (or strong specular solar reflections) in the field-of-view has not been considered either feasible or necessary.

2.4.2 Atmospheric Transmissibility - For links involving ground targets, two loss mechanisms have been considered, nominal atmospheric attenuation due to molecular and aerosol absorption and scattering, and degradations due to scintillation effects. The nominal atmospheric transmission model is shown in Figure 3 for 0.53 μm and 1.06 μm wavelengths, as a function of ground terminal altitude for zenith angles of 20°, 40° and 60°. The data is for a clear atmosphere, and Elterman's[5] model was used. At modest zenith angles, an atmospheric transmissibility (each way) of ∿60-70% is reasonable at 0.53 μm and 80%-90% at 1.06μm.

For link analysis purposes, we have arbitrarily allocated a 3 dB loss term to account for atmospheric scintillation. The basis for this allocation is an assumption that each ground target will be composed of a number of retro-reflectors. We further assumed that the retro-reflector spacing and arrangement would be such that each retro-reflector effectively contributing to the return signal energy could be considered as scintillating independently. Consequently,

[4] Pratt, W. K., "Laser Communication Systems," John Wiley & Sons, New York (1969), pg 121-125.

[5] Elterman, L., "UV, Visible, and IR Attenuation for Altitudes to 50 km, 1968," AFCRL, ERP NO. 285 (1968).

even under severe scintillation conditions, the worst case fade depth should be relatively modest if the number of retro-reflectors contributing to the return is large.

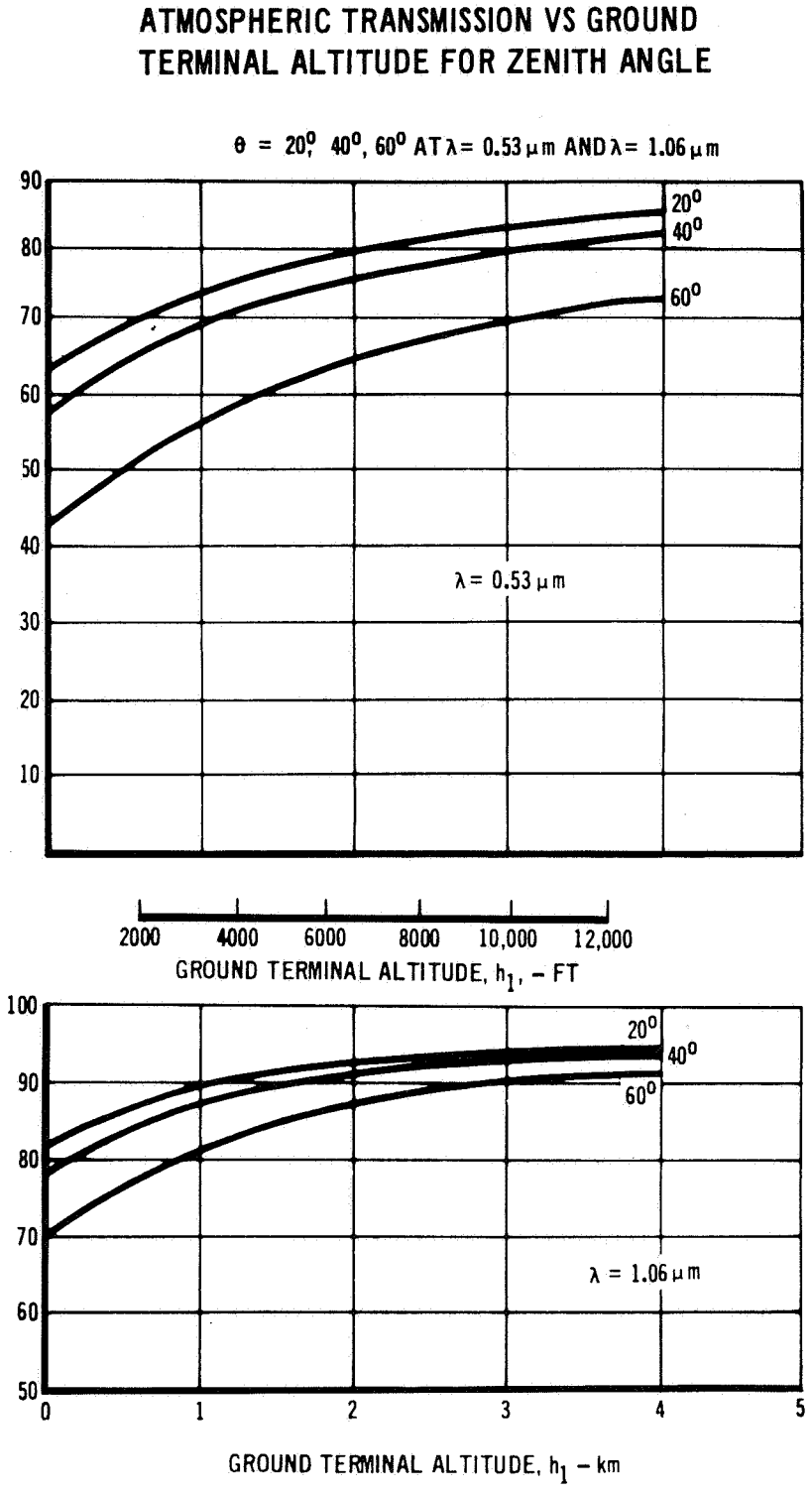

FIGURE 3

2.5 TARGET SIGNATURE AND GAIN PRODUCT. The passive targets considered in this study are all augmented with one or more high quality, optical retro-reflectors, also referred to as cube-corners or corner reflectors. In order to determine the amount of signal energy returned to the radar, it is necessary to determine the energy returned from each reflector on the target, and to combine the reflections from each reflector at the radar. The return from each reflector is a function of the angle of incidence of the incoming wave, and the magnitude and direction of the velocity aberration vector, also referred to as point-ahead angle. The individual reflector gains were computed as discussed in Appendix F.

2.6 SIGNAL POWER REQUIREMENTS. The required signal photoelectrons (pe) per pulse, to achieve the desired range estimation accuracy goals, is a function of the laser pulse shape, the target characteristics, and the range estimation process employed. The candidate range estimation processes may be categorized as estimation processes which are optimum, in some sense, and those which are sub-optimum but offer implementation advantages. These range estimation processes depend on sensing the time when a laser pulse is emitted and when the reflected pulse is detected. The time of arrival (TOA) of the reflected pulse can be estimated in many ways.

A TOA estimation process, which is optimum in a maximum likelihood sense, is described in Appendix E. Also discussed and analyzed in Appendix E are several other estimation processes which offer implementation advantages, and approach the performance of the maximum likelihood estimator. These techniques and their analytical treatments are appropriate for shot-noise limited applications where the target is a single cube-corner retro-reflector in a nondispersive channel.

However, when the target is composed of multiple retro-reflectors, which is characteristic of targets which have been synthesized for the HATRS links, scintillation is encountered, due to coherent interference, at the detectors, resulting from summing the returns from each retro-reflector. This type of scintillation is discussed in Appendix F, and the mean detected signal amplitude is shown to have an exponential distribution in the limiting case.

The remaining system functions which are covered in the link margin analysis program result from the postulated use of a ground based beacon, of some sort, to aid in the initial acquisition (spacially) of a set of ground-based retro-reflectors clustered in a small geographical area on the ground. Two types of

beacon systems were hypothesized to span the spectrum of feasible types for active ground beacons.

First, a relatively high PRF, low energy per pulse system, such as might be obtained from a GaAs laser diode beacon, was postulated. For this technique, the angle tracking loop bandwidth and the beacon PRF determine the required beacon energy in pe/pulse.

The other type of beacon considered was a low PRF, modest energy per pulse beacon, similar to existing ruby lasers. In this case, the spatial acquisition and tracking function is better described as a bang-bang system, where the primary considerations are false alarm and missed detection probabilities. The computation algorithm which is employed for this purpose is based on estimating the threshold setting, and subsequently the required signal, to satisfy the Chernov bounds.[6] This technique is modestly conservative, and was chosen to evade numerical difficulties for large signal and background level conditions. These bounds are determined, using transform techniques, as shown in Equations (12) through (17).

The second moment generating function is defined as,

$$\psi_x(s) \triangleq \ln \left[\int_{-\infty}^{\infty} f_x(x)\ e^{sx}\ dx \right] \tag{12}$$

For a Poisson process, with mean intensity m,

$$\psi_x(s) = \ln \left[\sum_{k=0}^{\infty} \frac{m^k}{k!} e^{-m+sk} \right]$$

$$= m(e^s - 1) \tag{13}$$

The Chernov bounds are then, for false alarms,

$$P_{FA} = \Pr\{x > \gamma\} \leq \exp\{\psi_x(s) - s\psi_x^1(s)\} \Big|_{\gamma = \psi_x^1(s)} \tag{14}$$

$$\text{provided } s > 0$$

(6) Van Trees, H.L., "Detection, Estimation, and Modulation, Vol. I", Wiley and Sons, New York (1967), pages 121-122

and, for missed detection,

$$P_{MD} = Pr\{x < \gamma\} \leq \exp\{\psi_x(s) - s\psi_x^1(s)\} \Big|_{\gamma = \psi_x^1(s)} \qquad (15)$$

provided $s < o$

In these expressions, γ is the threshold setting in photo-electrons.

Then, with $m = n_b T$, equation (14) bounds the false alarm probability. Thus,

$$P_{FA} \leq \exp\{\gamma - m - \gamma \ln(\gamma/m)\}, \qquad m = n_b T, \quad \gamma > m \qquad (16)$$

The first step, therefore is to find the threshold setting, γ, which just satisfies this criterion. Then, with $m = n_s + n_b T$, we iteratively solve to find the value of m, hence n_s, which just satisfies Equation (17), derived from Equation (15).

$$P_{MD} \leq \exp\{\gamma - m - \gamma \ln(\gamma/m)\}, \qquad m = n_s + n_b T, \quad \gamma < m \qquad (17)$$

These equations and algorithms have been implemented in the link margin analysis program presented in Appendix D.

3.0 LASER RANGING SYSTEM CONFIGURATIONS

The laser ranging system configurations developed during the study were selected to maximize the achievable ranging accuracy and to be compatible with a variety of targets. Two major active terminals were defined. First, a terminal suitable for use in a high altitude, transmit/receive satellite (HATRS), was defined to operate with low altitude target satellites (LATS), either active or passive, and ground based retro-reflectors. The other terminal was configured for use as an experiment carried on a Spacelab mission, and is primarily intended for operation with ground-based retro-reflectors. Target configurations were defined for both the active and the passive targets, either orbital or ground based.

System performance is limited by the type of laser selected. From a ranging accuracy standpoint, the most attractive laser is a mode-locked, cavity dumped Nd:YAG laser, which outputs very narrow (<0.2 ns) pulses of modest energy. However, this laser does not exist in space qualified form at this time, although all of the (known) necessary elements have been developed for different applications. Thus, it was deemed advisable to have an alternate system configuration based on the current state-of-the-art, a Q-switched, cavity dumped Nd:YAG laser, with a characteristic pulse-width of 4 to 6 ns. The choice between the two laser types is a matter of risk assessment. In the narrow pulse case, the risk is principally that unknown factors may delay the development of the new laser configuration. The risk, for the more conventional laser techniques is on developing a space qualified laser with sufficient amplitude and pulse shape stability to enable meeting an over-all rms ranging accuracy equivalent to 1/30th to 1/50th of the pulse width, which is a nontrival goal under the best of circumstances. There are, of course, other components which present development risks. These components, however, are common to both concepts, and limit, if at all, only the time scale for implementation.

3.1 HATRS TERMINAL. The HATRS terminal is configured to operate with a variety of targets at very long range. The key terminal parameters postulated for this study are summarized in Table 3 for both the short pulse and the long pulse laser configurations.

TABLE 3
HATRS TERMINAL PARAMETERS

PARAMETER	SHORT PULSE CONFIGURATION	LONG PULSE CONFIGURATION
Wavelength	0.53 μm	0.53 μm
Pulsewidth	0.2 ns	4.0 ns
Transmit Energy	1.0 mJ/pulse	10.0 mJ/pulse
PRF	10 pps	10 pps
Average Transmit Power	10.0 mW	100.0 mW
Transmit Beamwidth	5.0 μrad	5.0 μrad
Telescope Primary Diameter	0.61m	1.0m
Detector Quantum Efficiency	25%	25%
Detector Field of View	50. μrad	50. μrad
Optical Filter Bandwidth	5Å	5Å

The physical configuration which was adopted is illustrated in Figure 4. The interface with the host spacecraft may be either hard or gimbals, depending on the host spacecraft design and functional requirements. The basic assumption is provision of a precision optical bench, which supports all alignment critical components. The alignment critical components include the transmit and receive optics, the laser and the detectors, and the attitude reference sensors. The attitude reference system is a steller-inertial system which employs strapdown precision rate-integrating gyros, strapdown star sensors, and a radar telescope focal plane mounted star tracker to establish and maintain a precision attitude reference of the radar receiver boresight vector.

A typical ranging operation begins with establishing an inertial attitude reference update, accomplished by slewing the receiver telescope to one or more known stars. The star position with respect to the receiver boresight is established, using either an offset star sensor located on the telescope focal plane or the radar system quadrant PMT detectors with the narrow bandwidth optical filters temporarily removed. Once the attitude reference is established, the telescope can be open-loop pointed at the expected target position. The radar system employs a narrow transmit beam and a relatively wide receiver field-of-view, thus the acquisition process is principally a matter of scanning the transmit beam until the target is illuminated.

HATRS TERMINAL PHYSICAL CONFIGURATION

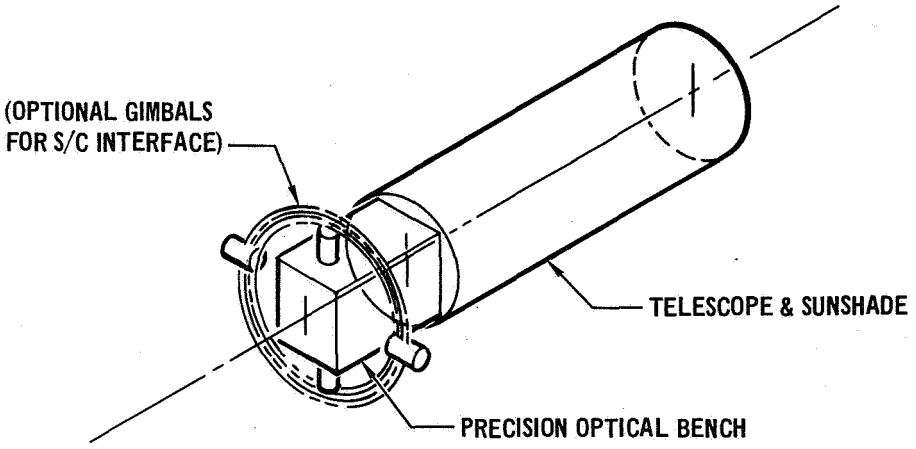

FIGURE 4

The nominal region of pointing uncertainty includes components due to uncertainty in both the HATRS and the target ephemeris data, attitude reference errors, and transmit/receive alignment errors. Since the transmit and receive boresight vectors must be offset to account for velocity aberration (point-ahead angle) effects, there is also a transmit beam deflection drift and scale factor error included in the pointing uncertainty.

Once the target is illuminated, the receiver detects the angle of arrival of the reflected signal, and slews to zero the mean receiver pointing error. The alignment error between the transmit beam and the receiver boresight is detected and corrected by dithering the transmit beam. The system maintains pointing control using the inertial reference system; the corrections are filtered and used to eliminate bias errors. Range measurements are obtained in a similar manner. For spatial acquisition, the range gate is widened to account for range prediction uncertainties. Once the target is reliably detected, a split-gate range tracker is used to extract a range prediction error estimate which is filtered and used to bias the range prediction to zero the mean range tracking error.

One implementation approach is shown summarized in Figure 5 . A central computer is used to perform the necessary data processing and prediction functions. A typical range measurement begins with selection of a nominal transmit pulse departure time. This departure time is chosen to ensure that the receiver will

not be blanked by the TR shutter at a time when a return pulse is expected. The desired departure time is delivered to the pulse generation electronics unit (PGE). The PGE compares the commanded departure time with the central clock time, and at a programmed time prior to coincidence, the PGE initiates the pulse generation sequence. The sequence begins by energizing the lamp pump. Subsequently, the cavity is Q-switched, and lasing begins. For the mode-locked laser technique, the mode-locking RF signal is also applied to the intracavity mode-locking element. After the laser has reached stable conditions, the cavity is dumped and the high energy pulse proceeds through the optics system. Prior to dumping the cavity, the receiver is temporarily blanked by a switchable attenuator or shutter, and a sizable bias voltage is applied to the quadrant PMTs photocathodes to gate them off.

The laser output pulse passes through a frequency doubler. Then a small amount of the optical pulse energy is extracted and delivered to the pulse departure time detector. The output from this detector is delivered to a threshold detector, which strobes the departure time estimator at threshold crossing. The departure time detector output is also integrated and it's magnitude is converted to digital format for subsequent processing in the central computer to correct the departure time estimate for actual pulse amplitude. The optical pulse proceeds through the transmit beam steering mirror assembly, which establishes the desired transmit offset angles. The pulse then passes through a hole in the beam combining mirror, and exits the telescope assembly in an offset position, as shown in Figure 5. Subsequently, the switchable attenuator in the receiver is opened.

The next pulse arrival time, estimated from the vehicle ephemeris data, the pulse departure time, and the filtered range tracking error, is delivered to the receiver gate timer. At a programmed time prior to coincidence with the central clock time, the receive gate timer issues a PMT enable command, and subsequently issues gate sample commands as shown schematically in the figure. Four sampling modules, one for each PMT, are used to measure the intensity of the received signal at three sampling times, the early gate, the center gate, and the late gate sample times. The sampling modules employ a sliding window integrator technique to measure the PMT output during the three overlapping time periods. The sampling module outputs are then converted to digital data, and delivered to the central computer for subsequent processing.

A B

FUNCTIONAL BLOCK DIAGRAM – HATRS LASER RANGING SYSTEM

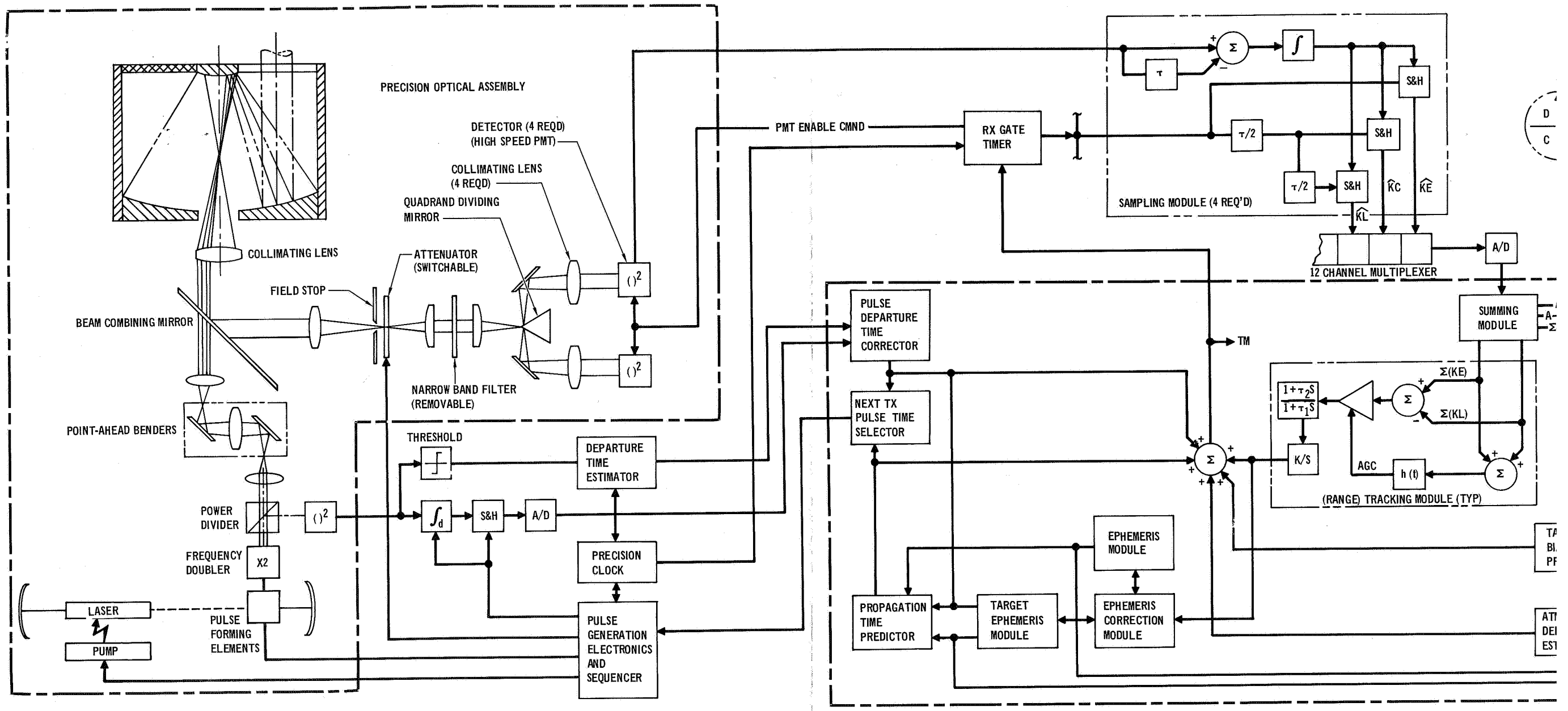

FIGURE 5

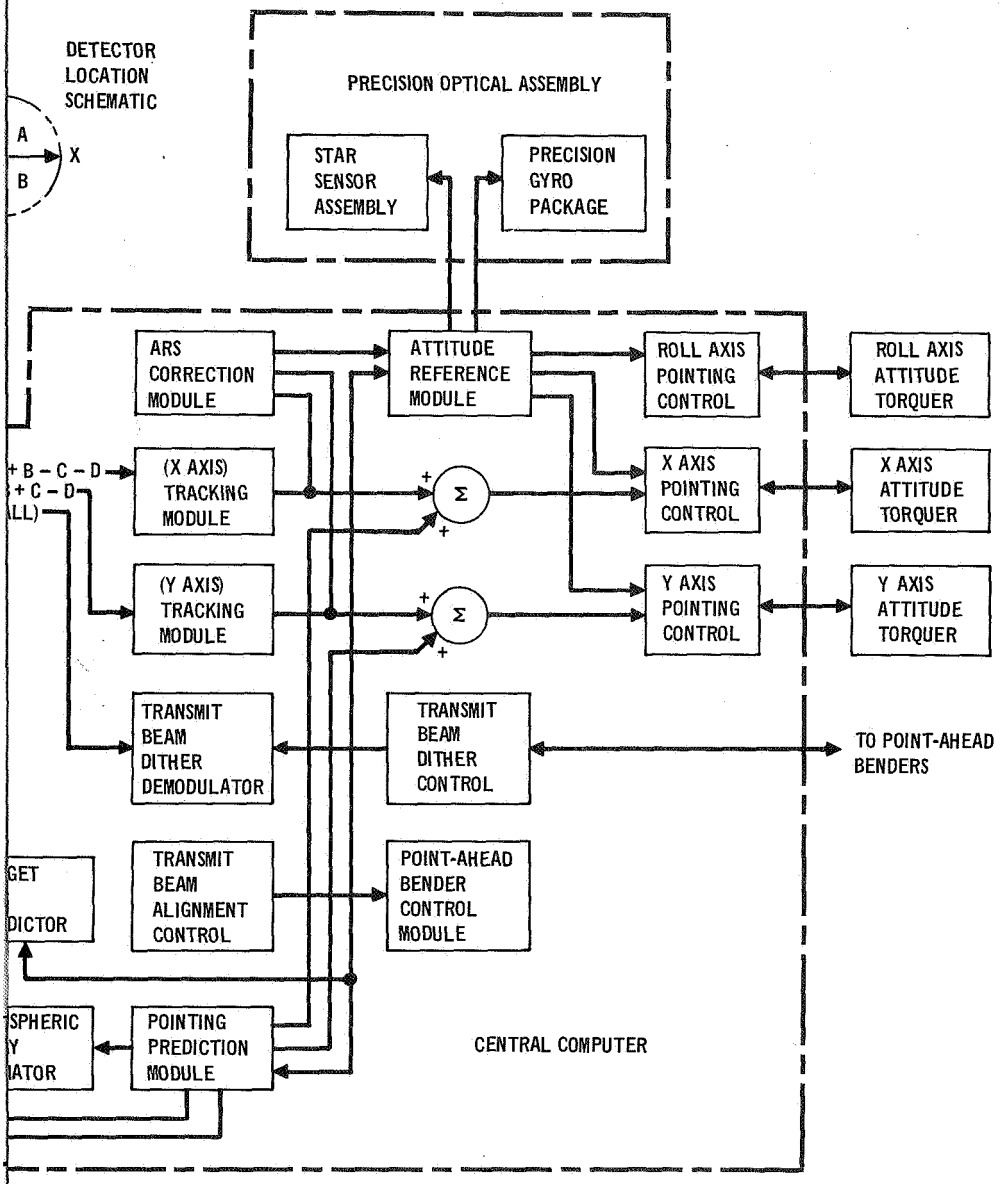
DETECTOR
LOCATION
SCHEMATIC
A
B
X
PRECISION OPTICAL ASSEMBLY
STAR
SENSOR
ASSEMBLY
PRECISION
GYRO
PACKAGE
ARS
CORRECTION
MODULE
ATTITUDE
REFERENCE
MODULE
ROLL AXIS
POINTING
CONTROL
ROLL AXIS
ATTITUDE
TORQUER
+ B – C – D
+ C – D
LL)
(X AXIS)
TRACKING
MODULE
Σ
X AXIS
POINTING
CONTROL
X AXIS
ATTITUDE
TORQUER
(Y AXIS)
TRACKING
MODULE
Σ
Y AXIS
POINTING
CONTROL
Y AXIS
ATTITUDE
TORQUER
TRANSMIT
BEAM
DITHER
DEMODULATOR
TRANSMIT
BEAM
DITHER
CONTROL
TO POINT-AHEAD
BENDERS
GET
DICTOR
TRANSMIT
BEAM
ALIGNMENT
CONTROL
POINT-AHEAD
BENDER
CONTROL
MODULE
SPHERIC
Y
IATOR
POINTING
PREDICTION
MODULE
CENTRAL COMPUTER

The system can be most readily converted to operate with active targets by assuming two color operation, i.e., the HATRS radar transmits at 0.53 μm, and the target transmits at 1.06 μm. This would require inserting a dichroic beam splitter in the receive optics, and adding a detector, probably a silicon photodiode, or semiconductor photocathode PMT. The active target receiver signal processing will differ significantly from the passive target receiver signal processing techniques. The operational concept is based on recording pulse departure times and pulse arrival times at both ends of the link, with no attempt made to synchronize or provide a transponder function in the target. This free running operation provides all of the data necessary for subsequent estimation of range, assuming the data from both terminals is available. Both the HATRS and LATS transmit beamwidths and receiver-fields of view are selected to allow totally open loop pointing in this mode.

The selected configuration for the HATRS active LATS receiver is shown in Figure 6 and uses a PMT detector with a weighted counter approximation of a maximum likelihood time-of-arrival estimator. If a silicon photodiode detector were chosen, instead of the PMT, the time-of-arrival estimator module would be modified slightly to replace the weighted counter with an analog matched filter, since the signal would be preamplifier noise limited. In either case, the AGC amplifier maximum gain is clamped to minimize false alarms during high background level conditions.

3.2 SPACELAB LASER RADAR EXPERIMENT. The Spacelab radar terminal configuration employs many of the concepts evolved for the HATRS terminal, but is significantly different in several important areas. Table 4 shows the key terminal parameters assumed for each of the two candidate laser techniques.

One major difference between the HATRS and Spacelab terminal is inclusion of a two-color ranging technique in the Spacelab terminal to permit assessment of atmospheric delay by simultaneous ranging at 0.53 μm and 1.06 μm wavelength. A second significant difference is that the Spacelab terminal does not track the returned signal angle of arrival. The pointing technique is principally open-loop, with provisions for a ground beacon angle of arrival measurement to initialize the pointing system at the start of a ranging pass over a cluster of ground-based retroreflectors. Third, the range estimation technique is based on a pulse-by-pulse detection process, rather than by tracking the average signal over a number of pulses. Finally, less stringent pointing accuracy requirements and Shuttle attitude

HATRS ACTIVE LATS RECEIVER

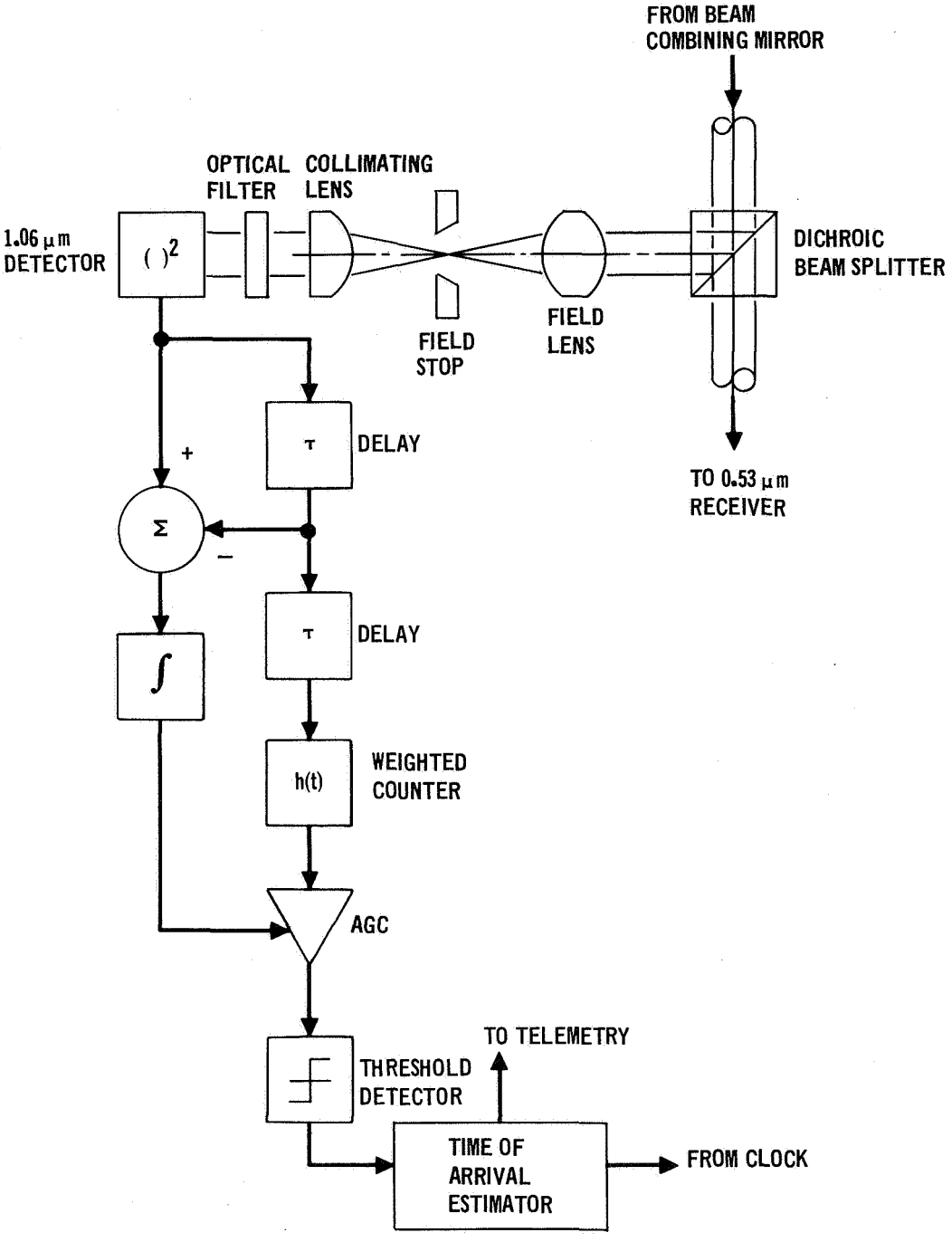

FIGURE 6

TABLE 4
SPACE LAB TERMINAL PARAMETERS

PARAMETER	SHORT PULSE CONFIGURATION		LONG PULSE CONFIGURATION	
Wavelength	0.53 μm	1.06 μm	0.53 μm	1.06 μm
Pulsewidth	0.2 ns	0.2 ns	4.0 ns	4.0 ns
Transmit Energy	1.0 mJ/pulse	4.0 mJ/pulse	10.0 mJ/pulse	40.0 mJ/pulse
PRF	1 pps	1 pps	1 pps	1 pps
Transmit Power	1.0 mW	4.0 mW	10 mW	40 mW
Transmit Beamwidth	375 μrad	750 μrad	375 μrad	750 μrad
Telescope Primary Diameter	0.3m	0.3m	0.46m	0.46m
Detector Quantum Efficiency	25%	1.0%	25%	1.0%
Detector Field of View	375 μrad	750 μrad	375 μrad	750 μrad
Optical Filter Bandwidth	5Å	5Å	5Å	5Å

motion disturbances are satisfied with a gimballed Cassegrain telescope in a Coude' configuration. Alternatively, a fixed telescope with a gimballed flat mirror could be employed, subject to installation limitations.

Figure 7 is a functional block diagram of the selected Spacelab laser configuration, and shows representative implementation techniques for these functions. The attitude reference sensors are considerably less critical than for the HATRS terminal, however they must still be tightly coupled to the laser radar optical reference bench.

Since the system functions on a pulse-by-pulse basis, transfer from one ground target to another can be accomplished readily between pulses, particularly if the angular separation is within the dynamic range of the tracking benders. The term, benders, is used generically, since it appears that torsion-bar-mounted torque motors may be more rugged and reliable than piezo-electric bender bimorphs for beam steering functions.

Since the Spacelab is in a low altitude orbit, for a relatively short mission duration, and is subject to potentially sizable ephemeris changing perturbations, difficulties in converting ranging data into data of geodedic significance are anticipated. One possible solution is to define a Spacelab laser radar experiment which provides "simultaneous" ranging measurements with two or more ground

A

B

FUNCTIONAL BLOCK DIAGRAM SPACE-LAB LASER RADAR EXPERIMENT

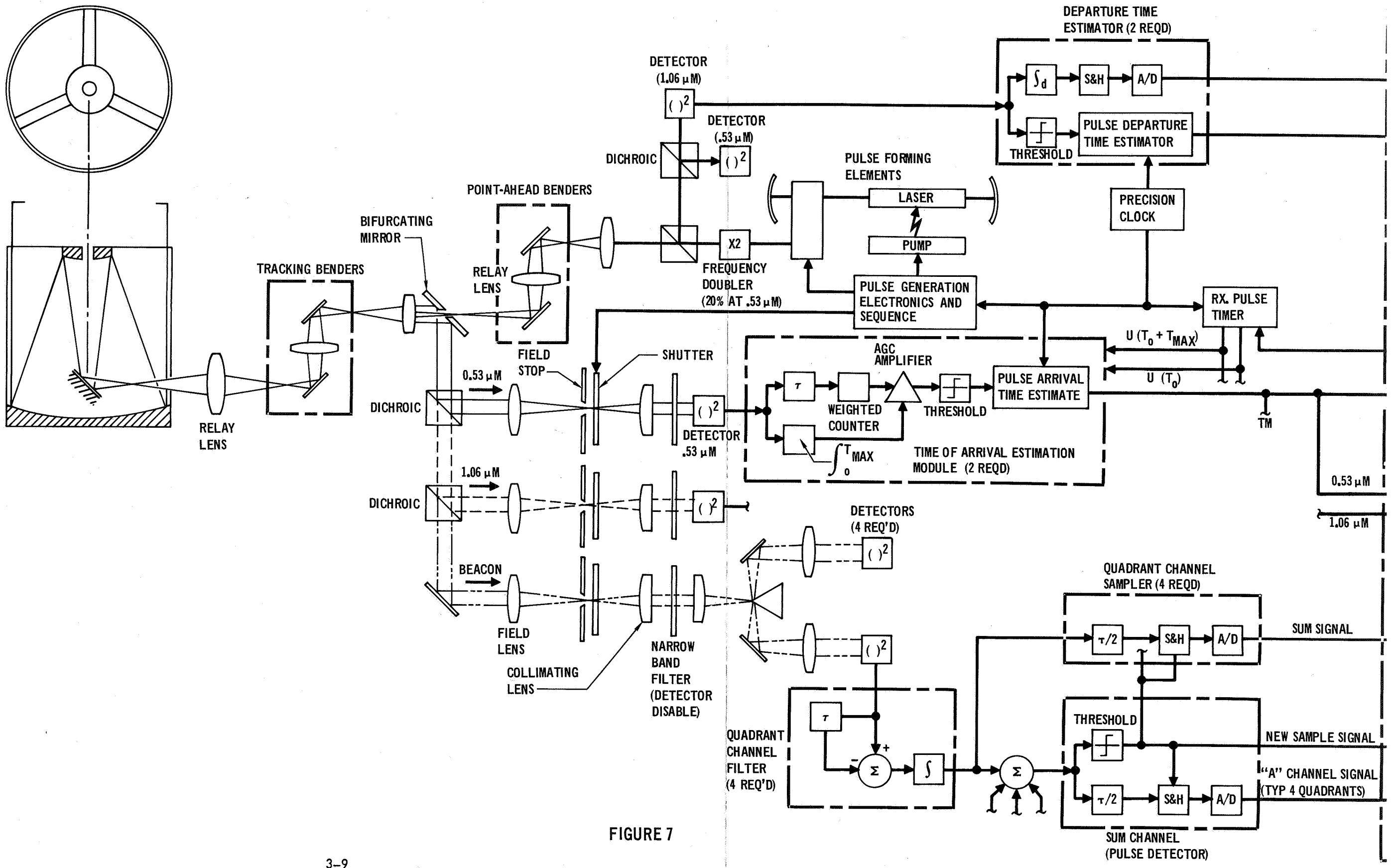

FIGURE 7

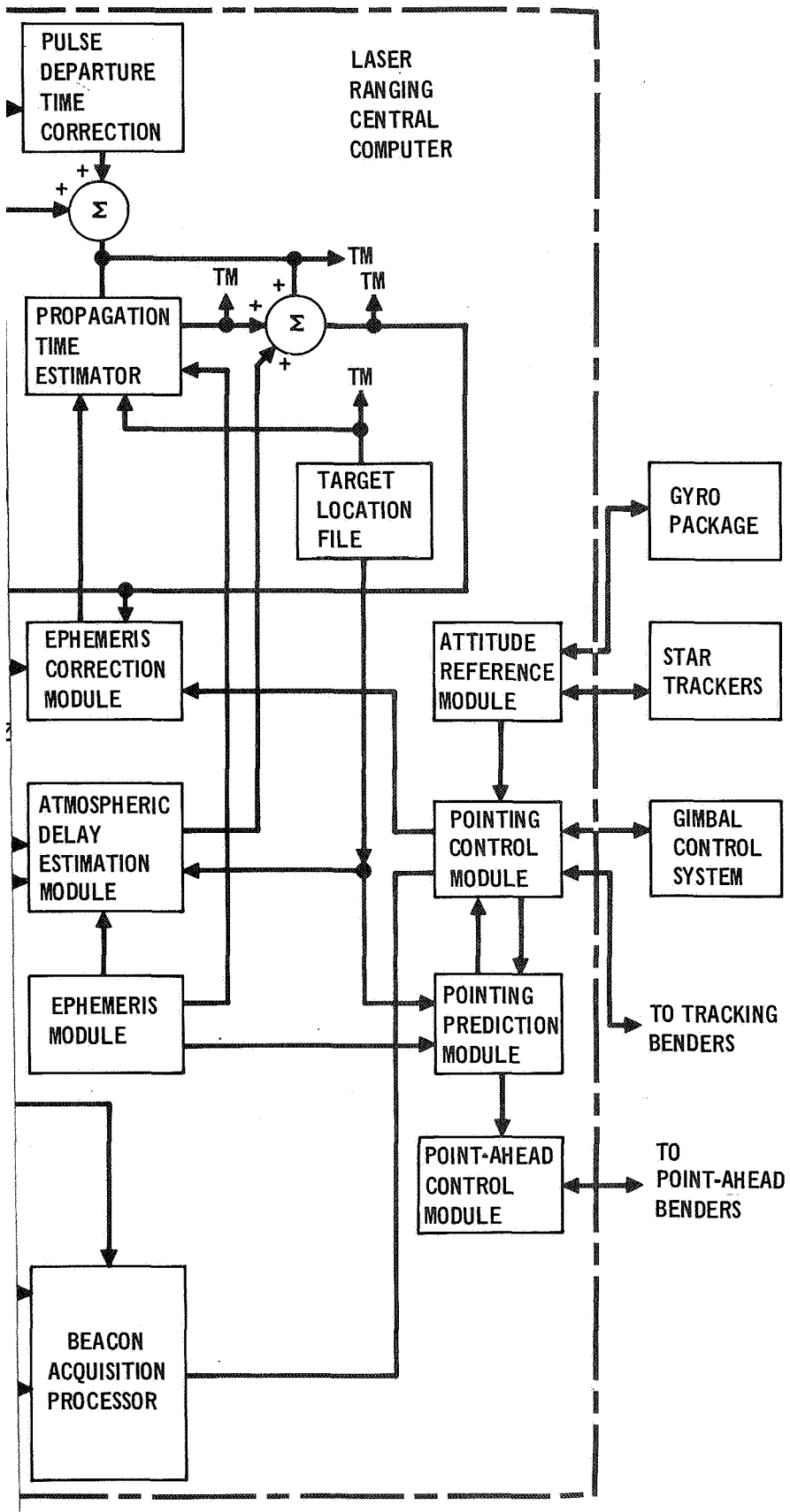
PULSE DEPARTURE TIME CORRECTION
LASER RANGING CENTRAL COMPUTER
Σ
TM
TM
TM
TM
PROPAGATION TIME ESTIMATOR
TARGET LOCATION FILE
GYRO PACKAGE
EPHEMERIS CORRECTION MODULE
ATTITUDE REFERENCE MODULE
STAR TRACKERS
ATMOSPHERIC DELAY ESTIMATION MODULE
POINTING CONTROL MODULE
GIMBAL CONTROL SYSTEM
EPHEMERIS MODULE
POINTING PREDICTION MODULE
TO TRACKING BENDERS
POINT-AHEAD CONTROL MODULE
TO POINT-AHEAD BENDERS
BEACON ACQUISITION PROCESSOR

targets. The most obvious technique is to increase the transmit beamwidth and receiver field-of-view, and provide some sort of dual return pulse detection technique. However, this approach appears to result in serious link margin problems even for targets relatively closely clustered. A more attractive technique from energy management considerations is to divide the transmit pulse into two equal parts, and form two individually targeted transmit beams. Individual beam steering for sizable angular offsets ($\sim \pm 1°$) requires a relatively good linearity device ($\sim$ 0.2%). The most attractive device for this application appears to be precision Risley prisms with 10 bit optical encoders for deflection and orientation feedback control.

The selected system concept can, however, roughly approximate this performance, by jumping from target-to-target between pulses, resulting in a tightly interlaced set of data. It was beyond the scope of this study to determine the impact of these competing concepts on the value of the measurements, thus these alternatives are simply presented for consideration.

3.3 ACTIVE LATS TERMINAL CONFIGURATION. The active LATS terminal is very similar, functionally, to the HATRS terminal, and most of the same support elements are required, although the performance requirements can be relaxed to some extent. Based on our evaluations, the receive aperature weight and cost are not a significant part of the subsystem weight and cost when the diameter is less than several inches A one-inch diameter (0.0254m) aperature was chosen as a reasonable value for the receiver. For the narrow pulse HATRS radar, with the beam spoiled to 100 μrad, this choice resulted in a 31.6 dB link margin, based on requiring $\sim$20 pe/pulse to ensure detection of every pulse. The rms time of arrival estimation error, for 20 pe/pulse is $\sim$32 ps.

For the transmitter, the required product of energy per pulse and transmit antenna gain, to provide a 6 dB margin above the 20 pe/pulse level, is $\sim$23 dBJ. If the transmitter outputs 0.1 mJ/pulse, the transmit beamwidth can be $\sim$4 mrad. We allowed about 0.5 mrad for pointing error, which is almost totally allocatable to attitude reference errors. This pointing accuracy (0.03°, 1σ) is well within the capabilities of relatively inexpensive stellar-inertial attitude reference systems, but considerably more stringent than normally achievable for simpler attitude reference techniques.

Figure 8 summarizes the selected terminal configuration. A fixed telescope with a gimballed flat was chosen for this terminal, to minimize complexity. An alternate design, with three additional folding mirrors, can be configured to

FIGURE 8 FUNCTIONAL BLOCK DIAGRAM – ACTIVE LATS TERMINAL

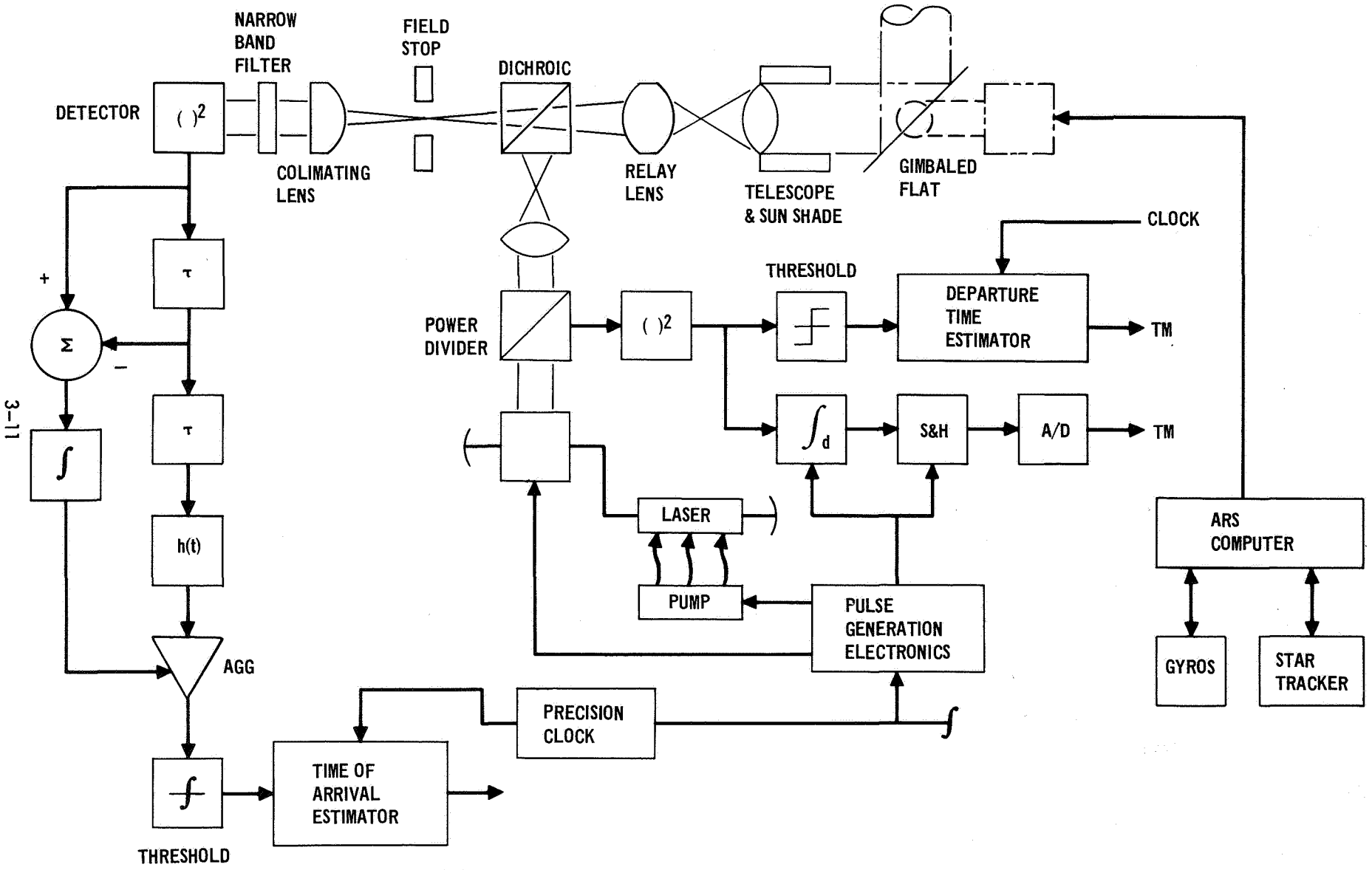

provide full hemispheric coverage for a minimal weight penalty.

An alternate functional concept is shown in Figure 9, which also shows the special HATRS receiver configuration to extract one-way Doppler frequency measurements. If a precision clock, with suitable frequency accuracy and stability, is provided, at both ends of the link, one-way Doppler frequency measurements can provide reasonably accurate range sum rate measurements. In this concept, the active LATS terminal is composed of a gimballed array of retro-reflectors, for ranging purposes, and a modest beamwidth (1.06 μm wavelength), 200 Mpps mode-locked laser, whose mode-lock frequency is phase-locked to a standard frequency derived from a precision Rubidium clock.

FUNCTIONAL BLOCK DIAGRAM – ALTERNATE ACTIVE LATS TERMINAL

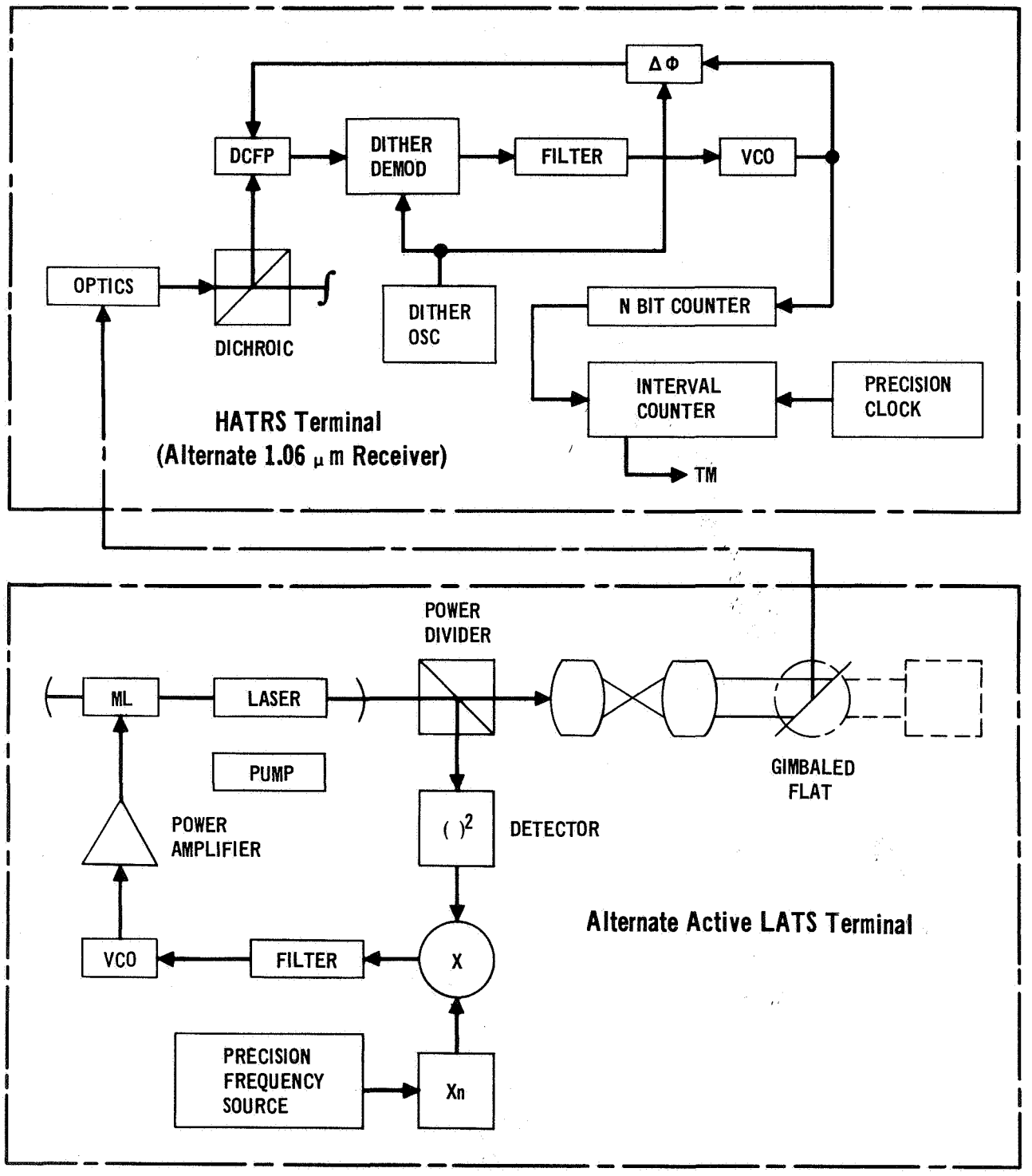

FIGURE 9

4.0 LINK DYNAMIC ANALYSES

Two of the ranging links evaluated in the Laser Ranging Systems Study involve a High Altitude Transmit-Receive Satellite (HATRS) in a 22,000 km circular orbit ranging from ground based retro-reflectors or retro-reflectors on a Low Altitude Target Satellite (LATS) in a 1000 km circular orbit. These passive ranging links are severely power limited due to the extremely long ranges, and hence very narrow laser transmit beamwidths (5 microradians) must be employed. The laser pulse rate for the selected HATRS terminal configuration is 10 pulses/second. The resulting laser telescope pointing requirements are very stringent for these long, passive links because of the narrow transmit beamwidth. Furthermore, the high accuracy pointing during target acquisition and tracking must be achieved in open-loop fashion to some extent since no wideband pointing error information is available with a 10 pps pulse rate and the low energy in the return signal collected at the HATRS.

At the beginning of the acquisition phase, laser telescope pointing angle commands are computed on the basis of HATRS attitude and position estimates and estimated target location. The pointing angle commands then are transformed into spacecraft attitude or gimbal position commands, depending upon the system mechanization, and the laser telescope is slewed to provide nominal alignment of the telescope boresight axis along the HATRS-to-target line of sight (LOS). The pointing error of the laser telescope boresight axis relative to the true HATRS-to-target LOS at initiation of acquisition is a function of HATRS and target ephemeris errors, HATRS attitude reference error, and misalignment between the HATRS attitude reference and laser ranging systems.

If the expected pointing error is larger than some specified fraction of a transmit beamwidth, a sequential search of the initial pointing uncertainty area must be performed until a return signal is received by detectors in the HATRS laser terminal. The acquisition strategy that is devised will be strongly influenced by short-term stability of the pointing error since it defines the overlap required between adjoining subareas during the sequential scan process and hence it affects acquisition time. Thus the open-loop pointing requirement for acquisition in the long, passive links is a function of the allowable acquisition time and the acquisition strategy employed. However, a preliminary requirement of 10 μrad or better is felt to be a reasonable performance objective.

Although wideband pointing error information is not available in the long, passive links, it is conceptually feasible to determine static and very low-frequency (i.e., less than 0.02 Hz) boresight errors since the reflected signal strength from a passive target is directly related to HATRS pointing error at the instant the laser pulse was transmitted. Two concepts for measuring the static and low-frequency boresight errors consist of (1) a quadrant array of ranging detectors for angle of arrival estimation augmented by a conical scan of the transmit beam to detect receiver/transmitter boresight errors and (2) a single ranging detector which employs a slow conical scan for transmit beam pointing error estimation from return signal amplitude measurements. Therefore, after the target is acquired, one of these techniques could be used to estimate the static and low-frequency boresight error and appropriate compensation for these errors could be provided during tracking. The primary pointing error contributors which are calibrated with these techniques are ephemeris errors and static misalignment between the attitude reference and the laser ranging system.

The most stringent pointing requirement for the long, passive links occurs during the tracking phase when the target must be tracked in an open-loop manner within 1.0 μrad pointing error. The achievable tracking accuracy depends upon spacecraft and environmental disturbances, attitude reference stability (i.e., short-term drift and noise), and HATRS-to-target LOS kinematics.

In summary, extremely accurate HATRS and target location prediction, precise HATRS attitude determination, and precision laser telescope slewing are required for acquisition and tracking in the long, passive links. The 10 μrad or better open-loop pointing requirement for acquisition is treated as a somewhat "soft" requirement since target acquisition can be achieved with larger pointing errors. The primary impact of larger pointing error at the beginning of acquisition is longer acquisition time. The 1 μrad open-loop pointing requirement for tracking is a firm one for a 5 μrad transmit beamwidth.

4.1 EPHEMERIS ERROR EFFECTS. The positions of the HATRS and the target must be known very accurately in order to define the HATRS-to-target line-of-sight vector with an accuracy compatible with open-loop pointing within five or ten microradians.

4.1.1 HATRS and LATS Ephemeris Prediction. The LATS and possibly the HATRS currently are envisioned to be drag-compensated spacecraft. An accelerometer is used to measure the effect of all nongravitational forces acting on this

type spacecraft such as the forces due to solar radiation or meterorite impact. Then a "compensation" system is exercised to cancel the sensed nongravitational forces. The important result is that orbit prediction errors with drag-compensated spacecraft are thought to result primarily from ground station tracking errors and errors in the geopotential field model used for orbit prediction.

GSFC performed an in-house study to assess ephemeris prediction capability for the HATRS and a drag-compensated satellite in a 300 KM circular orbit. Their computer program estimates 100 parameters including position and velocity components for both satellites, a tracking bias error for each of six tracking stations, a drag residual for the low altitude spacecraft, and 81 geopotential terms. Their conclusion is that for a drag-compensated satellite that has been tracked by six stations (2 passes per day) for ten days, the uncertainty associated with predicting the position of the satellite 24 hours ahead is approximately 3 meters (1σ) provided all terms are solved for. This total error can be broken down into a 2.5 meter cross track component, a one meter along track component and a two centimeter radial component. These projections serve as the basis for estimating effects of ephemeris errors on achievable open-loop pointing system accuracy.

4.1.2 Pointing Angle Error Sensitivities. Sensitivities of HATRS pointing angle error to HATRS and LATS position errors were derived for coplanar HATRS and LATS orbits (1) with the line-of-sight tangent to the low altitude orbit and (2) with the low altitude satellite directly under the HATRS in order to bound the effects of ephemeris errors. Similarly, pointing angle error sensitivities for the HATRS-to-ground links were derived with the ground site (1) on the HATRS horizon and (2) directly under the satellite. Analytical expressions for the pointing angle error sensitivities and numerical sensitivities for the HATRS-to-LATS link are presented in Table 5. The numerical sensitivities to ephemeris errors for the HATRS-to-ground link are somewhat smaller since the range is larger.

The numerical sensitivity values for the HATRS-to-LATS link show that the pointing angle error per unit position error is approximately 0.05 μrad/meter if acquisition is performed with the LATS directly below the HATRS. Assuming that the along track and cross track positions errors for both satellites are the same, the root-sum-square (RSS) HATRS pointing error is approximately 0.10 μrad/meter. The numerical sensitivities of pointing error to HATRS and LATS along track and cross track position errors are about 33 percent lower if acquisition is performed when the HATRS-to-LATS line of sight is tangent to the LATS orbit.

TABLE 5
HATRS POINTING ANGLE ERROR SENSITIVITIES TO HATRS AND LATS POSITION ERRORS
(COPLANAR ORBITS)

	LATS UNDER HATRS		LOS TANGENT TO LATS ORBIT	
	ANALYTICAL SENSITIVITY	NUMERICAL SENSITIVITY	ANALYTICAL SENSITIVITY	NUMERICAL SENSITIVITY
$\partial\phi/\partial D_H$	$\frac{1}{r_H - r_L}$	.048 μrad/meter	$\frac{1}{r_H}$	.035 μrad/meter
$\partial\phi/\partial R_H$	0	.0	$\frac{(r_L/r_H)}{R}$	.010 μrad/meter
$\partial\phi/\partial C_H$	$\frac{1}{r_H - r_L}$	.048 μrad/meter	$\frac{1}{R}$	.036 μrad/meter
$\partial\phi/\partial D_T$	$\frac{1}{r_H - r_L}$	.048 μrad/meter	$\frac{r_L}{R^2}$	.010 μrad/meter
$\partial\phi/\partial R_T$	0	.0	$\frac{1}{R}$	.036 μrad/meter
$\partial\phi/\partial C_T$	$\frac{1}{r_H - r_L}$	.048 μrad/meter	$\frac{1}{R}$	.036 μrad/meter

NOTES:
1) D_H, R_H, C_H are along track, radial, and cross track errors for HATRS.
2) D_C, R_L, C_L are along track, radial, and cross track errors for LATS.
3) r_H, r_L, R are HATRS radius, LATS radius, and HATRS-to-LATS range.

The effects of radial position errors are negligible in an RSS sense since the radial errors are much smaller than the along track and cross track errors, and the pointing angle error sensitivities also are much lower. The total RSS pointing error for acquisition with the LATS on the "horizon" is approximately 0.072 μrad/meter assuming equal errors.

4.2 ATTITUDE REFERENCE SYSTEMS. The sub-arc second open-loop pointing requirement for the long, passive links dictates stellar sensing, and hence only stellar-inertial attitude reference systems (ARS) are considered. High-quality reference gyros provide relatively high-bandwidth, short-term data and star sensors provide precise low-bandwidth attitude measurements at discrete times. Optimal filtering generally is employed to process these measurements in order to estimate and compensate for important measurement errors and to estimate spacecraft attitude. Spacecraft angular rates can be derived from incremental attitude data or can be measured with another set of gyros if higher bandwidth rate data is required.

Gyro drift rate bias must be estimated and appropriate compensation must be provided in the attitude estimation algorithms to achieve high-accuracy attitude determination. Sub-arc second attitude determination might also require periodic calibration of additional attitude reference sensor parameters such as gyro scale factor and gyro input axis alignment. Parameters which require infrequent calibration, say every few days, could be estimated using ground-based computer algorithms to minimize onboard computer requirements.

Gyro performance should not be a limiting factor in achieving sub-arc second attitude determination in the 1980's. Projected performance of the third generation gyros (TGG) is compatible with sub-arc second pointing, and current high-quality gyros such as the Honeywell GG334 are close to being adequate for some attitude reference system mechanizations. A comparison of current gyro performance and performance goals of the Draper Lab TGG is shown in Table 6. The Draper Laboratory TGG has undergone significant laboratory testing, and results of these tests demonstrate the feasibility of meeting the specified performance goals. The frequency response of the Draper Lab TGG is essentially flat out to 30 Hz which is significantly better than the frequency response of current high-quality reference gyros.

Gyro drift rate bias is a very large error contributor unless appropriately compensated. Random drift also is an important error source in any

TABLE 6
GYRO PERFORMANCE DATA

GYRO PERFORMANCE PARAMETER	HONEYWELL GG334 SERIES (SPARS)	NORTHRUP K7G (HONEYWELL PADS)	TRW PADS STUDY ASSUMPTIONS	C. S. DRAPER LAB TGG
RANDOM DRIFT (DEG/HR)	0.01 (1σ)	0.005 (1σ)	0.003 (1σ)	<0.005 $\widehat{\text{SEC}}$/HR*
SCALE FACTOR STABILITY (PARTS PER MILLION)	60 LONG TERM; CALIBRATE TO 10 OR LESS	300 (3σ) FOR 60 DAYS; 10 (1σ) FOR 15 MIN	100 (1σ)	<1.
INPUT AXIS ALIGNMENT STABILITY ($\widehat{\text{SEC}}$)	**	50 (3σ)	10 (1σ)	**
NOISE JITTER ($\widehat{\text{SEC}}$)	**	**	**	0.002 (0.1-4.0 Hz)

*TOTAL DRIFT UNCERTAINTY
**UNSPECIFIED

high-accuracy stellar-inertial reference system. The Honeywell GG334 gyro has a 0.01 deg/hr (1σ) random drift specification, but much better performance has been observed during laboratory testing. The drift uncertainty performance goal for the Draper Lab TGG is less than 0.004 sec/hour. This assumes that the absolute drift of the gyro can be calibrated and compensated with resolution that is commensurate with the 0.004 sec/hour specification.

Other important gyro performance parameters are scale factor stability and input axis alignment stability. Scale factor stability, which is a measure of the angular uncertainty associated with torquing the gyro through a specified angle, is extremely important if the spacecraft is slewed through large angles or if input rates to the gyro are high. A scale factor stability specification of 100 to 200 parts per million (PPM) represents current state-of-the-art gyro technology. However, the scale factor stability can be calibrated to 10 PPM or so. The performance objective of the TGG is quoted as 1 PPM with 0.1 PPM potentially achievable.

The current state-of-the-art in strapdown stellar-inertial attitude reference systems is exemplified by the Honeywell Space Precision Attitude Reference System (SPARS) to which 3 to 4 $\overset{\frown}{\text{sec}}$, 1σ, 3-axis performance capability is attributed. The SPARS employs two strapdown starsensors which are solid state devices utilizing a silicon photodetector array as the sensing element, and three strapdown pulse-rebalanced, rate integrating gyros (Honeywell GG334 series). Primary SPARS attitude error contributors are star sensor random error (2 sec, 1σ) and random gyro drift (0.01 deg/hr, 1σ). No full-up SPARS has flown to date, but a modified version with relaxed accuracy requirements (15 $\overset{\frown}{\text{sec}}$, 3σ per axis) is scheduled to be flown early in 1975.

The SPARS initially was designed for low altitude orbit missions, but Honeywell has performed a study for the Air Force in which they evaluated SPARS performance in high altitude orbits--up to synchronous altitude. The study results indicate that a SPARS type of attitude reference system warrants consideration for the HATRS application. Higher accuracy star mappers and higher quality gyros are required for the laser ranging system than for the SPARS, but the necessary components could be available by the early 1980's if projected improvements in sensor performance are realized.

The primary impact of high altitude orbits (hence lower orbit rates) on SPARS performance is increased acquisition time since it takes much longer for filter convergence with the less frequent observable star transits due to slower star field scan. The frequency of observable star transits also defines the attitude

reference update interval during normal operation, but the longer update intervals should not be a significant problem by the 1980's with the extremely low drift gyros currently being developed.

The state-of-the-art in stellar-inertial attitude reference systems using gimballed star trackers is typified by the TRW Precision Attitude Determination System (PADS) which was designed to provide a 3.6 $\overset{\frown}{\text{sec}}$, 1$\sigma$, per axis attitude reference in an equatorial, synchronous orbit. The PADS design activity is an outgrowth of the Precision Pointing Control System (PPCS) study performed by TRW for Goddard Space Flight Center since early 1970. The PADS employs a two-axis gimballed star sensor using a photomultiplier tube detector and precision strapdown, pulse-rebalanced, rate integrating gyros. Telescope gimbal angle is measured by an Inductosyn. Kalman filtering is used to incorporate the star sensor measurements and to provide periodic estimates of spacecraft attitude and gyro drift rate bias.

Higher accuracy stellar sensing is achievable on spacecraft such as the HATRS which have large optical systems if the star sensor is boresighted to the experiment optics. Integration of the star sensor and the large optical systems results in larger aperture diameter and focal length than normally is feasible within size and weight constraints of separate star sensor assemblies.

4.3 OPEN-LOOP POINTING SYSTEMS. Two generic approaches can be employed for pointing a space-based payload toward a desired target. One method of implementing the pointing requirement is to mount the payload on a set of gimbals and to slew the gimballed payload assembly in order to achieve and maintain alignment of the payload sensor boresight axis with the host spacecraft-to-target line-of-sight. The second approach, body pointing, is to rigidly attach the payload to the spacecraft structure and to perform the pointing function using the spacecraft attitude control system.

Brief descriptions and typical operational scenarios for three open-loop pointing system mechanization concepts are discussed in this section. Two of the pointing systems use the gimballed payload approach and the third employs body pointing. The objective of this section is to identify major system components and primary pointing error contributors in order to assess the feasibility of achieving open-loop pointing capability between 5 to 10 μrad by the early 1980's in the long passive links. All three mechanization concepts require significant improvements in component performance relative to current state-of-the-art in order to realize this open-loop pointing accuracy goal.

However, only components which currently are being developed or components which are reasonable extropolations from current state-of-the-art are acceptable since full implementation of the laser ranging system is planned for the early 1980's.

4.3.1 Gimbaled Telescope Pointing Systems. Numerous gimbaled telescope pointing system implementation concepts can be contrived, with the system differences being primarily the type and/or location of the attitude reference sensors. Two implementation concepts which characterize the basic options available with the gimbaled pointing system approach are discussed in this section.

One of the gimbaled telescope pointing systems evaluated in this study employs a SPARS type of ARS which consists of strapdown star sensors and strapdown reference gyros, all mounted on a precision optical assembly (POA) which is a precision mounting structure. The POA provides a stable thermomechanical interface to the spacecraft for establishing and maintaining precision alignment between pointing system components. Another star sensor is located on the focal plane of the laser telescope and is used solely for alignment calibration. The second gimbaled system employs a star sensor located on the laser telescope focal plane as the primary attitude reference sensor and strapdown gyros mounted inside the laser telescope gimbals. The telescope gimbals are rigidly attached to the POA in both systems.

Gimbaled System with SPARS Type of ARS (System I). The basic elements of this open-loop pointing system are a SPARS type of attitude reference system and a gimbaled laser telescope assembly. The ARS consists of two or more star mappers and high-quality strapdown reference gyros, probably third generation gyros. The star mappers are wide field-of-view sensors with no moving parts; they depend upon spacecraft motion for star field scan. They contain no servo loops or angle encoders, and hence these star sensors are mechanically simpler than gimbaled star trackers.

The gimbaled telescope assembly contains the laser telescope, gimbals and associated drive electronics, and gimbal angle encoders. Also, an image dissector type of star sensor is located on the laser telescope focal plane for use in calibrating alignment between the laser telescope and the attitude reference system.

The HATRS is controlled about a local vertical/orbit plane reference. Continuous star field scan is provided by the nominal spacecraft pitch rate that is required to maintain a local vertical orientation, and thus attitude reference updates can be provided throughout acquisition and tracking.

Whenever the laser ranging system is to be exercised, laser telescope pointing angles are computed using spacecraft attitude and position estimates and estimated target location. These desired pointing angles are transformed into laser telescope gimbal position commands, and nominal target acquisition is achieved by slewing the telescope through the required gimbal angles. The initial pointing uncertainty area then is searched to acquire the target, if necessary, and the static and low-frequency boresight errors are estimated. Then the tracking phase is initiated, and the gimbals are driven in accordance with measured or derived spacecraft angular rates during tracking.

The achievable pointing accuracy with this gimbaled system probably is limited by gimbal related errors. The two types of gimbal related errors which are of primary concern are gimbal position reference error due to angle encoder inaccuracy and gimbal control loop tracking error due to gimbal servo nonlinearities such as friction and torque motor hysteresis. Sub-arc second attitude determination should not be a limiting factor by the 1980's if projected improvements in sensor performance, particularly gyros, are realized. Gyro drift rate uncertainty is the most important gyro error contributor with this approach. Scale factor stability and input axis alignment stability are less important gyro errors since the spacecraft angular rates are fairly small with the spacecraft closely controlled about a local vertical/orbit plane reference. The largest spacecraft angular rate is orbit rate which is essentially constant in the nominally circular HATRS orbit.

Only the short-period rates, which are small, produce attitude reference error due to scale factor instability and gyro input axis misalignments. The gyro measurement error due to scale factor and input axis alignment stability effects with a constant input rate is compensated for in the state estimate of gyro drift rate since this measurement error is a bias error in the short term.

The current state-of-the-art in gimbal angle encoder performance is inadequate for the Laser Ranging System application with system mechanizations which rely upon these devices for gimbal position determination during target acquisition and tracking. No angle encoders with readout accuracy specifications in the sub-arc second region have been space qualified to date. Both Inductosyns and optical

shaft encoders have fractional sub-arc second measurement potential, but these high-accuracy angle encoders probably will be fairly large with diameters of twelve inches or greater since increased resolution is generally obtained by increasing encoder dimensions. An angle encoder with readout accuracy of 0.1 μrad or better is required with this gimbaled system in order to provide 1 μrad pointing during tracking, and this is well beyond the performance of any angle encoder currently being developed, to our knowledge.

Farrand Controls, Inc. has a twelve inch diameter Inductosyn with a $\pm$0.5 $\widehat{\text{sec}}$ accuracy specification if the discs are directly mounted to the shaft. The accuracy specification denotes the precision to which angular position can be measured with respect to an absolute external reference. This should not be confused with the resolution specification which defines the smallest movement which can be measured or reproduced by the angle encoder. Thus the accuracy specification includes mechanical misalignments and electronic noise and biases in addition to the resolution of the device.

Baldwin Electronics has a ten inch optical shaft encoder with 21 bit resolution (0.62 $\widehat{\text{sec}}$) and a full circle accuracy quoted as one bit RMS plus resolution. Baldwin currently is working on a 16-inch diameter optical encoder with a 24 bit resolution but they have not determined its readout accuracy capability so far. Their goal is to calibrate the 24 bit encoder within $\pm$0.1 $\widehat{\text{sec}}$ full circle accuracy.

ARS Sensors Inside Laser Telescope Gimbals (System II). One approach to improving open-loop pointing accuracy with a gimbaled laser telescope system is to locate the attitude reference sensors (i.e. star sensor and gyros) inside the laser telescope gimbals. The star sensor is located on the focal plane of the laser telescope and hence misalignment between the attitude reference axis and the laser telescope boresight axis is minimized. Also, integration of the star sensor with laser telescope optics results in larger aperture diameter and focal length than normally is feasible within size and weight constraints imposed upon a separate star sensor assembly, and hence utilization of laser telescope optics provides greater stellar sensing accuracy potential. The two primary advantages of placing the gyros on the gimbals is a significant relaxation in the gimbal angle encoder readout accuracy requirement and the availability of higher bandwidth gimbal motion data relative to System I.

The acquisition scenario with this gimbaled pointing system concept differs substantially from the acquisition scenario for the gimbaled pointing system with the attitude reference sensors strapped to the precision optical assembly.

When a command is received to perform a ranging experiment, the laser telescope assembly is slewed to acquire a specified guide star. The inertial reference is zeroed and a second guide star is acquired. Large angular separation of the two guide stars (ideally 90 degrees) is desired in order to derive accurate three-axis attitude information, but smaller angular separation is acceptable in order to maintain reasonable gimbal angle range requirements. The gimbal angle range required during acquisition depends primarily upon the number of star measurements which can be obtained within the allowable acquisition period and star measurement noise. Finally, after an attitude reference has been established, the laser telescope pointing angles are computed and the laser telescope is slewed through the commanded gimbal angles. Then the initial pointing uncertainty area is searched, the target is acquired, static and low-frequency boresight errors are estimated, and tracking is initiated.

The gimbal angle encoder provides gimbal position information during acquisition of the first guide star. The gyros, which are mounted on the telescope gimbals, are employed to provide a reference for precision slewing during subsequent guide star acquisition and target acquisition maneuvers. Therefore scale factor stability and input axis stability are very important error parameters with the high gyro input rates and the large angles through which the gyros must be torqued during the slewing maneuvers. Current gyros are inadequate but acceptable position measurement accuracy is achievable over fairly large angles using third generation gyros if their quoted performance goals are met. For example, the telescope boresight alignment error following a 30 degree maneuver is approximately 0.1 sec with a scale factor stability of 1 PPM.

Effects of gimbal dynamics such as friction probably are the largest tracking error contributors. However, with the gyros mounted within the gimbals, higher bandwidth gimbal jitter measurement is available than with the gyros strapped to the POA, since, for example, the frequency response of the Draper Lab TGG is essentially flat out to 30 Hz.

A disadvantage of boresighting the star sensor to laser telescope optics is that no star measurements can be obtained during tracking when the laser telescope is Earth oriented. Complete reliance is placed upon the gyros for maintaining an attitude reference of sufficient accuracy. However, attitude error propagation due to gyro drift uncertainty during tracking should not be a problem with the third generation gyros currently being developed. Attitude error due to a 0.10 sec/hour drift rate is a tolerable 0.05 sec for a 30 minute tracking period

assuming a linear relationship between attitude error buildup and time, and this is an order of magnitude larger drift uncertainty than is projected for the third generation gyros.

Comparative Evaluation of Gimbaled Pointing Systems. A qualitative comparison of the two gimbaled telescope pointing systems is presented in Table 7. There are many implementation options available within the class of gimbaled pointing systems, but the two implementation concepts compared in Table 7 adequately serve as a basis for discussing the important tradeoffs which should be considered in selecting a gimbaled pointing system for the HATRS.

The basic conclusion is that the attitude reference sensors should be located inside the payload gimbals in order to minimize the effects of gimbal angle encoder error and gimbal servo nonlinearities on pointing system performance. This conclusion is based upon projected gimbal angle encoder readout accuracy attainable with Inductosyns or optical encoders of reasonable size. If the ARS sensors are mounted within the gimbals, gimbal position information is required only during acquisition of the initial guide star, and hence a moderate accuracy angle encoder (say 18 to 20 bit full circle accuracy) is sufficient. Also, low frequency gimbal dynamics can be measured if the gyros are strapped to the gimbals.

The gimbaled pointing system with the ARS sensors mounted within the gimbals has other comparative advantages in addition to making achievable pointing accuracy essentially independent of gimbal angle encoder errors. Boresighting the primary star sensor to the laser telescope optics eliminates the need for a separate alignment calibration sensor, provides higher stellar sensing accuracy potential, and minimizes the misalignment between the laser telescope and star sensor boresight axes. However, star measurements cannot be performed while tracking ground based or near Earth targets, and large gimbal angle ranges are required for guide star acquisition. An additional star sensor mounted orthogonally to the primary sensor could be used to decrease gimbal range requirements and to provide periodic attitude reference updates during tracking, if required. This additional star sensor could be a lower accuracy device than the one boresighted with the laser telescope optics.

A comparative disadvantage of gyro placement inside the payload gimbals is increased sensitivity of laser telescope pointing error to gyro scale factor stability and input axis alignment stability errors due to higher gyro input rates and the larger angles through which the gyros are torqued during guide

TABLE 7
GIMBALED TELESCOPE POINTING SYSTEM COMPARISON

EVALUATION CRITERIA	SYSTEM I ARS SENSORS STRAPPED TO POA	SYSTEM II ARS SENSORS INSIDE GIMBALS
STAR SENSOR	o STRAPDOWN SENSORS (2) ON POA o IMAGE DISSECTOR TYPE SENSOR BORESIGHTED TO LASER TELESCOPE OPTICS FOR CALIBRATION o PERIODIC MEASUREMENTS DURING TRACKING	o IMAGE DISSECTOR TYPE SENSOR BORESIGHTED TO LASER TELESCOPE OPTICS o HIGHER ACCURACY POTENTIAL o NO MEASUREMENTS DURING TRACKING
GYROS	o LESS STRINGENT REQUIREMENT o IMPORTANT ERRORS--DRIFT	o MORE STRINGENT REQUIREMENT o IMPORTANT ERRORS--DRIFT, SCALE FACTOR STABILITY, INPUT AXIS ALIGNMENT STABILITY o MEASURES LOW-FREQUENCY GIMBAL DYNAMICS
LASER TELESCOPE GIMBALS	o $\pm 15^{o}$ GIMBAL ANGLE RANGE o $\overline{24}$-BIT ACCURACY ANGLE ENCODER	o LARGER GIMBAL ANGLE RANGE o LOWER ACCURACY ANGLE ENCODER (18-20 BIT)
ARS/LASER TELESCOPE MISALIGNMENT	o GIMBAL INTERFACE o LARGER THERMAL GRADIENTS	o MINIMIZED BY PROXIMITY OF LASER TELESCOPE AND ARS SENSORS

star acquisition maneuvers. However, the pointing error attributable to these gyro erros is compatible with sub-arc second pointing if projected TGG performance goals are met. Another adverse effect of mounting the gyros inside the gimbals is increased power dissipation in the gimbaled assembly and attendant thermal control problems.

Some advantages of the system in which the ARS sensors are strapped to the precision optical assembly (System I) are less stringent gyro requirements, "continuous" attitude reference update availability, and a smaller gimbal angle range requirement ($\simeq \pm 25$ degrees). However, it is felt that these advantages do not outweigh the primary comparative disadvantage of the system which is the requirement for an extremely accurate angle encoder.

4.3.2 Body Pointing System. Body pointing is an attractive alternative to gimbaled telescope pointing for the Laser Ranging System because it would eliminate the potential problems directly attributable to the gimbals. A brief description of a candidate body pointing system and a typical operational scenario are presented in this section.

A SPARS type of stellar-inertial attitude reference system is employed with two or more strapdown star sensors and strapdown, rate integrating, high quality reference gyros (third generation gyros) mounted on the precision optical assembly. The star sensors would be oriented to enable periodic attitude updates to be provided during laser ranging experimentation. The time between attitude reference updates depends primarily upon spacecraft angular rates and detector sensitivity. The laser telescope also is rigidly attached to the POA, and another star sensor, probably an image dissector type, is located on the laser telescope focal plane. This star sensor is used for initial on-orbit alignment and periodic calibration to compensate for alignment shifts due to thermal gradients.

A typical scenario for the acquisition and tracking phases with body pointing is as follows. The target acquisition phase begins with the HATRS in some orientation which enables a precise attitude reference to be maintained between ranging experiment periods. The desired inertial orientation of the laser telescope is determined on the basis of HATRS and target position estimates. Then the spacecraft attitude maneuvers required to point the laser telescope along the HATRS-to-target LOS are determined using the estimated inertial attitude of the HATRS, and the HATRS is slewed accordingly. The resulting orientation of the laser telescope boresight axis relative to the true HATRS-to-target LOS will be within

specified error limits which allows acquisition to be completed within a prescribed time interval using a sequential search technique if necessary. After the target is acquired, a conical scan boresighting technique is employed to estimate static and low-frequency boresight error. Then the tracking phase is initiated, and the spacecraft precisely tracks the HATRS-to-target LOS.

Precision spacecraft slewing throughout the acquisition and tracking phases is performed by the HATRS attitude control system using reaction wheels, control moment gyros, or some hybrid combination of the two control actuators. Attitude control accuracy requirements are tighter with body pointing than with gimbaled telescope pointing since spacecraft angular rates are a direct measure of laser telescope pointing stability with the body pointing approach. The factors affecting achievable pointing stability with a momentum exchange attitude control system include induced mechanical vibrations due to rotor imbalance and spin bearing imperfections, servo nonlinearities such as friction torques and CMG torquers ripple and compliance, and sensor noise. All these problems have been studied in depth within the industry for other space-based optical system applications (e.g., Large Space Telescope).

4.3.3 Body Pointing versus Gimbaled Telescope Pointing. A comparative evaluation of the body pointing system and the gimbaled telescope pointing system with the attitude reference sensors located inside the payload gimbals is presented in Table 8. Body pointing has the basic advantage of being the simpler to mechanize. There are no gimbals, and hence no gimbal servos and no gimbal angle encoders. However, more precise attitude control is required with body pointing than with the gimbaled systems since the gimbal control system can compensate for observable spacecraft motion.

Both pointing systems require high accuracy stellar sensing. Star sensors located on the focal plane of the laser telescope provide higher accuracy stellar sensing potential than is achievable with separate star sensor assemblies of reasonable weight and size, but the use of laser telescope optics precludes attitude reference updates when tracking ground based targets.

When body pointing is used, it is possible to locate star sensors on the precision optical assembly oriented to allow star measurements while the telescope is earth oriented (active ranging). The boresight star tracker is used only to periodically calibrate between the normal mode star sensors and the telescope boresight. For the gimballed system, however, it is not at all certain that

TABLE 8
BODY POINTING VERSUS GIMBALED TELESCOPE POINTING

EVALUATION CRITERIA	BODY POINTING	WITH ARS SENSORS INSIDE GIMBALS
ATTITUDE CONTROL	o VERY PRECISE CONTROL o FINE CONTROL TORQUES FOR SLEWING AND POINTING STABILITY o MANEUVER ENTIRE S/C TO POINT LASER TELESCOPE o REACTION WHEELS AND/OR CMG'S o HIGHER BW; MAY EXCITE STRUCTURAL MODES	o LESS ACCURATE CONTROL o MINIMIZES S/C ATTITUDE CONSTRAINTS o REACTION WHEELS AND/OR CMG'S
ATTITUDE REFERENCE REQUIREMENT	o HIGH ACCURACY; SOMEWHAT LOWER THAN FOR GIMBALED SYSTEM	o HIGH ACCURACY
STAR SENSOR	o STRAPDOWN STAR SENSORS ON POA FOR PRIMARY REFERENCE o STAR SENSOR ON FOCAL PLANE OF LASER TELESCOPE FOR CALIBRATION o PERIODIC ATTITUDE UPDATES DURING TRACKING	o STAR SENSOR ON FOCAL PLANE OF LASER TELESCOPE o HIGHER ACCURACY POTENTIAL o NO MEASUREMENTS WHEN TRACKING GROUND BASED OR NEAR EARTH TARGETS
REFERENCE GYROS	o THIRD GENERATION GYROS o STRAPPED TO POA o PRIMARY ERRORS--DRIFT UNCERTAINTY, SCALE FACTOR STABILITY, INPUT AXIS ALIGNMENT STABILITY	o THIRD GENERATION GYROS o MOUNTED ON PAYLOAD GIMBALS o PRIMARY ERRORS--SAME AS FOR BODY POINTING o INCREASED POWER DISSIPATION INSIDE GIMBALS
PAYLOAD GIMBALS	o NONE	o LARGE GIMBAL ANGLE RANGE REQUIRED o 18 TO 20-BIT GIMBAL ANGLE READOUT o TRACKING ERROR DUE TO GIMBAL DYNAMICS
DESIGN COMPLEXITY	o SIMPLER POINTING SYSTEM o LARGER IMPACT ON S/C DESIGN o EASIER TO IMPLEMENT REDUNDANCY o REDUNDANT CONTROL ACTUATORS PROBABLY USED ANYWAY	o MORE COMPLEX POINTING SYSTEM o WEIGHT AND COST OF REDUNDANT GIMBALED SYSTEM IS PROHIBITIVE

star sensors can be located for star measurements while the telescope is earth oriented (host vehicle interference), thus we elected to rely on the boresight star sensor for periodic ARS updates between ranging operations.

A very "quiet" spacecraft is required for both the body pointing and gimbaled telescope pointing systems. This is an inherent requirement with body pointing since laser telescope pointing stability is directly related to attitude control system performance and attitude control bandwidth is constrained by the lower structural modes. The "quiet" spacecraft requirement also is applicable to gimbaled pointing system for the long, passive ranging links since wideband pointing error information is not available due to severe power limitations and a low laser pulse rate, and hence no compensation for high-frequency pointing jitter can be provided.

Body pointing is the recommended approach for implementing the very stringent laser ranging system pointing requirements. Although attitude control accuracy requirements are tighter with body pointing, it is felt that this comparative disadvantage is heavily outweighed by the simpler mechanization and the absence of the performance-limiting gimbal related problems due to angle encoder readout error and gimbal dynamical errors. The body pointing approach contains fewer components, probably is lighter, and alleviates thermal design problems attendant to high energy dissipation rates inside the laser telescope gimbals. It also is easy to implement redundancy with body pointing, whereas, an equivalent level of redundancy is not feasible with the gimbaled system.

4.4 POINTING ERROR BUDGET FOR LONG, PASSIVE LINK. Preliminary pointing error budgets for the recommended body pointing system are presented in Tables 9 and 10 for the long, passive ranging links. The open-loop pointing requirements for the acquisition and tracking phases are 5.0 μrad and 1.0 μrad respectively. All pointing error contributors are assumed to be independent and normally distributed.

A 1.5 μrad pointing error allocation is specified for the effects of HATRS and target position errors during acquisition. This corresponds to approximately 20 meter (3σ) along track and cross track position errors for the HATRS and the target if acquisition is performed with the target on the horizon. This ephemeris error allocation is about three times higher than required if the 3 meter (1σ) prediction capability projected by Goddard is realized.

TABLE 9
ACQUISITION POINTING ERROR BUDGET FOR LONG, PASSIVE LINKS

POINTING ERROR CONTRIBUTOR	POINTING ERROR	REMARKS
HATRS & TARGET POSITION ERRORS	1.5 μRAD	o 20 METER ALONG TRACK AND CROSS TRACK ERROR FOR HATRS AND TARGET o <1 METER RADIAL POSITION ERROR
ARS/LASER RANGING SYSTEM MISALIGNMENT	2.5 μRAD	o RESIDUAL CALIBRATION ERROR o STRUCTURAL CREEP AND VIBRATIONS o ALIGNMENT SHIFTS BETWEEN CALIBRATION PERIODS DUE TO THERMAL GRADIENTS
ATTITUDE CONTROL ERROR	1.0 μRAD	o CONTROL ACTUATOR DYNAMICS o ENVIRONMENTAL DISTURBANCES o S/C DISTURBANCES o ORBIT KINEMATICS
ATTITUDE REFERENCE ERROR	4.0 μRAD	o STAR SENSOR ERROR o GYRO ERRORS o COMPUTATION ERROR
RSS ERROR	≈ 5.0 μRAD	
REQUIREMENT	5.0 μRAD	

TABLE 10
POINTING ERROR BUDGET FOR TRACKING PHASE

POINTING ERROR CONTRIBUTOR	POINTING ERROR	REMARKS
RESIDUAL CALIBRATION ERROR	0.33 μRAD	o ERROR IN ESTIMATING STATIC AND LOW-FREQUENCY BORESIGHT ERRORS USING CONICAL SCAN BORESIGHTING TECHNIQUE FOLLOWING ACQUISITION
ARS/LASER RANGING SYSTEM ALIGNMENT DYNAMICS	0.33 μRAD	o SHORT-TERM THERMAL EFFECTS o STRUCTURAL VIBRATIONS
ATTITUDE CONTROL ERROR	0.50 μRAD	o ACTUATOR DYNAMICS (i.e. FRICTION, ROTOR ASYMMETRY) o S/C AND ENVIRONMENTAL DISTURBANCES o ORBIT KINEMATICS
ATTITUDE REFERENCE ERROR	0.70 μRAD	o STAR SENSOR NOISE o GYRO ERRORS (DRIFT, SCALE FACTOR STABILITY) o COMPUTATIONAL ERROR
RSS POINTING ERROR	≈ 1. μRAD	
POINTING REQUIREMENT	1.0 μRAD	

On-orbit calibration of the alignment between the laser telescope boresight axis and attitude reference axes is required after the operational orbit has been achieved in order to remove static misalignments attributable to manufacturing tolerances and boost environment effects. Then, periodic on-orbit calibration must be performed during the mission to measure alignment shifts due to thermal gradients and structural creep. The pointing error budget for the acquisition phase contains a 2.5 μrad allocation for residual calibration error, low-frequency alignment shifts between calibration periods, and high-frequency dynamics such as structural vibrations.

A 1.0 μrad error allocation is specified for attitude control errors. This includes the effects of spacecraft and environmental disturbances plus actuator nonlinearities and asymmetries. The remaining allowable pointing error during acquisition is allocated to the attitude reference system. The ARS error components include star sensor error, gyro errors and computational error, with the primary gyro error sources being drift uncertainty, scale factor stability, and input axis alignment stability.

A preliminary pointing error budget for the tracking phase is presented in Table 10 for a 1.0 μrad tracking requirement. It is assumed that static and very low-frequency boresight errors are estimated using a conical scan boresighting technique following target acquisition and prior to the start of the tracking phase. Hence it is assumed that the only contribution of static boresight misalignment and low-frequency boresight alignment shifts to tracking error is a calibration or measurement residual. The boresight error estimator also measures the pointing error due to HATRS and target location errors. There are short-period ephemeris propagation errors but their effects on pointing error should be small in a "root-sum-square" sense compared to the 1.0 μrad tracking accuracy requirement. Thus, a preliminary allocation of 0.33 μrad is made for the residual calibration error (i.e. estimation error) plus short-term ephemeris effects.

A 0.33 μrad error allocation also is specified for attitude reference system to laser ranging system misalignment due to short-period thermal effects and structural vibrations. This imposes stringent requirements on the precision optical assembly which is the thermo-mechanical interface between the ARS sensors and the laser telescope. The HATRS attitude control accuracy requirement is defined as 0.50 μrad in the tracking error budget. This defines the allowable pointing error due to angular deviation of the spacecraft relative to a desired

reference as defined by the attitude reference system. The achievable attitude control accuracy is influenced by HATRS and environmental disturbances, control actuator performance, and the degree of interaction of the attitude control system with spacecraft structure.

The remaining approximately 0.70 μrad allowable pointing error is allocated to the attitude reference system. The 0.70 μrad error allocation includes effects of star sensor error, gyro error, and computational errors. In order to satisfy this requirement, third generation gyros and star sensors with an overall accuracy of 0.25 μrad or so are required. The availability of adequate gyros should not be a problem, but the availability of star sensors with the accuracy just quoted is less certain.

The pointing error budgets for the Laser Ranging System acquisition and tracking phases impose very stringent requirements for ephemeris prediction, attitude determination, attitude control, and spacecraft structural and thermal design. However, it is felt that the 5 μrad open-loop pointing requirement can be met by the early 1980's with reasonable extrapolations from the current state-of-the-art in ephemeris prediction capability, attitude sensor technology, and attitude control system performance. Achievement of a 1 μrad pointing capability for tracking also appears to be feasible if an acceptable boresighting technique can be developed to estimate static boresight errors following target acquisition.

5.0 PERFORMANCE ANALYSES

Many types of system configurations were examined, and performance analyses made, prior to selecting the preferred systems configurations, described in Section 3. In this section, the performance analyses for these alternate configurations are described and compared to the performance predictions for the preferred systems. Additional performance analyses for the preferred system configurations are also presented.

5.1 HATRS RANGING MEASUREMENTS. The first, and most fundamental, concern is to determine the amount of received signal energy necessary to meet the rms range measurement accuracy requirements. This can be expressed in several ways. The most useful measures are in terms of detected photoelectrons per pulse and detected photoelectrons per second. The former is used for systems which make range estimates on a single pulse or average over a few pulses. The latter description is more appropriate for systems which average over many pulses to obtain range estimates.

All of the systems considered in this study employed side-band ranging techniques, due to unresolved problems of coherent carrier detection at or near visible frequencies. Side-band ranging techniques rely on estimating the range by measuring the phase delay of the modulation waveform which is imposed on the (optical frequency) carrier. When the modulation waveform is periodic, and the period is less than the maximum possible propagation time, a range ambiguity condition exists, which must be resolved in some manner for true range measurements. When the modulation waveform period is significantly larger than the range uncertainty, the ambiguity can be readily resolved. However, when the waveform period is much less than the range uncertainty, the ambiguity cannot be easily resolved, and the system is limited to estimating the rate-of-change of the phase path length, commonly referred to as Doppler frequency measurements or range-sum-rate measurements.

These techniques can be used in either a closed-loop system or an open-loop system. In this context, an open-loop system implies that the receiver and the transmitter are physically separated, and the reference (transmitter) phase is estimated at the receiver (as opposed to measured). An open-loop system, by way of illustration, can be configured by providing precision clocks at both the receiver and the transmitter, and requiring that the transmitted modulation waveform reflect the state of the transmitter clock at the time of transmission.

The receiver then estimates the phase path length by subtracting the estimate of the transmitted clock state from the receiver clock state to obtain a propogation time estimate. The preceding arguments on waveform period apply also to this system, thus, either open-loop range estimates or range-rate estimates can be made.

5.1.1 Ranging with Passive Targets. Ranging measurement accuracy is fundamentally a function of the signal strength, the magnitude of the system noise, the net system bandwidth, and various uncompensated error sources within the system. At optical frequencies, with high quality detectors and optical systems, the received signal is said to be shot-noise limited, i.e., individual photoelectron emissions are detectable. Under these conditions, the detector output can be considered as a series of impulses, each signifying a photoelectron event, which are passed through a filter representing the impulse response of the detector and the amplifiers that precede the signal processing electronics.

Under ideal circumstances, the time of arrival of each detected photoelectron event can be determined, and used to estimate the phase of the received signal modulation waveform. If the estimation process is optimum, in some sense, the expected accuracy (as a function of received signal energy) of this system is a lower bound on the achievable range estimation process in a realizable system. In Appendix E, a maximum likelihood estimation process is defined for the generalized modulation waveform, and evaluated for the specific case where the waveform is a series of pulses. Several sub-optimum estimation algorithms are also synthesized and compared to the maximum likelihood estimation algorithm for the pulse modulation format.

Two basic approaches to range measurements using pulsed systems are the single pulse estimates, and estimates derived from the average of multiple pulses. For the single pulse case, an estimate of the range or propagation time is made for each received pulse which is detected. For the multiple pulse case it is necessary to average over several received pulses prior to making an estimate, hence we must include a predictor module, since the pulses are spaced in time. In the simplest form, the signal waveform has a periodic component, and the predictor module is a simple phase-locked loop. The loop bandwidth is chosen on the basis of the link dynamics. However, when the pulse rate or the usable loop bandwidths must be reduced below the level necessary for tracking with a simple (second order) phase-locked loop, a more powerful

predictor module must be employed. This is possible if the link dynamics are governed by a known set of laws. In general, this is the case for ranging between two satellites in orbit about the earth; the laws of motion are well known, only the initial conditions and the exact magnitude of the gravitational harmonic terms and the disturbances are unknown. The results of these uncertainties are what we refer to as prediction noise, i.e., errors in predicting the propagation time. In general, the effective bandwidth of the prediction noise is much less than the effective bandwidth of the link dynamics.

CW Mode-Locked Laser Analysis - A cw mode-locked laser was initially considered a viable approach for ranging applications. Conceptually, either dual apertures or an interrupted cw mode could be used. However, the link was found to be seriously background limited, which resulted in requiring excessive transmitter power, a very large aperture, or a very large cross-section target. Further, if the target has a finite dimension in range, the return pulse is broadened, and the effective background level increased still further. These considerations led to removal of the cw mode-locked laser from the viable candidate list.

Pulse-burst Mode-locked Laser Concept - Initially, we considered the pulse-burst, mode-locked laser technique as an alternative to the CW mode-locked laser, which could, conceivably, provide the advantages of narrow pulses, but with a reduced duty cycle to reduce the effects of background. Conceptually, the laser would be very similar to the CW mode-locked laser, with the exception that the laser would be pulse pumped with a low duty cycle, high energy lamp. The resulting output would be a series of mode-locked pulses, with a duration of about one microsecond ($\sim$200 pulses/burst). The pulse bursts would be repeated periodically, effectively resulting in a sampled system approach to maintaining the phase-lock-loop in operation. A relatively high pulse burst frequency is necessary to maintain phase-lock, since it would be very difficult to acquire phase-lock during a pulse burst. Since the pulse-burst laser does not now exist, and significant development would be required to ascertain feasibility, and no significant advantages (over the single pulse techniques) could be found, this measurement concept was also judged inappropriate.

Single Pulse Laser Measurement Concepts - Two types of lasers were included in this category, a Q-switched, cavity dumped laser, with a typical pulse-width of $\sim$4 to 6 ns FWHM, and a Q-switched, mode-locked, cavity dumped laser with

a typical pulsewidth of 0.1 ns FWHM. The two lasers are very similar, the basic difference is the addition of a mode-locking crystal in the cavity for the short pulse laser. Clearly, addition of an intra-cavity element will reduce the output power, thus we assumed 10 dB less output power for the short pulse laser than the long pulse laser to account for this difference. Since the short pulse laser does not exist even in breadboard form, the conservatism of this assumption is unknown.

Two basic measurement concepts were investigated for these two low PRF lasers. First, we investigated the performance of single pulse estimation techniques, where each received pulse is processed to make a range estimate. Subsequently, we analyzed a split gate rate tracking technique. This analysis was also applicable to angle tracking when using a quadrant detection technique.

The single pulse estimation techniques were based on the concept of measuring the time at which a transmit pulse is emitted, and estimating the time of arrival of this pulse after reflection from the target. Even with an ideal target, an infinite resolution clock, an infinite bandwidth detector, and a perfectly stable laser, errors in estimating the time-of-arrival of the reflected pulse will be encountered due to the statics of the detection process (shot noise). Appendix E describes an analysis conducted to determine the optimum detection accuracy, and to evaluate the performance of several suboptimum, but potentially more readily implemented, time-of-arrival estimation techniques. The fundamental concept was that a signal pulse was contained within a finite time "window", and the problem was to estimate its location within this window. A number of approximations were necessary to arrive at usable answers, so a simulation was performed to verify the validity of the results. The simulation results matched the theoretical predictions within the expected error of the simulation under the conditions examined ($N_s \geq 12$ pe/pulse).

At lower signal levels, however, the accuracy is expected to degrade significantly, since there is an increasing probability that few or no signal photoelectrons will be detected. In a practical system, we would impose a threshold criterion, such that no time of arrival estimate would be made unless the detected signal were above this threshold. In order to determine the effect of a threshold limit on the variance of the estimation error, we will begin with Equation (8) of Appendix E. If the expectations are evaluated conditioned on the occurance of L

or more photoelectron events in the pulsewidth, we find, for the maximum likelihood filter and a raised cosine pulse shape,

$$\overline{\varepsilon_\alpha^2}\Big|_{ML} = \left(\frac{T}{2\pi}\right)^2 \left[N_s + n_b T - \sqrt{2\,N_s n_b T + n_b^2 T^2}\right]^{-1} \left[\frac{\sum_{K=L}^{\infty} \frac{(N_s + n_b T)^K}{K!}}{\sum_{K=L-1}^{\infty} \frac{(N_s + n_b T)^K}{K!}}\right] \tag{18}$$

This is exactly the same expression obtained previously (Equation 31, Appendix E) with a multiplicative threshold function. For the mismatched filter case (correlator),

$$\overline{\varepsilon_\alpha^2}\Big|_{COR} = \left(\frac{T^2}{2\pi^2}\right)\left[\frac{N_s + n_b T}{N_s^2}\right]\left[\frac{\sum_{K=L}^{\infty} \frac{(N_s + n_b T)^K}{K!}}{\sum_{K=L-1}^{\infty} \frac{(N_s + n_b T)^K}{K!}}\right] \tag{19}$$

This is also exactly the same expression obtained previously (Equation 32, Appendix E) with the multiplicative threshold function. If we choose L=1, the threshold function reduces to,

$$g(1) = 1 - e^{-(N_s + n_b T)} \tag{20}$$

Then, for $n_b = 0$, and N_s small,

$$\lim_{N_s \to 0} \overline{\varepsilon_\alpha^2}\Big|_{\substack{ML \\ n_b=0}} = \frac{T^2}{4\pi^2} \tag{21}$$

$$\lim_{N_s \to 0} \overline{\varepsilon_\alpha^2}\Big|_{\substack{COR \\ n_b=0}} = \frac{T^2}{2\pi^2} \tag{22}$$

Simply stated, these expressions show that if at least one photoelectron event occurs, the variance of the time-of-arrival estimation error will not exceed

$(T/2\pi)^2$ for a maximum likelihood estimator with zero background, or $2(T/2\pi)^2$ for a correlator or matched filter. Thus, for a 4 ns FWHM pulse, the limiting rms error, assuming a ML estimator, would be 1.275 ns rms (19 cm rms); for an 0.2 ns FWHM pulse, the error would be .064 ns rms (.95 cm rms). Clearly, for the short pulse laser under these conditions, detection probabilities will govern the requirements for signal energy.

For the long pulse laser, however, $\tilde{N}_s = (4/\pi(.133))^2 = 91.2$ pe/pulse is required to achieve the accuracy requirement. This implies, of course, an ultra-stable pulse shape, optimum processing, and an ideal target.

As noted in Appendix F, the targets considered in this study are far from ideal. Two significant effects are noted, pulse stretching and scintillation resulting from coherent interference. When the target has finite range dimensions, such as the LAGEOS, coherent interference may result in a random variation of the apparent mean of the return pulse. When the transmit pulse is short with respect to the effective target dimension, the individual pulse shape can be grossly distorted by the coherent interference, and the mean pulse shape will be distorted by the impulse response of the target. Distortion of the mean pulse shape can be countered, to some extent, by using optimal filtering in the receiver, however, note that this pulse distortion results in an increase in the effective pulsewidth and time-of-arrival estimation error, requiring an increase in mean signal level to maintain acceptable performance levels.

Scintillation resulting from coherent interference can have a much more profound effect on the performance of the system. These effects arise from two distinct causes. First, consider the case where the target is a planar array of cube-corners at, or near, normal incidence. In Appendix F we show that the optical pulse energy (N_s) of the return signal from such a target has a random variation, with an approximately exponential probability distribution. The expected value of this pulse energy is simply the mean energy computed assuming noncoherent summing of the returns from each cube-corner. Since a maximum likelihood estimator requires knowledge (or estimation) of the signal and background levels, this technique appears to be inappropriate when the signal energy is a pulse to pulse random variable. The correlator approach, however, does not require estimating these parameters, and is, therefore, a usable process.

The effect of coherent interference on the variance of the TOA estimation error can be determined for the zero background, unity threshold case by averaging

equation (19) over the probability space of N_s, resulting in,

$$\overline{\varepsilon_\alpha^2} = \frac{\bar{T}^2}{2\pi^2}\left[\frac{\ell n\ (1 + \bar{N}_s)}{\bar{N}_s}\right] \tag{23}$$

For comparison purposes, consider a 4 ns FWHM pulse. Inverting Equation (23) numerically to determine the required $\bar{N}_s$ to achieve 0.133 ns rms estimation error results in $\bar{N}_s$ = 1309.3, an 9.6 dB increase in required mean signal energy compared to a nonscintillating target.

Next, we consider the case where a larger threshold criterion (L > 1) is used. To accomplish this objective, we return to equation (8) of Appendix E, and evaluate the expectations conditioned on the occurance of exactly K photoelectrons in the pulse width. The result is,

$$\left.\overline{\varepsilon_\alpha^2}\right|_K = \frac{T^2}{2\pi^2 K}\left(\frac{N_s + n_b T}{N_s}\right) \tag{24}$$

Now, suppose we set the threshold for accepting a measurement large enough such that the probability of obtaining a measurement is negligible unless N_s is much greater than $n_b T$. Then, the variance of the error, given K, is effectively dependent only on K and T. We could therefore choose L such that if a measurement is accepted, the variance will not exceed the accuracy goal. For the 4 ns pulse, this results in L = 183. If we assume that the background is negligible, the probability of obtaining K pe events from the scintillating target was shown in Appendix F to be given by,

$$f_K(K) = \left(\frac{1}{1 + \bar{N}_s}\right)\left(\frac{\bar{N}_s}{1 + \bar{N}_s}\right)^K \tag{25}$$

Hence, the detection probability is,

$$P_D = 1 - \sum_{K=0}^{L-1}\left(\frac{1}{1 + \bar{N}_s}\right)\left(\frac{\bar{N}_s}{1 + \bar{N}_s}\right)^K = \left(\frac{\bar{N}_s}{1 + \bar{N}_s}\right)^L \tag{26}$$

Now, if we assume the system can emit 10 pps, and we will accept an average of one measurement per second, $P_D = 0.1$, and $\overline{N}_s = 79$. However, since it requires 10 pulses, on the average, to obtain one measurement, the average required energy per measurement is 790 pe. Using the concept of minimum energy per measurement as a criterion, we select $P_D = 0.366872$ and $\overline{N}_s = 182$ pe/pulse, which results in $\sim$496 pe/measurement, on the average. Thus, at best, we find the scintillation has cost $\sim$4 dB in link margin for the long pulse laser. The short pulse laser concept is also affected, although the criterion for selecting a threshold is more likely to be minimization of false alarms due to background.

The next phase of the analysis will consider a split-gate tracking loop as an alternative to single pulse detection techniques. Since the link dynamics are such that a 10 pps system cannot track unaided, a range prediction module is required to drive the loop. The phase-locked-loop is used to correct low frequency errors and static biases in the range predictions. Consider a phase-locked-loop constructed using a split-gate integrator to derive an error signal. The split-gate integrator simply counts the photoelectron events in two disjoint segments of the signal field, and uses the difference in the two counts as an error signal to guide the repositioning of the partition boundary to the center of the signal field. Since the events are not weighted by time of arrival, the technique is suboptimum. Background photoelectrons do not bias the estimate, provided the gates are balanced. When the loop is locked up, the center of the window, on the average, will coincide with the mean centroid of the received pulse, thus the time of transition from early gate to late gate is the estimate of the time-of-arrival of the centroid of the received pulse.

The analysis begins by noting, for a fixed mean number of photoelectrons detected per pulse, that the number of photoelectrons detected in each half of the gate are random variables, governed by the Poisson distribution. For simplicity, let us define the observed count (for one pulse) in the "early" gate as KE, and KL for the late gate. Then, assume that the pulse is positioned in the vicinity of the partition, such that $Z(1+\varepsilon)/2$ is the pulse energy in the late gate, and ε is a positioning error term, $-1>\varepsilon<1$. Define V = KE-KL. The next step is to determine the mean and variance of V. These are most easily determined in the transform domain. It can be shown that $\emptyset_E(w)$ and $\emptyset_L(w)$, the characteristic functions for the early and late gates are:

$$\phi_E(\omega) = \exp \; Z_1(e^{j\omega}-1) \qquad\qquad \phi_L(\omega) = \exp \; Z_2(e^{j\omega}-1)$$

Then, the characteristic function of V = KE + (-KL) is the product of $\phi_E(\omega)$ and $\phi_L(-\omega)$, since,

$$E\left\{e^{j\omega(-KL)}\right\} = E\left\{e^{-j\omega(KL)}\right\}$$

Thus,

$$\phi_V(\omega) = \exp\left(Z_1(e^{j\omega}-1) + Z_2(e^{-j\omega}-1)\right)$$

Since, $$E\{V\} = \frac{1}{j}\left[\frac{d\phi_V(\omega)}{d\omega}\right]_{\omega = 0}$$

and $$E\left\{V^2\right\} = \frac{d^2\phi_V(\omega)}{d\omega^2}$$

we find, $$E\{V\} = Z_1 - Z_2 = Z\varepsilon$$

$$E\left\{V^2\right\} = n_bT + Z + (Z\varepsilon)^2 \qquad (27)$$

Then, if Z is governed by an exponential distribution, as shown in Appendix E, $f_Z(Z) = 1/m \exp(-Z/m)$,

$$E\{V\} = \int_0^\infty E\{V/Z\} f_Z(Z)\, dZ = m\varepsilon \qquad (28)$$

$$E\left\{V^2\right\} = n_bT + m + 2(m\varepsilon)^2 \qquad (29)$$

$$\sigma_V^2 = n_bT + m + (m\varepsilon)^2 \qquad (30)$$

Then, the expected signal-to-noise ratio in the tracking loop is simply, $SNR = Nm^2/(n_bT + m)$, where N is the number of pulses used to form the estimate (N = 1/loop bandwidth). Then, the rms tracking error, in the normalized form, is simply $\varepsilon_{RMS} = 1/\sqrt{SNR}$. For large SNR conditions (6-9 dB or more), and a temporally Gaussian pulse, $\varepsilon_{RMS} = \tau\sqrt{2\pi/SNR}$, where 2τ is the pulse width at the 60% power points. For zero background, this becomes $\varepsilon_{RMS} = \tau\sqrt{2\pi/NM}$. Assume τ = 0.2 ns. Then, we see that Nm > 3.53 is required to meet ε_{RMS} > 0.133 ns.

The rms error for a maximum likelihood detector, under zero background conditions, never becomes as large as 0.133 ns for a 0.2 ns pulse ($\varepsilon_{rms\ MAX}$ = 0.061 ns) by equation 21, if an estimate can be made at all ($\geq$ 1 pe detected). However, the assumption of zero, or at least negligible, background level is meaningful only as long as the observation time, i.e., the period of time over which the return pulse is expected is comparable to the pulsewidth.

In order to determine realistic estimates of required mean signal energy under dynamic conditions, a series of simulations were performed for the split-gate range tracking system concept. The first series of runs were made to determine optimum system parameters, and employed a first order range tracking loop, with no range prediction errors.

The simulation results indicated that an AGC function of the form, $1/\overline{(KE+KL)}$, yielded the best results, provided the AGC amplifier gain was clamped to a maximum value of unity.

The simple first order loop was then replaced with a second order loop as shown in figure 10. Conceptually, the transmit pulse departure time is used to estimate the arrival time of the reflected pulse. This estimate is summed with the output of the range tracking loop, and delivered to the gate timer. The sequence is that the early gate is opened prior to the expected arrival time. At the expected arrival time, the early gate is closed and the late gate opened. Subsequently, the late gate is closed. Then, the sum and difference values of the two integrator outputs are used to update the range tracking loop.

The return pulse arrival time prediction will be in error by some amount, due to factors such as quantization noise, interpolation errors, unmodeled (or incorrectly modeled) perturbations of the orbit path(s), and errors in the initial conditions. The unmodeled perturbations were considered the most difficult error source to control, since hard data on the higher ordered harmonics of the Earth's gravitational field simply do not exist at this time, and, in fact, one of the scientific objectives for this ranging system is to obtain this data. In view of the lack of hard data, we elected to estimate the unmodeled perturbations and then apply a suitable safety factor to the model and examine the effects on ranging system performance.

The first step was to compute the frequency spectrum of gravitation forces on a low altitude spacecraft due to a small point mass concentration on or near the surface of the Earth. This was done by computing the radial acceleration

FUNCTIONAL BLOCK DIAGRAM
SPLIT GATE RANGE TRACKING CONCEPT

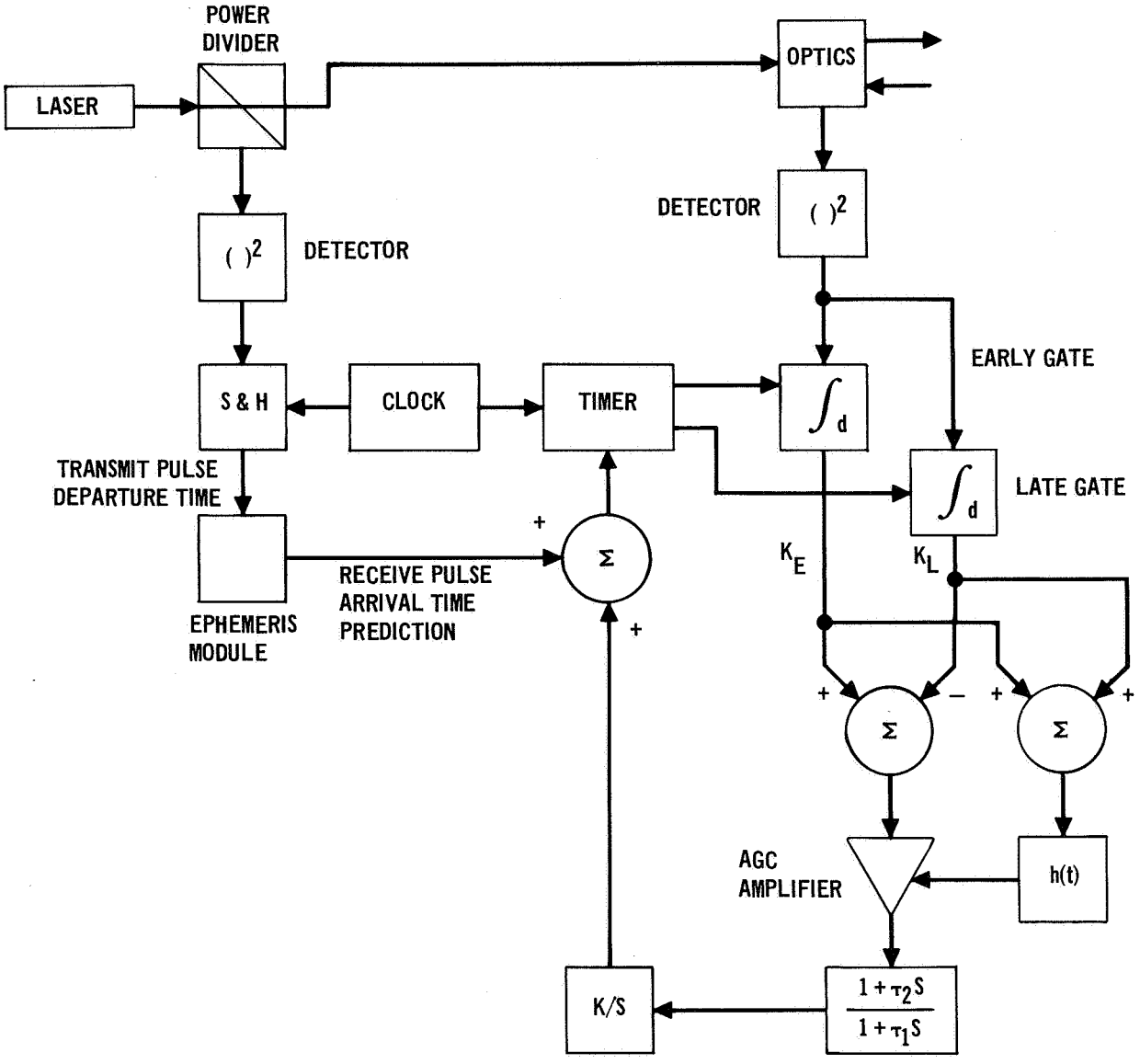

FIGURE 10

force, as a function of time in the orbit plane, and then taking the Fourier transform of the data. We used the fast Fourier transform (FFT) technique, so the output is a line spectrum, in terms of harmonics of the orbit period, i.e.,

$$a(t) = \sum_{n=-\infty}^{\infty} D_n e^{j2\pi nt/\tau} \tag{31}$$

The n = 0 term was dropped, and the remaining terms normalized by dividing by the magnitude of the first harmonic term. The resulting data, plotted in Figure 13, shows that the magnitude of the coefficients (D_n) decreases in a nearly exponential manner with increasing frequency.

If we assume the radial displacement function can be adequately modeled by simply integrating twice, we obtain,

$$d(t) = C \sum_{\substack{n=-\infty \\ n\neq 0}}^{\infty} \frac{D_n}{n^2} e^{j(2\pi nt/\tau)} \tag{32}$$

The next step in this process is to sum the contributions of many coplanar mass concentrations at various locations. Thus, each term in the harmonic expansion is,

$$\frac{C\, D_n}{n^2} e^{j2\pi nt/\tau} \sum_{j=1}^{J} \left(\frac{m_j}{m_o}\right) e^{jn\phi J}$$

Where m_j is the mass surface concentration and ϕ_j is the angular location with respect to the orbit plane. If we assume m_j and ϕ_j, are independent random variables, we can express the autocorrelation function as,

$$R(T) = \sum_{n=-\infty}^{\infty} \alpha_n e^{j2\pi nT/\tau}$$

where

$$\alpha_n = \left(\frac{C\, D_n}{n^2}\right)^2 E\left\{\left|\sum_{j=1}^{J} \frac{m_j}{m_o} e^{jn\phi_j}\right|^2\right\}$$

SPECTRUM OF RADIAL ACCELERATION HARMONICS

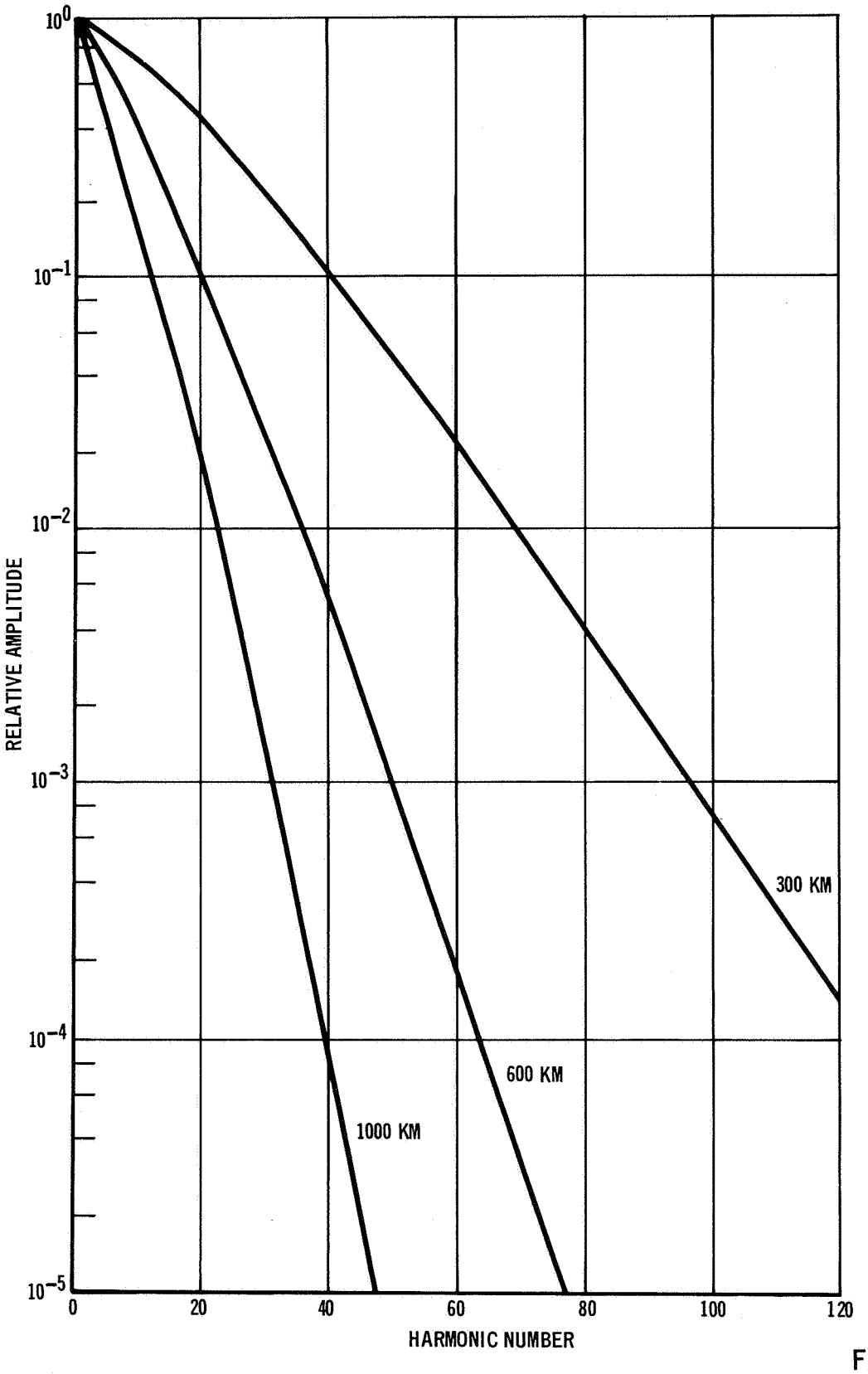

FIGURE 11

Thus, assuming independence,

$$R(T) = C^2 \sum_{n=-\infty}^{\infty} \left(\frac{D_n}{n^2}\right)^2 e^{j2\pi nT/\tau} \qquad (33)$$

The next step is to assess the magnitude of the constant C. The simplest approach is to compare the differences in position for a spacecraft under the influence of two slightly differing gravitation models. Figure 12 presents the results of one such internal study, performed in 1971. The traces show reasonably periodic deviations, with an estimated fundamental (one orbit period) component of about $\pm$ 60 feet. Improvements in models and increased number of gravitational harmonics considered should significantly reduce this deviation, perhaps to more on the order of a few feet by the 1980 time period. Thus, if we assign a value of "C" equivalent to 60 feet, we are probably conservative by an order of magnitude.

Figure 13 shows the simulation results, for a 200 ps laser system, obtained for three values of C, equivalent to 0, 60 feet, and 120 feet, with mean signal energies of 1, 2, and 5 pe/pulse, a scintillating target, and loop bandwidths on the order of 0.5 Hz. This bandwidth setting appeared to be near optimum, as wider loop bandwidths had markedly increased variances, while narrower loop bandwidths experienced increasing bias terms. At 1 pe/pulse signal levels, increasing "C" to 120 feet resulted in one loss of lock in ten trials, indicating near marginal operation. Loss of lock was not observed at any other condition examined. Thus, we can confidently predict that the system will function satisfactorily at 1 pe/pulse, provided the prediction error does not materially exceed the nominal 60 foot peak (120 foot peak-to-peak) level.

5.1.2 Ranging With Active Targets: The target was assumed to have a receiver and a transmitter, and a precision clock. Both the ranging system and the target would emit pulses repetitively, and record in local clock time, the transmitted pulse departure time and the times when received pulses were detected. These disjoint event time recordings are used for subsequent processing to extract range data.

EFFECT OF POINT MASS PORTION OF EM 1.0 GRAVITY MODEL

NOMINAL ORBIT: h_p = 80 NMI; h_A = 200 NMI; INCLINATION = 110°

REFERENCE MODEL: WGS 66 THROUGH 8, 8

ALTERNATE MODEL: COMPLETE EM 1.0;
WGS 66 THROUGH 8, 8
PLUS 1662 POINT MASSES

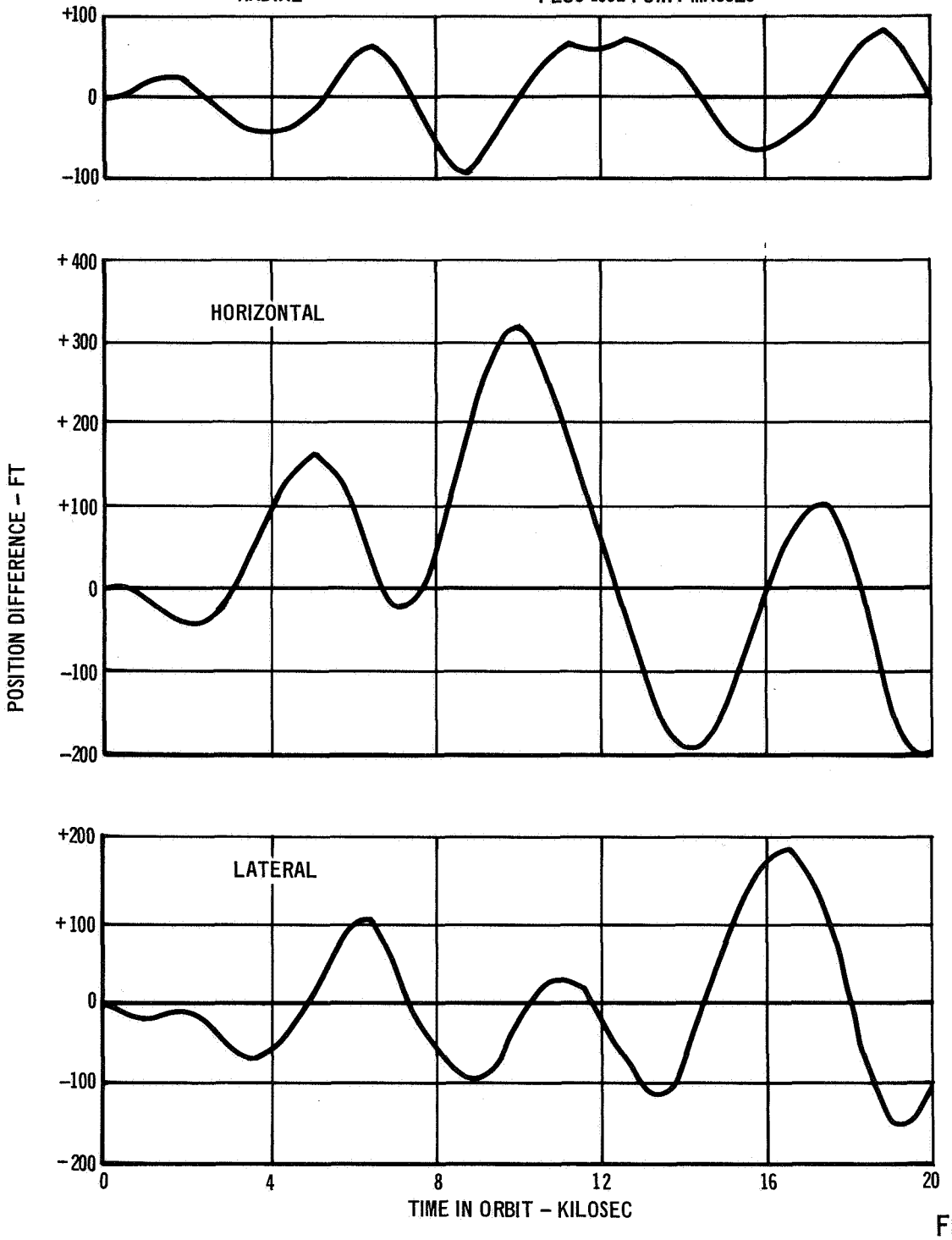

FIGURE 12

EFFECT OF DYNAMIC PREDICTION ERRORS ON RMS RANGE TRACKING ERROR (HARMONIC PREDICTION ERROR MODEL) 200 ps LASER PULSEWIDTH

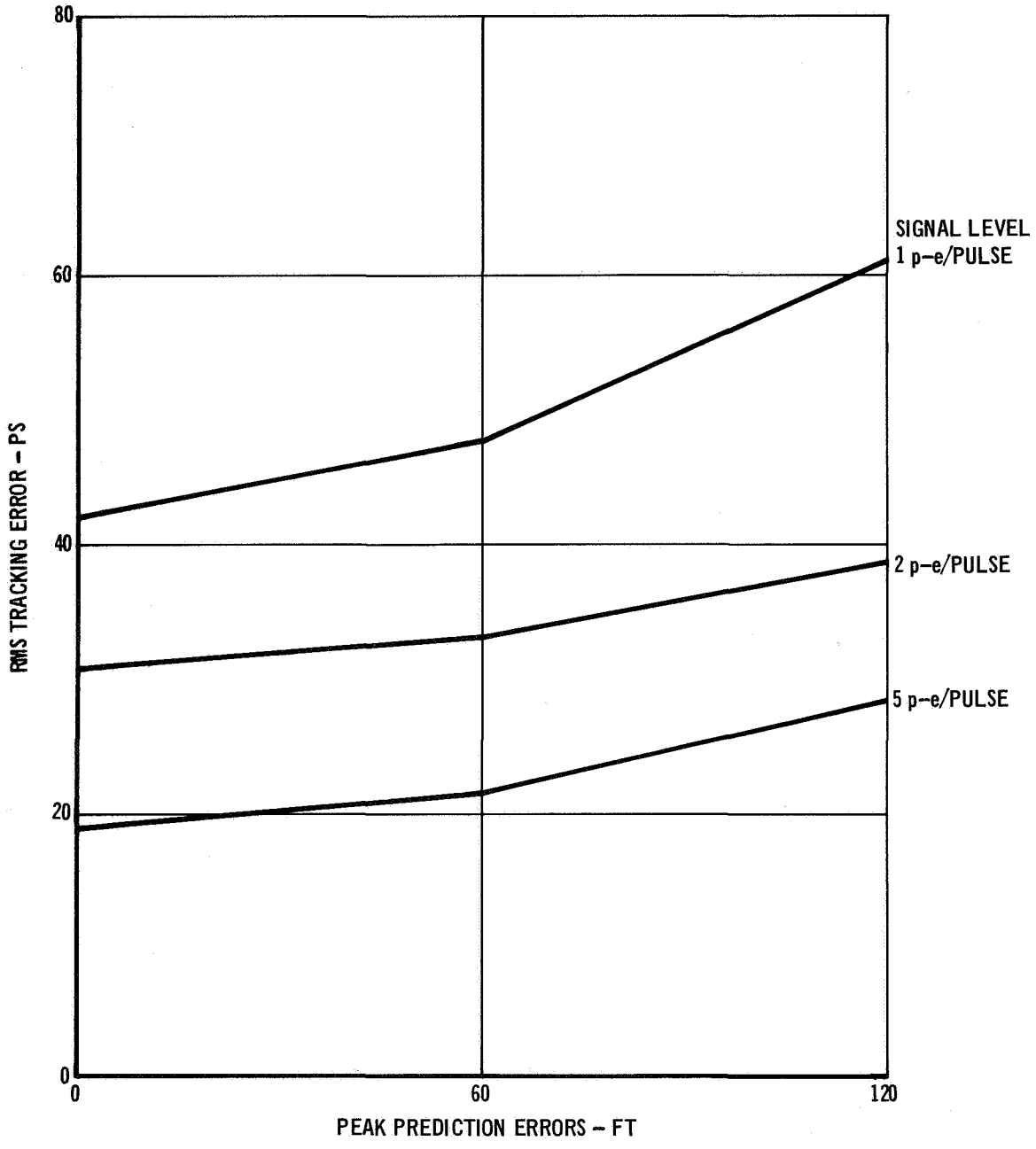

FIGURE 13

When the active target contains a receiver and a transmitter, the detection problem is much the same as for passive target ranging, except that our ability to predict the arrival time of the next received pulse is degraded considerably. First, since we are not obtaining real time ranging data, ephemeris errors are not reduced and the range will be changing in a different manner than expected. Second, the receiver does not have knowledge of when the pulse was actually emitted. If the transmit pulses could be emitted at very precise intervals, it would be possible to reduce the uncertainty by extrapolating from the last received pulse. However, this is the only known situation where precise control of emission time is advantageous. Consequently, we elected not to require precise emission time control, and to use a time of arrival estimation technique which does not require tight range gating. When operating with an active target, the links are not seriously power limited, thus a suboptimum TOA algorithm does not impose a serious penalty. A modified version of the weighted counter with an adaptive threshold, discussed in Appendix E, is shown in figure 14. The modifications are intended to adapt this concept to ungated operation. When a signal is encountered, the operation is identical to the circuit of Appendix E. When only background is present, however, an AGC clamp is applied to reduce the false alarm probabilities to acceptable levels. Also, the simple integrator has been replaced with a sliding window integrator to permit continuous scan.

5.2 POINTING CONTROL SYSTEM ANALYSIS. The fundamental problem in the pointing control system for the HATRS terminal is to control the direction of propagation of the very narrow (5 μrad) transmit beam to ensure that the transmit energy illuminates the target. The sources of error in this control process include prediction errors (ephemeris uncertainties), attitude reference uncertainties, and thermal and mechanical errors. Many of these uncertainties have a low frequency content, i.e., they change in magnitude very slowly, and thus can be combatted with active signal sensing techniques. The energy of signal reflected from the target can be used to form an estimate of the pointing error if the transmit beam is dithered (systematically varied) about the nominal expected direction. These estimates can then be used to bias the pointing commands to center the transmit beam on the target. The accuracy of this centering process is dependent on the mean reflected signal energy, the type and magnitude of the dither process, and the bandwidth of both the disturbance spectrum and

WEIGHTED COUNTER WITH ADAPTIVE THRESHOLD FOR CONTINUOUS SCAN OPERATION

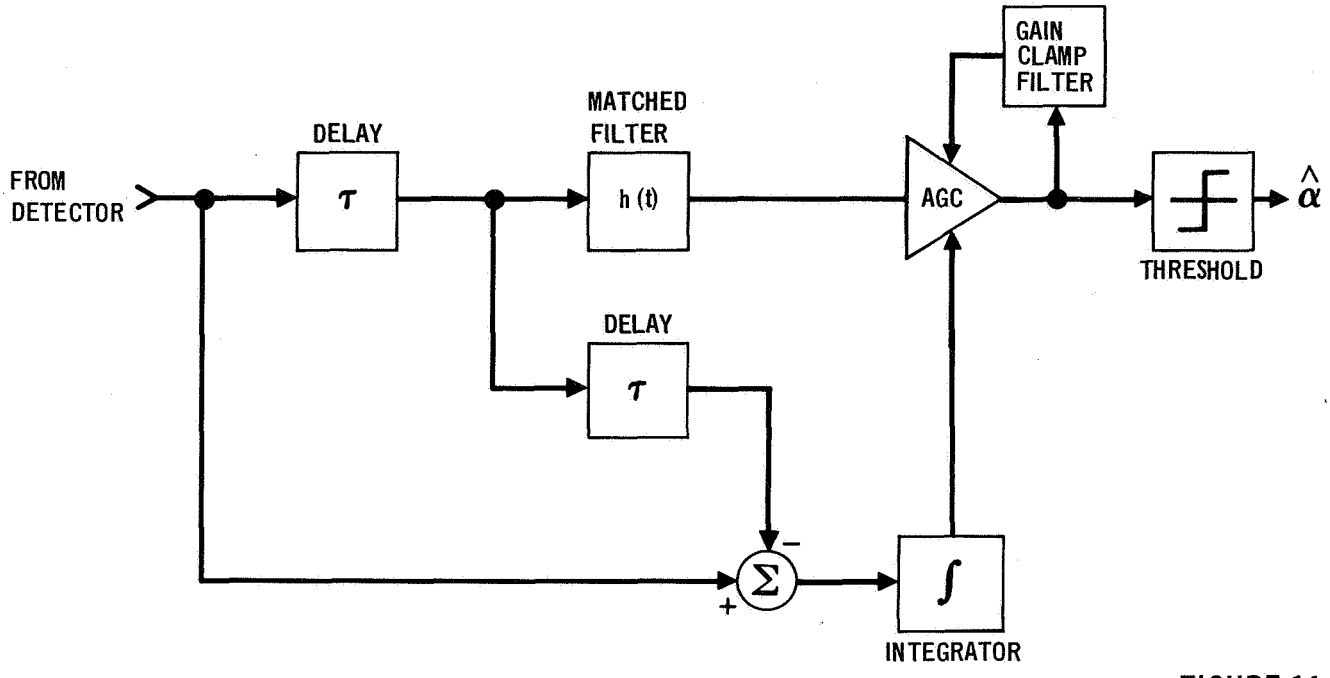

FIGURE 14

the filter used to smooth the error estimates. The pointing control concept requires very precise open-loop pointing, which is augmented with heavily filtered pointing error estimates to reduce static pointing errors. The attitude reference system inputs the estimated boresight direction vector to the ephemeris computer, which computes the desired boresight direction vector, and outputs a pointing error estimate to the pointing control loop filter. The loop filter sums the computer error estimate the dither command, and the filtered bias error signal and outputs acceleration commands to the pointing control actuators.

The open-loop error can be expected to contain very low frequency error sources (thermal drift), moderate frequency error sources (ephemeris prediction errors), and wide-bandwidth error sources (vibration). The boundaries of these domains are related to the transmit pulse rate. The very low frequency error sources are highly correlated over many transmit pulse periods. The moderate frequency error sources are characterized by auto-correlation functions which decay significantly in a finite number of pulse periods. The wide bandwidth error sources result in errors which are virtually uncorrelated from pulse-to-pulse. We note that the pointing error estimation process is noisy, and that this noise is virtually uncorrelated from pulse-to-pulse. The pointing control

system filter acts as a low pass filter to the estimation error noise, and as a high pass filter to the pointing error noise. The optimum control system filter is the filter which minimizes the residual mean square pointing error, which is simply the sum of the estimation error noise which passes through the system filter and the pointing error noise which is outside the system filter.

The first step in determining the performance of the system is to select a dither process. We evaluated two techniques and found virtually identical performance. The first dither process used a conical scan about the nominal pointing direction. The second technique employed a bang-bang type of dither, where the beam was deflected by a small angle ($\Delta\theta$) is each of four directions (+x, -x, +y, -y). The latter approach was chosen as the best approach since only four pulses were required to form a pointing error estimate.

The transmit beam has a nearly Gaussian spatial intensity distribution, thus the mean reflected signal energy (m) is related to the pointing error at the instant a pulse is transmitted by

$$m = m_0 \exp\ -(x^2 + y^2)/R^2$$

where m_0 is the received signal energy when $x = y = 0$, x and y are the coordinates of the pointing error, and R is the transmit beam radius at the e^{-1} power point. x, y, and R may be expressed in linear dimensions (meters) or angular dimensions (radians), or simply normalized in terms of the beam radius. The latter approach simplifies the notation and is used subsequently.

Now, assume that the mean prediction pointing error (x_0, y_0) is constant for four successive pulses. Denote the receiver output for these four pulses as Z_i, i = 1, 2, 3, 4. We will assume the receiver is an ideal photoelectron counter. Thus, the Z_i are independent, Poisson random variables. Next, assume that the actual pointing direction is offset from the nominal direction by an amount Δx for the first pulse, $-\Delta x$ for the second pulse, Δy for the third pulse, and $-\Delta y$ for the fourth pulse. Then, let g_x and g_y be defined,

$$g_x = Z_1 - Z_2$$

$$g_y = Z_3 - Z_4$$

Consequently, g_x and g_x are random variables with means n_x and n_y, and variances σx^2 and $\sigma_y{}^2$, given by

$$n_x = m_o \left\{ e^{-(x_o + \Delta x)^2 - y_o^2} - e^{-(x_o - \Delta x)^2 - y_o^2} \right\}$$

$$\sigma_x{}^2 = 2n_bT + m_o \left\{ e^{-(x_o+\Delta x)^2 - y_o{}^2} + e^{-(x_o - \Delta X)^2} - y_o{}^2 \right\}$$

for x, and similarly for y, and n_bT is the background photo-electrons/gate. These equations can be rewritten,

$$n_x = 2\, m_o \sinh (2X_o \Delta x)\, e^{-(x_o{}^2 + y_o{}^2 + \Delta x^2)}$$

$$\sigma_x{}^2 = 2n_bT + 2m_o \cosh (2X_o\, \Delta X) e^{-(x_o{}^2 + y_o{}^2 + \Delta x^2)}$$

When x_o, y_o and Δx are small, $n_x \simeq -4m_o\, x_o\, \Delta x$, thus the estimate of x_o is simply,

$$x_o = -n_x / 4m_o \Delta x$$

and the variance of the estimate of x_o is,

$$\sigma_{xo}{}^2 = \sigma_x{}^2 / (4m_o \Delta x)^2$$

Thus far, however, we have not employed all of the information available from the return signal. If the receiver field-of-view is divided into four or more non-overlapping detection areas, we can obtain an estimate, from each received pulse, of the received signal angle-of-arrival with respect to the receiver boresight. If the error between the transmit boresight and receive boresight is small, the angle-of-arrival estimates are a good approximation of the transmitter pointing error. Ignoring signal to noise ratio considerations, the usable bandwidth of the angle-of-arrival estimation process is four times the bandwidth of the transmitter pointing error estimation process.

The simplest solution to the angle-of-arrival estimation process is to divide the receiver field-of-view into four quadrants. The angle-of-arrival estimates are based on the detected signals from each quadrant, f(y) = A+B-C-D, and f(x) = A-B-C+D, where the quadrants are lettered counter-clockwise from the conventional first quadrant in an x, y coordinate system. As noted previously, each signal is a Poisson random variable, whose mean is determined by the amount of the target image energy on that quadrant. Now, A, B, C, and D

are independent (Poisson distributed) random variables, thus the sum of any two is also a Poisson distributed random variable, with a mean rate equal to the sum of the mean rates. Consequently, we can use the analytical form developed for the split-gate range tracker, where ε, the division parameter, now refers to the spatial (or angular error) division parameter.

As discussed previously, the split gate tracker was evaluated by simulation, and we found under typical conditions that at one signal pe/pulse, it was possible to achieve $\sim$ 0.03 ns rms tracking error for a temporarily Gaussian pulse of 0.2 ns width at the e^{-2} power points. Thus, the achieved performance is $\sim$ 0.15 ns rms per ns pulse width, which would scale to 0.15 μrad rms per μrad image diameter at the detectors. For a one meter diameter collector, the diffraction limited image diameter is 2.44 $\lambda/D \simeq$ 1.3 μrad, (at the first null). Thus, with diffraction limited optics the rms angle of arrival estimation error would be less than 0.2 μrad, which is well within the 0.5 μrad budget.

In the split gate tracker simulation, prediction noise was a major consideration in choosing the tracking loop bandwidth. For angle of arrival estimation, prediction noise is several orders of magnitude smaller in angular units and, hence, virtually negligible. The other pointing error sources, such as mechanical vibration, must simply be controlled to acceptable limits. Under these assumptions, therefore, we can confidently predict that if the range tracking functions can be accomplished, angle of arrival tracking to $\sim$ 0.4 μrad rms can also be accomplished.

6.0 CONCLUSIONS

Laser ranging from a space-borne terminal to active and passive targets in space or on the ground has been shown to be feasible, and that 2-cm rms range measurement accuracy is achievable. Two laser ranging systems have been synthesized, one to meet the requirements for very long range measurements, and the other for relatively short range measurements. The very long range links ($\sim$30,000 km) are severely power limited, requiring precision optical systems, narrow transmit beamwidths (5 μrad), and sophisticated signal processing techniques if the ranging accuracy goals are to be met. These requirements can be met with implementable systems provided the target is suitably configured. A LAGEOS type of target was evaluated in detail, and found to contribute significantly to the uncertainties in range measurement accuracy. Both narrow pulse ($\sim$200 ps) and wide pulse (4 ns) lasers were considered for the terminals. If the narrow pulse laser can be developed for this application, the inherent ranging accuracy capability is well within the sub-centimeter region, and will be most seriously limited by the target characteristics and signal processing implementations. These limitations do not appear insurmountable, although development is required. The wide pulse laser concept theoretically capable of meeting the range estimation accuracy goals, provided the output pulses are very stable and repeatable. The required precision pointing control and alignment control functions are well within the state-of-the-art projected for the 1980's time frame.

A laser ranging system concept for the relatively short range (300-500 km) measurements was evolved for a Space Shuttle or Spacelab experimental mission, with ranging to ground based retro-reflectors the fundamental requirement. For this application, limitations in ephemeris prediction accuracy and available target viewing time resulted in significant differences from the long range terminal concept, although many of the components are identical. This concept is considered feasible and implementable, but several unresolved questions remain to be studied before the requirements for the experiment can be established.

Measurement strategy was discovered to be a major factor affecting both the experiment results and the design of the laser ranging system. Detailed evaluation of the effect of measurement strategy on the target grid relative position reconstruction accuracy is needed to determine whether simultaneous (multiple

beam) ranging is needed, or if sequential ranging measurements can meet the experiment objectives.

Another unresolved question of potential significance concerns the integration of the experiment and the Shuttle/Spacelab. The Shuttle requirements and capabilities are not ideally matched to the laser ranging experiment. Factors such as c.g. uncertainty, structural flexure, empheris uncertainties and vibration spectrum may be very significant to the design and feasibility of the laser ranging experiment, and deserve more attention than could be allocated in this study.

APPENDIX A

FAR FIELD RADIATION PATTERNS - LAGEOS CUBE-CORNERS

1.0 INTRODUCTION

The far field radiation patterns and the programs used to generate this data are included in this appendix. The data file generated in this activity was also used by the program, discussed in Appendix B, to compute the return pulse shapes.

2.0 RADIATION PATTERN ANALYSIS PROGRAM

The program used to compute the radiation pattern and gain was written in Fortran IV, for MDAC's Sigma 9 time sharing computer system, and was used in the batch (off-line) mode. The program is listed in the following pages.

```
RAY5    07:59 MAR 06,'75


100$PS=2000
110 COMPLEX AX(512),AY(100,100),ELEMT
120 COMPLEX ALEMT
130 DIMENSION DP(6),TRAN(116)
140 COMMON AIN,AROT,FRAD,FR2,ADROT,ALAM,AGRAD,ICON,BMSPRD
150 NAMELIST FDIACM,ALAM,AIND,ADIHED,IREND,NMAX
160 PI=3.1415926535898
170 NMAX=256
180 NDIM=50
190NDIM2=100
200 FDIACM=3.8
210 ALAM=.53
220 AIND=0
230 ADIHED=7.3
240 CALL OPENF1('RAYDAT',1)
245 CALL OPENF2('RAYOUT',2)
250 IREND=0
260 1 CONTINUE
270 INPUT(1)
280 IF(IREND.EQ.0)GOTO210
290 CALL CLOSF1
295 CALL CLOSF2
300 STOP
310 210 CONTINUE
```

```
320 PRINT301,NMAX,FDIACM,ALAM,AIND,ADIHED
330 301 FORMAT(//'SAMPLE SPACING,FACE DIA,LAMBDA,INCIDENCE,DIH.'
340&/5F12.2)
345 WRITE(2,)FDIACM,ALAM,AIND,ADIHED
350 FRAD=5*FDIACM
360 FR2=FRAD**2
370 DELX=FDIACM/5.
380 DELTHE=ALAM*1000./NMAX/DELX
400 AIN=AIND*PI/180.
410 DELZ=DELX/COS(AIN)
420 DELY=DELX
430 BMSPRD=4.75351*ADIHED
440 ADROT=ADIHED/2.
450 AINDF=ASIN(.6849*SIN(AIN))
460 ALP=COS(AINDF)
470D1=1./SQRT(3.)
480D2=1./SQRT(2.)
490 D3=1./SQRT(6.)
500 AN=COS(.955317+AINDF)
510 AM=SQRT((1.-AN**2)/2.)
520 AL=AM
530 P=FRAD/D2
540 X0=P*D1
550 DSTOP=2*P/ALP
560 DO 2 I=1,100
570 ZP=DELZ*(I-NDIM+.5)
580 DO 2 J=1,100
590 YP=DELY*(J-NDIM+.5)
600RAD=ZP**2+YP**2
610 ELEMT=0
620 IF(RAD.GT.FR2)GOTO201
630 X1=X0-YP*D2-ZP*D3
640 Y1=X0+YP*D2-ZP*D3
650 Z1=X0+2*ZP*D3
660 X2=AL*DSTOP-X0-X1
670 Y2=AM*DSTOP-X0-Y1
680 Z2=AN*DSTOP-X0-Z1
690 RAD2=X2**2+Y2**2+Z2**2
700 IF(RAD2.GT.FR2)GOTO201
710 PHA1=6.2832E3/ALAM*BMSPRD
720 IF(YP.EQ.0)YP=1.E-9
730 DX=X1/AL
740 DY=Y1/AM
750 DZ=Z1/AN
760 IF((DX.LE.DY).AND.(DY.LE.DZ))PHA2=PHA1*(ZP*.86603+YP/2.);GOTO303
770 IF((DX.LE.DZ).AND.(DZ.LE.DY))PHA2=PHA1*YP;GOTO303
780 IF((DZ.LE.DX).AND.(DX.LE.DY))PHA2=-PHA1*(ZP*.86603-YP/2.);GOTO303
790 IF((DZ.LE.DY).AND.(DY.LE.DX))PHA2=PHA1*(-ZP*.86603-YP/2.);GOTO303
800 IF((DY.LE.DZ).AND.(DZ.LE.DX))PHA2=PHA1*(-YP);GOTO303
810 PHA2=-PHA1*(-ZP*.86603+YP/2.)
820 303 PHA2=PHA2/ALP
830 PHA=PHA2*1.E-6
840 ELEMT=CMPLX(COS(PHA),SIN(PHA))
```

```
850 201 CONTINUE
860 AY(I,J)=ELEMT
870 2 CONTINUE
880 ISIGN=-1
890 DO 3 I=1,100
900 DO 20 J=101,NMAX
910 20 AX(J)=0
920 DO 4 J=1,100
930 4 AX(J)=AY(I,J)
940 CALL FFT(NMAX,AX,ISIGN)
950 DO 5 J=1,51
960 5 AY(I,J)=AX(J)
970 DO 21 J=52,100
980 21 AY(I,J)=AX(J+NMAX-100)
990 3 CONTINUE
1000 DO 6 I=1,100
1010 DO 22 J=101,NMAX
1020 22 AX(J)=0
1030 DO 7 J=1,100
1040 7 AX(J)=AY(J,I)
1050 CALL FFT(NMAX,AX,ISIGN)
1060 DO 8 J=1,51
1070 ELEMT=AX(J)*CONJG(AX(J))
1080 8 AY(J,I)=ELEMT
1090 DO 23 J=52,100
1100 ELEMT=AX(J+NMAX-100)*CONJG(AX(J+NMAX-100))
1110 23 AY(J,I)=ELEMT
1120 6 CONTINUE
1130 FACTOR=(4*PI*(1000.*DELX/ALAM)**2)**2
1150 CALL STATS(FACTOR,AY,DELTHE,TRAN)
1155 WRITE(2,)TRAN
1160 GOTO 1
1170 END
1180       SUBROUTINE FFT(NE,X,NASGN)
1190C      NMAX=LARGEST VALUE OF N TO BE PROCESSED
1200C      NONDUMMY DIMENSION M(NMAX)
1210C      FOR EXAMPLE, IF NMAX=25 THEN
1220       DIMENSION M(9)
1230C      DIMENSION X(2**N)
1240       DIMENSION X(NE)
1250       COMPLEX X,WK,HOLD,C
1260       ASIGN=NASGN
1270       IF(NE-1)10,10,11
1280  11   DO 12 I=1,15
1290       II=NE/(2**I)
1300       III=I
1310       IF(II-1)12,13,12
1320  12   CONTINUE
1330       GO TO 10
1340  13   N=III
1350       LX=NE
1360       FLX=LX
1370       DO 1 I=1,N
```

```
1380     1 M(I)=2**(N-I)
1390       DO 4 L=1,N
1400       NBLOCK=2**(L-1)
1410       LBLOCK=LX/NBLOCK
1420       LBHALF=LBLOCK/2
1430       K=0
1440       DO 4 IBLOCK=1,NBLOCK
1450       FK=K
1460       V=ASIGN*6.2831853*FK/FLX
1470       WK=CMPLX(COS(V),SIN(V))
1480       ISTART=LBLOCK*(IBLOCK-1)
1490       DO 2 I=1,LBHALF
1500       J=ISTART+I
1510       JH=J+LBHALF
1520       Q=X(JH)*WK
1530       X(JH)=X(J)-Q
1540       X(J)=X(J)+Q
1550     2 CONTINUE
1560       DO 3 I=2,N
1570       II=I
1580       IF(K.LT.M(I)) GO TO 4
1590     3 K=K-M(I)
1600     4 K=K+M(II)
1610       K=0
1620       DO 7 J=1,LX
1630       IF(K.LT.J) GO TO 5
1640       HOLD=X(J)
1650       X(J)=X(K+1)
1660       X(K+1)=HOLD
1670     5 DO 6 I=1,N
1680       II=I
1690       IF(K.LT.M(I)) GO TO 7
1700     6 K=K-M(I)
1710     7 K=K+M(II)
1720       IF(ASIGN.LT.0.0) RETURN
1730       DO 8 I=1,LX
1740     8 X(I)=X(I)/FLX
1750 10 CONTINUE
1760       RETURN
1770       END
2370 SUBROUTINE STATS(F,A,DEL,TRAN)
2380 COMPLEX A(100,100)
2390 DIMENSION VAL(50,3),TRAN(116)
2400 ASP=2.5/DEL
2410 AMIN=ASP/2
2420 AMAX=69.5/DEL+AMIN
2430 DO 1 I=1,50
2440 DO 1 J=1,3
2450 1 VAL(I,J)=0
2460 DO 2 I=1,100
2470 II=I
2480 IF(II.GT.51)II=102-I
2490 DO 2 J=1,100
2500 JJ=J
```

```
2510 IF(JJ.GT.51)JJ=102-J
2520 ARG2=FLOAT((II-1)**2+(JJ-1)**2)+1.E-6
2530 ARG=SQRT(ARG2)
2540 IF(ARG.LT.AMIN)GOTO4
2550 IF(ARG.GT.AMAX+ASP)GOTO4
2560 ID=1+INT((ARG-AMIN)/ASP)
2570 IF(ID.GT.50)GOTO4
2580 X=REAL(A(I,J))*F
2590 X2=X*X
2600 VAL(ID,1)=VAL(ID,1)+1
2610 VAL(ID,2)=VAL(ID,2)+X
2620 VAL(ID,3)=VAL(ID,3)+X2
2630 4 CONTINUE
2640 2 CONTINUE
2650 DO 3 I=1,29
2660 XI=VAL(I,1)
2670 X2=VAL(I,2)
2680 X3=VAL(I,3)
2690 XM=X2/XI
2700VAR=X3/XI-XM*XM
2710 STD=SQRT(VAR+1.E-20)
2720 ANG=AMIN+ASP*(FLOAT(I)-.5)
2740 ANG=ANG*DEL
2741 II=4*I
2742 TRAN(II-3)=ANG
2743 TRAN(II-2)=XI
2744 TRAN(II-1)=ALOG(XM)
2745 TRAN(II)=ALOG(STD)
2750 PRINT 100,ANG,XI,XM,STD
2760 3 CONTINUE
2770 RETURN
2780 100 FORMAT(G12.4,F6.0,2G12.4)
2790 END
```

3.0 RADIATION PATTERN DATA

Two programs were used to process the data, from the preceding program, for presentation. These programs and the resulting data are presented in the following pages. The first set of data, program GAINPLOT, shows the mean gain as a function of point-ahead angle, for incidence angles from 0 (normal) to 40 degrees. The left-hand number is the point-ahead angle in micro-radians. The number on the right-hand side is the gain product in dB. The plotting field has 50 increments, with the scale factor shown in the heading. The first half of the data is for 0.53 μm wavelength illumination, the second half is for 1.06 μm wavelength.

The second set of data, program CROSPLOT, shows the mean gain as a function of incidence angle, for point-ahead angles from 5 to 60 microradians. The same conventions and scale factors were used, except that the left most column of numbers are the incidence angle in degrees.

GAINPLOT 08:06 MAR 06,'75

```
      DIMENSION TRAN(8),ALIST(18,24)
      DATA STAR,X/'*','X'/,DB/4.34294/
      CALL OPENF1('TEDAT',1)
      DO 1 I=1,18
      READ(1,)D1,D2,D3,D4
      PRINT,D1,D2,D3,D4
      DO2 J=1,12
      READ(1,)TRAN
      ALIST(I,2*J-1)=TRAN(3)
      ALIST(I,2*J)=TRAN(7)
    2 CONTINUE
      DO3 J=1,3
    3 READ(1,)DUM
    1 CONTINUE
      CALL CLOSF1
      AMAX=0.
      AMIN=1.E4
      DO4 I=1,18
      DO4 J=1,24
      DUM=ALIST(I,J)
      IF(DUM.GT.AMAX)AMAX=DUM
      IF(DUM.LT.AMIN)AMIN=DUM
    4 CONTINUE
      VO=170
      VX=INT(DB*AMAX)+1.
      DV=VX-VO
      SCALE=DV/50.
      PRINT100,VX,VO,SCALE
      DPA=2.5
      DO10 I=1,18
      IF(I.EQ.1)OUTPUT'.53 MICROMETERS WAVELENGTH'
      IF(I.EQ.10)OUTPUT'1.06 MICROMETERS WAVELENGTH'
      AINC=5.*(I-1)
      IF(I.GT.9)AINC=AINC-45.
      PRINT101,AINC
      DO10 J=1,24
      DUM=DB*ALIST(I,J)
      DS=(DUM-VO)/SCALE
      ID=INT(DS)+10
      IF(ID.LT.10)ID=10
      PA=J*DPA
      PRINT102,PA,STAR,ID,X,STAR,DUM
   10 CONTINUE
      STOP
  100 FORMAT('MAX,MIN',2F8.2/'SCALE=',F6.2,'/DIV')
  101 FORMAT(/'INCIDENCE ANGLE',F4.0,' DEGREES'
     &,/T4,'PA',T65,'GAIN')
  102 FORMAT(F6.1,T10,A,TN,A,T60,A,F6.2)
      END
```

GAINPLOT 08:08 MAR 06,'75

3.80000	.530000	.000000	7.30000
3.80000	.530000	5.00000	7.30000
3.80000	.530000	10.0000	7.30000
3.80000	.530000	15.0000	7.30000
3.80000	.530000	20.0000	7.30000
3.80000	.530000	25.0000	7.30000
3.80000	.530000	30.0000	7.30000
3.80000	.530000	35.0000	7.30000
3.80000	.530000	40.0000	7.30000
3.80000	1.06000	.000000	7.30000
3.80000	1.06000	5.00000	7.30000
3.80000	1.06000	10.0000	7.30000
3.80000	1.06000	15.0000	7.30000
3.80000	1.06000	20.0000	7.30000
3.80000	1.06000	25.0000	7.30000
3.80000	1.06000	30.0000	7.30000
3.80000	1.06000	35.0000	7.30000
3.80000	1.06000	40.0000	7.30000

MAX,MIN 201.00 170.00
SCALE= .62/DIV
.53 MICROMETERS WAVELENGTH

INCIDENCE ANGLE 0. DEGREES

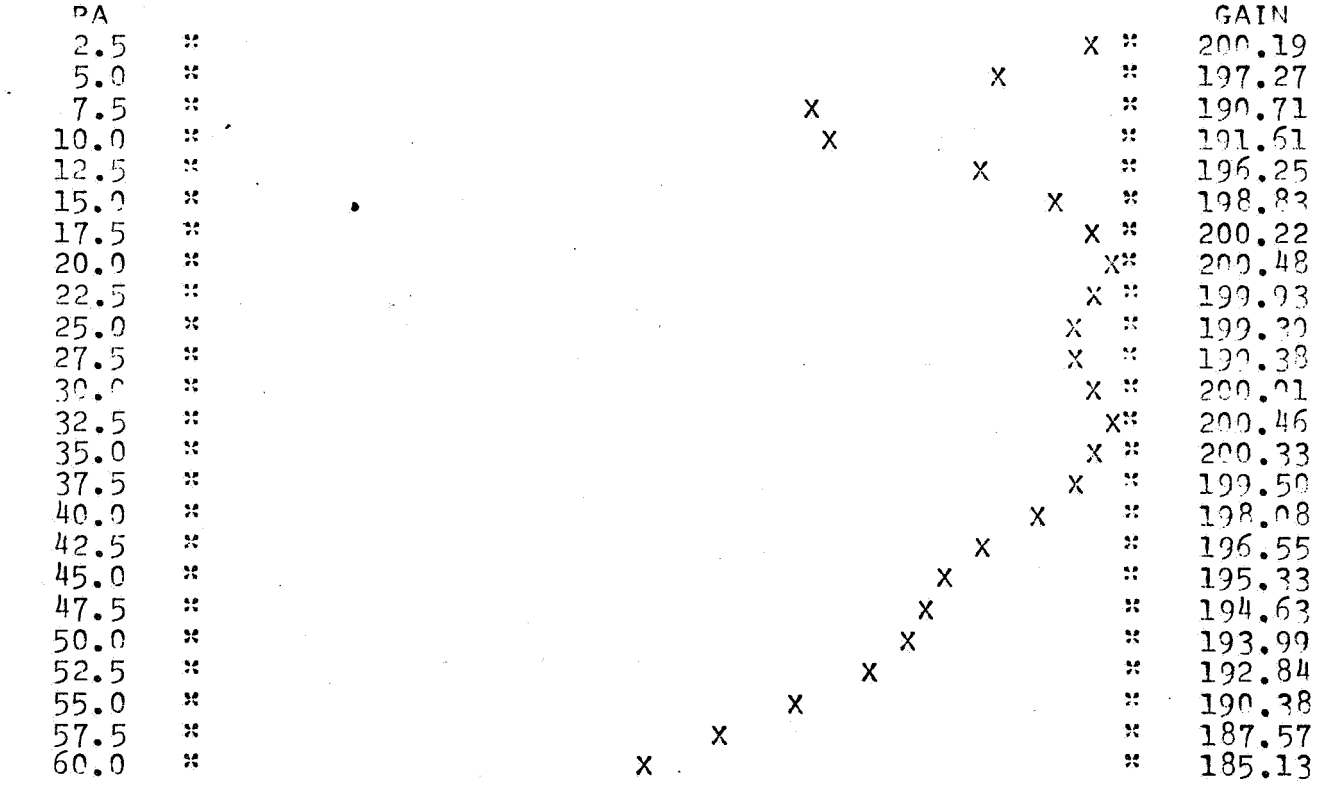

INCIDENCE ANGLE 5. DEGREES

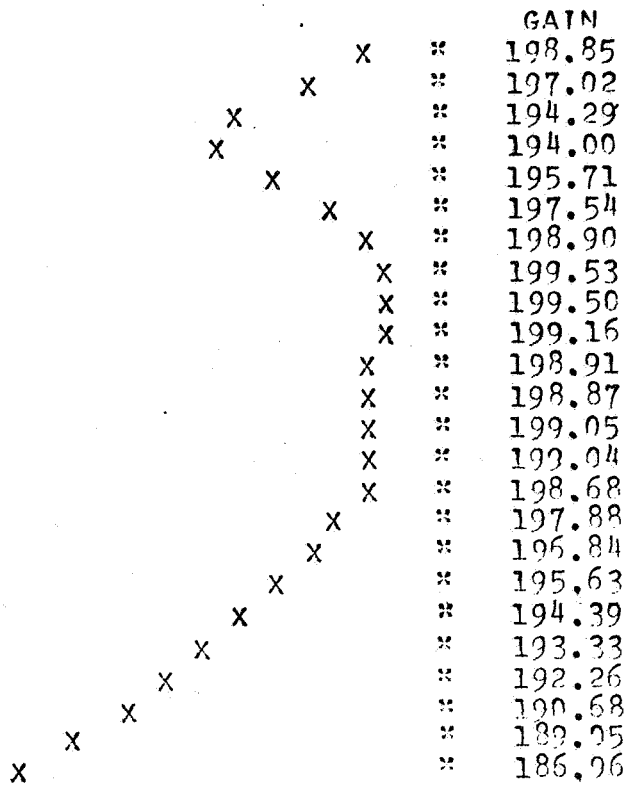

PA	GAIN
2.5	198.85
5.0	197.02
7.5	194.29
10.0	194.00
12.5	195.71
15.0	197.54
17.5	198.90
20.0	199.53
22.5	199.50
25.0	199.16
27.5	198.91
30.0	198.87
32.5	199.05
35.0	199.04
37.5	198.68
40.0	197.88
42.5	196.84
45.0	195.63
47.5	194.39
50.0	193.33
52.5	192.26
55.0	190.68
57.5	189.05
60.0	186.96

INCIDENCE ANGLE 10. DEGREES

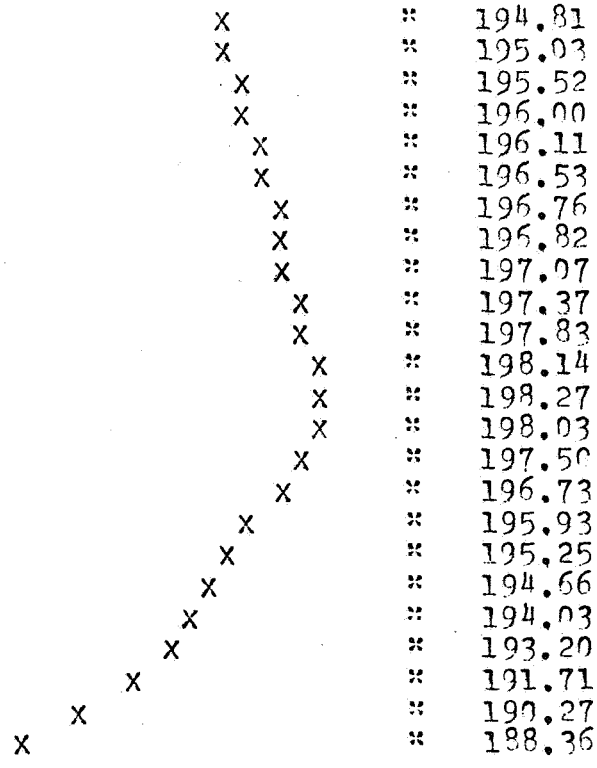

PA	GAIN
2.5	194.81
5.0	195.03
7.5	195.52
10.0	196.00
12.5	196.11
15.0	196.53
17.5	196.76
20.0	196.82
22.5	197.07
25.0	197.37
27.5	197.83
30.0	198.14
32.5	198.27
35.0	198.03
37.5	197.50
40.0	196.73
42.5	195.93
45.0	195.25
47.5	194.66
50.0	194.03
52.5	193.20
55.0	191.71
57.5	190.27
60.0	188.36

INCIDENCE ANGLE 15. DEGREES

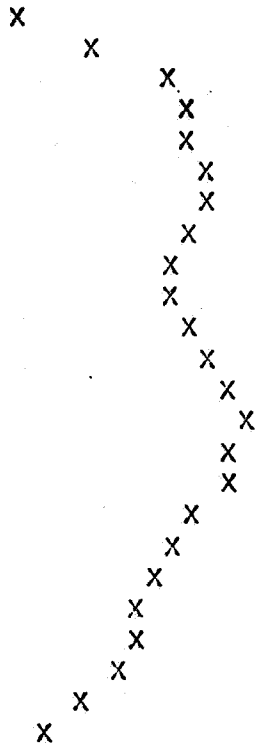

PA	GAIN
2.5	189.34
5.0	192.01
7.5	194.21
10.0	195.31
12.5	195.33
15.0	195.62
17.5	195.52
20.0	194.92
22.5	194.37
25.0	194.39
27.5	195.03
30.0	195.93
32.5	196.55
35.0	196.75
37.5	196.53
40.0	196.09
42.5	195.30
45.0	194.48
47.5	194.03
50.0	193.55
52.5	193.07
55.0	192.37
57.5	191.58
60.0	190.42

INCIDENCE ANGLE 20. DEGREES

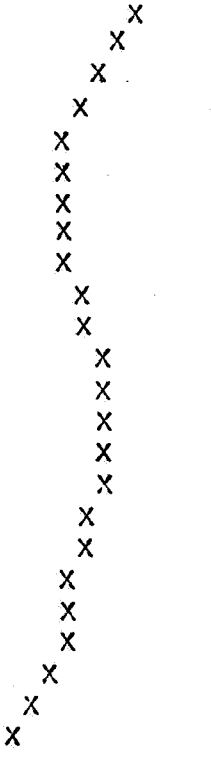

PA	GAIN
2.5	195.34
5.0	194.77
7.5	193.99
10.0	193.43
12.5	192.41
15.0	192.36
17.5	192.66
20.0	192.81
22.5	192.64
25.0	193.11
27.5	193.42
30.0	193.58
32.5	194.03
35.0	194.09
37.5	193.96
40.0	193.89
42.5	193.48
45.0	193.02
47.5	192.84
50.0	192.74
52.5	192.48
55.0	192.01
57.5	191.70
60.0	191.03

INCIDENCE ANGLE 25. DEGREES

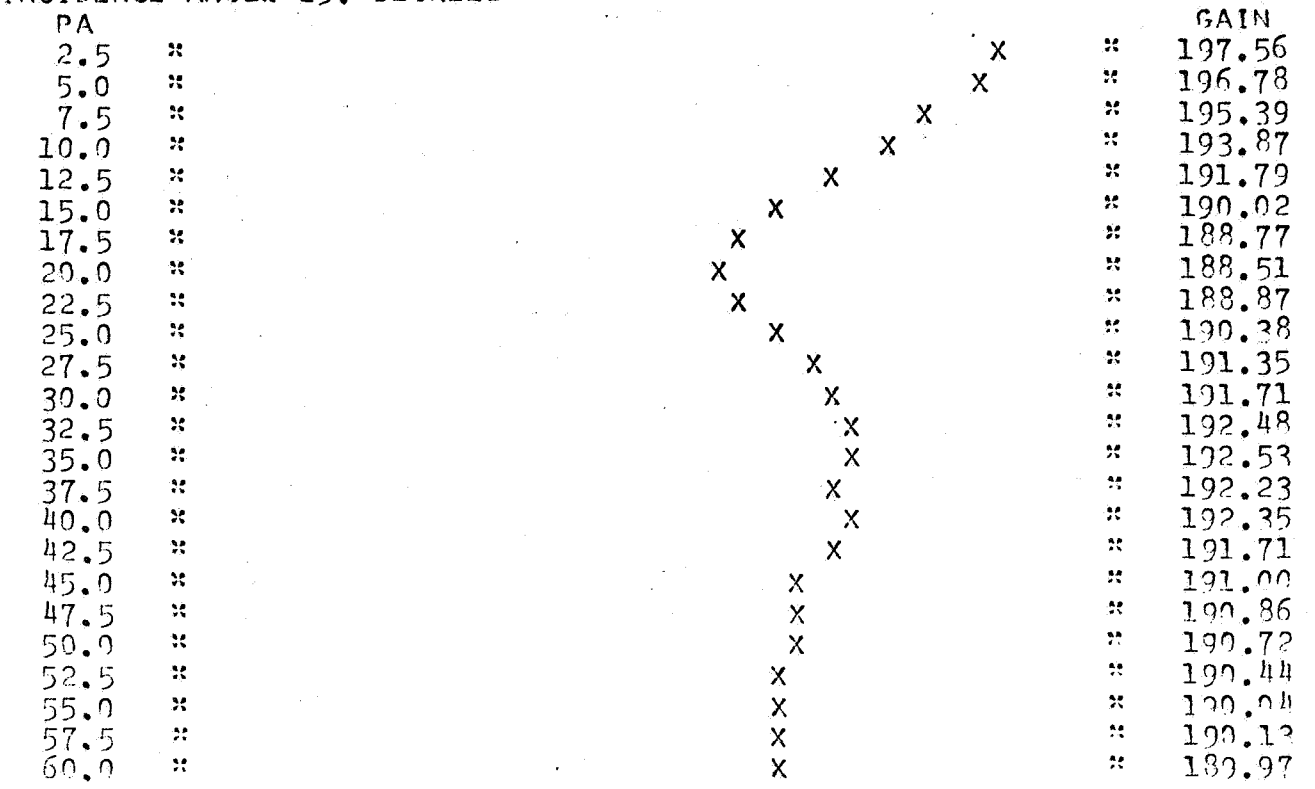

PA	GAIN
2.5	197.56
5.0	196.78
7.5	195.39
10.0	193.87
12.5	191.79
15.0	190.02
17.5	188.77
20.0	188.51
22.5	188.87
25.0	190.38
27.5	191.35
30.0	191.71
32.5	192.48
35.0	192.53
37.5	192.23
40.0	192.35
42.5	191.71
45.0	191.00
47.5	190.86
50.0	190.72
52.5	190.44
55.0	190.04
57.5	190.13
60.0	189.97

INCIDENCE ANGLE 30. DEGREES

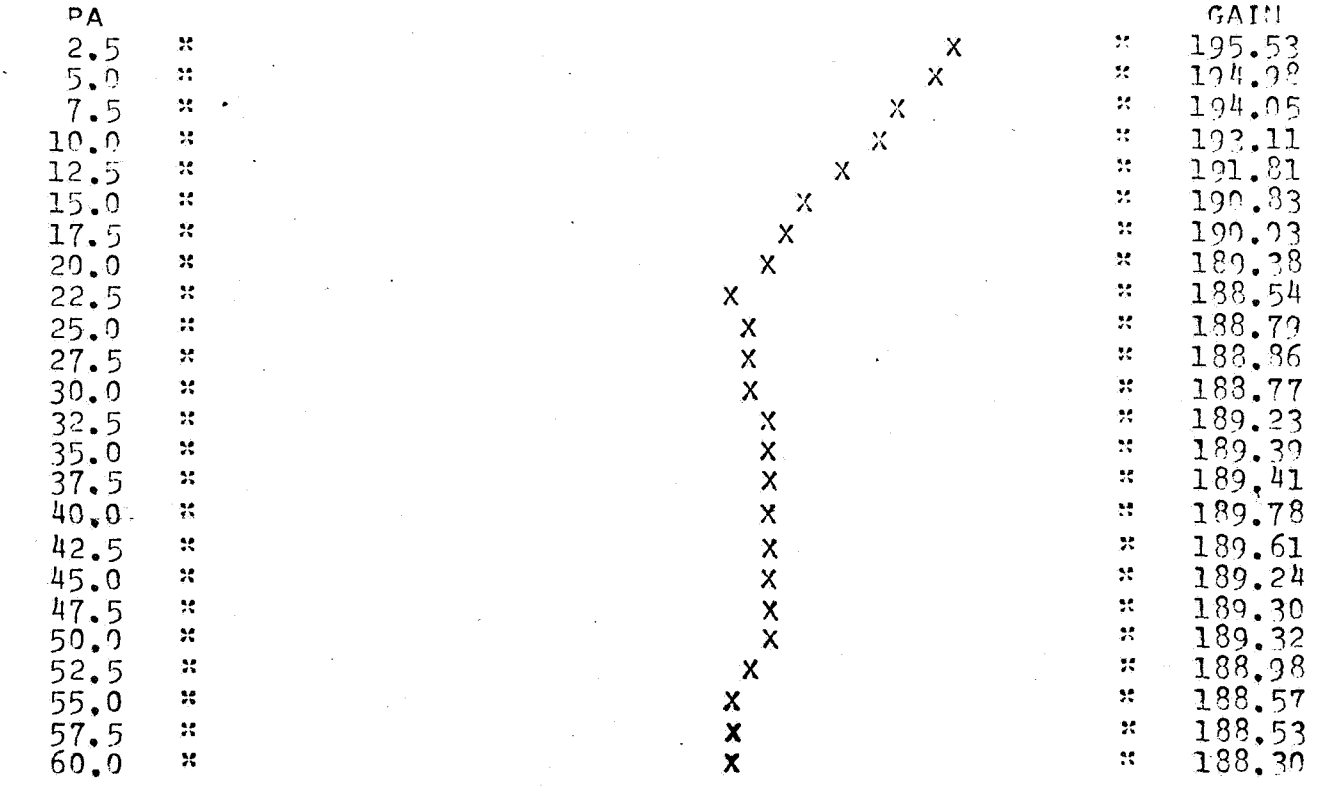

PA	GAIN
2.5	195.53
5.0	194.98
7.5	194.05
10.0	193.11
12.5	191.81
15.0	190.83
17.5	190.03
20.0	189.38
22.5	188.54
25.0	188.79
27.5	188.86
30.0	188.77
32.5	189.23
35.0	189.39
37.5	189.41
40.0	189.78
42.5	189.61
45.0	189.24
47.5	189.30
50.0	189.32
52.5	188.98
55.0	188.57
57.5	188.53
60.0	188.30

INCIDENCE ANGLE 35. DEGREES

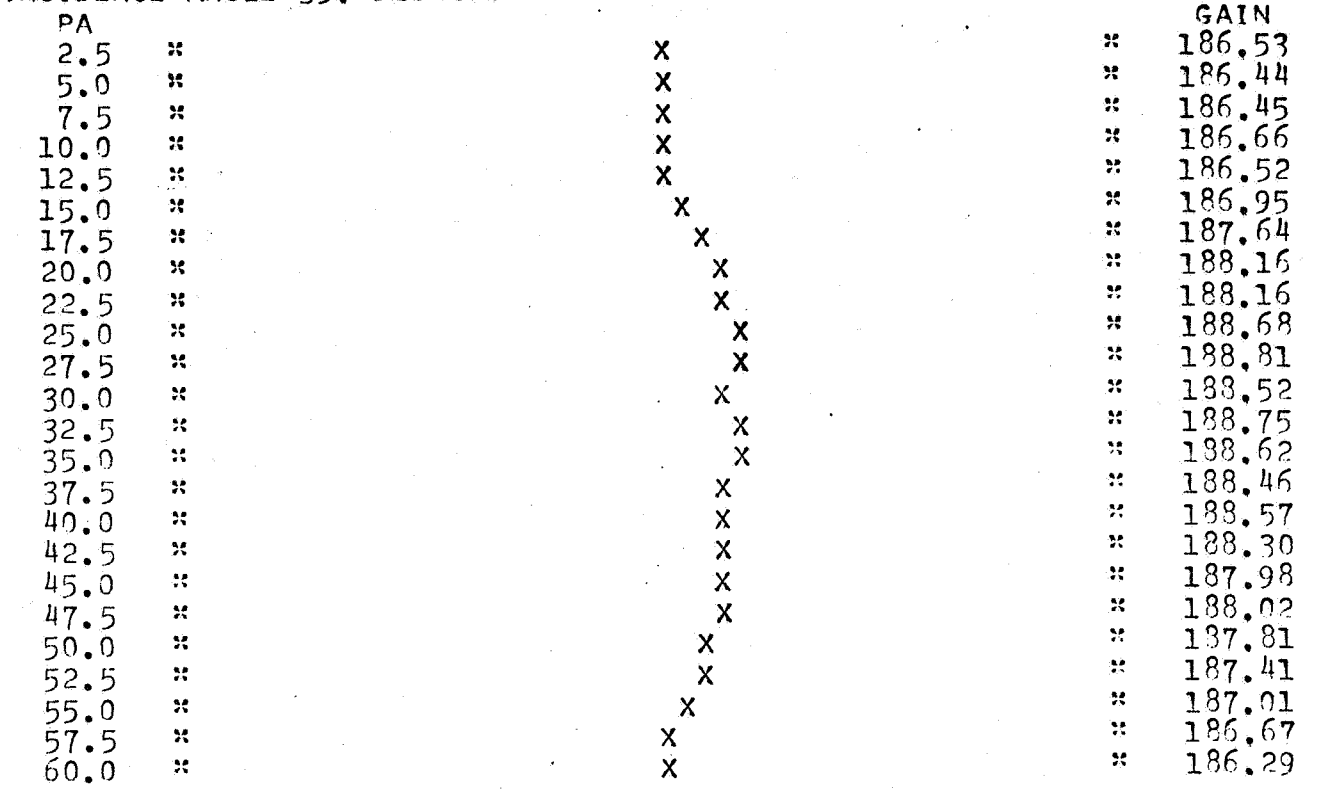

PA	GAIN
2.5	186.53
5.0	186.44
7.5	186.45
10.0	186.66
12.5	186.52
15.0	186.95
17.5	187.64
20.0	188.16
22.5	188.16
25.0	188.68
27.5	188.81
30.0	188.52
32.5	188.75
35.0	188.62
37.5	188.46
40.0	188.57
42.5	188.30
45.0	187.98
47.5	188.02
50.0	187.81
52.5	187.41
55.0	187.01
57.5	186.67
60.0	186.29

INCIDENCE ANGLE 40. DEGREES

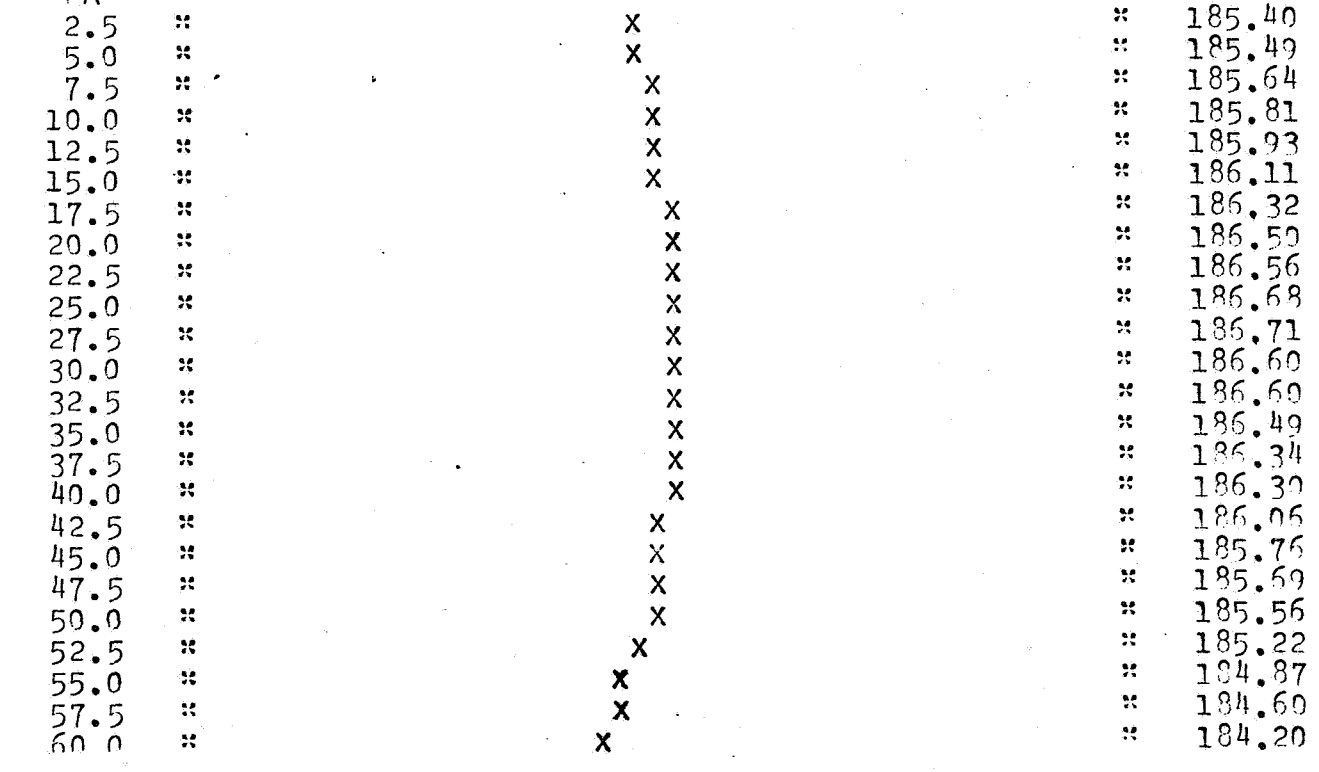

PA	GAIN
2.5	185.40
5.0	185.49
7.5	185.64
10.0	185.81
12.5	185.93
15.0	186.11
17.5	186.32
20.0	186.59
22.5	186.56
25.0	186.68
27.5	186.71
30.0	186.60
32.5	186.69
35.0	186.49
37.5	186.34
40.0	186.30
42.5	186.06
45.0	185.76
47.5	185.69
50.0	185.56
52.5	185.22
55.0	184.87
57.5	184.60
60.0	184.20

1.06 MICROMETERS WAVELENGTH

INCIDENCE ANGLE 0. DEGREES

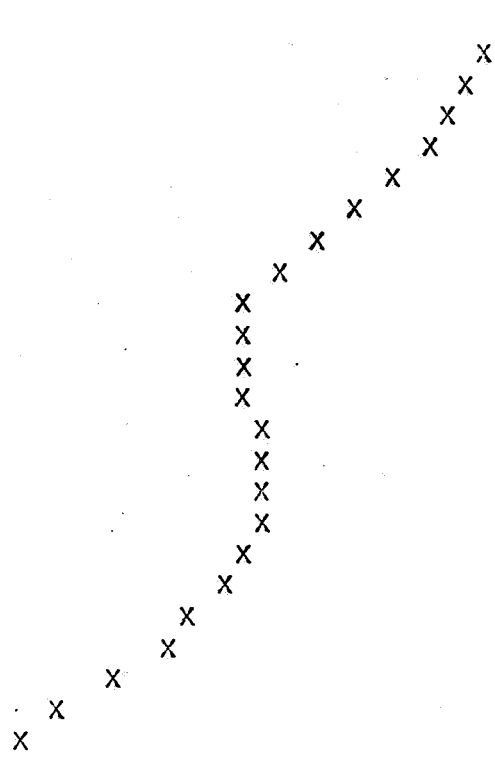

PA	GAIN
2.5	.00
5.0	198.09
7.5	197.63
10.0	196.69
12.5	196.22
15.0	194.81
17.5	194.05
20.0	192.60
22.5	191.17
25.0	190.40
27.5	189.84
30.0	189.96
32.5	190.34
35.0	190.68
37.5	190.95
40.0	190.98
42.5	190.75
45.0	190.35
47.5	189.54
50.0	188.57
52.5	187.38
55.0	185.77
57.5	184.04
60.0	182.87

INCIDENCE ANGLE 5. DEGREES

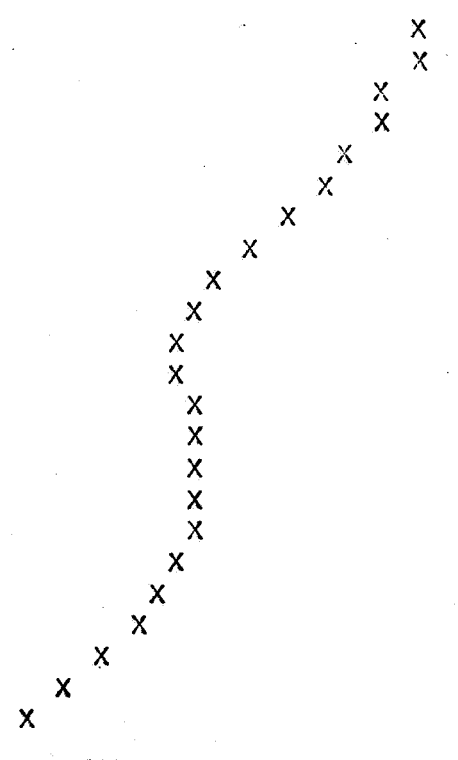

PA	GAIN
2.5	.00
5.0	197.21
7.5	196.82
10.0	196.04
12.5	195.64
15.0	194.45
17.5	193.31
20.0	192.55
22.5	191.22
25.0	190.36
27.5	189.37
30.0	189.05
32.5	189.01
35.0	189.26
37.5	189.48
40.0	189.64
42.5	189.64
45.0	189.40
47.5	189.05
50.0	188.28
52.5	187.59
55.0	186.36
57.5	184.98
60.0	183.75

INCIDENCE ANGLE 10. DEGREES

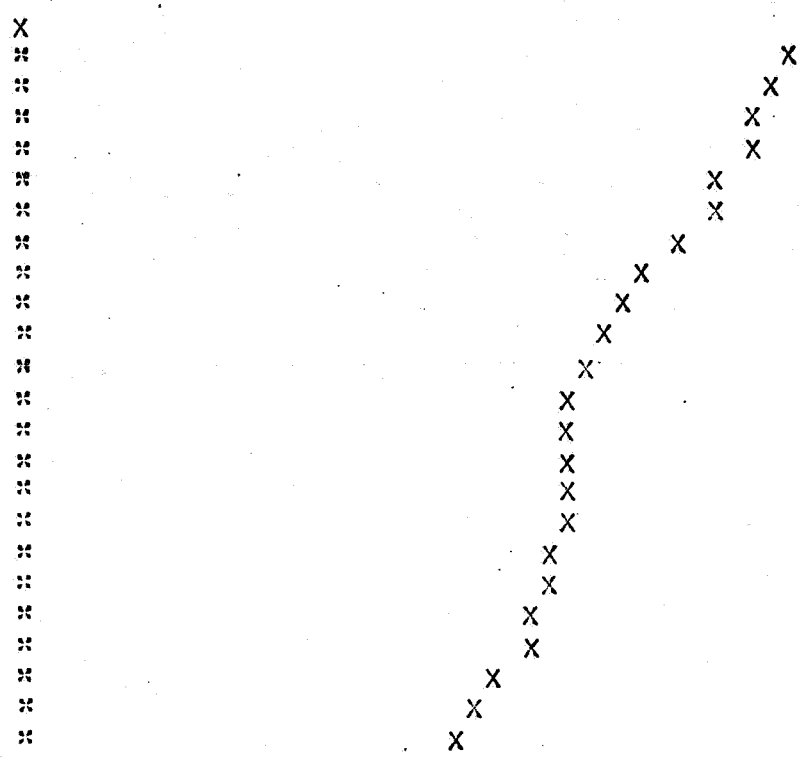

PA	GAIN
2.5	.00
5.0	195.54
7.5	195.23
10.0	194.63
12.5	194.32
15.0	193.40
17.5	192.97
20.0	191.98
22.5	191.06
25.0	190.33
27.5	189.46
30.0	188.84
32.5	188.53
35.0	188.32
37.5	188.21
40.0	188.23
42.5	188.18
45.0	187.94
47.5	187.86
50.0	187.13
52.5	186.92
55.0	186.07
57.5	185.35
60.0	184.39

INCIDENCE ANGLE 15. DEGREES

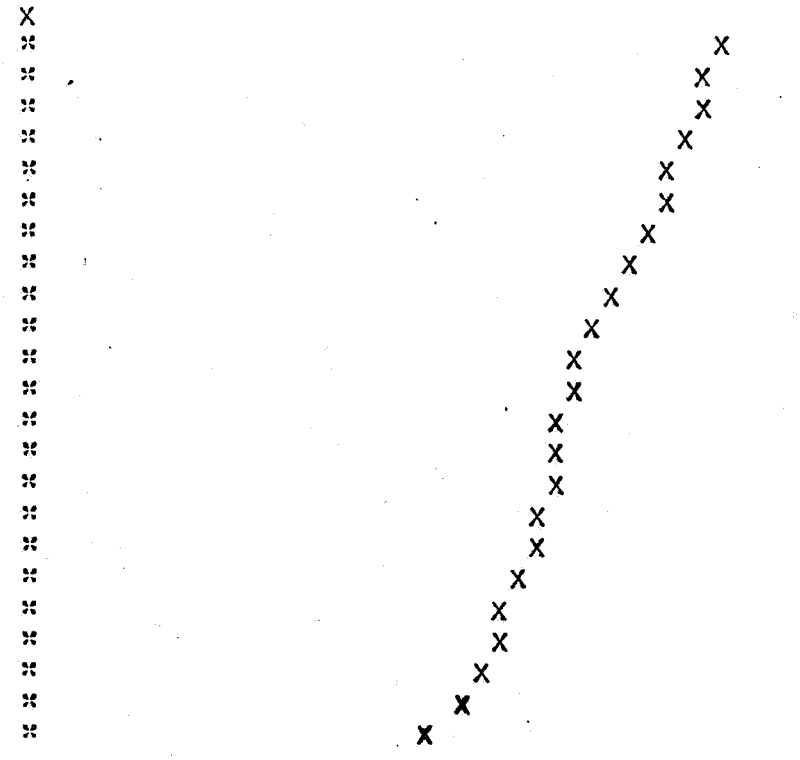

PA	GAIN
2.5	.00
5.0	192.96
7.5	192.74
10.0	192.35
12.5	192.13
15.0	191.49
17.5	191.30
20.0	190.58
22.5	190.17
25.0	189.62
27.5	189.20
30.0	188.58
32.5	188.53
35.0	187.91
37.5	187.82
40.0	187.49
42.5	187.17
45.0	186.96
47.5	186.57
50.0	185.98
52.5	185.69
55.0	185.00
57.5	184.60
60.0	183.61

INCIDENCE ANGLE 20. DEGREES

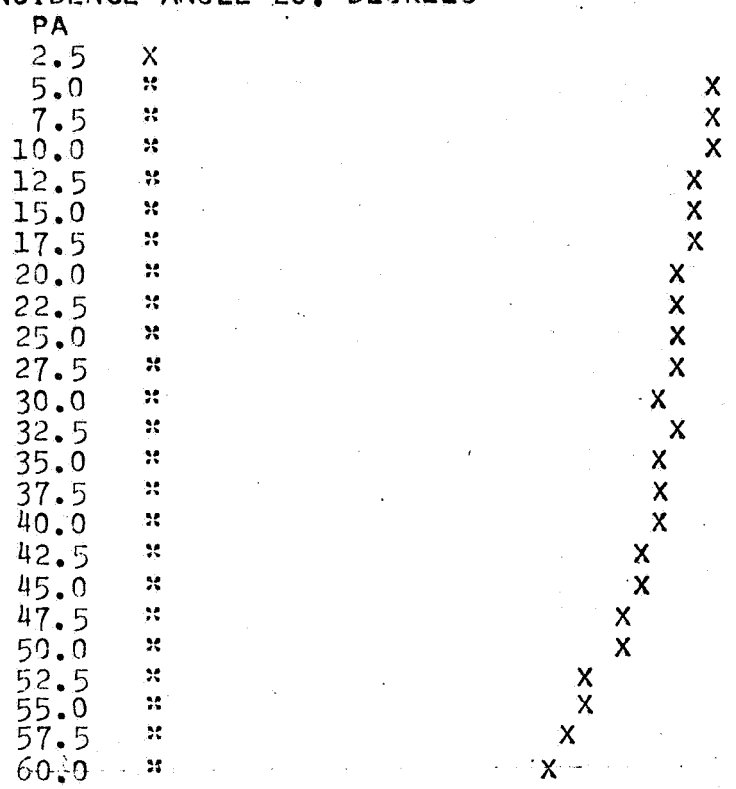

PA	GAIN
2.5	.00
5.0	188.85
7.5	188.74
10.0	188.60
12.5	188.47
15.0	188.14
17.5	188.26
20.0	187.79
22.5	187.96
25.0	187.60
27.5	187.76
30.0	187.25
32.5	187.75
35.0	186.96
37.5	187.35
40.0	186.81
42.5	186.46
45.0	186.58
47.5	185.57
50.0	185.90
52.5	184.79
55.0	184.52
57.5	183.68
60.0	183.18

INCIDENCE ANGLE 25. DEGREES

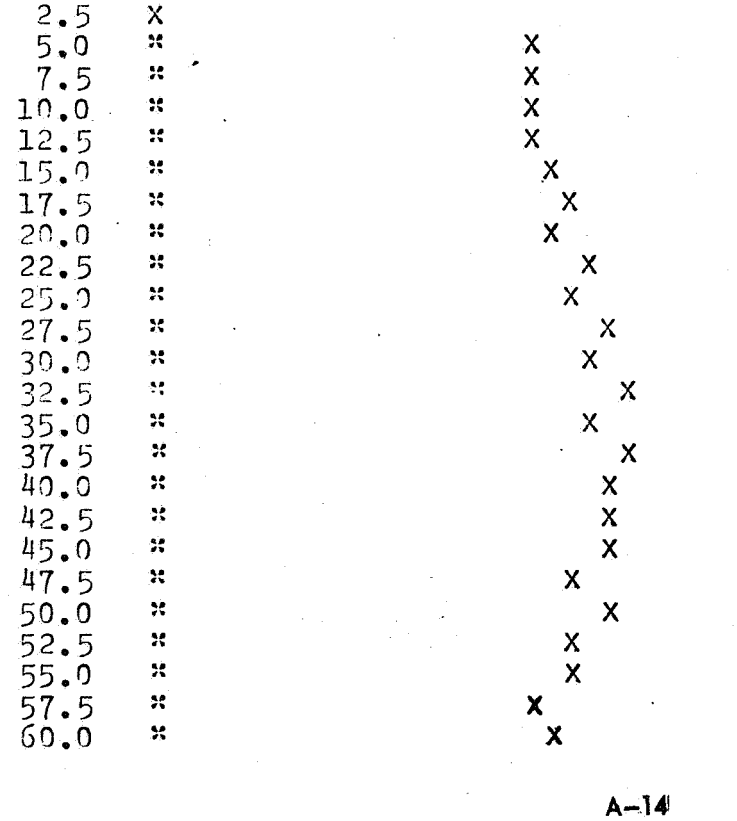

PA	GAIN
2.5	.00
5.0	182.62
7.5	182.70
10.0	183.00
12.5	183.00
15.0	183.11
17.5	183.66
20.0	183.49
22.5	184.33
25.0	184.18
27.5	184.90
30.0	184.57
32.5	185.56
35.0	184.80
37.5	185.65
40.0	185.12
42.5	184.95
45.0	185.38
47.5	184.20
50.0	185.30
52.5	183.81
55.0	184.12
57.5	182.93
60.0	183.47

INCIDENCE ANGLE 30. DEGREES

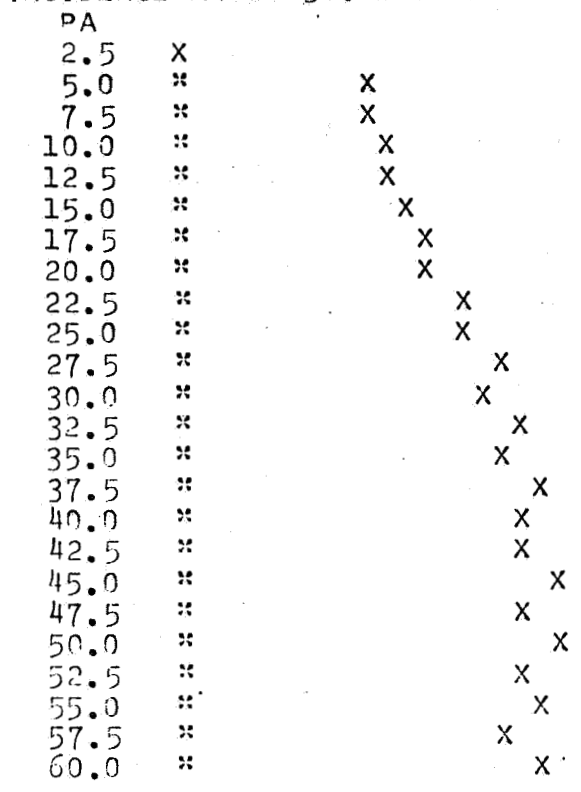

PA	GAIN
2.5	.00
5.0	176.45
7.5	176.67
10.0	177.30
12.5	177.39
15.0	177.77
17.5	178.60
20.0	178.57
22.5	179.77
25.0	179.72
27.5	180.74
30.0	180.51
32.5	181.78
35.0	181.06
37.5	182.22
40.0	181.73
42.5	181.75
45.0	182.40
47.5	181.27
50.0	182.83
52.5	181.34
55.0	182.97
57.5	180.89
60.0	182.11

INCIDENCE ANGLE 35. DEGREES

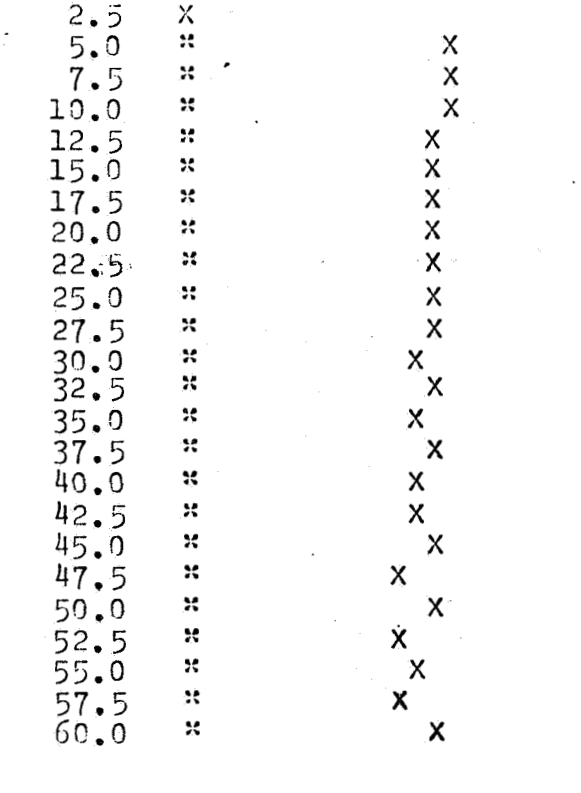

PA	GAIN
2.5	.00
5.0	178.83
7.5	178.77
10.0	178.68
12.5	178.61
15.0	178.41
17.5	178.48
20.0	178.20
22.5	178.31
25.0	178.09
27.5	178.24
30.0	177.90
32.5	178.39
35.0	177.78
37.5	178.35
40.0	177.92
42.5	177.81
45.0	178.23
47.5	177.29
50.0	178.52
52.5	177.27
55.0	177.90
57.5	176.90
60.0	178.08

```
INCIDENCE ANGLE 40. DEGREES
   PA                                                    GAIN
  2.5   X                                          *       .00
  5.0   *                  X                       *    179.45
  7.5   *                  X                       *    179.38
 10.0   *                 X                        *    179.25
 12.5   *                 X                        *    179.10
 15.0   *                 X                        *    178.96
 17.5   *                 X                        *    178.87
 20.0   *                X                         *    178.62
 22.5   *                X                         *    178.41
 25.0   *                X                         *    178.18
 27.5   *               X                          *    177.90
 30.0   *               X                          *    177.56
 32.5   *              X                           *    177.38
 35.0   *              X                           *    176.94
 37.5   *             X                            *    176.71
 40.0   *             X                            *    176.34
 42.5   *            X                             *    175.91
 45.0   *            X                             *    175.78
 47.5   *           X                              *    175.01
 50.0   *           X                              *    175.24
 52.5   *      X                                   *    174.33
 55.0   *      X                                   *    174.25
 57.5   *     X                                    *    173.37
 60.0   *      X                                   *    173.77
*STOP*
```

```
CROSPLOT   08:50 MAR 06,'75

100 DIMENSION TRAN(8),ALIST(18,24)
110 DATA STAR,X/'*','X'/,DB/4.34294/
120 CALL OPENF1('TEDAT',1)
130 DO 1 I=1,18
140 READ(1,)D1,D2,D3,D4
150 PRINT,D1,D2,D3,D4
160 DO2 J=1,12
170 READ(1,)TRAN
180 ALIST(I,2*J-1)=TRAN(3)
190 ALIST(I,2*J)=TRAN(7)
200 2 CONTINUE
210 DO3 J=1,3
220 3 READ(1,)DUM
230 1 CONTINUE
240 CALL CLOSF1
250 AMAX=0.
260 AMIN=1.E4
270 DO4 I=1,18
```

```
280 DO4 J=1,24
290 DUM=ALIST(I,J)
300 IF(DUM.GT.AMAX)AMAX=DUM
310 IF(DUM.LT.AMIN)AMIN=DUM
320 4 CONTINUE
330 VO=170
340 VX=INT(DB*AMAX)+1.
350 DV=VX-VO
360 SCALE=DV/50.
370 PRINT100,VX,VO,SCALE
380 DPA=2.5
390 DO11 IW=1,2
400 IADD=9*(IW-1)
401 IF(IW.EQ.1)PRINT104
402 IF(IW.EQ.2)PRINT105
403 104 FORMAT('.53 MICROMETERS WAVELENGTH')
404 105 FORMAT('1.06 MICROMETERS WAVELENGTH')
410 DO11 J=2,24,2
420 PA=J*DPA
430 PRINT103,PA
440 103 FORMAT(/'POINT-AHEAD ANGLE',F4.0,'MICRORADIANS'
441&,/T4,'INC.',T65,'GAIN')
450 DO11 I=1,9
460 DUM=DB*ALIST(I+IADD,J)
470 ID=10+INT((DUM-VO)/SCALE)
480 IF(ID.LT.10)ID=10
490 AINC=5.*(I-1)
500 PRINT102,AINC,STAR,ID,X,STAR,DUM
510 11 CONTINUE
520 STOP
530 100 FORMAT('MAX,MIN',2F8.2/'SCALE=',F6.2,'/DIV')
540 101 FORMAT(/'INCIDENCE ANGLE',F4.0,' DEGREES')
550 102 FORMAT(F6.1,T10,A,TN,A,T60,A,F6.2)
560 END
```

```
#RUN CROSPLOT

CROSPLOT   08:52 MAR 06,'75

  3.80000   .530000   .000000   7.30000
  3.80000   .530000   5.00000   7.30000
  3.80000   .530000   10.0000   7.30000
  3.80000   .530000   15.0000   7.30000
  3.80000   .530000   20.0000   7.30000
  3.80000   .530000   25.0000   7.30000
  3.80000   .530000   30.0000   7.30000
  3.80000   .530000   35.0000   7.30000
  3.80000   .530000   40.0000   7.30000
  3.80000   1.06000   .000000   7.30000
```

3.80000	1.06000	5.00000	7.30000
3.80000	1.06000	10.0000	7.30000
3.80000	1.06000	15.0000	7.30000
3.80000	1.06000	20.0000	7.30000
3.80000	1.06000	25.0000	7.30000
3.80000	1.06000	30.0000	7.30000
3.80000	1.06000	35.0000	7.30000
3.80000	1.06000	40.0000	7.30000

MAX,MIN 201.00 170.00
SCALE= .62/DIV
.53 MICROMETERS WAVELENGTH

POINT-AHEAD ANGLE 5.MICRORADIANS

INC.		GAIN
.0		197.27
5.0		197.02
10.0		195.03
15.0		192.01
20.0		194.77
25.0		196.78
30.0		194.98
35.0		186.44
40.0		185.49

POINT-AHEAD ANGLE 10.MICRORADIANS

INC.		GAIN
.0		191.61
5.0		194.00
10.0		196.00
15.0		195.31
20.0		193.43
25.0		193.87
30.0		193.11
35.0		186.66
40.0		185.81

POINT-AHEAD ANGLE 15.MICRORADIANS

INC.		GAIN
.0		198.83
5.0		197.54
10.0		196.53
15.0		195.62
20.0		192.36
25.0		190.02
30.0		190.83
35.0		186.95
40.0		186.11

POINT-AHEAD ANGLE 20.MICRORADIANS

INC.		GAIN
.0		200.48
5.0		199.53

```
 10.0   *                                                  X       *   196.82
 15.0   *                                                X         *   194.92
 20.0   *                                              X           *   192.81
 25.0   *                                            X             *   188.51
 30.0   *                                          X               *   189.38
 35.0   *                                            X             *   188.16
 40.0   *                                  X                       *   186.50
```

POINT-AHEAD ANGLE 25.MICRORADIANS

```
   INC.                                                                GAIN
    .0    *                                                    X  *   199.30
   5.0    *                                                    X  *   199.16
  10.0    *                                                 X     *   197.37
  15.0    *                                               X       *   194.39
  20.0    *                                             X         *   193.11
  25.0    *                                           X           *   190.38
  30.0    *                                         X             *   188.79
  35.0    *                                         X             *   188.68
  40.0    *                                  X                    *   186.68
```

POINT-AHEAD ANGLE 30.MICRORADIANS

```
   INC.                                                                GAIN
    .0    *                                                     X *   200.01
   5.0    *                                                   X   *   198.87
  10.0    *                                                 X     *   198.14
  15.0    *                                              X        *   195.93
  20.0    *                                            X          *   193.58
  25.0    *                                          X            *   191.71
  30.0    *                                        X              *   188.77
  35.0    *                                       X               *   188.52
  40.0    *                                  X                    *   186.60
```

POINT-AHEAD ANGLE 35.MICRORADIANS

```
   INC.                                                                GAIN
    .0    *                                                     X *   200.33
   5.0    *                                                   X   *   199.04
  10.0    *                                                 X     *   198.03
  15.0    *                                               X       *   196.75
  20.0    *                                             X         *   194.09
  25.0    *                                           X           *   192.53
  30.0    *                                         X             *   189.39
  35.0    *                                         X             *   188.62
  40.0    *                                  X                    *   186.49
```

POINT-AHEAD ANGLE 40.MICRORADIANS

```
   INC.                                                                GAIN
    .0    *                                                   X   *   198.08
   5.0    *                                                 X     *   197.88
  10.0    *                                               X       *   196.73
  15.0    *                                             X         *   196.09
  20.0    *                                           X           *   193.89
  25.0    *                                         X             *   192.35
  30.0    *                                       X               *   189.78
  35.0    *                                       X               *   188.57
  40.0    *                                  X                    *   186.30
```

POINT-AHEAD ANGLE 45.MICRORADIANS

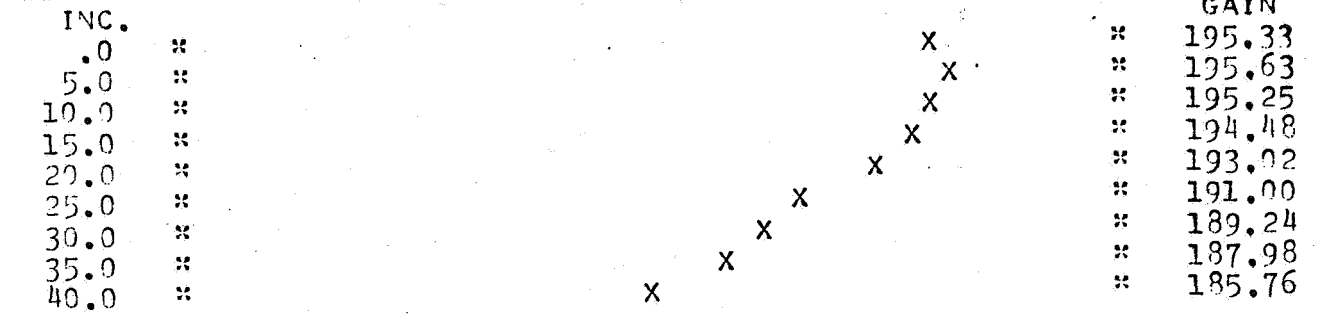

INC.		GAIN
.0	*	195.33
5.0	*	195.63
10.0	*	195.25
15.0	*	194.48
20.0	*	193.02
25.0	*	191.00
30.0	*	189.24
35.0	*	187.98
40.0	*	185.76

POINT-AHEAD ANGLE 50.MICRORADIANS

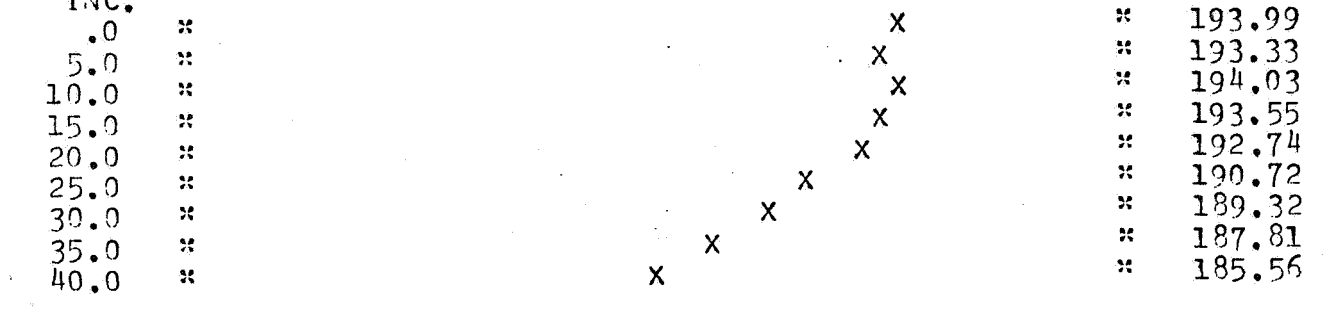

INC.		GAIN
.0	*	193.99
5.0	*	193.33
10.0	*	194.03
15.0	*	193.55
20.0	*	192.74
25.0	*	190.72
30.0	*	189.32
35.0	*	187.81
40.0	*	185.56

POINT-AHEAD ANGLE 55.MICRORADIANS

INC.		GAIN
.0	*	190.38
5.0	*	190.68
10.0	*	191.71
15.0	*	192.37
20.0	*	192.01
25.0	*	190.04
30.0	*	188.57
35.0	*	187.01
40.0	*	184.87

POINT-AHEAD ANGLE 60.MICRORADIANS

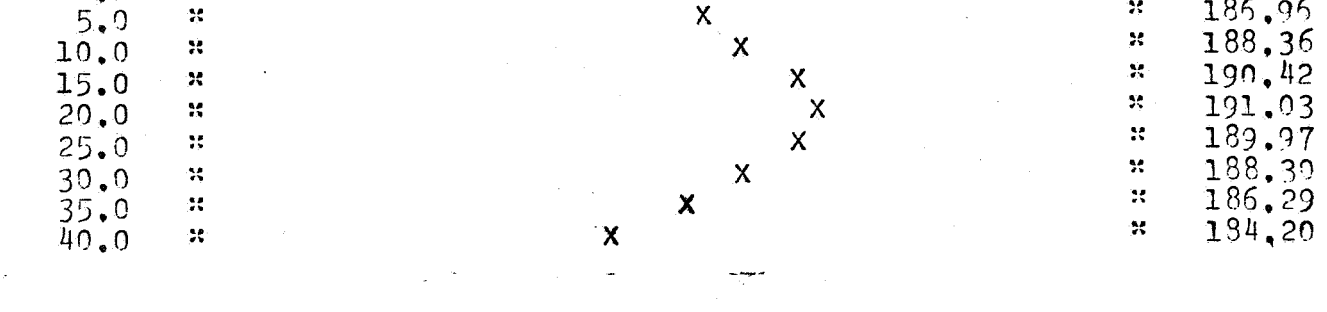

INC.		GAIN
.0	*	185.13
5.0	*	186.96
10.0	*	188.36
15.0	*	190.42
20.0	*	191.03
25.0	*	189.97
30.0	*	188.39
35.0	*	186.29
40.0	*	184.20

.06 MICROMETERS WAVELENGTH

POINT-AHEAD ANGLE 5.MICRORADIANS

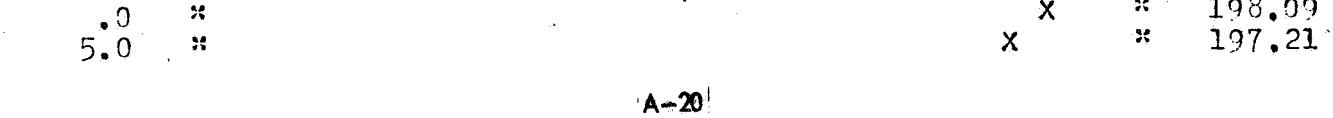

INC.		GAIN
.0	*	198.09
5.0	*	197.21

```
 10.0   *                                                  X        *   195.54
 15.0   *                                                X          *   192.96
 20.0   *                                             X             *   188.85
 25.0   *                                          X                *   182.62
 30.0   *                                    X                      *   176.45
 35.0   *                                       X                   *   178.83
 40.0   *                                        X                  *   179.45
```

POINT-AHEAD ANGLE 10.MICRORADIANS

```
   INC.                                                                GAIN
    .0   *                                                       X    *   196.69
   5.0   *                                                    X       *   196.04
  10.0   *                                                 X          *   194.63
  15.0   *                                              X             *   192.35
  20.0   *                                           X                *   188.60
  25.0   *                                        X                   *   183.00
  30.0   *                                     X                      *   177.30
  35.0   *                                        X                   *   178.68
  40.0   *                                        X                   *   179.25
```

POINT-AHEAD ANGLE 15.MICRORADIANS

```
   INC.                                                                GAIN
    .0   *                                                    X       *   194.81
   5.0   *                                                 X          *   194.45
  10.0   *                                              X             *   193.40
  15.0   *                                           X                *   191.49
  20.0   *                                        X                   *   188.14
  25.0   *                                     X                      *   183.11
  30.0   *                                  X                         *   177.77
  35.0   *                                    X                       *   178.41
  40.0   *                                     X                      *   178.96
```

POINT-AHEAD ANGLE 20.MICRORADIANS

```
   INC.                                                                GAIN
    .0   *                                                       X    *   192.60
   5.0   *                                                       X    *   192.55
  10.0   *                                                    X       *   191.98
  15.0   *                                                 X          *   190.58
  20.0   *                                              X             *   187.79
  25.0   *                                           X                *   183.49
  30.0   *                                        X                   *   178.57
  35.0   *                                        X                   *   178.20
  40.0   *                                        X                   *   178.62
```

POINT-AHEAD ANGLE 25.MICRORADIANS

```
   INC.                                                                GAIN
    .0   *                                                       X    *   190.40
   5.0   *                                                       X    *   190.36
  10.0   *                                                       X    *   190.33
  15.0   *                                                    X       *   189.62
  20.0   *                                                 X          *   187.60
  25.0   *                                              X             *   184.18
  30.0   *                                           X                *   179.72
  35.0   *                                        X                   *   178.09
  40.0   *                                        X                   *   178.18
```

POINT-AHEAD ANGLE 30.MICRORADIANS

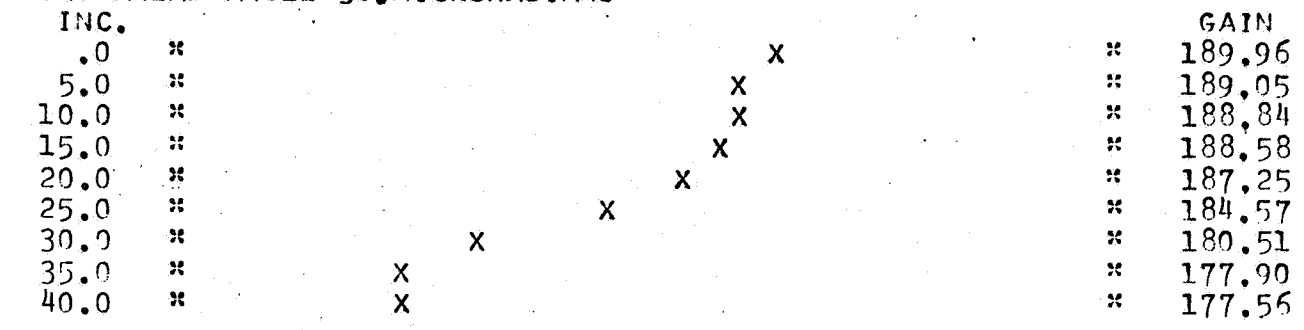

INC.	GAIN
.0	189.96
5.0	189.05
10.0	188.84
15.0	188.58
20.0	187.25
25.0	184.57
30.0	180.51
35.0	177.90
40.0	177.56

POINT-AHEAD ANGLE 35.MICRORADIANS

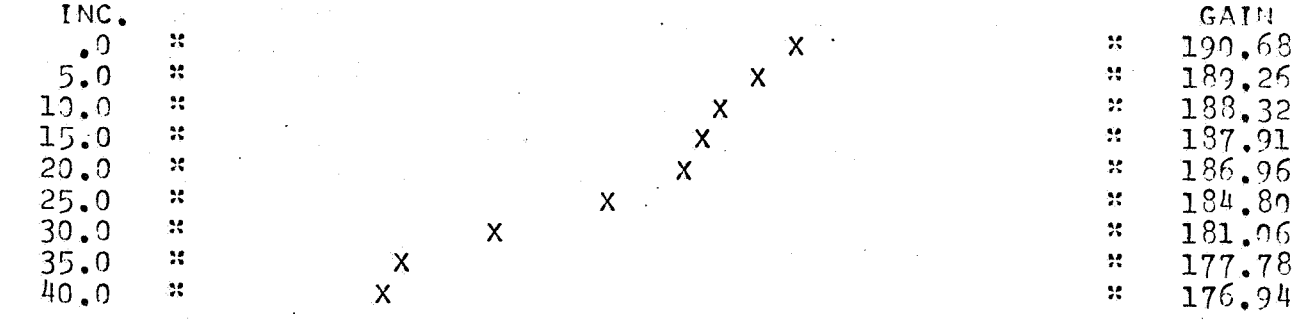

INC.	GAIN
.0	190.68
5.0	189.26
10.0	188.32
15.0	187.91
20.0	186.96
25.0	184.80
30.0	181.06
35.0	177.78
40.0	176.94

POINT-AHEAD ANGLE 40.MICRORADIANS

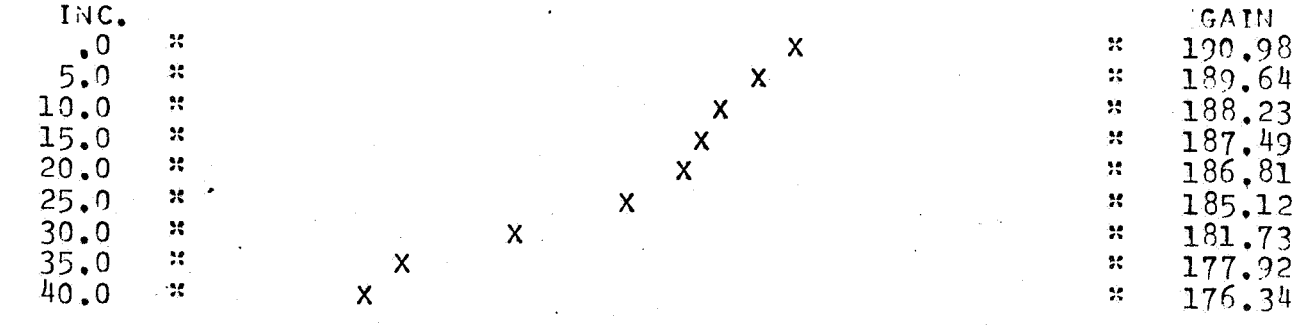

INC.	GAIN
.0	190.98
5.0	189.64
10.0	188.23
15.0	187.49
20.0	186.81
25.0	185.12
30.0	181.73
35.0	177.92
40.0	176.34

POINT-AHEAD ANGLE 45.MICRORADIANS

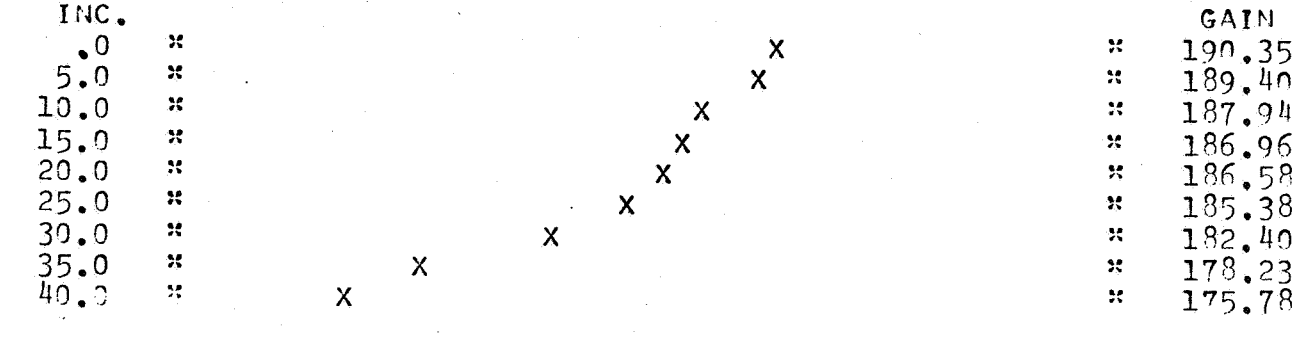

INC.	GAIN
.0	190.35
5.0	189.40
10.0	187.94
15.0	186.96
20.0	186.58
25.0	185.38
30.0	182.40
35.0	178.23
40.0	175.78

POINT-AHEAD ANGLE 50.MICRORADIANS

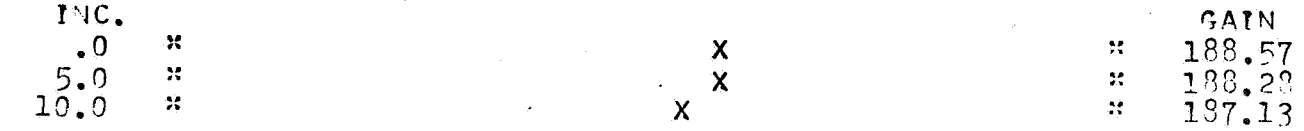

INC.	GAIN
.0	188.57
5.0	188.29
10.0	187.13

```
 15.0   *                                X      *   185.98
 20.0   *                                X      *   185.90
 25.0   *                               X       *   185.30
 30.0   *                            X          *   182.83
 35.0   *                        X              *   178.52
 40.0   *                   X                   *   175.24
```

POINT-AHEAD ANGLE 55.MICRORADIANS

```
   INC.                                                GAIN
    .0    *                                X      *   185.77
   5.0    *                                 X     *   186.36
  10.0    *                                X      *   186.07
  15.0    *                               X       *   185.00
  20.0    *                              X        *   184.52
  25.0    *                             X         *   184.12
  30.0    *                          X            *   182.07
  35.0    *                     X                 *   177.90
  40.0    *                X                      *   174.25
```

POINT-AHEAD ANGLE 60.MICRORADIANS

```
   INC.                                                GAIN
    .0    *                            X          *   182.87
   5.0    *                              X        *   183.75
  10.0    *                               X       *   184.39
  15.0    *                             X         *   183.61
  20.0    *                             X         *   183.18
  25.0    *                             X         *   183.47
  30.0    *                          X            *   182.11
  35.0    *                     X                 *   178.08
  40.0    *                X                      *   173.77
 *STOP*
```

APPENDIX B

LAGEOS SIGNATURE DATA

1.0 INTRODUCTION

The temporal response of the model LAGEOS target varies with point-ahead angle, wavelength, and illuminating pulse width. The data and the program used to generate this data is presented in this appendix. The gain data used in this analysis was generated by the program in Appendix A.

2.0 SIGNATURE ANALYSIS PROGRAM

The program used to compute the temporal response of the LAGEOS target is presented in the following pages. The program was written in Fortran IV for the MDAC Sigma 9 time-sharing computer system.

```
CONVV    09:16 MAR 06,'75

100 DIMENSION AM(9,24),AV(9,24),TRAN(8)
110 COMMON AM,AV
120 DATA DELT,CON1/1.87794E-11,2.5E8/
130 WAVE=.53
140 22 OUTPUT WAVE
150 READ,WAVE
160 CALL OPENF1('TEDAT',1)
170 IF(WAVE.LT.1.)GOTO25
180 DO21 I=1,144
190 READ(1,)D1,D2,D3,D4
200 21 CONTINUE
210  25 CONTINUE
220 DO 20 I=1,9
230 READ(1,)D1,D2,D3,D4
240 PRINT,D1,D2,D3,D4
250 DO 23 J=1,12
260 READ(1,)TRAN
270 AM(I,2*J-1)=TRAN(3)
280 AM(I,2*J)=TRAN(7)
290 AV(I,2*J-1)=TRAN(4)
300 AV(I,2*J)=TRAN(8)
310 23 CONTINUE
320 READ(1,)DUM
330 READ(1,)DUM
340 READ(1,)DUM
```

```
350 20  CONTINUE
360 CALL CLOSFL
370 1 OUTPUT'PULSE WIDTH'
380 READ,TPW
390 2 OUTPUT'TMIN,TMAX,TSTEP'
400 READ,TMIN,TMAX,TSTEP
410 DO5 I=1,12
420 II=2**I
430 PA=5.**I
440 T=TMIN
450 4 TN=-.5*DELT
460 SUM=0
470 SUMVAR=0.
480 SUM1=0.
490 VS1=0.
500 DO 3 N=1,76
510 TN=TN+DELT
520 GAM=ACOS(1.-TN*CON1)
530 IF(GAM.GT.0.7854)D1=0.;GOTO10
540 CALL ESTVAL(D1,VAR,GAM,II)
550 SUM1=SUM1+D1
560 VS1=VS1+VAR
570 DUM=EXP(-2.*((T-TN)/TPW)**2)
580 SUMVAR=SUMVAR+VAR*DUM**2
590 10 CONTINUE
600 3 SUM=SUM+D1*DUM
610 IF((T-TMIN).GT.TSTEP/2.)GOTO6
620 GAVE=10.*ALOG10(SUM1)
630 SNR=2.*GAVE-10.*ALOG10(VS1)
640 PRINT 101,PA,GAVE,SNR
650 101 FORMAT(/F7.0,F8.2,F7.2)
660 6 CONTINUE
670 GAVE=10.*ALOG10(SUM)
680 SNR=2*GAVE-10.*ALOG10(SUMVAR)
690 PRINT 100,T,GAVE,SNR
700 100 FORMAT(9PF7.2,PF8.2,F7.2)
710 T=T+TSTEP
720 IF(T.LE.TMAX)GOTO4
730 5 CONTINUE
740 OUTPUT'NEW VALUES OR NEW RUN'
750 IM=0
760 READ,IM
770 IF(IM.EQ.1)GOTO2
780 IF(IM.EQ.2)GOTO1
790 IF(IM.EQ.3)GOTO22
800 STOP
810 END
820 SUBROUTINE ESTVAL(GNU,VAR,THE,JP)
830 DIMENSION AM(9,24),AV(9,24)
840 COMMON AM,AV
850 GNU=0.
860 VAR=0.
870 XI=THE*11.4592
```

```
880 IL=INT(XI)+1
890 IF(JP.GT.24)RETURN
900 IF(IL.GT.9)RETURN
910 G2=0.
920 V2=0.
930 G1=AM(IL,JP)
940 V1=AV(IL,JP)
950 IF(IL.EQ.9)GOTO1
960 G2=AM(IL+1,JP)
970 V2=AV(IL+1,JP)
980 1 G=G1+(G2-G1)*(XI+1-IL)
990 V=V1+(V2-V1)*(XI+1-IL)
1000 GNU=EXP(G)
1010 VAR=EXP(2*V)
1020 RETURN
1030 END
```

3.0 SIGNATURE DATA

The following pages present the temporal response characteristics of a LAGEOS type target, when illuminated by a 200 ps pulse at 0.53 μm and at 1.06 μm wavelengths.

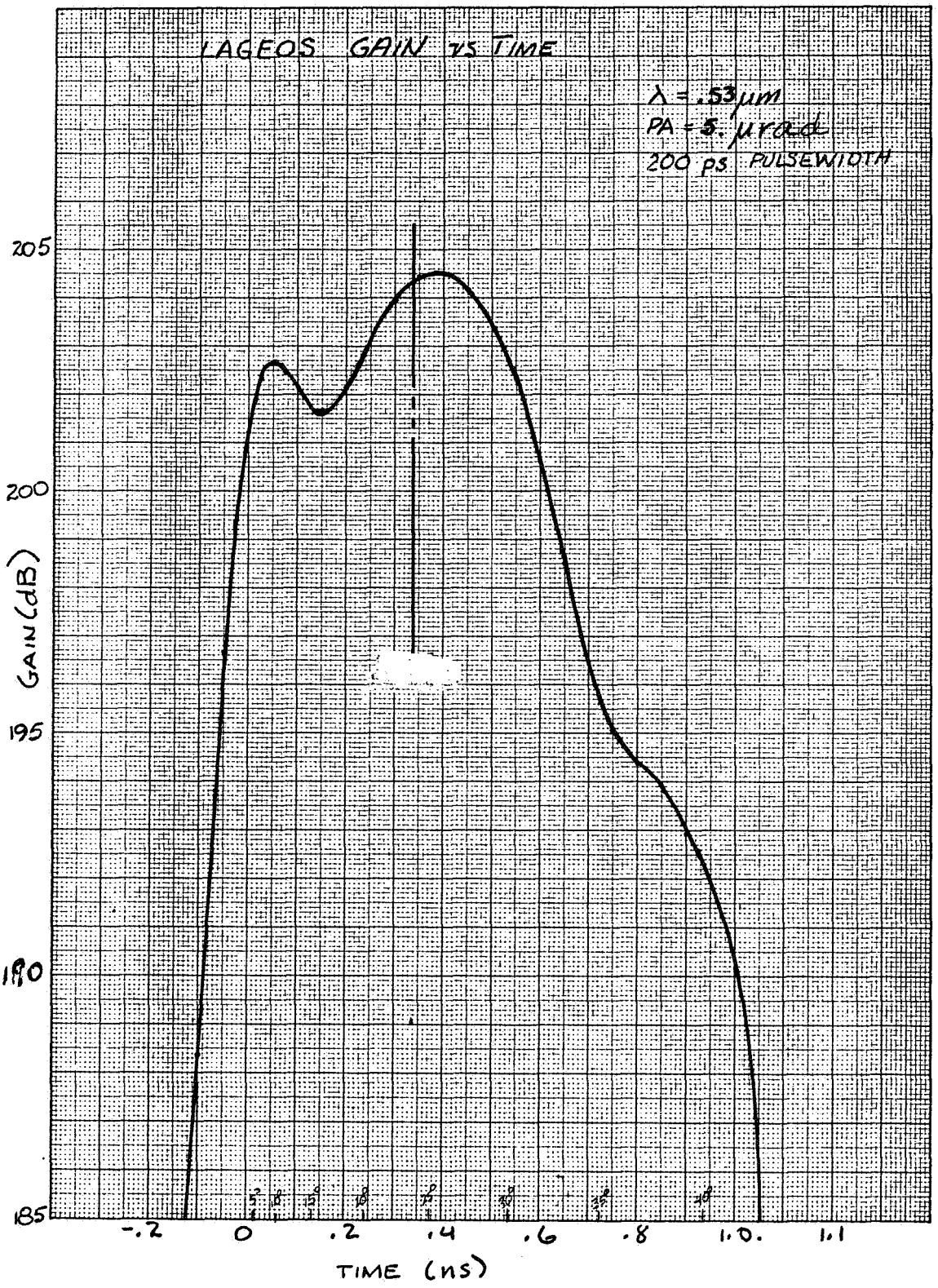
LAGEOS GAIN vs TIME
λ = .53μm
PA = 5. μrad
200 ps PULSEWIDTH
205
200
195
190
185
GAIN (dB)
-.2
0
.2
.4
.6
.8
1.0
1.1
TIME (ns)

FIGURE B–1

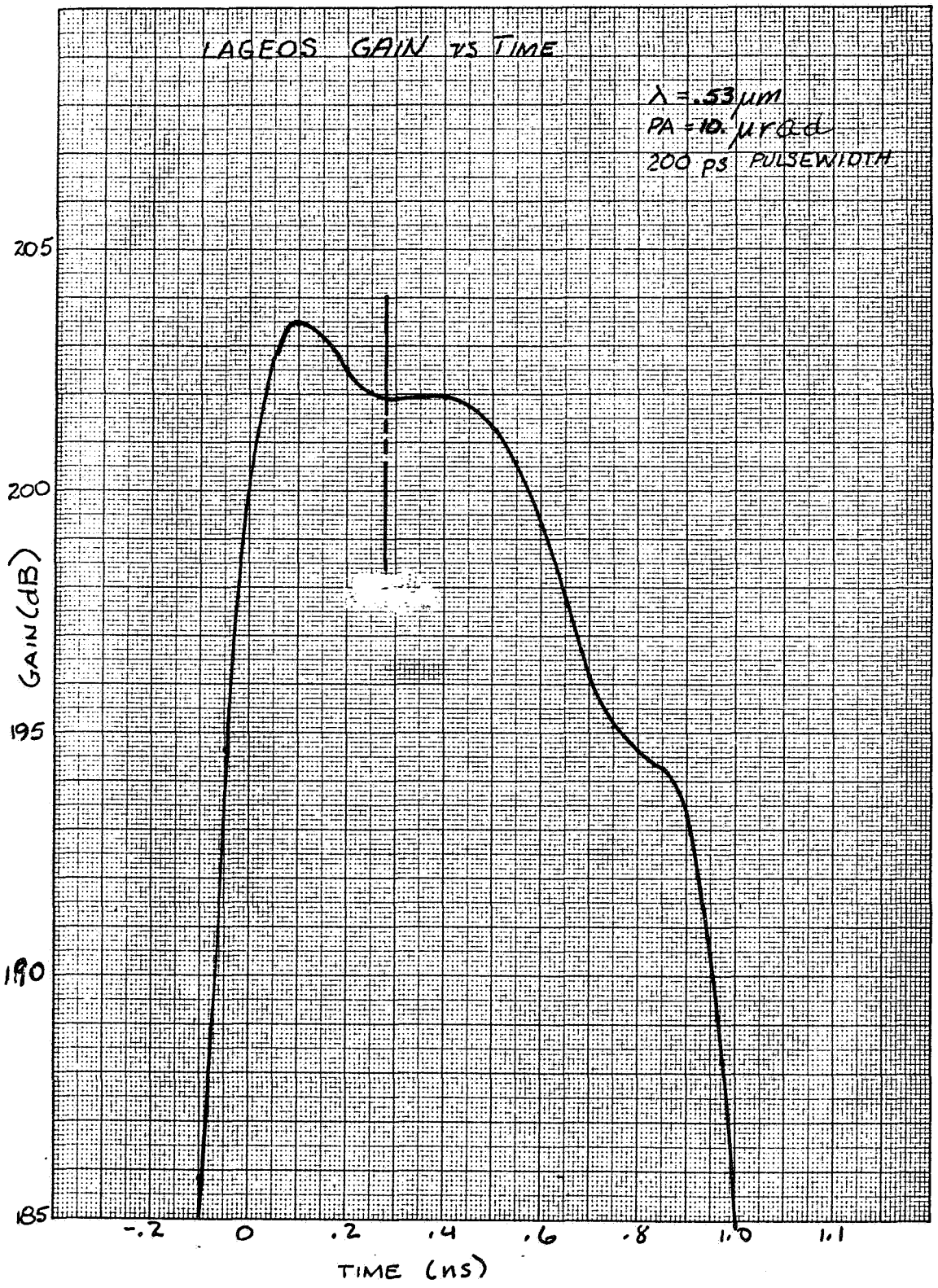
LAGEOS GAIN VS TIME
λ = .53 μm
PA = 10. μ r a d
200 ps PULSEWIDTH
205
200
195
190
185
GAIN (dB)
-.2
0
.2
.4
.6
.8
1.0
1.1
TIME (ns)

FIGURE B–2

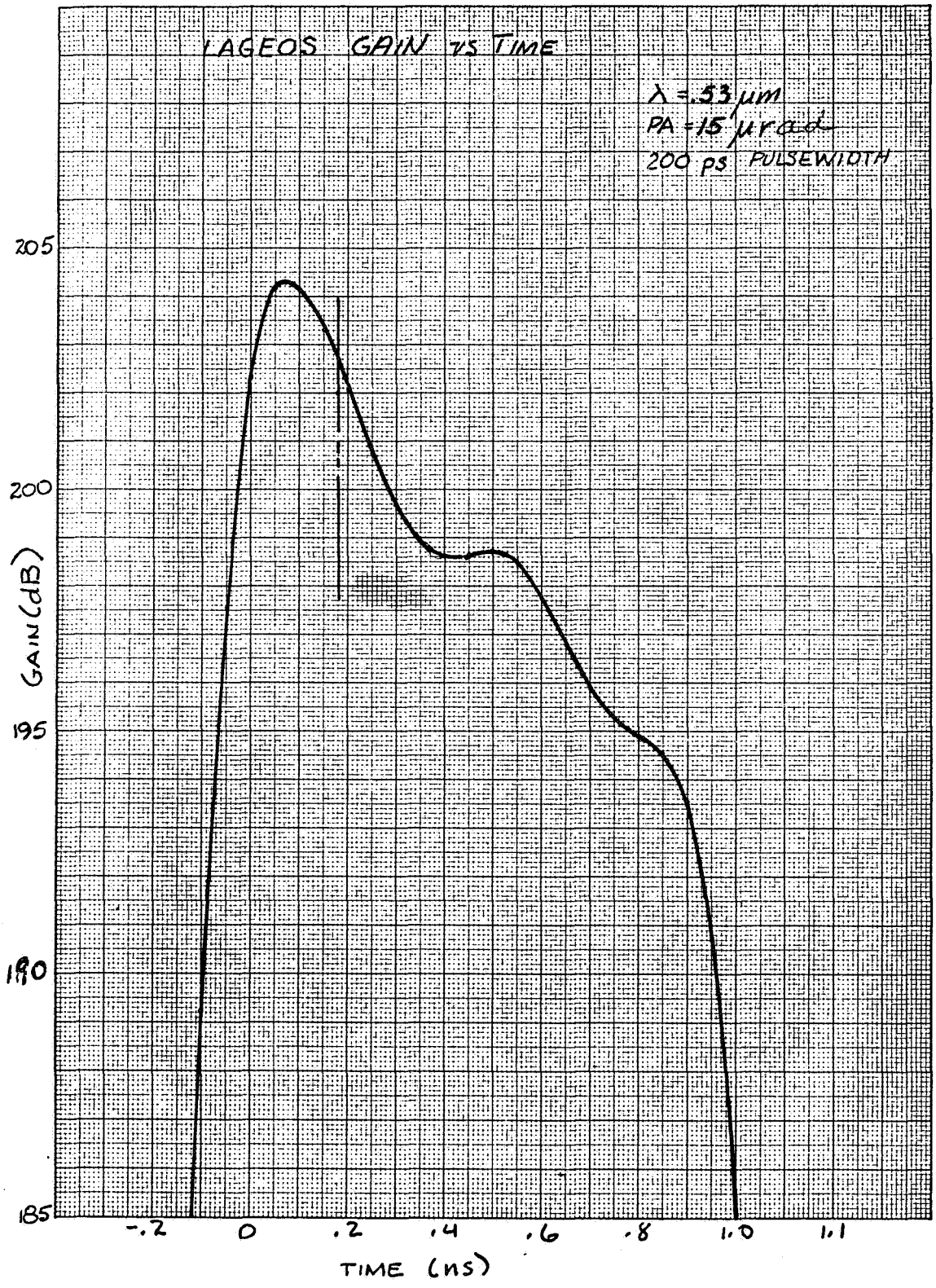
LAGEOS GAIN vs TIME
λ = .53 μm
PA = 15 μrad
200 ps PULSEWIDTH
205
200
195
190
185
GAIN (dB)
-.2
0
.2
.4
.6
.8
1.0
1.1
TIME (ns)

FIGURE B–3

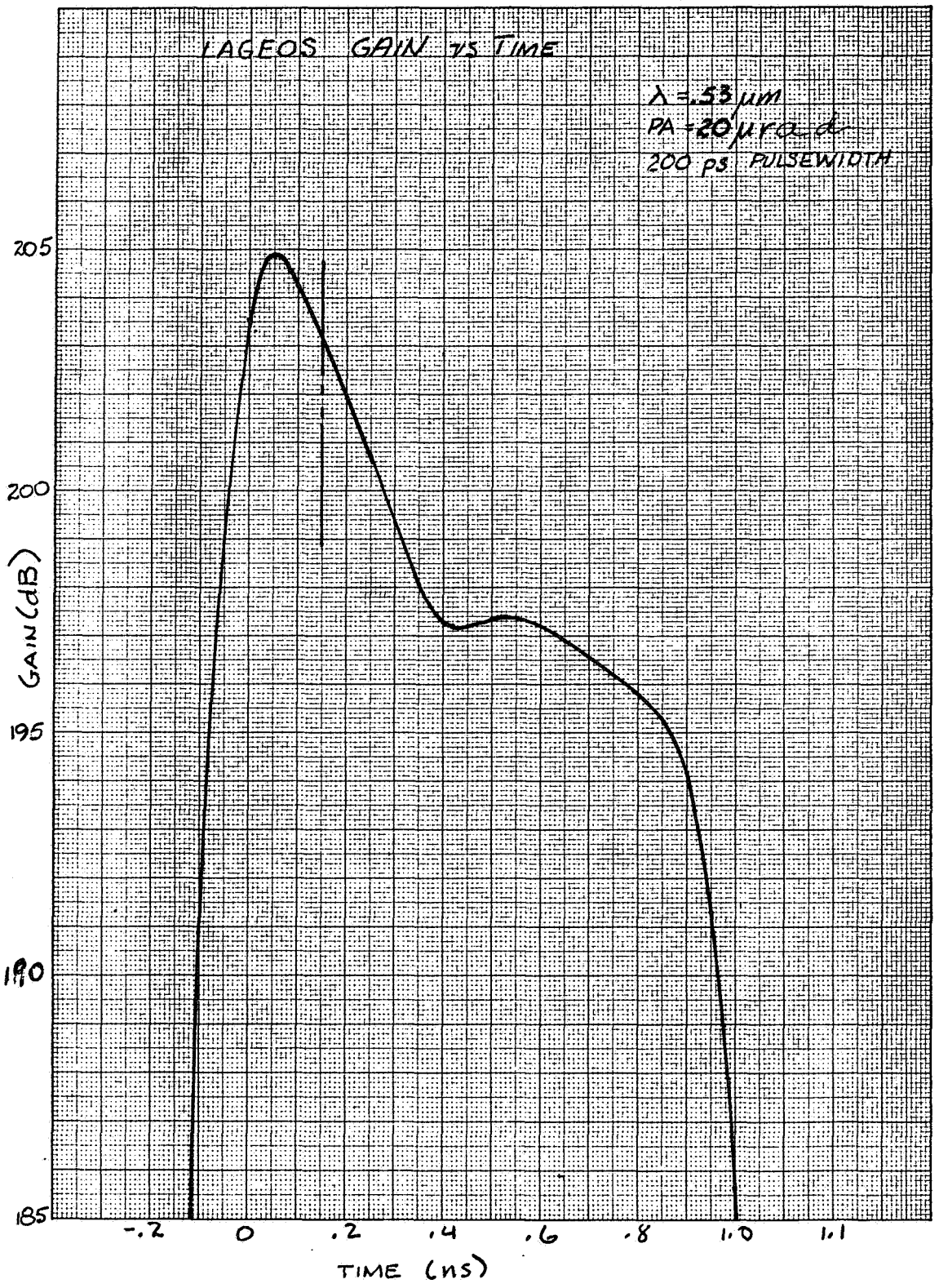
LAGEOS GAIN vs TIME
λ = .53 μm
PA = 20 μrad
200 ps PULSEWIDTH
205
200
195
190
185
GAIN (dB)
-.2
0
.2
.4
.6
.8
1.0
1.1
TIME (ns)

FIGURE B–4

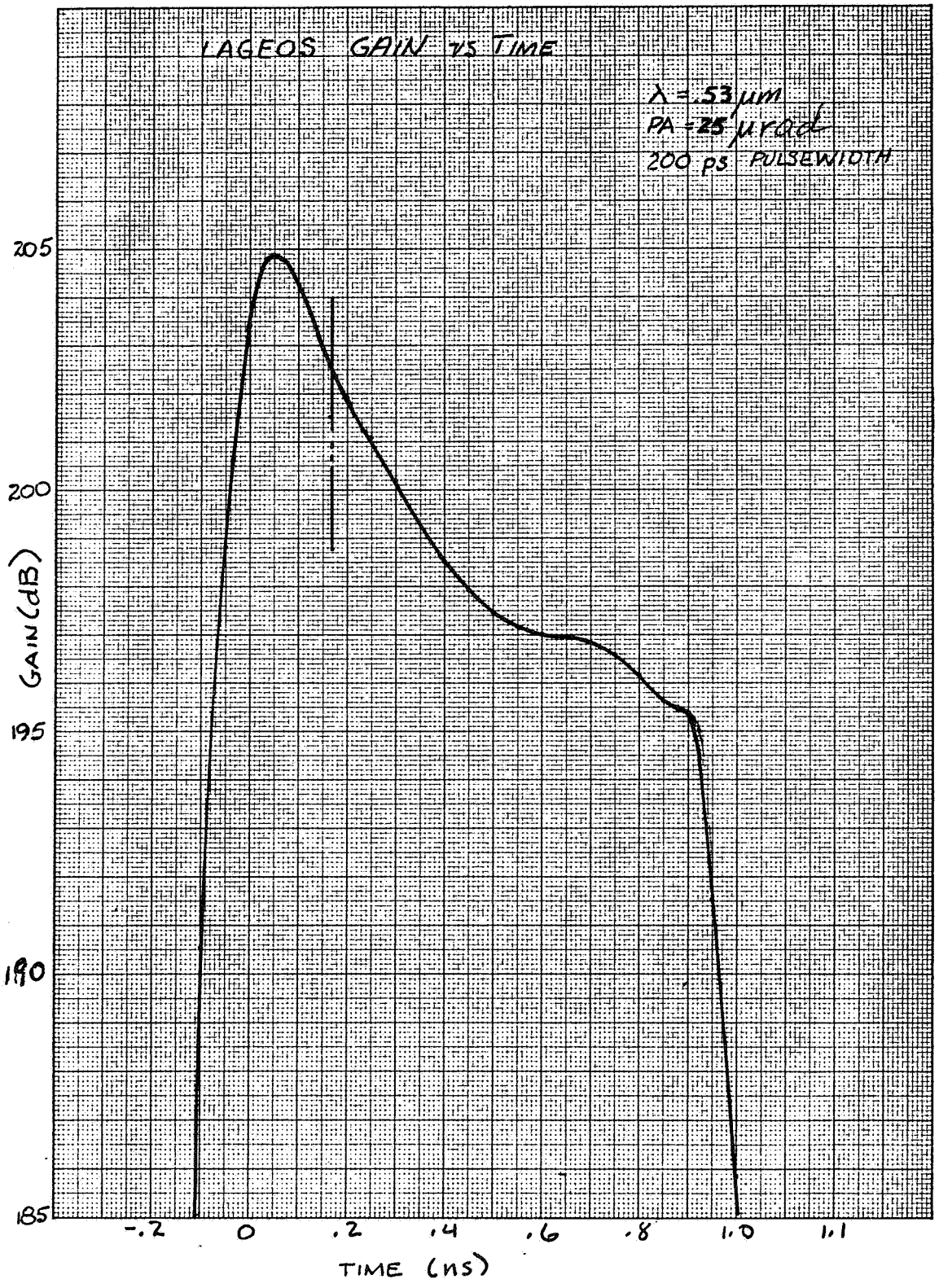
LAGEOS GAIN VS TIME
λ = .53 μm
PA = 25 μrad
200 ps PULSEWIDTH
205
200
195
190
185
GAIN (dB)
-.2
0
.2
.4
.6
.8
1.0
1.1
TIME (ns)

FIGURE B–5

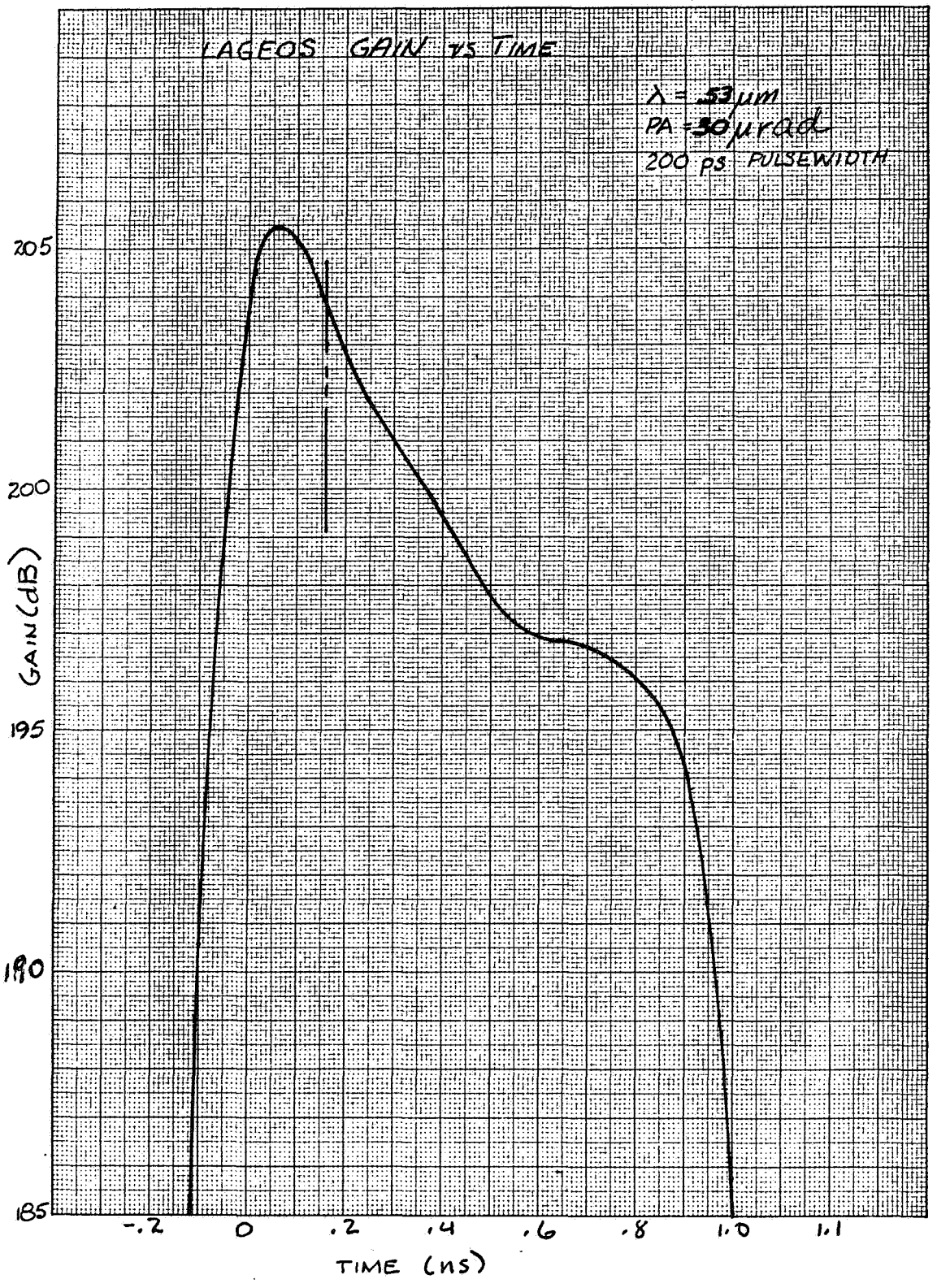
LAGEOS GAIN VS TIME
λ = .53μm
PA = 50μrad
200 ps PULSEWIDTH
205
200
195
190
185
GAIN (dB)
-.2
0
.2
.4
.6
.8
1.0
1.1
TIME (ns)

FIGURE B–6

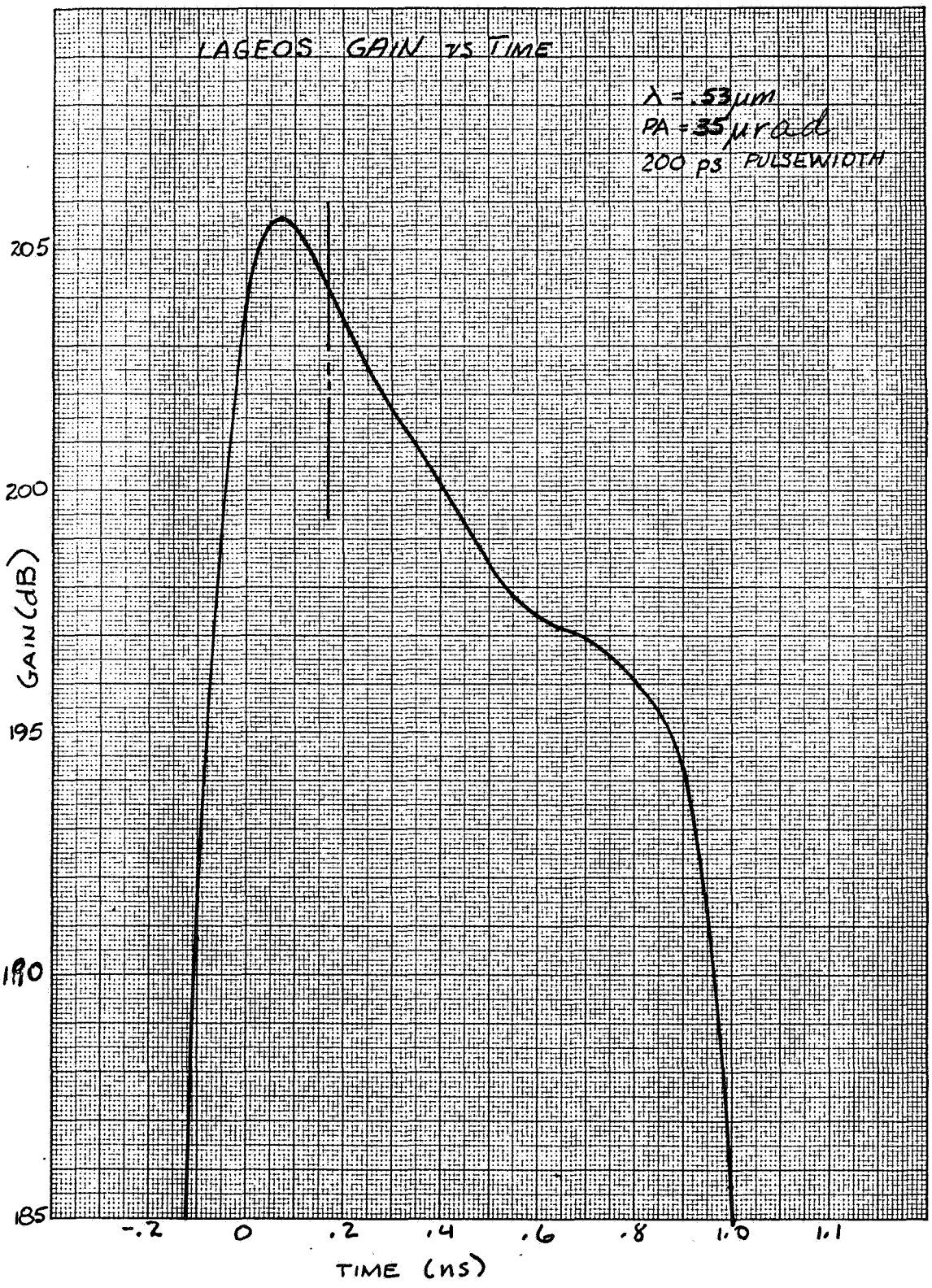
LAGEOS GAIN vs TIME
λ = .53 μm
PA = 35 μrad
200 ps PULSEWIDTH
205
200
195
190
185
GAIN (dB)
-.2
0
.2
.4
.6
.8
1.0
1.1
TIME (ns)

FIGURE B–7

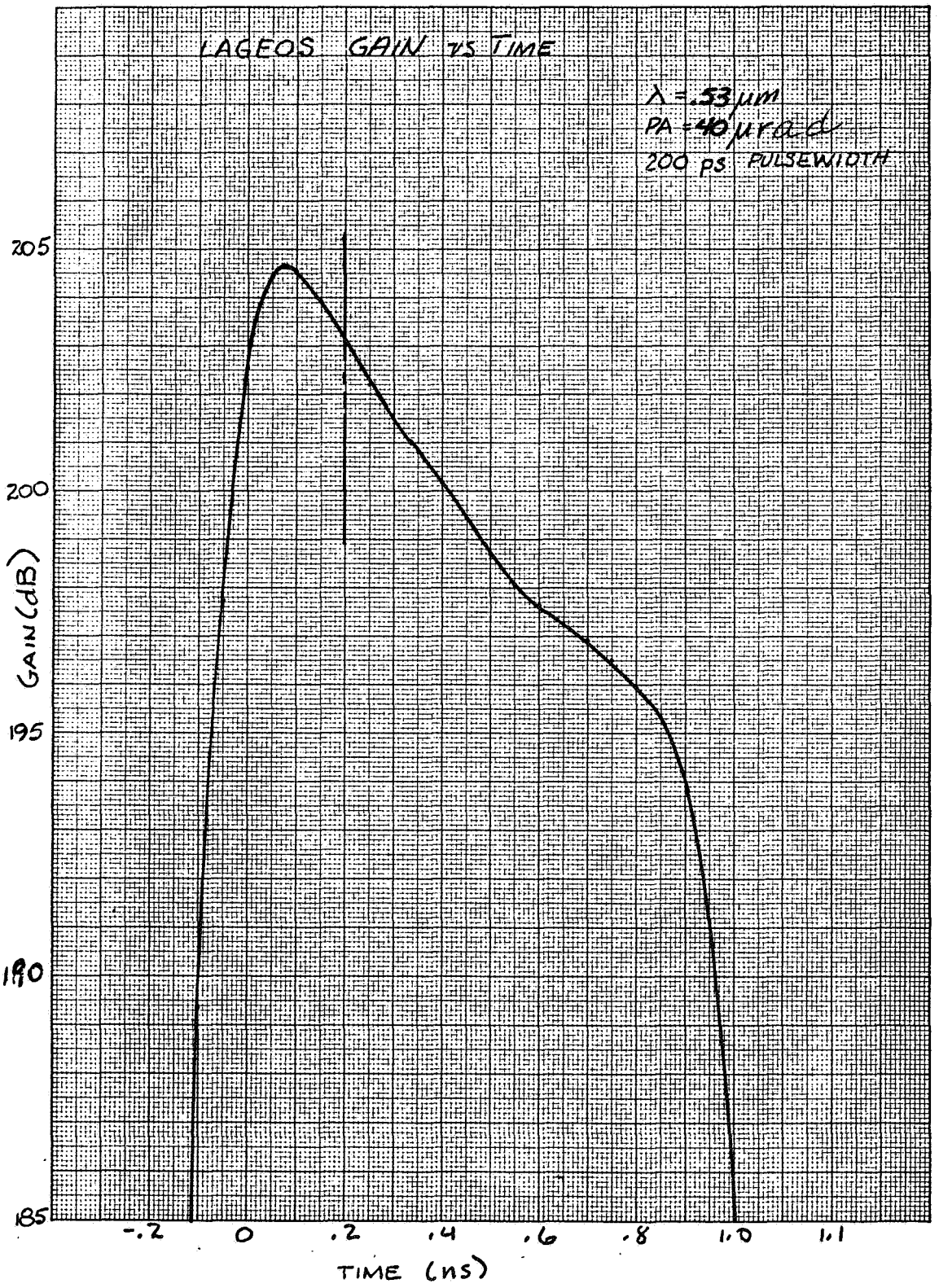
LAGEOS GAIN VS TIME
λ = .53 μm
PA = 40 μrad
200 ps PULSEWIDTH
205
200
195
190
185
GAIN (dB)
-.2
0
.2
.4
.6
.8
1.0
1.1
TIME (ns)

FIGURE B-8

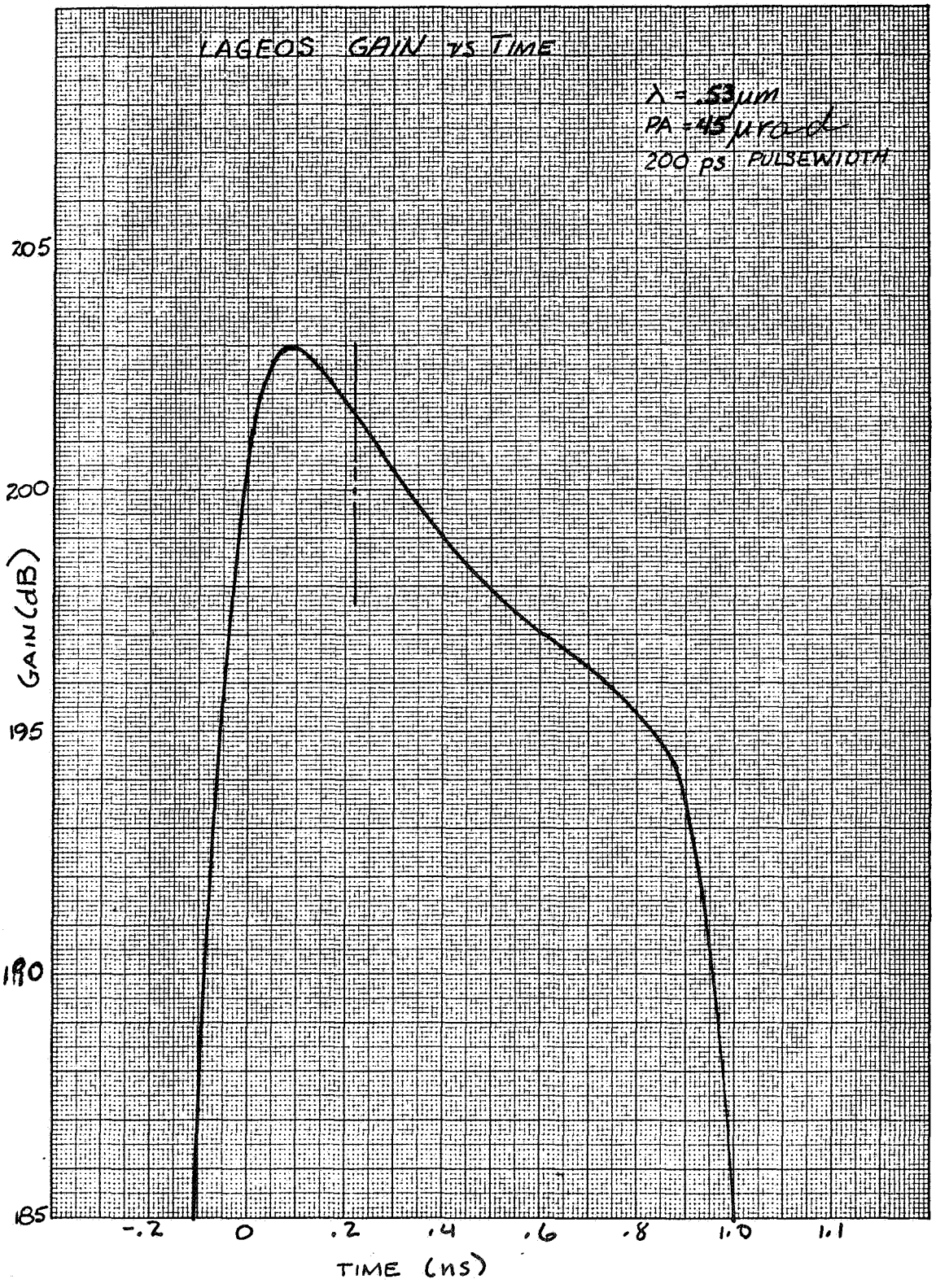
LAGEOS GAIN vs TIME
λ = .53 μm
PA = 45 μrad
200 ps PULSEWIDTH
205
200
195
190
185
GAIN (dB)
-.2
0
.2
.4
.6
.8
1.0
1.1
TIME (ns)

FIGURE B–9

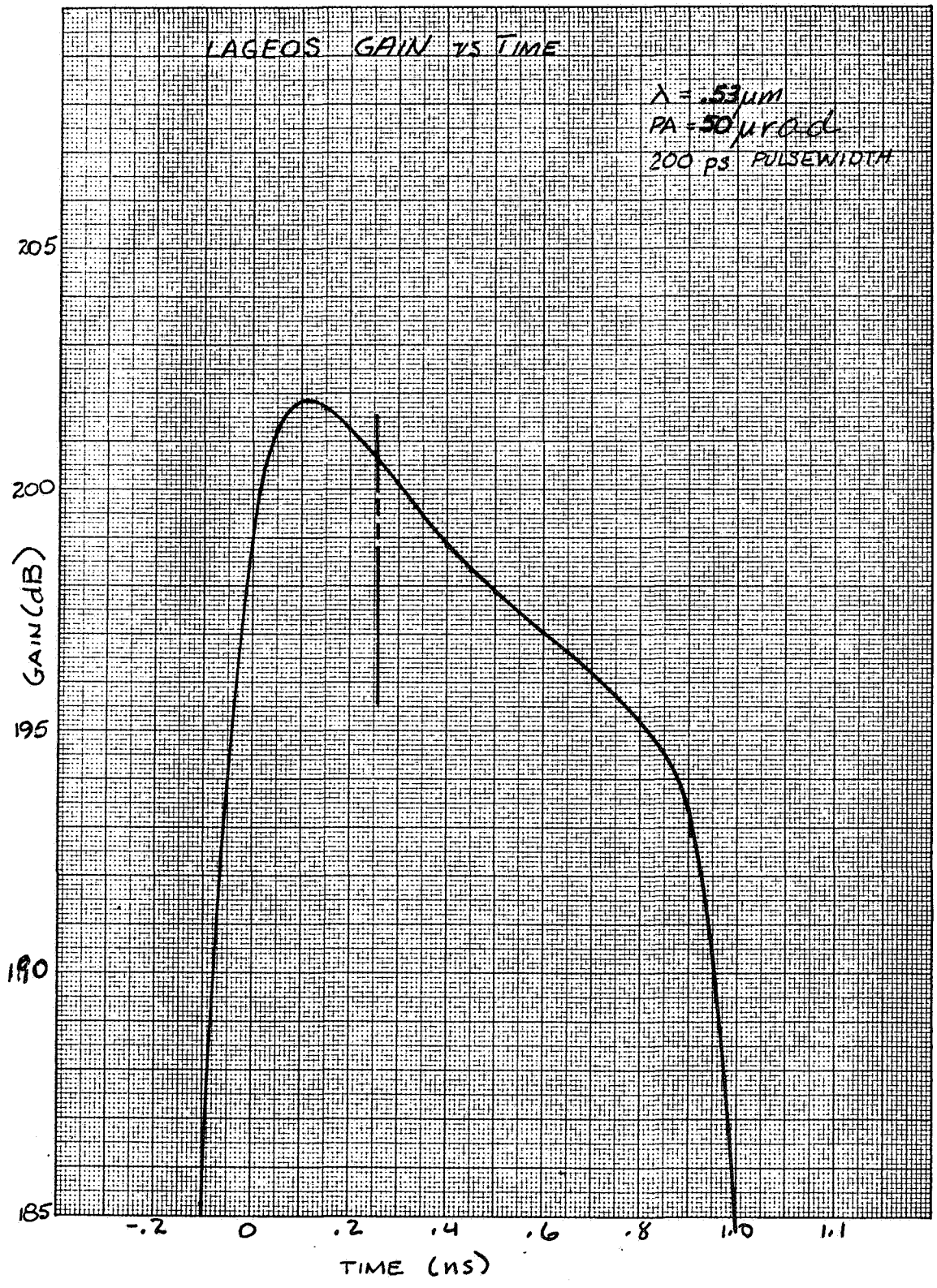
LAGEOS GAIN VS TIME
λ = .53μm
PA = 50 μrad
200 ps PULSEWIDTH
205
200
195
190
185
GAIN (dB)
-.2
0
.2
.4
.6
.8
1.0
1.1
TIME (ns)

FIGURE B–10

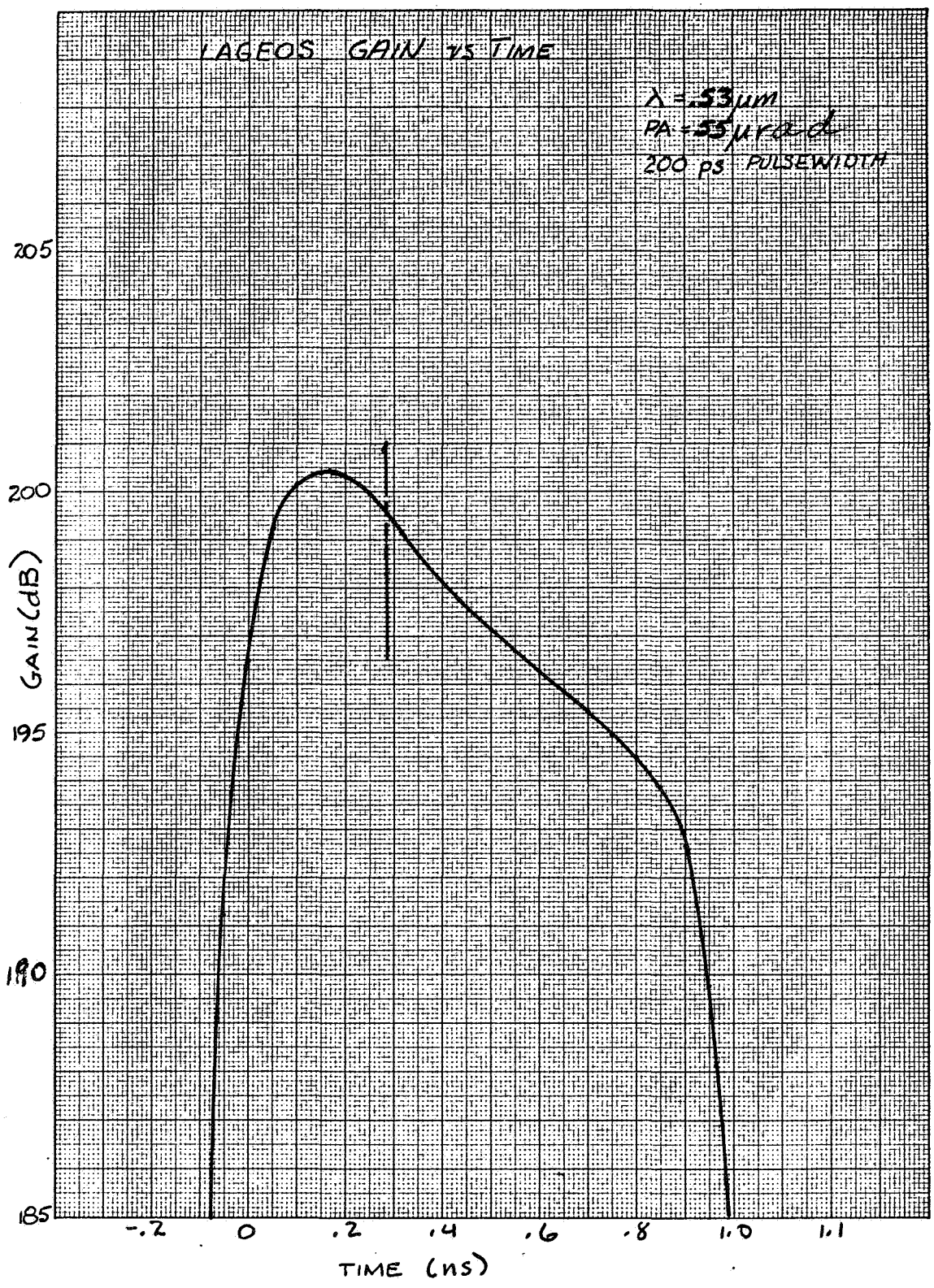
LAGEOS GAIN vs TIME
λ = .53 μm
PA = 55 μrad-cm
200 ps PULSEWIDTH
205
200
195
190
185
GAIN (dB)
-.2
0
.2
.4
.6
.8
1.0
1.1
TIME (ns)

FIGURE B–11

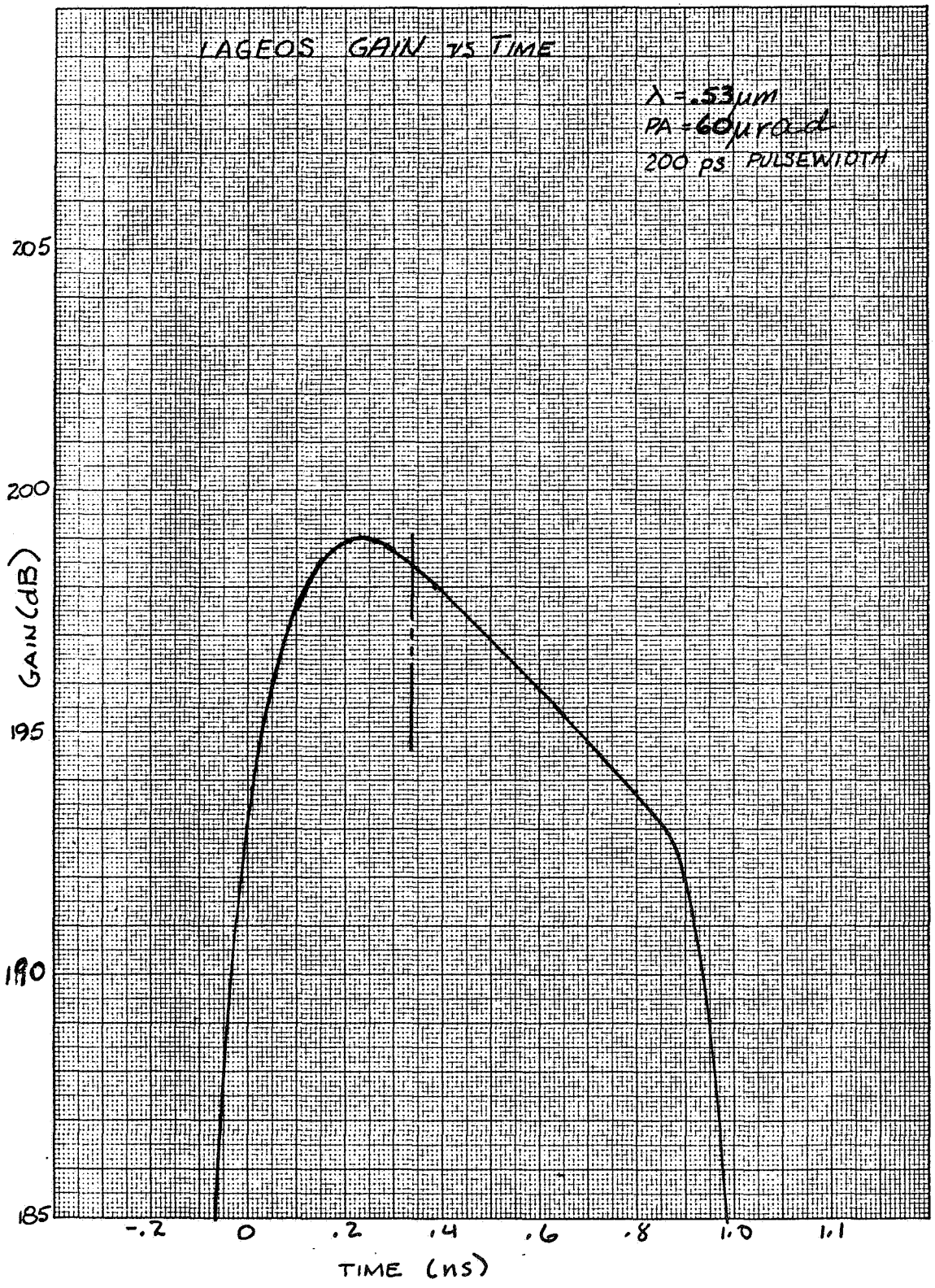
LAGEOS GAIN VS TIME
λ = .53μm
PA = 60μrad
200 ps PULSEWIDTH
205
200
195
190
185
GAIN (dB)
-.2
0
.2
.4
.6
.8
1.0
1.1
TIME (ns)

FIGURE B–12

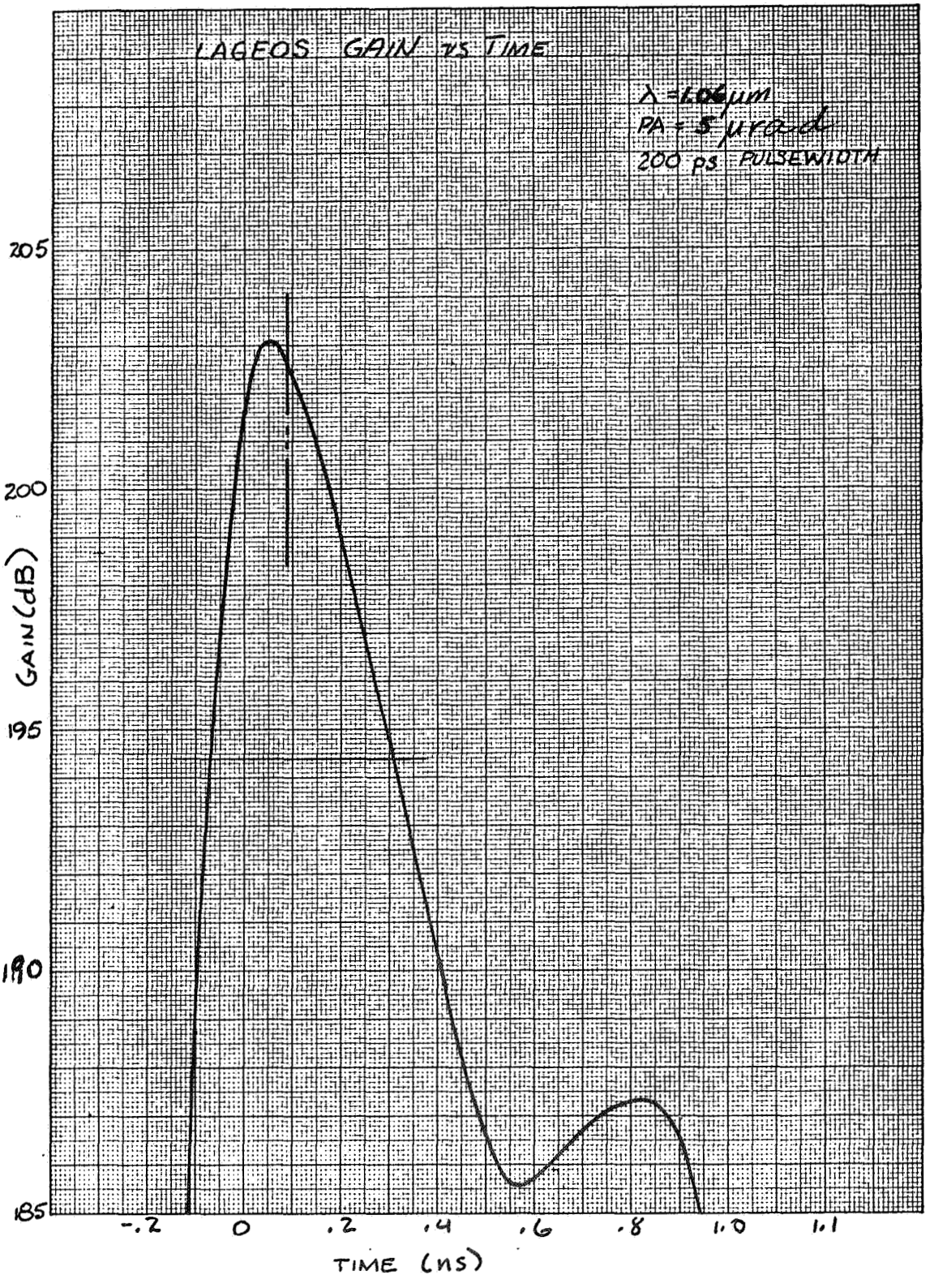
LAGEOS GAIN vs TIME
λ = 1.06 μm
PA = 5 μ rad
200 ps PULSEWIDTH
205
200
195
190
185
GAIN (dB)
-.2
0
.2
.4
.6
.8
1.0
1.1
TIME (ns)

FIGURE B–13

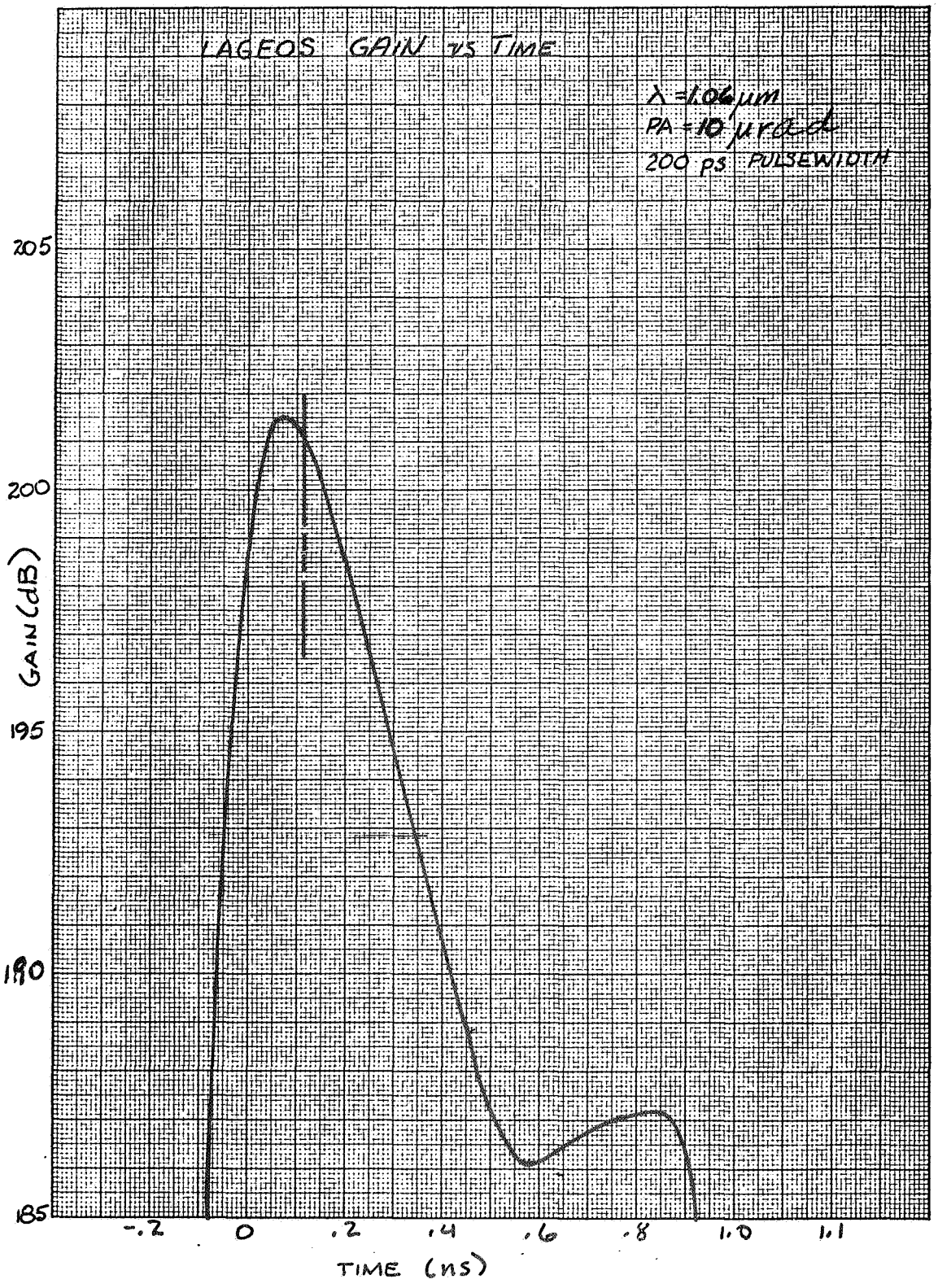
LAGEOS GAIN vs TIME
λ = 1.06 μm
PA = 10 μrad-dk
200 ps PULSEWIDTH
205
200
195
190
185
GAIN (dB)
-.2
0
.2
.4
.6
.8
1.0
1.1
TIME (ns)

FIGURE B–14

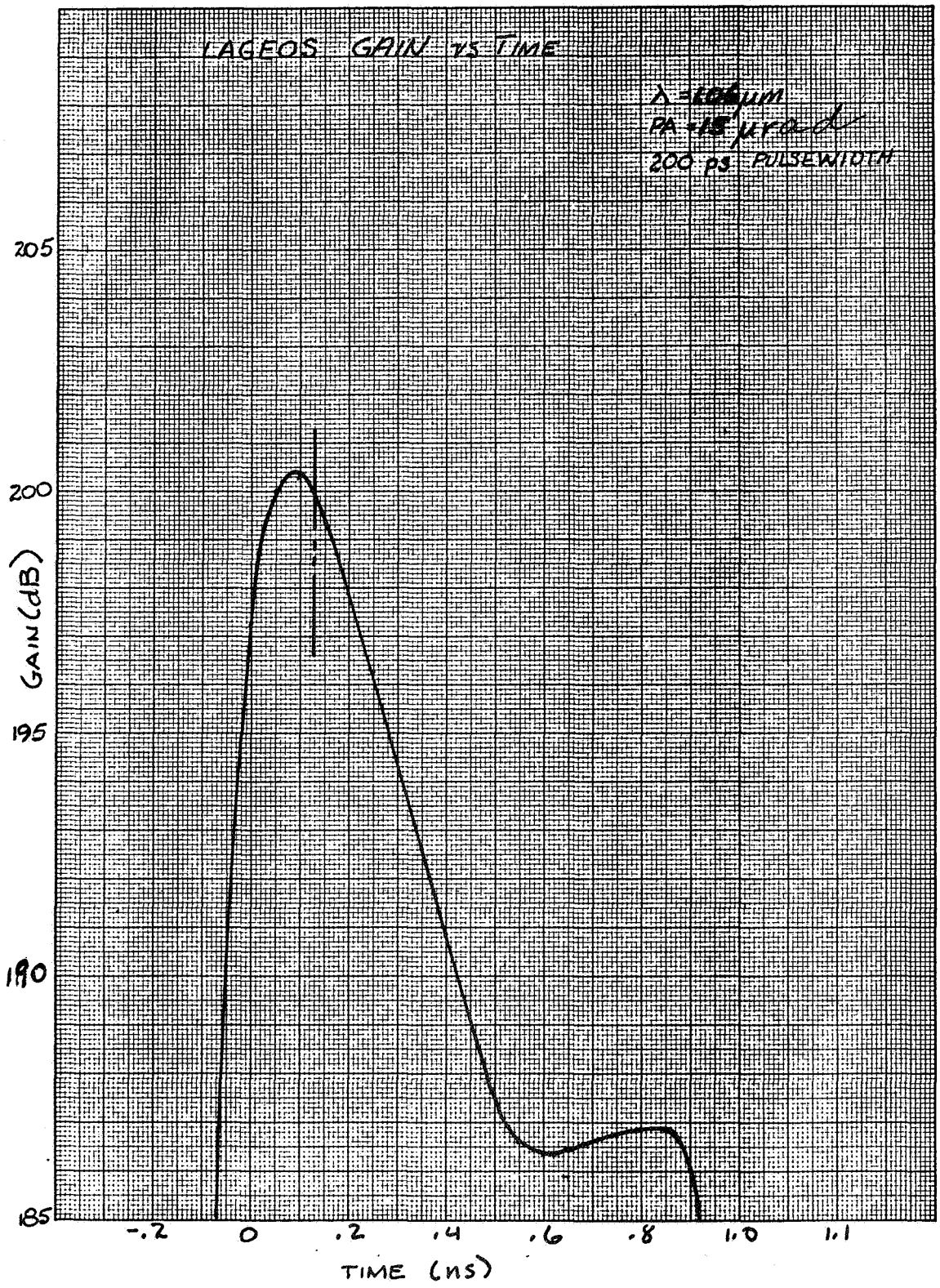
LAGEOS GAIN vs TIME
λ = 532 nm
PA = 15 μrad
200 ps PULSEWIDTH
205
200
195
190
185
GAIN (dB)
-.2
0
.2
.4
.6
.8
1.0
1.1
TIME (ns)

FIGURE B–15

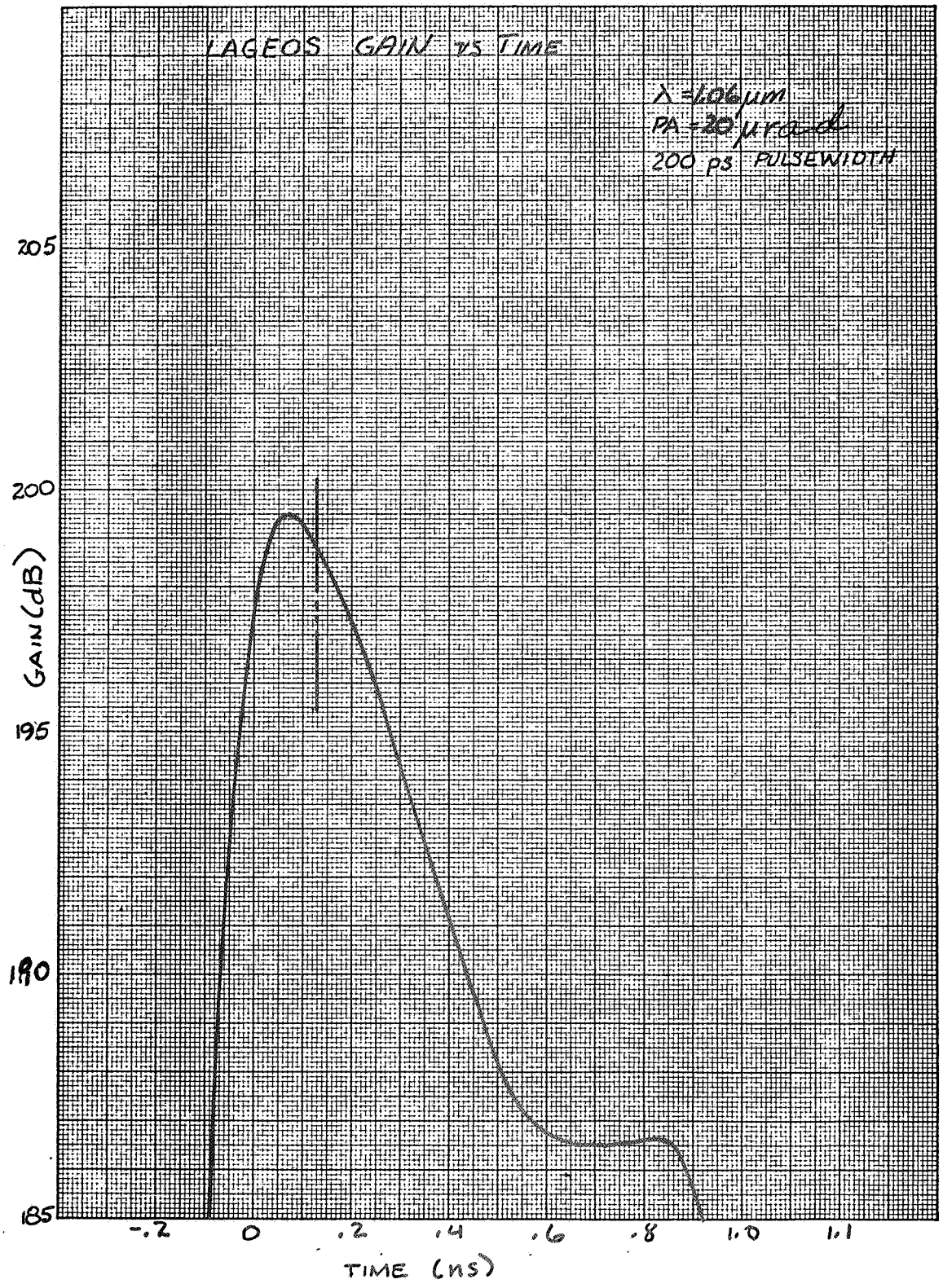
LAGEOS GAIN vs TIME
λ = 1.06 μm
PA = 20 μ rad
200 ps PULSEWIDTH
205
200
195
190
185
GAIN (dB)
-.2
0
.2
.4
.6
.8
1.0
1.1
TIME (ns)

FIGURE B–16

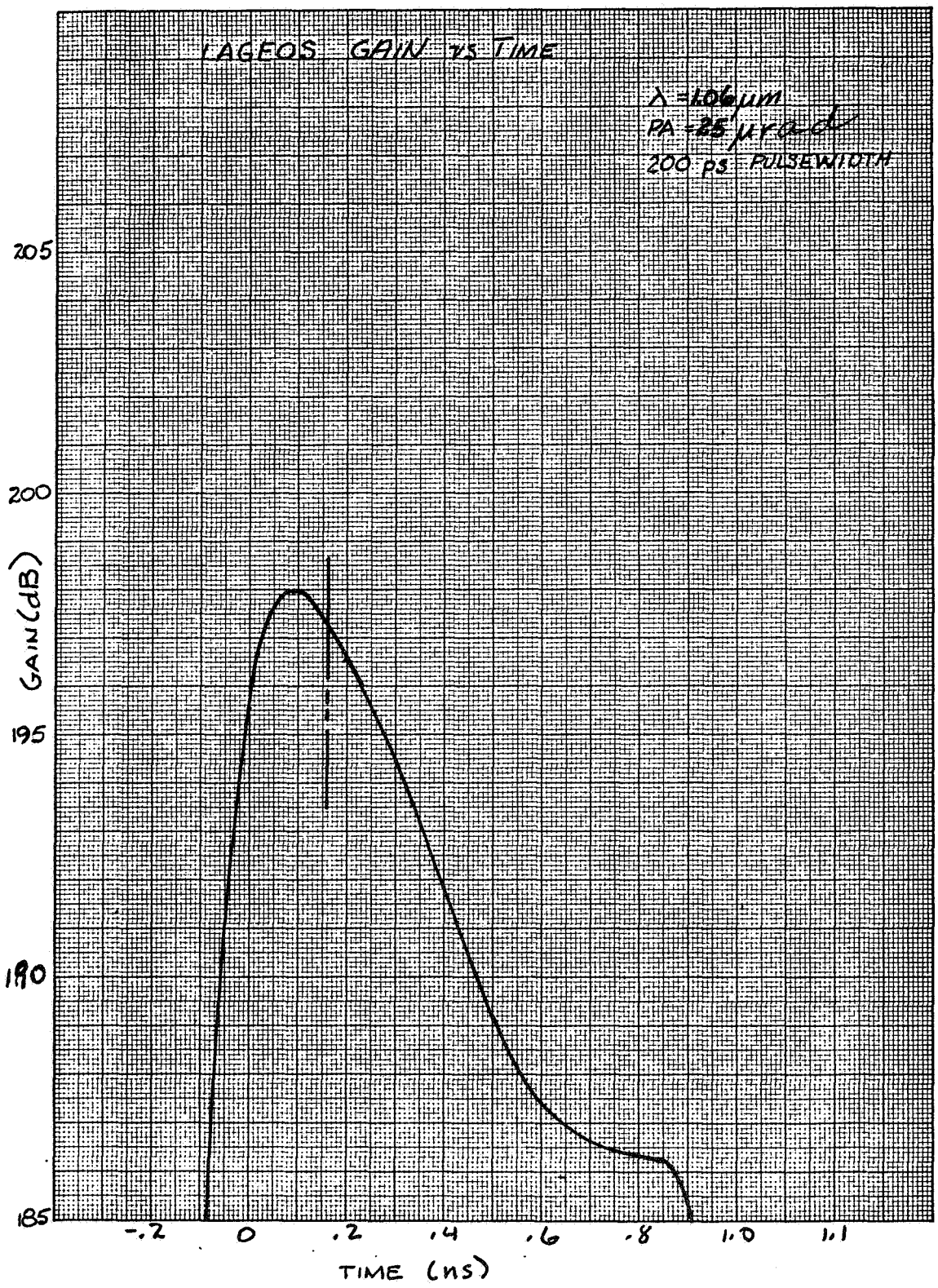
LAGEOS GAIN VS TIME
λ = 1.06 μm
PA = 25 μrad
200 ps PULSEWIDTH
205
200
195
190
185
GAIN (dB)
-.2
0
.2
.4
.6
.8
1.0
1.1
TIME (ns)

FIGURE B–17

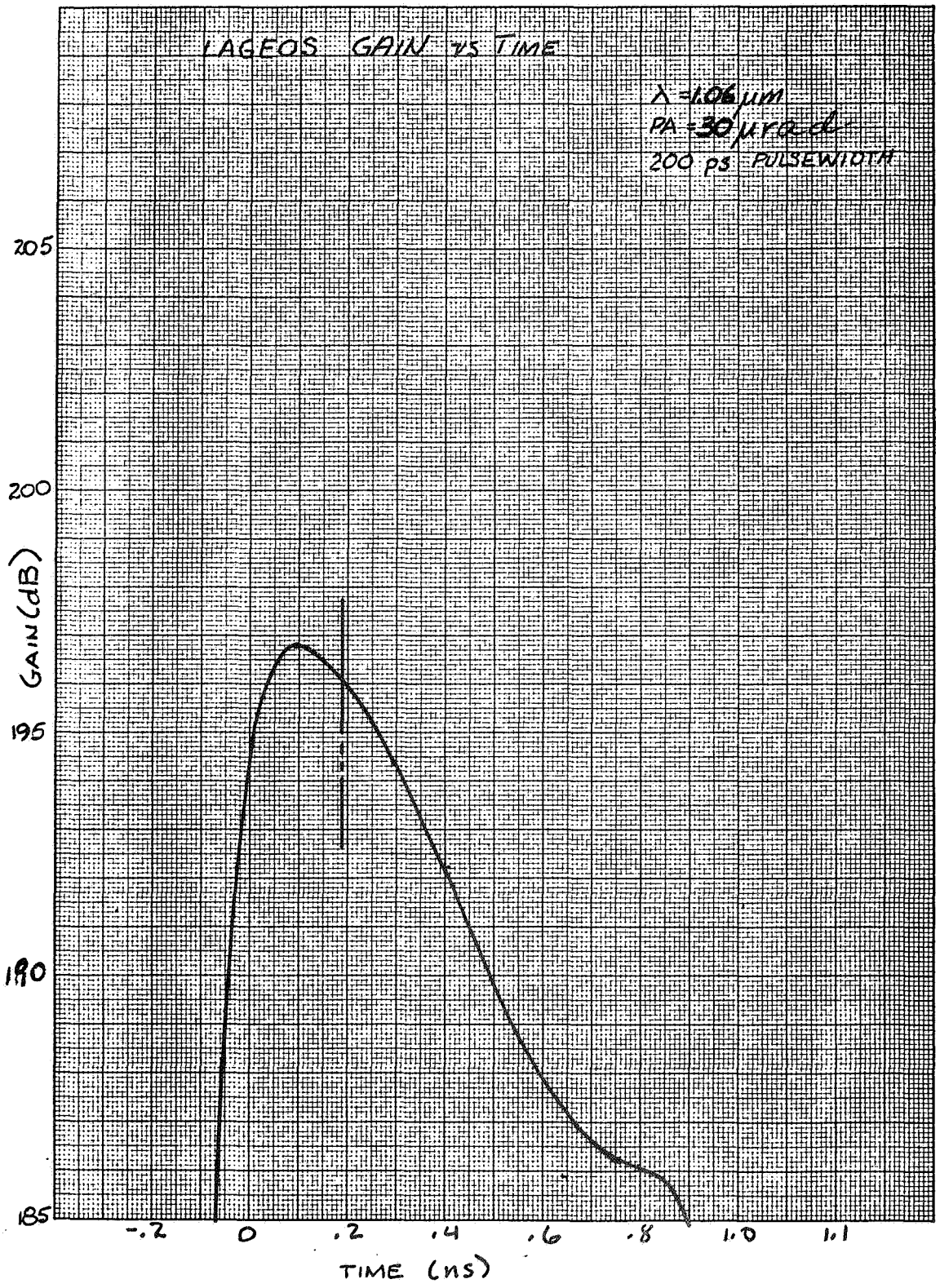
LAGEOS GAIN vs TIME
λ = 1.06 μm
PA = 30 μ r.c.d.
200 ps PULSEWIDTH
205
200
195
190
185
GAIN (dB)
-.2
0
.2
.4
.6
.8
1.0
1.1
TIME (ns)

FIGURE B–18

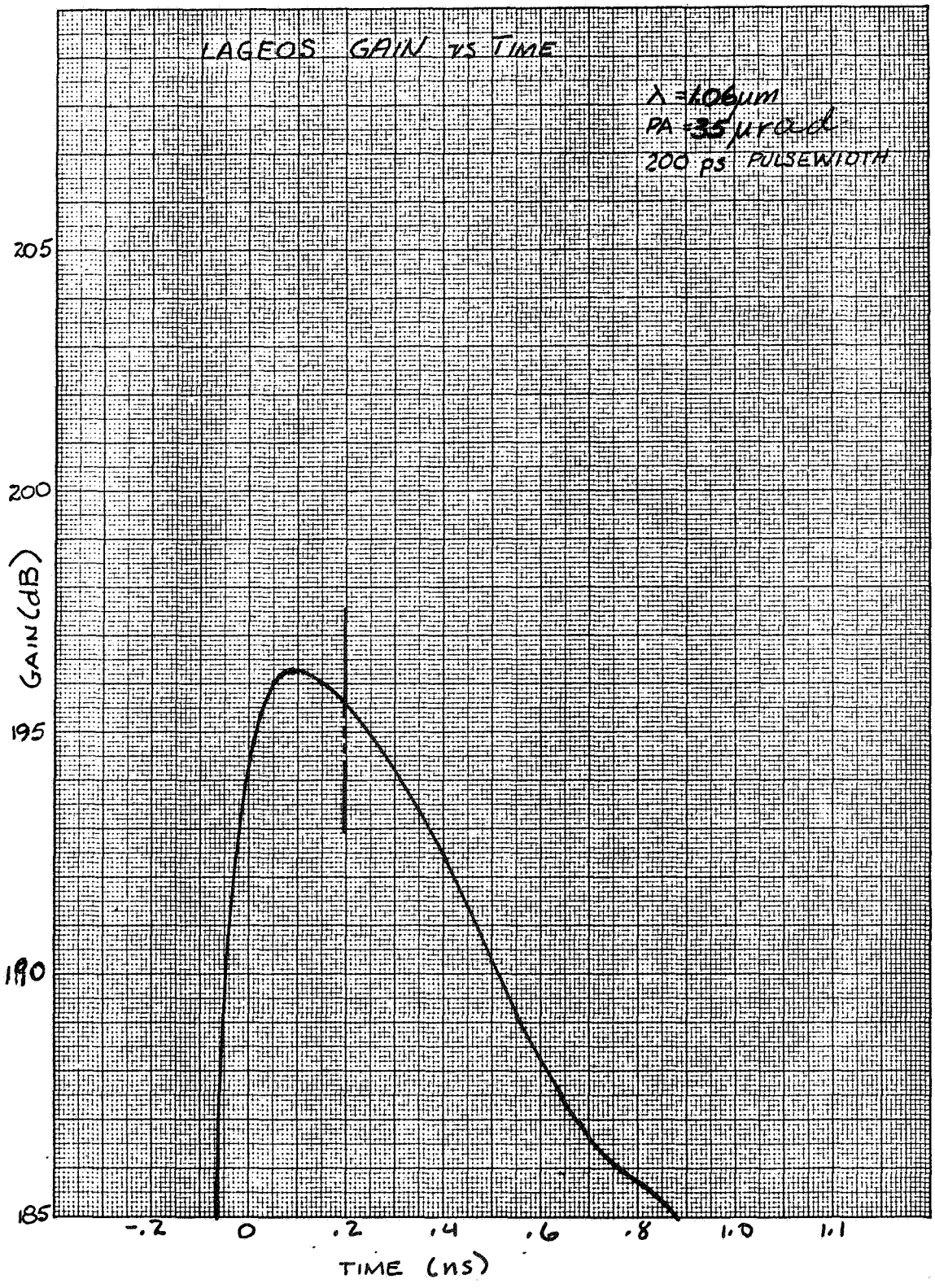
LAGEOS GAIN vs TIME
λ = 1.06μm
PA = 35 μ rad
200 ps PULSEWIDTH
205
200
195
190
185
GAIN (dB)
-.2
0
.2
.4
.6
.8
1.0
1.1
TIME (ns)

FIGURE B–19

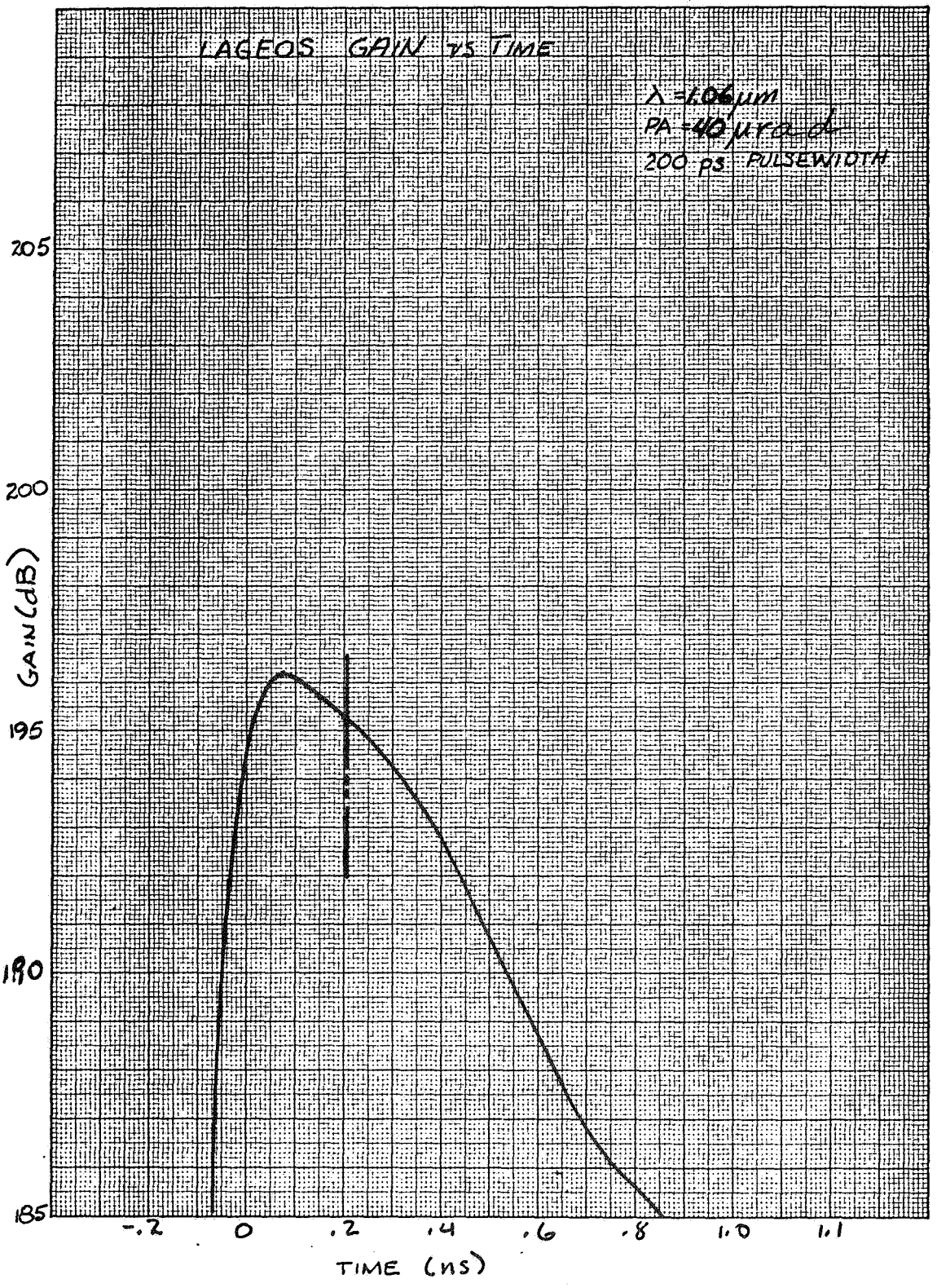
LAGEOS GAIN vs TIME
λ = 1.06 μm
PA = 40 μrad
200 PS PULSEWIDTH
205
200
195
190
185
GAIN (dB)
-.2
0
.2
.4
.6
.8
1.0
1.1
TIME (ns)

FIGURE B–20

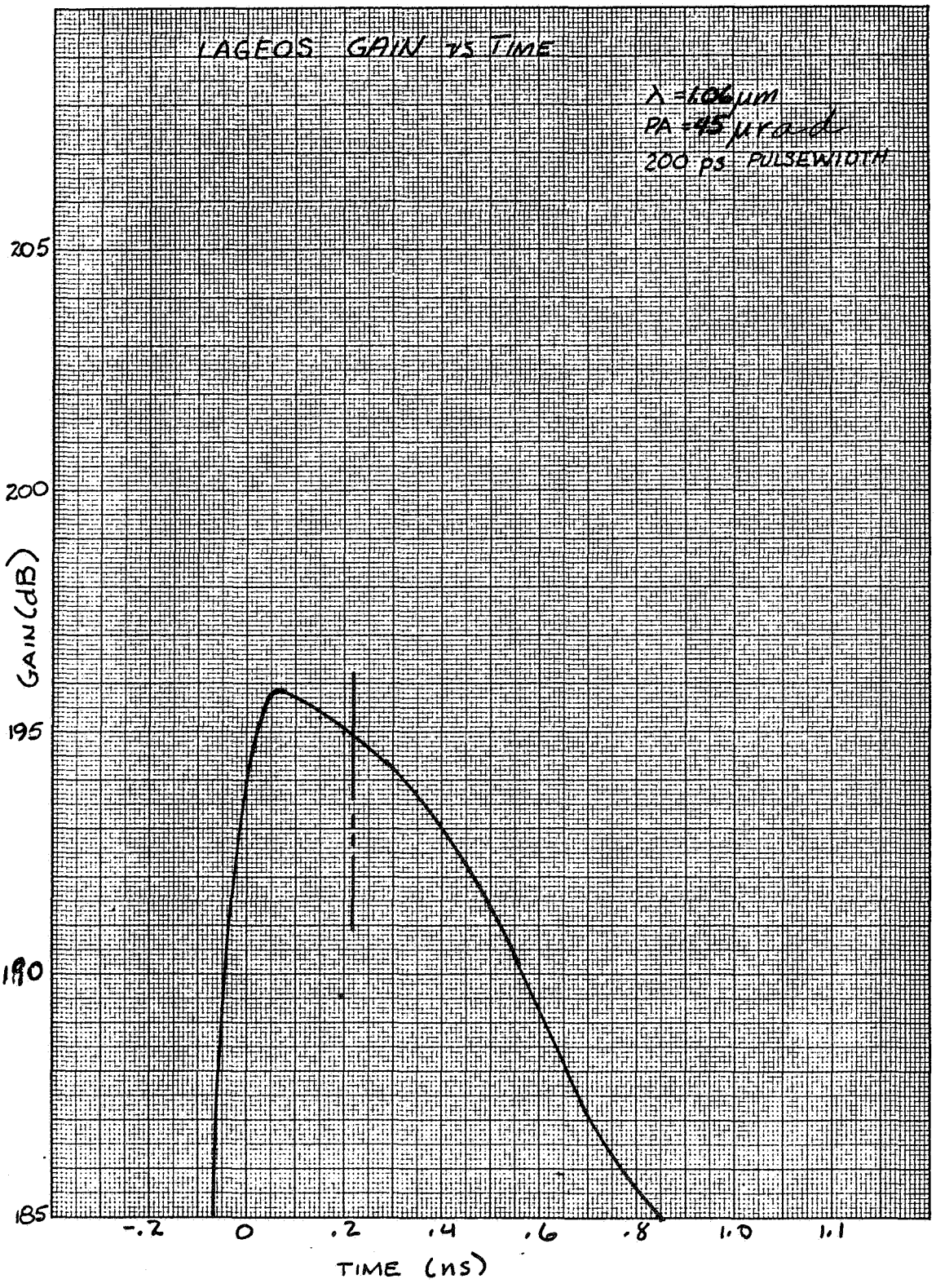
LAGEOS GAIN VS TIME
λ = 1.06 μm
PA = 45 μrad
200 ps PULSEWIDTH
205
200
195
190
185
GAIN (dB)
-.2
0
.2
.4
.6
.8
1.0
1.1
TIME (ns)

FIGURE B–21

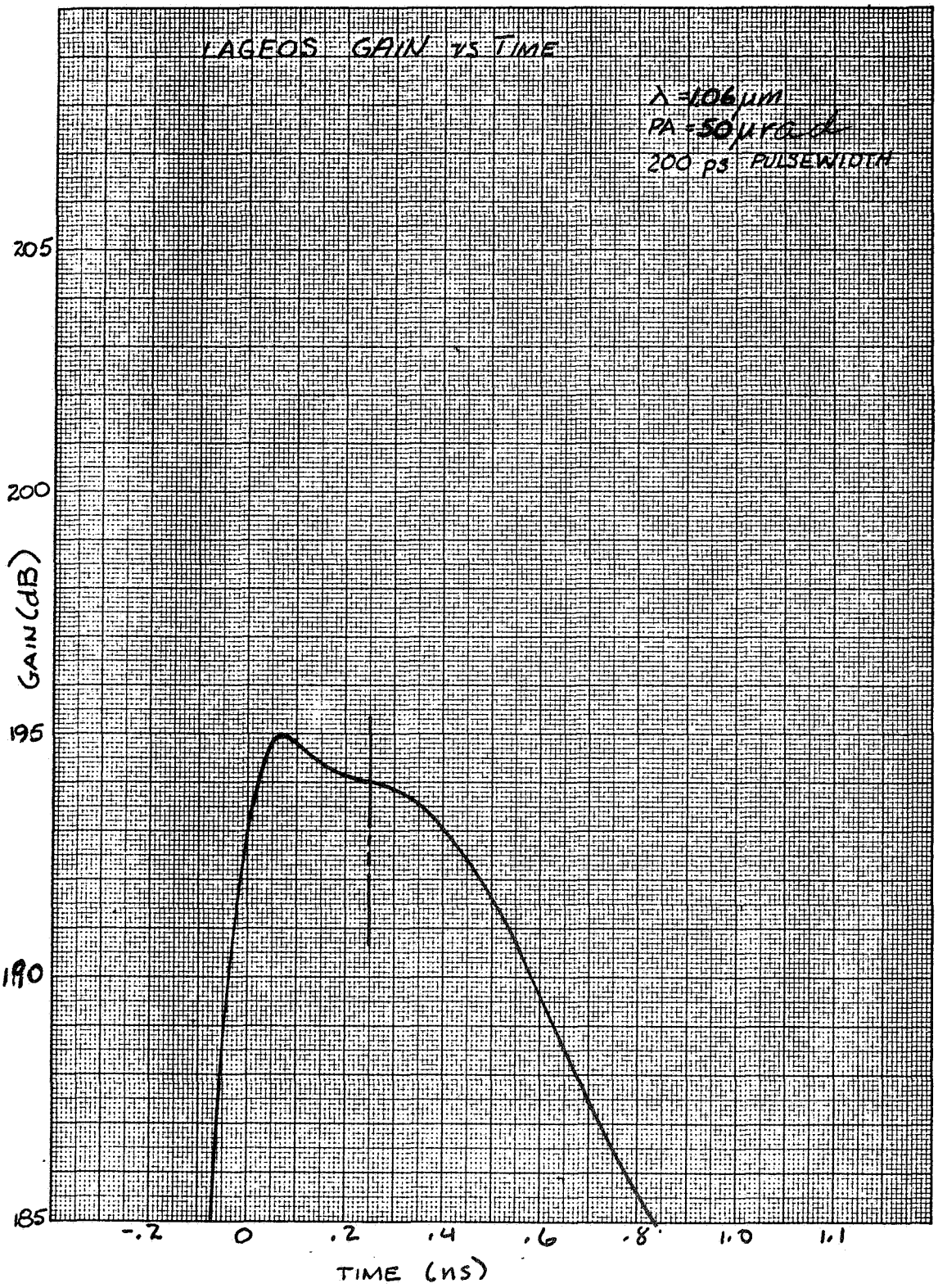
LAGEOS GAIN VS TIME
λ = 1.06 μm
PA = 50 μ rad
200 ps PULSEWIDTH
205
200
195
190
185
GAIN (dB)
-.2
0
.2
.4
.6
.8
1.0
1.1
TIME (ns)

FIGURE B–22

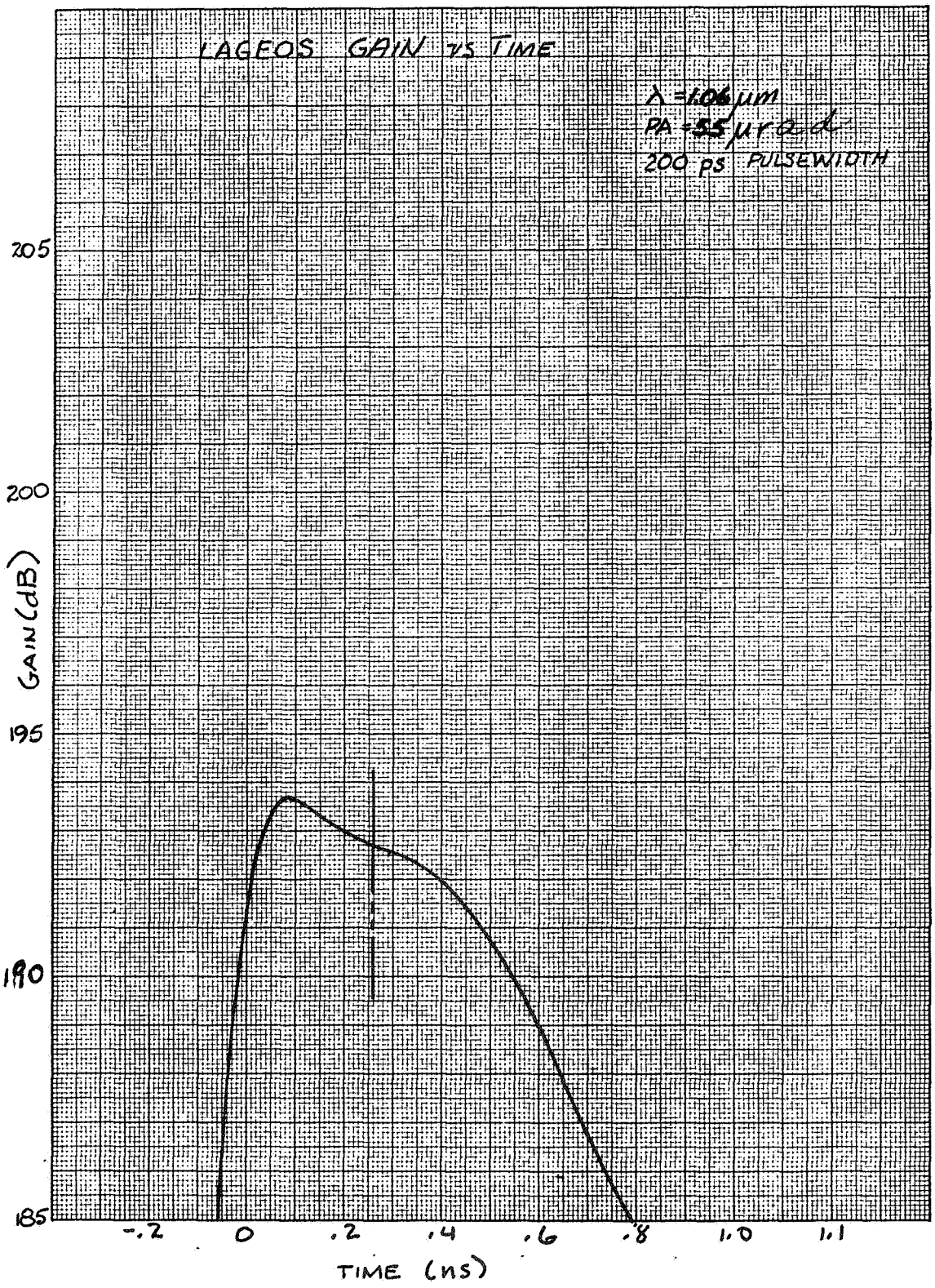
LAGEOS GAIN VS TIME
λ = 1.06 μm
PA = 55 μrad
200 ps PULSEWIDTH
205
200
195
190
185
GAIN (dB)
-.2
0
.2
.4
.6
.8
1.0
1.1
TIME (ns)

FIGURE B–23

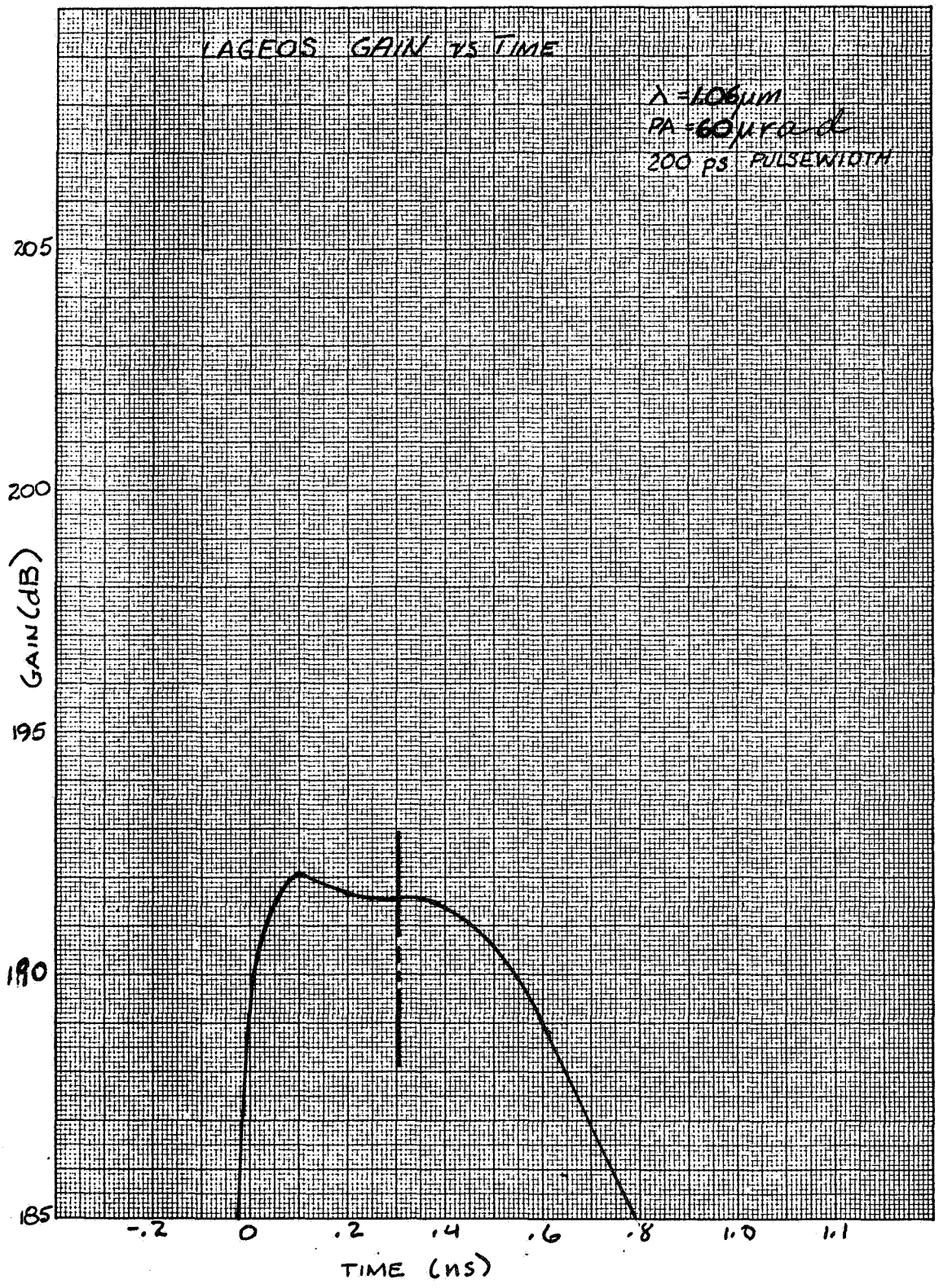
LAGEOS GAIN vs TIME
λ = 1.06μm
PA = 60μrad
200 ps PULSEWIDTH
205
200
195
190
185
GAIN (dB)
-.2
0
.2
.4
.6
.8
1.0
1.1
TIME (ns)

FIGURE B–24

APPENDIX C

LAGEOS SIGNATURE CENTROID CALCULATION

1.0 INTRODUCTION

The nonsymmetrical shape of the return pulse (Appendix B) from LAGEOS results in the pulse centroid varying considerably with conditions and pulse width. This program used to calculate the centroid and the resulting data are included in this appendix. The data used for these calculations were generated by the programs presented in Appendix A.

2.0 BIAS ESTIMATION PROGRAM

The program used to compute the centroid of the pulse was written in Fortran IV for MDAC's Sigma 9 time-sharing computer system, and was used in the on-line mode. The program is listed in the following pages.

```
BIASEST    10:30 MAR 06, '75

100 DIMENSION AM(9,24),AV(9,24),TRAN(3),A(76)
110 COMMON AM,AV
120 DATA DELT,CON1/1.37794E-11,2.5E3/
130 DATA A1,A2,A3,A4/.278393,.230389,.000972,.078108/,RTPI/1.77245/
140 ERF(X)=1.-1./(1.+X*(A1+X*(A2+X*(A3+X*A4))))**4
150 WAVE=.53
160 22 OUTPUT WAVE
170 READ,WAVE
180 CALL OPENF1('TEDAT',1)
190 IF(WAVE.LT.1.)GOTO25
200 DO21 I=1,144
210 READ(1,)D1,D2,D3,D4
220 21 CONTINUE
230  25 CONTINUE
240 DO 20 I=1,9
250 READ(1,)D1,D2,D3,D4
260 PRINT,D1,D2,D3,D4
270 DO 23 J=1,12
280 READ(1,)TRAN
290 AM(I,2*J-1)=TRAN(3)
300 AM(I,2*J)=TRAN(7)
310 AV(I,2*J-1)=TRAN(4)
```

```
320 AV(I,2*J)=TRAN(8)
330 23 CONTINUE
340 READ(1,)DUM
350 READ(1,)DUM
360 READ(1,)DUM
370 20  CONTINUE
380 CALL CLOSF1
390 1 OUTPUT'PULSE WIDTH'
400 READ,TPW
410 DO5 I=1,12
420 II=2*I
430 PA=5.*I
440 4 TN=-.5*DELT
450 DO 7 J=1,76
460 7 A(J)=0.
470 DO 10 N=1,76
480 TN=TN+DELT
490 GAM=ACOS(1.-TN*CON1)
500 CALL ESTVAL(D1,VAR,GAM,II)
510 A(N)=D1
520 10 CONTINUE
530 SUM1=0.
540 SUM2=0.
550 DO 3 N=1,76
560 SUM1=SUM1+DELT*(N-1)*A(N)
570 3 SUM2=SUM2+A(N)
580 SDLT=SUM1/SUM2
590 SUM1=0.
600 DO8 N=1,76
610 NN=N
620 SUM1=SUM1+A(N)
630 IF(SUM1.GT.SUM2/2.)GOTO9
640 8 CONTINUE
650 9 SDST=(FLOAT(NN)-.5)*DELT
660 ERR=SDST
670 IF(TPW.GT.0.5E-9)ERR=SDLT
680 11 SUMF=0.
690 SUMDF=0.
700 DO 12 N=1,76
710 DUM=(DELT*(N-1)-ERR)/TPW
720 DUM1=ERF(ABS(DUM))
730 DUM2=SIGN(DUM1,DUM)
740 SUMF=SUMF+A(N)*DUM2
750 12 SUMDF=SUMDF+A(N)*EXP(-DUM**2)
760 DELERR=SUMF*TPW*RTPI/SUMDF/2.
770 ERR=ERR+DELERR
780 IF(ABS(DELERR/ERR).GT.1.E-4)GOTO11
790 PRINT100,PA,ERR,SDST,SDLT
800 100 FORMAT(F7.0,9PF8.3,2F8.3)
810 5 CONTINUE
820 OUTPUT'NEW VALUES OR NEW RUN'
830 IM=0
840 READ,IM
```

```
 850  IF(IM.EQ.2)GOTO1
 860  IF(IM.EQ.3)GOTO22
 870  STOP
 880  END
 890  SUBROUTINE ESTVAL(GNU,VAR,THE,JP)
 900  DIMENSION AM(9,24),AV(9,24)
 910  COMMON AM,AV
 920  GNU=0.
 930  VAR=0.
 940  XI=THE*11.4592
 950  IL=INT(XI)+1
 960  IF(JP.GT.24)RETURN
 970  IF(IL.GT.9)RETURN
 980  G2=0.
 990  V2=0.
1000  G1=AM(IL,JP)
1010  V1=AV(IL,JP)
1020  IF(IL.EQ.9)GOTO1
1030  G2=AM(IL+1,JP)
1040  V2=AV(IL+1,JP)
1050  1 G=G1+(G2-G1)*(XI+1-IL)
1060  V=V1+(V2-V1)*(XI+1-IL)
1070  GNU=EXP(G)
1080  VAR=EXP(2*V)
1090  RETURN
1100  END
```

3.0 DATA

The data resulting from running this program is presented in the following pages. The printout is in two distinctive parts. The first part of the printout contains 9 lines of data, read from the data file containing the LAGEOS cube-corner gain data, and is printed to ensure a correct data input has accured. Following entry of the (half) pulsewidth, the next twelve lines of data list the pointahead angle in microradians, the computed pulse centroid (nanoseconds) for the chosen pulsewidth, and the short and long pulsewidth approximations for the centroid (nanoseconds).

```
BIASEST    10:34 MAR 06, '75

 WAVE = .530000
?
  3.80000    .530000    .000000    7.30000
  3.80000    .530000    5.00000    7.30000
  3.80000    .530000    10.0000    7.30000
  3.80000    .530000    15.0000    7.30000
```

```
  3.80000    .530000    20.0000    7.30000
  3.80000    .530000    25.0000    7.30000
  3.80000    .530000    30.0000    7.30000
  3.80000    .530000    35.0000    7.30000
  3.80000    .530000    40.0000    7.30000
 PULSE WIDTH
?.1E-9
     5.     .333     .347     .333
    10.     .279     .291     .308
    15.     .180     .178     .255
    20.     .152     .141     .238
    25.     .166     .160     .247
    30.     .163     .160     .236
    35.     .170     .160     .238
    40.     .198     .197     .262
    45.     .222     .216     .285
    50.     .255     .254     .311
    55.     .284     .291     .333
    60.     .336     .347     .372
 NEW VALUES OR NEW RUN
?2
 PULSE WIDTH
?2.E-9
     5.     .333     .347     .333
    10.     .307     .291     .308
    15.     .254     .178     .255
    20.     .236     .141     .238
    25.     .246     .160     .247
    30.     .235     .160     .236
    35.     .237     .160     .238
    40.     .251     .197     .262
    45.     .284     .216     .285
    50.     .310     .254     .311
    55.     .333     .291     .333
    60.     .371     .347     .372
 NEW VALUES OR NEW RUN
?3


 WAVE = .530000
?1.06
  3.80000    1.06000    .000000    7.30000
  3.80000    1.06000    5.00000    7.30000
  3.80000    1.06000    10.0000    7.30000
  3.80000    1.06000    15.0000    7.30000
  3.80000    1.06000    20.0000    7.30000
  3.80000    1.06000    25.0000    7.30000
  3.80000    1.06000    30.0000    7.30000
  3.80000    1.06000    35.0000    7.30000
  3.80000    1.06000    40.0000    7.30000
 PULSE WIDTH
?.1E-9
     5.     .088     .085     .125
    10.     .098     .085     .138
```

```
    15.     .110     .103     .155
    20.     .130     .122     .179
    25.     .161     .160     .211
    30.     .187     .197     .235
    35.     .196     .197     .241
    40.     .204     .216     .246
    45.     .220     .235     .258
    50.     .248     .254     .280
    55.     .258     .272     .291
    60.     .304     .310     .326
 NEW VALUES OR NEW RUN
?2
 PULSE WIDTH
?2.E-9
     5.     .124     .085     .125
    10.     .137     .085     .138
    15.     .154     .103     .155
    20.     .179     .122     .179
    25.     .210     .160     .211
    30.     .234     .197     .235
    35.     .241     .197     .241
    40.     .246     .216     .246
    45.     .258     .235     .258
    50.     .230     .254     .280
    55.     .290     .272     .291
    60.     .326     .310     .326
 NEW VALUES OR NEW RUN
?
```

APPENDIX D

LINK MARGIN ANALYSIS

1.0 INTRODUCTION

The link margin analysis summaries and the program used to generate them are presented in this appendix.

2.0 LINK MARGIN ANALYSIS PROGRAM

The program used to compute the link margins for the various links and terminals was written in Fortran IV, for MDAC's Sigma 9 time-sharing computer system, and may be used either on-line or in the batch mode. The program is listed in the following pages.

```
RADAR1   11:48 MAR 06,'75

100 INTEGER LIST(240),LINK(36)
110 DIMENSION VAL(30)
120 DATA PI,PLANCK,SPDL/3.141592653,6.6256E-34,2.997925E8/
130 DATA LIST/'TRANSMITTER POWER        DBW     ',
1408'TRANSMITTER LOSSES       DB      ',
1508'TRANSMIT ANTENNA GAIN    DB      ',
1608'POINTING LOSS            DB      ',
1708'FREE SPACE LOSS          DB      ',
1808'ATMOSPHERIC LOSS(DOWN)   DB      ',
1908'TARGET GAIN PRODUCT      DB      ',
2008'ATMOSPHERIC LOSS(UP)     DB      ',
2108'FREE SPACE LOSS          DB      ',
2208'RECEIVE ANTENNA GAIN     DB      ',
2308'RECEIVER LOSSES          DB      ',
2408'RECEIVED SIGNAL POWER    DBW     ',
2508'TRANSMIT PULSE RATE      DB/SEC  ',
2608'ENERGY PER PULSE         DBJ     ',
2708'ENERGY PER PHOTON        DBJ     ',
2808'RECEIVED PHOTONS/PULSE   DB      ',
2908'QUANTUM EFFICIENCY       DB      ',
3008'RECEIVED P-E/PULSE       DB      ',
3108'BACKGROUND RADIANCE      DBW     ',
3208'RECEIVER FOV(STERRAD.)   DB      ',
3308'OPTICAL FILTER BAND WIDTHDB      ',
3408'RECEIVE ANTENNA AREA     DBM2    ',
3508'RECEIVER LOSSES          DB      ',
3608'RECEIVED BACK. POWER     DBW     ',
```

```
3700'ENERGY PER PHOTON        DBJ      ',
3800'RECEIVED PHOTONS/SEC     DB/SEC   ',
3900'QUANTUM EFFICIENCY       DB       ',
4000'BACKGROUND P-E/SEC       DB/SEC   ',
4100'RECEIVER GATE WIDTH      DB-SEC   ',
4200'BACKGROUND P-E/GATE      DB     '/
430 DATA LINK/'MATRS TO LATS(PASSIVE)  ',
4400'MATRS TO LATS(ACTIVE)    '
4500,'LATS TO MATRS             '
4600,'MATRS TO GROUND(PASSIVE)'
4700'SHUTTLE TO GROUND        '
4800'GROUND BEACON TO SHUTTLE'/
490 DATA SIGMA,PWDTH,IMAR/.13333E-9,.2E-9,0/
500 DATA APT,ALT,BWDTH,POINT,WAVE/.001,.8,5.E-6,1.E-6,.53E-6/
5100,RANGE,ATMD,DTAR,ATMU/3.E7,1.,208.5,1./
5200,PRIDIA,SECDIA,ALR,PRATE,DE/1.,.19,.4,1.,.25/
5300,BRAD,FOV,FILTER,RGN,SPG,LTROL,NEXT/.017,.5E-4,5.,2.E-9,1.,1,1/
5400,PND,PFA,BLOOP/1.E-6,1.E-8,10./
550 NAMELIST
560 DB(X)=10.*ALOG10(X)
570 CALL OPENF1('PARAM',1)
580 GOTO21
590 22 CONTINUE
600 IF(NEXT.EQ.1)GOTO20
610 CALL CLOSF1
620 STOP
630 20 CONTINUE
640C COMPUTE LINK PARAMETERS
650 DUM=SIGMA
660 IF(DUM.GT.0.2*PWDTH)DUM=0.2*PWDTH
670 ACON=(PI*DUM/PWDTH)**2
680 INDEX=0
690 IF(LTROL.EQ.2)INDEX=1
700 IF(LTROL.EQ.3)INDEX=1
710 IF(LTROL.EQ.6)INDEX=2
720 DPT=DB(APT)
730 DLT=DB(ALT)
740 DUM=32./BWDTH**2
750 GTX=DB(DUM)
760 DLPTG=-8.68589*(2*POINT/BWDTH)**2
770 DUM=WAVE/4./PI/RANGE
780 FSL=2.*DB(DUM)
790 DATMD=DB(ATMD)
800 DATMU=DB(ATMU)
810 RAA=PI*(PRIDIA**2-SECDIA**2)/4.
820 TRG=RAA*4.*PI/WAVE**2
830 GTRG=DB(TRG)
840 DLR=DB(ALR)
850 DPRX=DPT+DLT+GTX+DLPTG+2*FSL+DATMD+DTAR+DATMU+GTRG+DLP
860 IF(INDEX.EQ.0)GOTO10
870 DPRX=DPRX-FSL-DATMU-DTAR
880 IF(INDEX.EQ.2)DPRX=DPRX+DATMU-DATMD
890 10 CONTINUE
```

```
900 DPRATE=DB(PRATE)
910 DEP=DPRX-DPRATE
920 EPP=PLANCK*SPDL/WAVE
930 DEPP=DB(EPP)
940 DRPP=DEP-DEPP
950 DOE=DB(OE)
960 DRPEP=DRPP+DOE
970 RPEP=10.**(DRPEP/10.)
980  DBRAD=DB(BRAD)
990 DUM=PI*(FOV/2.)**2
1000 DFOV=DB(DUM)
1010 DFILT=DB(FILTER)
1020 DRAA=DB(RAA)
1030 DRBP=DBRAD+DFOV+DFILT+DRAA+DLR
1040 DRPS=DRBP-DEPP
1050 DBPES=DRPS+DOE
1060 DRGN=DB(RGN)
1070 DBPEG=DBPES+DRGN
1080 BPEG=10.**(DBPEG/10.)
1090 IF(IMAR.EQ.1)GOTO250
1100 ROSIG=(1.+SQRT(1.+2*BPEG*ACON))/ACON
1110 IF(IMAR.EQ.2)ROSIG=5*BLOOP*(1.+SQRT(1.+.4*BPEG*PRATE/BLOOP))/PRATE
1115 IF(IMAR.EQ.3)CALL THRESH(PFA,PND,BPEG,ROSIG)
1120 250 CONTINUE
1130 DROSIG=DB(ROSIG)
1140 AMARG=RPEP/ROSIG
1150 DMARG=DB(AMARG)
1160C PUT OUTPUT PARAMETERS INTO VALUE LIST
1170 VAL(1)=DPT
1180 VAL(2)=DLT
1190 VAL(3)=GTX
1200 VAL(4)=DLPTG
1210 VAL(5)=FSL
1220 VAL(6)=DATMD
1230 VAL(7)=DTAR
1240 VAL(8)=DATMU
1250 VAL(9)=FSL
1260 VAL(10)=GTRG
1270 VAL(11)=DLR
1280 VAL(12)=DPRX
1290 VAL(13)=DPRATE
1300 VAL(14)=DEP
1310 VAL(15)=DEPP
1320 VAL(16)=DRPP
1330 VAL(17)=DOE
1340 VAL(18)=DRPEP
1350 VAL(19)=DBRAD
1360 VAL(20)=DFOV
1370 VAL(21)=DFILT
1380 VAL(22)=DRAA
1390 VAL(23)=DLR
1400 VAL(24)=DRBP
1410 VAL(25)=DEPP
1420 VAL(26)=DRPS
```

```
1430 VAL(27)=DQE
1440 VAL(28)=D3PES
1450 VAL(29)=DRGW
1460 VAL(30)=D3PEG
1470C PRINT LINK SUMMARY
1480 JJJ=6*LTROL
1490 JJ=JJJ-5
1500 PRINT200,(LINK(J),J=JJ,JJJ)
1510 200 FORMAT(//6A4)
1520 PRINT100,WAVE,RANGE,PWDTH
1530 100 FORMAT('CIRCUIT  MARGIN  SUMMARY'//'OPTICAL WAVELENGTH',
1540&6PF6.2,' MICROMETERS,RANGE',-3PF7.0,' KM'/
1550&'PULSEWIDTH=',9PF4.2,' NANOSECONDS'//T6,'PARAMETER',
1560&T32,'UNITS',T44,'VALUE')
1570 DO 3 I=1,30
1580 IF(INDEX.EQ.0)GOTO11
1590 IF(((I.LT.7).OR.(I.GT.9)).AND.INDEX.EQ.1)GOTO11
1600 IF(((I.LT.5).OR.(I.GT.7)).AND.INDEX.EQ.2)GOTO11
1610 GOTO12
1620 11 CONTINUE
1630 III=8*I
1640 II=III-7
1650 IF(I.EQ.1)PRINT105,I,(LIST(J),J=II,III),VAL(I),APT;GOTO12
1660 IF(I.EQ.3)PRINT106,I,(LIST(J),J=II,III),VAL(I),BWDTH;GOTO12
1670 IF(I.EQ.4)PRINT106,I,(LIST(J),J=II,III),VAL(I),POINT;GOTO12
1680 IF(I.EQ.10)PRINT110,I,(LIST(J),J=II,III),VAL(I),PRIDIA;GOTO12
1690 IF(I.EQ.13)PRINT111,I,(LIST(J),J=II,III),VAL(I),PRATE;GOTO12
1700 IF(I.EQ.29)PRINT112,I,(LIST(J),J=II,III),VAL(I),RGT;GOTO12
1710 IF(I.EQ.17)PRINT107,I,(LIST(J),J=II,III),VAL(I),QE;GOTO12
1720 IF(I.EQ.18)PRINT108,I,(LIST(J),J=II,III),VAL(I),RPEP;GOTO12
1730 IF(I.EQ.19)PRINT109,I,(LIST(J),J=II,III),VAL(I),BRAD;GOTO12
1740 IF(I.EQ.20)PRINT106,I,(LIST(J),J=II,III),VAL(I),EQV;GOTO12
1750 IF(I.EQ.30)PRINT108,I,(LIST(J),J=II,III),VAL(I),BPEG;GOTO12
1760 PRINT101,I,(LIST(J),J=II,III),VAL(I)
1770 IF((I.EQ.12).OR.(I.EQ.24))PRINT102
1780 12 CONTINUE
1790 IF((I.EQ.18).OR.(I.EQ.30))PRINT103
1800 3 CONTINUE
```

3.0 LINK MARGIN SUMMARIES

The link margin summaries are listed in the following pages.

```
1810 IF(IMAR.EQ.1)PRINT251
1820 251 FORMAT(T6,11HLINK MARGIN)
1830 IF(IMAR.EQ.0)PRINT252
1840 252 FORMAT(T6,'LINK MARGIN-MAX LIKELYHOOD DETECTOR')
1850 IF(IMAR.EQ.2)PRINT253,BLOOP
```

```
1860 253 FORMAT(T6,'LINK MARGIN,LOOP BANDWIDTH=',G8.3,' HERTZ')
1862 IF(IMAR.EQ.3)PRINT254,PFA,PND
1864 254 FORMAT(T6,'LINK MARGIN,PFA,PND',2G10.2)
1870 I=18
1880 III=8*I
1890 II=III-7
1900 PRINT108,I,(LIST(J),J=II,III),VAL(I),RDEP
1910 PRINT113,DROSIG,ROSIG
1920 PRINT114,DMARG,AMARG
1930 113 FORMAT(T3,'31',T6,'REQUIRED P-E/PULSE',T32,'DB',T42,F8.2,
1940&F9.2,' P-E')
1950 114 FORMAT(T3,'32',T6,'LINK MARGIN',T32,'DB',T42,F8.2,F9.2)
1960 PRINT104
1970 21 CONTINUE
1980 INPUT(1)
1990 GOTO 22
2000 101 FORMAT(T3,I2,T6,6A4,T32,2A4,T42,F8.2)
2010 105 FORMAT(T3,I2,T6,6A4,T32,2A4,T42,F8.2,3PF9.1,' MILLIWATTS')
2020 106 FORMAT(T3,I2,T6,6A4,T32,2A4,T42,F8.2,6PF9.0,' MICRORADIANS')
2030 107 FORMAT(T3,I2,T6,6A4,T32,2A4,T42,F8.2,2PF9.1,' PERCENT')
2040 108 FORMAT(T3,I2,T6,6A4,T32,2A4,T42,F8.2,F9.2,' P-E')
2050 109 FORMAT(T3,I2,T6,6A4,T32,2A4,T42,F8.2,F9.4,' WATTS/M2-A-ST')
2060 110 FORMAT(T3,I2,T6,6A4,T32,2A4,T42,F8.2,F9.2,' METERS  DIA.')
2070 111 FORMAT(T3,I2,T6,6A4,T32,2A4,T42,F8.2,F9.0,' PULSES/SEC.')
2080 112 FORMAT(T3,I2,T6,6A4,T32,2A4,T42,F8.2,9PF9.2,' NANOSECONDS')
2090 102 FORMAT(1H )
2100 103 FORMAT(/)
2110 104 FORMAT(//////)
2120 END
2200 SUBROUTINE THRESH(PFA,PND,BACK,SIG)
2210 ALPFA=ALOG(PFA)
2220 ALPND=ALOG(PND)
2230 GAM=BACK+5.6*SQRT(BACK)
2240 1 DUM=ALOG(GAM/BACK)
2250 F=GAM*(1.-DUM)-BACK-ALPFA
2260 DG=F/DUM
2270 GAM=GAM+DG
2280 IF(ABS(DG/GAM).GT.1.E-4)GOTO1
2290 SIG=GAM-BACK+5.*SQRT(GAM)
2300 2 DUM=GAM/(BACK+SIG)
2310 F=GAM-BACK-SIG-GAM*ALOG(DUM)-ALPND
2320 FD=DUM-1.
2330 DS=-F/FD
2340 SIG=SIG+DS
2350 IF(ABS(DS/SIG).GT.1.E-4)GOTO2
2360 RETURN
2370 END
```

.IATRS TO LATS(PASSIVE)
CIRCUIT MARGIN SUMMARY
OPTICAL WAVELENGTH .53 MICROMETERS,RANGE 30000. KM
PULSEWIDTH= .20 NANOSECONDS

	PARAMETER	UNITS	VALUE	
1	TRANSMITTER POWER	DBW	-20.00	10.0 MILLIWATTS
2	TRANSMITTER LOSSES	DB	-.97	
3	TRANSMIT ANTENNA GAIN	DB	121.07	5. MICRORADIANS
4	POINTING LOSS	DB	-1.39	1. MICRORADIANS
5	FREE SPACE LOSS	DB	-297.04	
6	ATMOSPHERIC LOSS(DOWN)	DB	.00	
7	TARGET GAIN PRODUCT	DB	209.00	
8	ATMOSPHERIC LOSS(UP)	DB	.00	
9	FREE SPACE LOSS	DB	-297.04	
10	RECEIVE ANTENNA GAIN	DB	131.00	.61 METERS DIA.
11	RECEIVER LOSSES	DB	-3.98	
12	RECEIVED SIGNAL POWER	DBW	-159.35	
13	TRANSMIT PULSE RATE	DB/SEC	10.00	10. PULSES/SEC.
14	ENERGY PER PULSE	DBJ	-169.35	
15	ENERGY PER PHOTON	DBJ	-184.26	
16	RECEIVED PHOTONS/PULSE	DB	14.91	
17	QUANTUM EFFICIENCY	DB	-6.02	25.0 PERCENT
18	RECEIVED P-E/PULSE	DB	8.89	7.75 P-E
19	BACKGROUND RADIANCE	DBW	-17.70	.0170 WATTS/M2-A-ST
20	RECEIVER FOV(STERRAD.)	DB	-87.07	50. MICRORADIANS
21	OPTICAL FILTER BANDWIDTH	DB	6.99	
22	RECEIVE ANTENNA AREA	DBM2	-5.51	
23	RECEIVER LOSSES	DB	-3.98	
24	RECEIVED BACK. POWER	DBW	-107.26	
25	ENERGY PER PHOTON	DBJ	-184.26	
26	RECEIVED PHOTONS/SEC	DB/SEC	77.00	
27	QUANTUM EFFICIENCY	DB	-6.02	
28	BACKGROUND P-E/SEC	DB/SEC	70.98	
29	RECEIVER GATE WIDTH	DB-SEC	-86.99	2.00 NANOSECONDS
30	BACKGROUND P-E/GATE	DB	-16.01	.03 P-E
	LINK MARGIN			
18	RECEIVED P-E/PULSE	DB	8.89	7.75 P-E
31	REQUIRED P-E/PULSE	DB	.00	1.00 P-E
32	LINK MARGIN	DB	8.89	7.75

HATRS TO GROUND(PASSIVE)
CIRCUIT MARGIN SUMMARY
OPTICAL WAVELENGTH .53 MICROMETERS,RANGE 24000. KM
PULSEWIDTH= .20 NANOSECONDS

	PARAMETER	UNITS	VALUE	
1	TRANSMITTER POWER	DBW	-20.00	10.0 MILLIWATTS
2	TRANSMITTER LOSSES	DB	-.97	
3	TRANSMIT ANTENNA GAIN	DB	121.07	5. MICRORADIANS
4	POINTING LOSS	DB	-1.39	1. MICRORADIANS
5	FREE SPACE LOSS	DB	-295.10	
6	ATMOSPHERIC LOSS(DOWN)	DB	-1.65	
7	TARGET GAIN PRODUCT	DB	210.00	
8	ATMOSPHERIC LOSS(UP)	DB	-4.66	
9	FREE SPACE LOSS	DB	-295.10	
10	RECEIVE ANTENNA GAIN	DB	131.00	.61 METERS DIA.
11	RECEIVER LOSSES	DB	-3.98	
12	RECEIVED SIGNAL POWER	DBW	-160.78	
13	TRANSMIT PULSE RATE	DB/SEC	10.00	10. PULSES/SEC.
14	ENERGY PER PULSE	DBJ	-170.78	
15	ENERGY PER PHOTON	DBJ	-184.26	
16	RECEIVED PHOTONS/PULSE	DB	13.48	
17	QUANTUM EFFICIENCY	DB	-6.02	25.0 PERCENT
18	RECEIVED P-E/PULSE	DB	7.46	5.57 P-E
19	BACKGROUND RADIANCE	DBW	-17.70	.0170 WATTS/M2-A-ST
20	RECEIVER FOV(STERRAD.)	DB	-87.07	50. MICRORADIANS
21	OPTICAL FILTER BANDWIDTH	DB	6.99	
22	RECEIVE ANTENNA AREA	DBM2	-5.51	
23	RECEIVER LOSSES	DB	-3.98	
24	RECEIVED BACK. POWER	DBW	-107.26	
25	ENERGY PER PHOTON	DBJ	-184.26	
26	RECEIVED PHOTONS/SEC	DB/SEC	77.00	
27	QUANTUM EFFICIENCY	DB	-6.02	
28	BACKGROUND P-E/SEC	DB/SEC	70.98	
29	RECEIVER GATE WIDTH	DB-SEC	-86.99	2.00 NANOSECONDS
30	BACKGROUND P-E/GATE	DB	-16.01	.03 P-E
	LINK MARGIN			
18	RECEIVED P-E/PULSE	DB	7.46	5.57 P-E
31	REQUIRED P-E/PULSE	DB	.00	1.00 P-E
32	LINK MARGIN	DB	7.46	5.57

MATRS TO LATS(PASSIVE)
CIRCUIT MARGIN SUMMARY
OPTICAL WAVELENGTH .53 MICROMETERS,RANGE 30000. KM
PULSEWIDTH=4.00 NANOSECONDS

	PARAMETER	UNITS	VALUE		
1	TRANSMITTER POWER	DBW	-10.00	100.0	MILLIWATTS
2	TRANSMITTER LOSSES	DB	-.97		
3	TRANSMIT ANTENNA GAIN	DB	121.07	5.	MICRORADIANS
4	POINTING LOSS	DB	-1.39	1.	MICRORADIANS
5	FREE SPACE LOSS	DB	-297.04		
6	ATMOSPHERIC LOSS(DOWN)	DB	.00		
7	TARGET GAIN PRODUCT	DB	209.00		
8	ATMOSPHERIC LOSS(UP)	DB	.00		
9	FREE SPACE LOSS	DB	-297.04		
10	RECEIVE ANTENNA GAIN	DB	135.30	1.00	METERS DIA.
11	RECEIVER LOSSES	DB	-3.98		
12	RECEIVED SIGNAL POWER	DBW	-145.05		
13	TRANSMIT PULSE RATE	DB/SEC	10.00	10.	PULSES/SEC.
14	ENERGY PER PULSE	DBJ	-155.05		
15	ENERGY PER PHOTON	DBJ	-184.26		
16	RECEIVED PHOTONS/PULSE	DB	29.21		
17	QUANTUM EFFICIENCY	DB	-6.02	25.0	PERCENT
18	RECEIVED P-E/PULSE	DB	23.19	208.51	P-E
19	BACKGROUND RADIANCE	DBW	-17.70	.0170	WATTS/M2-A-ST
20	RECEIVER FOV(STERRAD.)	DB	-87.07	50.	MICRORADIANS
21	OPTICAL FILTER BANDWIDTH	DB	6.99		
22	RECEIVE ANTENNA AREA	DBM2	-1.21		
23	RECEIVER LOSSES	DB	-3.98		
24	RECEIVED BACK. POWER	DBW	-102.96		
25	ENERGY PER PHOTON	DBJ	-184.26		
26	RECEIVED PHOTONS/SEC	DB/SEC	81.30		
27	QUANTUM EFFICIENCY	DB	-6.02		
28	BACKGROUND P-E/SEC	DB/SEC	75.28		
29	RECEIVER GATE WIDTH	DB-SEC	-83.01	5.00	NANOSECONDS
30	BACKGROUND P-E/GATE	DB	-7.73	.17	P-E
	LINK MARGIN				
18	RECEIVED P-E/PULSE	DB	23.19	208.51	P-E
31	REQUIRED P-E/PULSE	DB	14.77	30.00	P-E
32	LINK MARGIN	DB	8.42	6.95	

MATRS TO GROUND(PASSIVE)
CIRCUIT MARGIN SUMMARY
OPTICAL WAVELENGTH .53 MICROMETERS,RANGE 24000. KM
PULSEWIDTH=4.00 NANOSECONDS

	PARAMETER	UNITS	VALUE	
1	TRANSMITTER POWER	DBW	-10.00	100.0 MILLIWATTS
2	TRANSMITTER LOSSES	DB	-.97	
3	TRANSMIT ANTENNA GAIN	DB	121.07	5. MICRORADIANS
4	POINTING LOSS	DB	-1.39	1. MICRORADIANS
5	FREE SPACE LOSS	DB	-295.10	
6	ATMOSPHERIC LOSS(DOWN)	DB	-1.65	
7	TARGET GAIN PRODUCT	DB	210.00	
8	ATMOSPHERIC LOSS(UP)	DB	-4.66	
9	FREE SPACE LOSS	DB	-295.10	
10	RECEIVE ANTENNA GAIN	DB	135.30	1.00 METERS DIA.
11	RECEIVER LOSSES	DB	-3.98	
12	RECEIVED SIGNAL POWER	DBW	-146.48	
13	TRANSMIT PULSE RATE	DB/SEC	10.00	10. PULSES/SEC.
14	ENERGY PER PULSE	DBJ	-156.48	
15	ENERGY PER PHOTON	DBJ	-184.26	
16	RECEIVED PHOTONS/PULSE	DB	27.78	
17	QUANTUM EFFICIENCY	DB	-6.02	25.0 PERCENT
18	RECEIVED P-E/PULSE	DB	21.76	149.92 P-E
19	BACKGROUND RADIANCE	DBW	-17.70	.0170 WATTS/M2-A-ST
20	RECEIVER FOV(STERRAD.)	DB	-37.07	50. MICRORADIANS
21	OPTICAL FILTER BANDWIDTH	DB	6.99	
22	RECEIVE ANTENNA AREA	DBM2	-1.21	
23	RECEIVER LOSSES	DB	-3.98	
24	RECEIVED BACK. POWER	DBW	-102.96	
25	ENERGY PER PHOTON	DBJ	-184.26	
26	RECEIVED PHOTONS/SEC	DB/SEC	81.30	
27	QUANTUM EFFICIENCY	DB	-6.02	
28	BACKGROUND P-E/SEC	DB/SEC	75.28	
29	RECEIVER GATE WIDTH	DB-SEC	-83.01	5.00 NANOSECONDS
30	BACKGROUND P-E/GATE	DB	-7.73	.17 P-E
	LINK MARGIN			
18	RECEIVED P-E/PULSE	DB	21.76	149.92 P-E
31	REQUIRED P-E/PULSE	DB	14.77	30.00 P-E
32	LINK MARGIN	DB	6.99	5.00

SHUTTLE TO GROUND
CIRCUIT MARGIN SUMMARY
OPTICAL WAVELENGTH .53 MICROMETERS, RANGE 350. KM
PULSEWIDTH= .20 NANOSECONDS

	PARAMETER	UNITS	VALUE	
1	TRANSMITTER POWER	DBW	-30.00	1.0 MILLIWATTS
2	TRANSMITTER LOSSES	DB	-.97	
3	TRANSMIT ANTENNA GAIN	DB	83.57	375. MICRORADIANS
4	POINTING LOSS	DB	-.62	50. MICRORADIANS
5	FREE SPACE LOSS	DB	-258.38	
6	ATMOSPHERIC LOSS(DOWN)	DB	-1.65	
7	TARGET GAIN PRODUCT	DB	196.00	
8	ATMOSPHERIC LOSS(UP)	DB	-4.66	
9	FREE SPACE LOSS	DB	-258.38	
10	RECEIVE ANTENNA GAIN	DB	125.01	.30 METERS DIA.
11	RECEIVER LOSSES	DB	-3.98	
12	RECEIVED SIGNAL POWER	DBW	-154.05	
13	TRANSMIT PULSE RATE	DB/SEC	.00	1. PULSES/SEC.
14	ENERGY PER PULSE	DBJ	-154.05	
15	ENERGY PER PHOTON	DBJ	-184.26	
16	RECEIVED PHOTONS/PULSE	DB	30.21	
17	QUANTUM EFFICIENCY	DB	-6.02	25.0 PERCENT
18	RECEIVED P-E/PULSE	DB	24.19	262.24 P-E
19	BACKGROUND RADIANCE	DBW	-17.70	.0170 WATTS/M2-A-ST
20	RECEIVER FOV(STERRAD.)	DB	-69.57	375. MICRORADIANS
21	OPTICAL FILTER BANDWIDTH	DB	6.99	
22	RECEIVE ANTENNA AREA	DBM2	-11.50	
23	RECEIVER LOSSES	DB	-3.98	
24	RECEIVED BACK. POWER	DBW	-95.75	
25	ENERGY PER PHOTON	DBJ	-184.26	
26	RECEIVED PHOTONS/SEC	DB/SEC	88.51	
27	QUANTUM EFFICIENCY	DB	-6.02	
28	BACKGROUND P-E/SEC	DB/SEC	82.49	
29	RECEIVER GATE WIDTH	DB-SEC	-96.02	.25 NANOSECONDS
30	BACKGROUND P-E/GATE	DB	-13.53	.04 P-E
	LINK MARGIN-MAX LIKELYHOOD DETECTOR			
18	RECEIVED P-E/PULSE	DB	24.19	262.24 P-E
31	REQUIRED P-E/PULSE	DB	7.08	5.11 P-E
32	LINK MARGIN	DB	17.10	51.32

SHUTTLE TO GROUND
CIRCUIT MARGIN SUMMARY
OPTICAL WAVELENGTH 1.06 MICROMETERS, RANGE 350. KM
PULSEWIDTH= .20 NANOSECONDS

	PARAMETER	UNITS	VALUE	
1	TRANSMITTER POWER	DBW	-23.98	4.0 MILLIWATTS
2	TRANSMITTER LOSSES	DB	-.97	
3	TRANSMIT ANTENNA GAIN	DB	77.55	750. MICRORADIANS
4	POINTING LOSS	DB	-.15	50. MICRORADIANS
5	FREE SPACE LOSS	DB	-252.36	
6	ATMOSPHERIC LOSS(DOWN)	DB	-.56	
7	TARGET GAIN PRODUCT	DB	190.00	
8	ATMOSPHERIC LOSS(UP)	DB	-3.57	
9	FREE SPACE LOSS	DB	-252.36	
10	RECEIVE ANTENNA GAIN	DB	118.99	.30 METERS DIA.
11	RECEIVER LOSSES	DB	-3.98	
12	RECEIVED SIGNAL POWER	DBW	-151.38	
13	TRANSMIT PULSE RATE	DB/SEC	.00	1. PULSES/SEC.
14	ENERGY PER PULSE	DBJ	-151.38	
15	ENERGY PER PHOTON	DBJ	-187.27	
16	RECEIVED PHOTONS/PULSE	DB	35.89	
17	QUANTUM EFFICIENCY	DB	-20.00	1.0 PERCENT
18	RECEIVED P-E/PULSE	DB	15.89	38.82 P-E
19	BACKGROUND RADIANCE	DBW	-20.58	.0087 WATTS/M2-A-ST
20	RECEIVER FOV(STERRAD.)	DB	-63.55	750. MICRORADIANS
21	OPTICAL FILTER BANDWIDTH	DB	6.99	
22	RECEIVE ANTENNA AREA	DBM2	-11.50	
23	RECEIVER LOSSES	DB	-3.98	
24	RECEIVED BACK. POWER	DBW	-92.61	
25	ENERGY PER PHOTON	DBJ	-187.27	
26	RECEIVED PHOTONS/SEC	DB/SEC	94.66	
27	QUANTUM EFFICIENCY	DB	-20.00	
28	BACKGROUND P-E/SEC	DB/SEC	74.66	
29	RECEIVER GATE WIDTH	DB-SEC	-96.02	.25 NANOSECONDS
30	BACKGROUND P-E/GATE	DB	-21.36	.01 P-E
	LINK MARGIN-MAX LIKELYHOOD DETECTOR			
18	RECEIVED P-E/PULSE	DB	15.89	38.82 P-E
31	REQUIRED P-E/PULSE	DB	7.05	5.07 P-E
32	LINK MARGIN	DB	8.84	7.65

SHUTTLE TO GROUND
CIRCUIT MARGIN SUMMARY
OPTICAL WAVELENGTH .53 MICROMETERS, RANGE 350. KM
PULSEWIDTH=4.00 NANOSECONDS

	PARAMETER	UNITS	VALUE		
1	TRANSMITTER POWER	DBW	-20.00	10.0	MILLIWATTS
2	TRANSMITTER LOSSES	DB	-.97		
3	TRANSMIT ANTENNA GAIN	DB	83.57	375.	MICRORADIANS
4	POINTING LOSS	DB	-.62	50.	MICRORADIANS
5	FREE SPACE LOSS	DB	-258.38		
6	ATMOSPHERIC LOSS(DOWN)	DB	-1.65		
7	TARGET GAIN PRODUCT	DB	196.00		
8	ATMOSPHERIC LOSS(UP)	DB	-4.66		
9	FREE SPACE LOSS	DB	-258.38		
10	RECEIVE ANTENNA GAIN	DB	128.53	.46	METERS DIA.
11	RECEIVER LOSSES	DB	-3.98		
12	RECEIVED SIGNAL POWER	DBW	-140.53		
13	TRANSMIT PULSE RATE	DB/SEC	.00	1.	PULSES/SEC.
14	ENERGY PER PULSE	DBJ	-140.53		
15	ENERGY PER PHOTON	DBJ	-184.26		
16	RECEIVED PHOTONS/PULSE	DB	43.73		
17	QUANTUM EFFICIENCY	DB	-6.02	25.0	PERCENT
18	RECEIVED P-E/PULSE	DB	37.71	5900.40	P-E
19	BACKGROUND RADIANCE	DBW	-17.70	.0170	WATTS/M2-A-ST
20	RECEIVER FOV(STERRAD.)	DB	-69.57	375.	MICRORADIANS
21	OPTICAL FILTER BANDWIDTH	DB	6.99		
22	RECEIVE ANTENNA AREA	DBM2	-7.98		
23	RECEIVER LOSSES	DB	-3.98		
24	RECEIVED BACK. POWER	DBW	-92.23		
25	ENERGY PER PHOTON	DBJ	-184.26		
26	RECEIVED PHOTONS/SEC	DB/SEC	92.03		
27	QUANTUM EFFICIENCY	DB	-6.02		
28	BACKGROUND P-E/SEC	DB/SEC	86.01		
29	RECEIVER GATE WIDTH	DB-SEC	-83.01	5.00	NANOSECONDS
30	BACKGROUND P-E/GATE	DB	3.00	2.00	P-E
	LINK MARGIN-MAX LIKELYHOOD DETECTOR				
18	RECEIVED P-E/PULSE	DB	37.71	5900.40	P-E
31	REQUIRED P-E/PULSE	DB	22.66	184.36	P-E
32	LINK MARGIN	DB	15.05	32.00	

SHUTTLE TO GROUND
CIRCUIT MARGIN SUMMARY
OPTICAL WAVELENGTH 1.06 MICROMETERS, RANGE 350. KM
PULSEWIDTH=4.00 NANOSECONDS

	PARAMETER	UNITS	VALUE		
1	TRANSMITTER POWER	DBW	-13.98	40.0	MILLIWATTS
2	TRANSMITTER LOSSES	DB	-.97		
3	TRANSMIT ANTENNA GAIN	DB	77.55	750.	MICRORADIANS
4	POINTING LOSS	DB	-.15	50.	MICRORADIANS
5	FREE SPACE LOSS	DB	-252.36		
6	ATMOSPHERIC LOSS(DOWN)	DB	-.56		
7	TARGET GAIN PRODUCT	DB	190.00		
8	ATMOSPHERIC LOSS(UP)	DB	-3.57		
9	FREE SPACE LOSS	DB	-252.36		
10	RECEIVE ANTENNA GAIN	DB	122.51	.46	METERS DIA.
11	RECEIVER LOSSES	DB	-3.98		
12	RECEIVED SIGNAL POWER	DBW	-137.86		
13	TRANSMIT PULSE RATE	DB/SEC	.00	1.	PULSES/SEC.
14	ENERGY PER PULSE	DBJ	-137.86		
15	ENERGY PER PHOTON	DBJ	-187.27		
16	RECEIVED PHOTONS/PULSE	DB	49.41		
17	QUANTUM EFFICIENCY	DB	-20.00	1.0	PERCENT
18	RECEIVED P-E/PULSE	DB	29.41	873.46	P-E
19	BACKGROUND RADIANCE	DBW	-20.58	.0087	WATTS/M2-A-ST
20	RECEIVER FOV(STERRAD.)	DB	-63.55	750.	MICRORADIANS
21	OPTICAL FILTER BANDWIDTH	DB	6.99		
22	RECEIVE ANTENNA AREA	DBM2	-7.98		
23	RECEIVER LOSSES	DB	-3.98		
24	RECEIVED BACK. POWER	DBW	-89.09		
25	ENERGY PER PHOTON	DBJ	-187.27		
26	RECEIVED PHOTONS/SEC	DB/SEC	98.18		
27	QUANTUM EFFICIENCY	DB	-20.00		
28	BACKGROUND P-E/SEC	DB/SEC	78.18		
29	RECEIVER GATE WIDTH	DB-SEC	-83.01	5.00	NANOSECONDS
30	BACKGROUND P-E/GATE	DB	-4.83	.33	P-E
	LINK MARGIN-MAX LIKELYHOOD DETECTOR				
18	RECEIVED P-E/PULSE	DB	29.41	873.46	P-E
31	REQUIRED P-E/PULSE	DB	22.62	182.72	P-E
32	LINK MARGIN	DB	6.79	4.73	

GROUND BEACON TO SHUTTLE
CIRCUIT MARGIN SUMMARY
OPTICAL WAVELENGTH .88 MICROMETERS, RANGE 564. KM
PULSEWIDTH=5.00 NANOSECONDS

	PARAMETER	UNITS	VALUE	
1	TRANSMITTER POWER	DBW	-33.01	.5 MILLIWATTS
2	TRANSMITTER LOSSES	DB	-.97	
3	TRANSMIT ANTENNA GAIN	DB	69.03	2000. MICRORADIANS
4	POINTING LOSS	DB	-2.17	500. MICRORADIANS
8	ATMOSPHERIC LOSS(UP)	DB	-3.01	
9	FREE SPACE LOSS	DB	-259.12	
10	RECEIVE ANTENNA GAIN	DB	120.61	.30 METERS DIA.
11	RECEIVER LOSSES	DB	-3.93	
12	RECEIVED SIGNAL POWER	DBW	-111.62	
13	TRANSMIT PULSE RATE	DB/SEC	50.00	100000. PULSES/SEC.
14	ENERGY PER PULSE	DBJ	-161.62	
15	ENERGY PER PHOTON	DBJ	-186.46	
16	RECEIVED PHOTONS/PULSE	DB	24.84	
17	QUANTUM EFFICIENCY	DB	-16.99	2.0 PERCENT
18	RECEIVED P-E/PULSE	DB	7.85	6.10 P-E
19	BACKGROUND RADIANCE	DBW	-20.00	.0100 WATTS/M2-A-ST
20	RECEIVER FOV(STERRAD.)	DB	-55.03	2000. MICRORADIANS
21	OPTICAL FILTER BANDWIDTH	DB	13.98	
22	RECEIVE ANTENNA AREA	DBM2	-11.50	
23	RECEIVER LOSSES	DB	-3.98	
24	RECEIVED BACK. POWER	DBW	-76.53	
25	ENERGY PER PHOTON	DBJ	-186.46	
26	RECEIVED PHOTONS/SEC	DB/SEC	109.94	
27	QUANTUM EFFICIENCY	DB	-16.99	
28	BACKGROUND P-E/SEC	DB/SEC	92.95	
29	RECEIVER GATE WIDTH	DB-SEC	-80.00	10.00 NANOSECONDS
30	BACKGROUND P-E/GATE	DB	12.95	19.72 P-E
	LINK MARGIN, LOOP BANDWIDTH=100.		HERTZ	
18	RECEIVED P-E/PULSE	DB	7.85	6.10 P-E
31	REQUIRED P-E/PULSE	DB	-3.48	.45 P-E
32	LINK MARGIN	DB	11.33	13.57

GROUND BEACON TO SHUTTLE
CIRCUIT MARGIN SUMMARY
OPTICAL WAVELENGTH .69 MICROMETERS, RANGE 564. KM
PULSEWIDTH=5.00 NANOSECONDS

	PARAMETER	UNITS	VALUE		
1	TRANSMITTER POWER	DBW	-30.00	1.0	MILLIWATTS
2	TRANSMITTER LOSSES	DB	-.97		
3	TRANSMIT ANTENNA GAIN	DB	44.17	35000.	MICRORADIANS
4	POINTING LOSS	DB	-.71	5000.	MICRORADIANS
8	ATMOSPHERIC LOSS(UP)	DB	-3.01		
9	FREE SPACE LOSS	DB	-260.18		
10	RECEIVE ANTENNA GAIN	DB	122.66	.30	METERS DIA.
11	RECEIVER LOSSES	DB	-3.98		
12	RECEIVED SIGNAL POWER	DBW	-132.01		
13	TRANSMIT PULSE RATE	DB/SEC	10.00	10.	PULSES/SEC.
14	ENERGY PER PULSE	DBJ	-142.01		
15	ENERGY PER PHOTON	DBJ	-185.43		
16	RECEIVED PHOTONS/PULSE	DB	43.42		
17	QUANTUM EFFICIENCY	DB	-10.00	10.0	PERCENT
18	RECEIVED P-E/PULSE	DB	33.42	2199.34	P-E
19	BACKGROUND RADIANCE	DBW	-17.70	.0170	WATTS/M2-A-ST
20	RECEIVER FOV(STERRAD.)	DB	-55.03	3000.	MICRORADIANS
21	OPTICAL FILTER BANDWIDTH	DB	13.98		
22	RECEIVE ANTENNA AREA	DBM2	-11.50		
23	RECEIVER LOSSES	DB	-3.98		
24	RECEIVED BACK. POWER	DBW	-74.22		
25	ENERGY PER PHOTON	DBJ	-185.43		
26	RECEIVED PHOTONS/SEC	DB/SEC	111.21		
27	QUANTUM EFFICIENCY	DB	-10.00		
28	BACKGROUND P-E/SEC	DB/SEC	101.21		
29	RECEIVER GATE WIDTH	DB-SEC	-80.00	10.00	NANOSECONDS
30	BACKGROUND P-E/GATE	DB	21.21	132.25	P-E

	LINK MARGIN, PFA, PND	.10E-07	.10E-05	
18	RECEIVED P-E/PULSE	DB	33.42	2199.34 P-E
31	REQUIRED P-E/PULSE	DB	22.07	160.98 P-E
32	LINK MARGIN	DB	11.36	13.66

APPENDIX E

PRECISE OPTICAL PULSE TIMING

1.0 INTRODUCTION

The data in this Appendix presents fundamental results of investigations into optimal range estimation techniques, and was partially funded under this study. This material was presented in IEEE Southeastcon '75, in April, 1975, and published in the proceedings. The reprint is included in this Appendix for completeness.

PRECISE OPTICAL PULSE TIMING*

by Gary Lee and George Schroeder†

McDonnell-Douglas Astronautics Company

St. Louis, Missouri

ABSTRACT

This paper evaluates the performance of the ML and several sub-optimum arrival time estimators for optical pulses. The performance analysis of a "sliding window" counter followed by a threshold detector is achieved by deriving an expression for the first crossing density of the output of the counter. A sub-optimum arrival time estimator using a threshold rather than a maximum detector is suggested and evaluated by simulation. It appears to provide near optimum performance.

INTRODUCTION

Lasers permit the use of very narrow pulse widths for both communication and ranging. The combination of very narrow pulses and narrow beamwidths offers the promise of heretofore unachievable efficiencies in terms of the power required to achieve a given data rate or ranging accuracy.

Pulse position modulation allows the conversion of precise pulse arrival time resolution into high data rates with minimal transmitted power per pulse. If reasonable data rates are to be achieved, it is necessary that the pulse detection technique not be so complex that it limits the rate at which pulses can be detected. Thus it is desired to achieve the best possible pulse resolution without limiting the usable pulse rate. The number of received signal photoelectrons per pulse will always be small (i.e. on the order of 50 or less) so that analyses of achievable pulse resolution with non-coherent detection depend on the properties of non-stationary Poisson processes.

Ranging requires lower pulse rates than communication and thus may, depending on the application, use more complex pulse detection techniques. Some programs (such as the NASA EOPAP program) require satellite borne ranging systems with very precise (centimeter) range resolution. These systems must be small, light and reliable but yet capable of less than a hundred picosecond pulse arrival time resolution with only a few received signal photoelectrons per pulse.

This paper defines achievable optical pulse resolution as a function of the pulse shape, received signal and background power, and the pulse detection technique. Optimum (maximum likelihood) detectors, simple counters and weighted counters are evaluated both analytically and by simulation. A novel approximate solution for the first crossing density of the output of a "finite window" counter or integrator is used to define both false alarm rates and pulse resolution properties for the "finite window" counter case.

ANALYSES

It is desired to determine the achievable pulse arrival time resolution for a single 200 picosecond optical pulse. Two hundred picoseconds is about the minimum presently achievable pulse width from a Nd:YAG laser. Since non-coherent detection must be used, the output of the optical detector will be assumed to be a non-stationary Poisson process. Thus the output of the optical detector consists of a Poisson process whose mean rate $\lambda(t, \alpha)$ is given by

$$\lambda(t, \alpha) = S(t, \alpha) + n_b \tag{1}$$

where $S(t, \alpha)$ represents the contribution of the signal pulse and n_b represents the uniform background level. α is the unknown pulse arrival time and $[0, T_{max}]$ is the total observation interval.

Hoversten et al [1, 2] obtained a partial differential equation for the conditional density of α using non-linear filter theory. These results, although useful for developing insight into optimal estimator structures, are not directly implementable into hardware without a considerable number of approximations.

Bar-David [3] derived an expression for the maximum likelihood estimate of α conditioned upon the observations obtained during a fixed observation interval. Let $\{t_1, t_2, \ldots t_m\} = \{T_M\}$ be the set of observed photoelectron arrival times. Bar-David showed that the probability of $\{T_M\}$, given α, is

$$P\{T_M\} = \exp[-Q(\alpha)] \prod_{j=1}^{M} \lambda(t_j, \alpha) \tag{2}$$

where

$$Q(\alpha) = \int_0^{T_{max}} \lambda(t, \alpha)\, dt$$

The maximum likelihood estimate of α is the value which maximizes the value of $P\{T_M\}$ or equivalently $\log P\{T_M\}$. Bar-David also determined the following approximate expression for the variance, $\overline{\varepsilon_\alpha^2}$, of the estimate of α for the special case of $S(t,\alpha)$ everywhere differentiable and $S(t, -T/2) = S(t) = 0$ for $|t| \geq T/2$.

$$\overline{\varepsilon_\alpha^2} = \left[\int_{-T/2}^{T/2} \frac{[\dot{S}(t)]^2}{S(t) + n_b}\, dt \right]^{-1} \tag{3}$$

Figure 1 shows a block diagram for generating $\log P\{T_M\}$ and the ML (maximum likelihood) estimates of α. It is probably possible to implement the ML detector digitally for the case where the average number of received photoelectrons per pulse is small, say less than 20. This could be accomplished by detecting the arrival time of individual photoelectrons (i.e. $\{t_1, t_2, \ldots t_m\}$), digitizing the arrival times, and using a computer to determine the value of α which maximizes $P\{T_M\}$. Individual arrival times can be resolved as close as 5 picoseconds using an optical detector with an image converter. An image converter is a rather complex device which first uses a cathode ray tube face to map and store an image of a received pulse. The tube face is then scanned and the output is sampled and A/D converted with a spatial sampling rate which corresponds to a 5 picosecond sampling rate across the original pulse. The tube has sufficient gain to detect the arrival of an individual photon within a resolution element. Note that this approach for implementing the ML detector is neither simple nor

†George Schroeder is also with the Department of Engineering, Southern Illinois University at Edwardsville.

*This work was partially supported by NAS5-20646.

capable of being performed rapidly enough not to be the limiting factor in determining data rate for an optical PPM communication system.

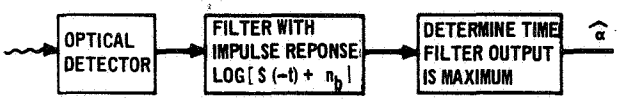

FIGURE 1 MAXIMUM LIKELIHOOD ESTIMATOR

Analog maximum detectors, though conceptually simple, are seldom practical. The basic approach is to first differentiate the signal representing log $P\{T_M\}$ and then use a threshold detector to determine when the derivative passes through zero. The value of the signal and the time of occurrence of these relative extrema are sampled and stored so that the time of the absolute maximum can be determined at the end of the measurement period. Note that for a small number of photoelectrons per pulse there will be several relative maxima per pulse. Thus the sampler must be capable of taking samples on the order of a few picoseconds apart in order that the detector look like an "ideal" maximum detector. This, if possible at all, would be very difficult.

The preceding discussion has been mainly concerned with the practical difficulties involved in building maximum detectors. Another area of difficulty with the ML detector is the uncertainty in knowledge of S(t). Laser amplitude instability and multi-path (for the ranging case) limit the ability of the receiver designer to specify S(t). Note also that even if S(t) is known exactly it may be very difficult to build a filter with several gigahertz bandwidth and an impulse response matched to log $[S(t) + n_b]$.

Thus, in summary, although it is probably possible to implement the ML detector at some cost in size, weight, and pulse rate, it is clear that this should only be attempted if the achievable gain in resolution of the ML detector over other simpler approaches is substantial. The goal of this paper is to define this gain so that the tradeoff can be made by each designer for his own application.

EFFECTS OF FILTER MISMATCH

First, the effect on resolution of mismatch between the signal and the filter response in the ML estimator will be determined. This is accomplished by deriving an approximate expression for the variance in the estimate of α assuming the filter response is designed for a signal S' (t) when, in fact, the signal is S(t). Since a signal pulse shape of S' (t) is used in the filter design

$$r(t) = \log [S'(t) + n_b] \tag{4}$$

and

$$F(\alpha) = \sum_j r(t_j - \alpha) \tag{5}$$

$F(\alpha)$ is the input to the maximum detector and the t_j's are the times of occurrence of the received photoelectrons. Proceeding in a manner similar to Bar-David, an approximation to the variance of the estimate is obtained.

Expanding $\dot{F}(\alpha)$ about the actual delay, α_0, and using the definition of $\hat{\alpha}$

$$\dot{F}(\hat{\alpha}) = 0 = \dot{F}(\alpha_0) + (\hat{\alpha} - \alpha_0)\,\ddot{F}(\alpha_0) + \ldots \tag{6}$$

This yields

$$\varepsilon_{\alpha x} = \alpha_0 - \hat{\alpha} \doteq \frac{\dot{F}(\alpha_0)}{\ddot{F}(\alpha_0)} \tag{7}$$

Thus

$$\overline{\varepsilon_\alpha^2} \doteq \frac{E\{[\dot{F}(\alpha_0)]^2\}}{[E\{\ddot{F}(\alpha_0)\}]^2} \tag{8}$$

where E (•) represents the expectation with respect to the time and number of occurrences in the input process. The characteristic functions of $\dot{F}(\alpha_0)$ and $\ddot{F}(\alpha_0)$ are found using the expectation of product functions with $\lambda(t) = S(t - \alpha) + n_b$

$$E\{\exp [ix\dot{F}(\alpha)]\} = E\{\exp [-ix \sum_j \dot{r}(t_j - \alpha)]\} = E\{\prod_j \exp [-ix\,\dot{r}(t_j - \alpha)]\} \tag{9}$$

This expectation can be evaluated in terms of

$$G = \int_0^{T_{max}} [S(t - \alpha_0) + n_b] \exp [-ix\dot{r}(t - \alpha_0)]\,dt \tag{10}$$

and

$$Q = \int_0^{T_{max}} \lambda(t)dt \tag{11}$$

Neglecting end effects, let, $\alpha_0 = T_{max}/2$. Then, with $\tau = t - T_{max}/2$

$$G = \int_{-\frac{T_{max}}{2}}^{\frac{T_{max}}{2}} [S(\tau) + n_b] \exp [-ix\dot{r}(\tau)]d\tau \tag{12}$$

and

$$Q = \int_{-\frac{T_{max}}{2}}^{\frac{T_{max}}{2}} [S(\tau) + n_b]d\tau \tag{13}$$

It can be shown that

$$E\{\exp [ix\dot{F}(\alpha)]\} = \exp (-Q + G) = \exp\left\{-Q + \int_{-\frac{T_{max}}{2}}^{\frac{T_{max}}{2}} [S(\tau) + \lambda_n] \exp [-ix\dot{r}(\tau)]d\tau\right\} \tag{14}$$

In the same manner, letting

$$G = \int_{-\frac{T_{max}}{2}}^{\frac{T_{max}}{2}} [S(\tau) + n_b] \exp [ix\,\ddot{r}(\tau)]d\tau$$

$$E\{\exp[ix\ddot{F}(\alpha)]\} = \exp(-Q + G) = \exp\left\{-Q + \int_{-\frac{T_{max}}{2}}^{\frac{T_{max}}{2}} [S(\tau) + n_b] \exp [ix\ddot{r}(\tau)]d\tau\right\} \tag{15}$$

Using these results

$$\overline{\varepsilon_\alpha^2} \doteq \frac{\left[\left\{\int_{-\frac{T_{max}}{2}}^{\frac{T_{max}}{2}} [S(\tau)+n_b]\dot{r}(\tau)d\tau\right\}^2 + \int_{-\frac{T_{max}}{2}}^{\frac{T_{max}}{2}} [S(\tau)+n_b][\dot{r}(\tau)]^2 d\tau\right]}{\left\{\int_{-\frac{T_{max}}{2}}^{\frac{T_{max}}{2}} [S(\tau)+n_b]\ddot{r}(\tau)d\tau\right\}^2} \quad (16)$$

Assuming that

$$r\left(\pm\frac{T_{max}}{2}\right) = \dot{r}\left(\pm\frac{T_{max}}{2}\right) = 0$$

$$\overline{\varepsilon_\alpha^2} = \frac{\left[\int_{-\frac{T_{max}}{2}}^{\frac{T_{max}}{2}} r(\tau)\dot{S}(\tau)d\tau\right]^2 + \int_{-\frac{T_{max}}{2}}^{\frac{T_{max}}{2}} [S(\tau)+n_b][\dot{r}(\tau)]^2 d\tau}{\left[\int_{-\frac{T_{max}}{2}}^{\frac{T_{max}}{2}} \dot{r}(\tau)\dot{S}(\tau)d\tau\right]^2} \quad (17)$$

and if $\dot{r}(\tau) = 0$ for $|\tau| > T/2$ the limits in the integrals of (17) can be replaced with $\pm T/2$.

SLIDING WINDOW COUNTER

By replacing the maximum detector with a threshold and the matched filter with a "sliding window" integrator or counter, a simple analog detection system is obtained (see Figure 2). This system estimates arrival time by observing the number of photoelectrons received during the previous T seconds and thresholding this value. Determination of the timing resolution of this system is not simple since it requires the calculation of the "first crossing" density of the output of a "finite window" counter. To the best of the authors knowledge, there are no other results for this problem (either exact or approximate).

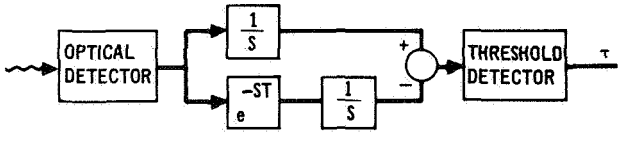

FIGURE 2 "SLIDING WINDOW" COUNTER ESTIMATOR

Lee and Fogle [4] obtained an expression for the "first crossing" density of a random process in terms of a function a(t) somewhat analogous to the infinitesimal transition probability for Markov processes. Appendix A summarizes this development and shows how a(t) can be approximated for a Poisson process and a "finite window" counter. Note that the optimum threshold value is determined by numerical optimization.

To calculate the variance in threshold crossing time, it is necessary to determine the probability density function, p(t), of the time of the first threshold crossing τ. From Appendix A,

$$p(t) = a(t)\exp\left[-\int_0^t a(x)dx\right] \quad (18)$$

where

$$a(t) = \lim_{\Delta\to 0}\frac{1}{\Delta}\text{Prob.}\{\text{crossing in } (t, t+\Delta) \mid \text{no crossing before } t\}$$

a(t) can be approximated by

$$a(t) \doteq \lambda(t,\alpha)\frac{(\overline{nT})^{L-1}}{(L-1)!}\left[\sum_{k=0}^{L-1}\frac{(\overline{nT})^k}{k!}\right]^{-1} \quad (19)$$

where L is the threshold and

$$\overline{nT} = \int_{t-T}^{t}\lambda(x,\alpha)dx \quad (20)$$

For the problem under consideration

$$\lambda(t,\alpha) = \begin{cases} n_b & 0 < t < \alpha - T/2 \\ n_b + S(t-\alpha) & \alpha - T/2 < t < \alpha + T/2 \\ n_b & \alpha + T/2 < t \end{cases} \quad (21)$$

And, ignoring end effects for $0 < t < T$

$$\overline{nT} = \begin{cases} n_bT & 0 < t < \alpha - T/2 \\ n_bT + \int_{-T/2}^{t-\alpha} S(x)dx & \alpha - T/2 < t < \alpha + T/2 \\ n_bT + \int_{t-\alpha-T}^{T/2} S(x)dx & \alpha + T/2 < t < \alpha + 3T/2 \\ n_bT & \alpha + 3T/2 < t \end{cases} \quad (22)$$

With a finite observation interval there is a non-zero probability of no threshold crossing. Therefore, for comparison purpose we determine the mean square error given that there has been a threshold crossing in $(0, T_{max})$.

$$\text{Prob}\{\tau < t \mid \tau < T_{max}\} = \frac{\text{Prob.}\{(\tau < t)\cap(\tau < T_{max})\}}{\text{Prob.}\{\tau < T_{max}\}}$$

$$= \begin{cases} \dfrac{\text{Prob.}\{\tau < t\}}{\text{Prob.}\{\tau < T_{max}\}} & t < T_{max} \\ 1 & t > T_{max} \end{cases} \quad (23)$$

Thus the conditional density used in finding the expected values given a threshold crossing before T_{max} is

$$p_{T_{max}}(t) = \begin{cases} \dfrac{p(t)}{\text{Prob.}\{\tau < T_{max}\}} & t < T_{max} \\ 0 & t > T_{max} \end{cases} \quad (24)$$

Thus the mean threshold crossing time, given there has been a crossing before T_{max}, is

$$E(\tau) \doteq \frac{1}{\text{Prob}\{\tau < T_{max}\}} \int_0^{T_{max}} t a(t) \exp\left[-\int_0^t a(x)dx\right] dt \quad (25)$$

and the mean square value of crossing time is

$$E(\tau^2) \doteq \frac{1}{\text{Prob}\{\tau < T_{max}\}} \int_0^{T_{max}} t^2 a(t) \exp\left[-\int_0^t a(x)dx\right] dt \quad (26)$$

Integrating (25) and (26) by parts

$$E(\tau) \doteq \frac{1}{\text{Prob}\{\tau < T_{max}\}} \left\{ -T_{max} \exp\left[-\int_0^{T_{max}} a(x)dx\right] + \int_0^{T_{max}} \exp\left[-\int_0^t a(x)dx\right] dt \right\} \quad (27)$$

and

$$E(\tau^2) \doteq \frac{1}{\text{Prob}\{\tau < T_{max}\}} \left\{ -T_{max}^2 \exp\left[-\int_0^{T_{max}} a(x)dx\right] + 2\int_0^{T_{max}} t \exp\left[-\int_0^t a(x)dx\right] dt \right\} \quad (28)$$

where

$$\text{Prob}\{\tau < T_{max}\} \doteq \int_0^{T_{max}} a(t) \exp\left[-\int_0^t a(x)dx\right] dt = 1 - \exp\left[-\int_0^{T_{max}} a(x)dx\right] \quad (29)$$

Note that by replacing T_{max} with the time the signal pulse begins one obtains the probability of an early detection. $\overline{\varepsilon_\alpha^2}$ can easily be obtained from equation (27) — (29).

COMPARISON OF ESTIMATION TECHNIQUES

Comparing the optimum (ML) arrival time estimator shown in Figure 1 with the more practical estimator configuration shown in Figure 2, two differences become obvious. The first difference is that the ML estimator uses a filter that is in some sense matched to the signal and background conditions whereas the "sliding window" counter configuration does not. The other difference is that the ML estimator requires a maximum detector where as the "sliding window" counter uses only a simple threshold detector.

The variance in arrival time estimation will now be computed assuming a raised cosine optical pulse shape. Note that this pulse shape was chosen in order to meet the conditions on S(t) required to derive equation (3). It is not required for evaluating variance for the "sliding window" counter.

$$S(t) = \begin{cases} \frac{n_s}{T}\left(1 + \cos\frac{2\pi}{T}t\right) & |t| < T/2 \\ 0 & |t| > T/2 \end{cases} \quad (30)$$

n_s is the mean number of received signal photoelectrons per p From (3) the mean square timing error using the ML estima:

$$\overline{\varepsilon_\alpha^2} \doteq \frac{T^2}{4\pi^2 \left[n_s + n_b T - \sqrt{n_b T (2 n_s + n_b T)}\right]} \quad (31)$$

To develop an intuitive feeling for how much of the performance difference between the "sliding window" counter and the ML estimator is due to the difference between a threshold and maximum detector and how much is due to mismatch between the integrator impulse response and the pulse shape, the performance of a mismatched ML estimator was also evaluated. Figure 3 compares the rms error for the ML estimator configuration just evaluated

$$r(t) = \log\left[\left(1 + \cos\frac{2\pi}{T}t\right)\frac{n_s}{T} + n_b\right] \text{ and } S(t) = \frac{n_s}{T}\left(1 + \cos\frac{2\pi}{T}t\right)$$

with the rms error for a mismatched ML estimator configuration with

$$r(t) = \left[1 + \cos\frac{2\pi}{T}t\right] \text{ and } S(t) = \frac{n_s}{T}\left(1 + \cos\frac{2\pi}{T}t\right)$$

The rms error for the latter case using equation (17) is given by

$$\overline{\varepsilon_\alpha^2} = \frac{n_s + n_b T}{2\pi^2 n_s^2} T^2 \quad (32)$$

Figure (3) also shows some computer simulation points for the mismatched case. The simulation is discussed later.

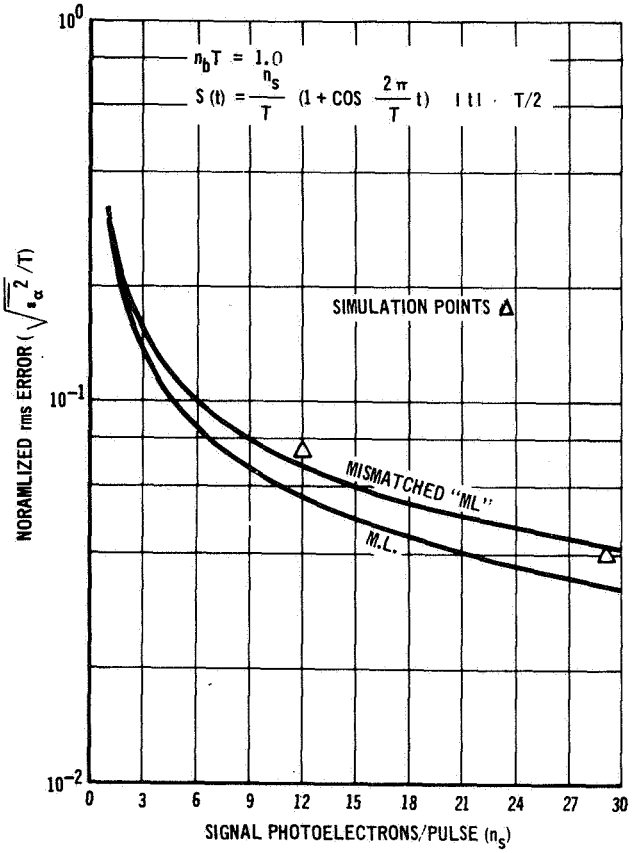

FIGURE 3

Note that for this particular case mismatch does not cause much degradation from the optimum.

The "sliding window" counter and ML estimator will now be compared.

For the sliding window counter and a raised cosine pulse shape,

$$\lambda(t,\alpha) = \begin{cases} n_b & 0 < t < \alpha - T/2 \\ n_b + \frac{n_s}{T}\left[1+\cos\frac{2\pi}{T}(t-\alpha)\right] & \alpha - T/2 < t < \alpha + T/2 \\ n_b & \alpha + T/2 < t \end{cases} \quad (33)$$

and

$$\overline{nT} = \begin{cases} n_b T & 0 < t < \alpha - T/2 \\ n_b T + n_s\left[\frac{1}{2} + \frac{t-\alpha}{T} + \frac{1}{2\pi}\sin\left(2\pi\frac{t-\alpha}{T}\right)\right] & \alpha - T/2 < t < \alpha + T/2 \\ n_b T + n_s\left[\frac{3}{2} - \frac{t-\alpha}{T} - \frac{1}{2\pi}\sin\left(2\pi\frac{t-\alpha}{T}\right)\right] & \alpha + T/2 < t < \alpha + 3T/2 \\ n_b T & \alpha + 3T/2 < t \end{cases} \quad (34)$$

Thus, equations (27) and (28) can now be evaluated numerically using equations (19), (29), (33), and (34).

Figure (4) compares the rms error in estimating arrival time (normalized by the pulse width) for the ML estimator and the "sliding window" counter for a background level of 0.1 and 1.0 photoelectrons per pulse width. Note that the ML estimator is roughly a factor of 2 superior to the counter in resolution. This corresponds to an extra 6 dB of required laser power which is definitely significant.

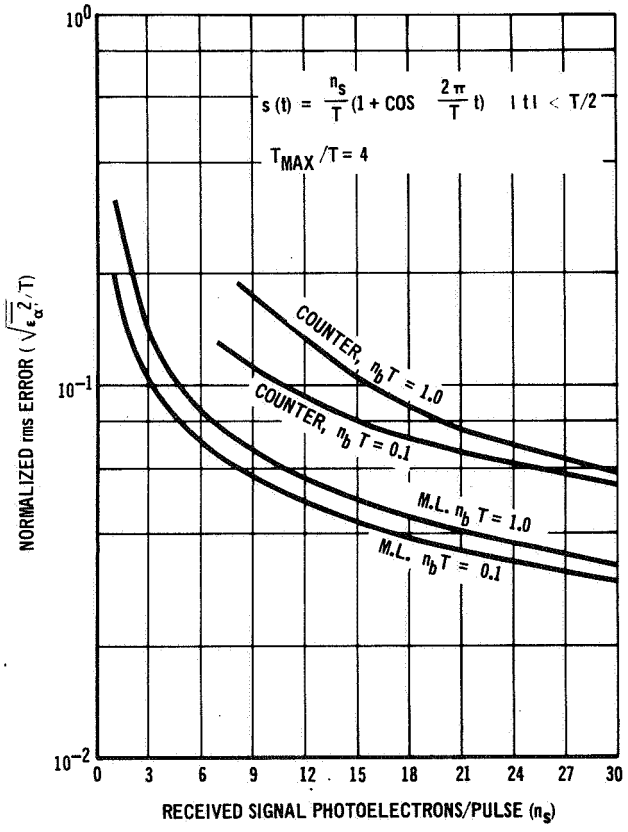

FIGURE 4 COMPARISON OF M.L. AND "SLIDING WINDOW" COUNTER ESTIMATORS

Based on a previous result for threshold detection [5], the optimum ranging threshold level for the counter is expected to be approximately given by

$$L' = \mathrm{InT}\left[\frac{n_s - n_b T + \log(T_{max}/T)}{\log(n_s/n_b T)}\right] \quad (35)$$

where InT(x) is the smallest integer greater than or equal to x.

Figure (5) compares L' with the optimum threshold determined numerically using equations (27) and (28). Note that L' appears to be a good approximation for the optimum threshold.

VALIDATION BY SIMULATION

Since the derivation of both the expressions for resolution of the ML estimator and the "sliding window" counter contain approximations, a computer simulation was performed to verify the analytical results.

The first step in the simulation is to generate the sequence of photoelectron arrival times. This is done by first dividing the pulse width, T, into 500 intervals each of width $\Delta = T/500$. The probability of receiving n photoelectrons in an interval centered about time t is approximately

n_s	$n_bT = 0.1$		$n_bT = 1.0$	
	L'	L_T	L'	L_T
8	3	3	5	7
9	3	3	5	7
10	3	3	5	7
11	3	3	5	7
12	3	4	5	7
13	3	4	6	7
14	4	4	6	7
15	4	4	6	7
16	4	4	6	8
17	4	4	7	8
18	4	4	7	8
19	4	4	7	8
20	5	4	7	8
21	5	4	8	8
22	5	4	8	8
23	5	4	8	8
24	5	5	8	8
25	5	5	8	9
26	5	5	9	9
27	6	5	9	9
28	6	5	9	9
29	6	5	9	9
30	6	5	9	9

FIGURE 5 COMPARISON OF EXACT AND APPROXIMATE THRESHOLDS

$$P(n) = \exp[-\Delta\lambda(t)] \cdot [\Delta\lambda(t)]^n/n! \quad (36)$$

(The approximation is due to the fact that $\lambda(t)$ is not constant over Δ.) For each interval a uniform random number, X, is

A value n is then determined such that $\sum_{j=0}^{n-1} P(j) \le X < \sum_{j=0}^{n} P(j)$

n is then the number of photoelectrons received in the interval. For our case with $\Delta = T/500$, n is never greater than 2 and is usually 1 or 0. When n = 2 occurs it is treated as a single occurrence of double strength.

The signal pulse is centered in an interval of length 4T. Since the effect of false alarms or anomalous errors on rms timing error is not considered in the analysis of the ML estimator performance, it

was desired to eliminate the effect of these errors on rms timing error of the "sliding window" counter so that a direct comparison could be made. The choice of $T_{max} = 4T$ was a compromise between minimizing these errors and eliminating end effects.

In the simulation of the "sliding window" counter, the number of photoelectrons received over the last T seconds are added and when the sum exceeds a set threshold, the threshold crossing time is used as an estimate of the pulse delay. To save computer time, several thresholds are considered simultaneously, and when the highest has been exceeded the generation of a new process is started. The minimum value of $\left(\sqrt{\overline{\epsilon_\alpha^2}}\right)/T$ from the values obtained for the different thresholds is plotted.

The ML estimator applies a weighting function obtained from the desired filter response, sums the values obtained, and selects the time of the absolute maximum of this sum as the estimate of the delay. The weighting function corresponds to a filter matched to log $[S(t) + n_b]$.

Figure (6) compares the simulation and analytical results for rms timing error for both the ML and "sliding window" counter estimators. Note that even though both analytical results involve approximations, the simulation results for both are identical with

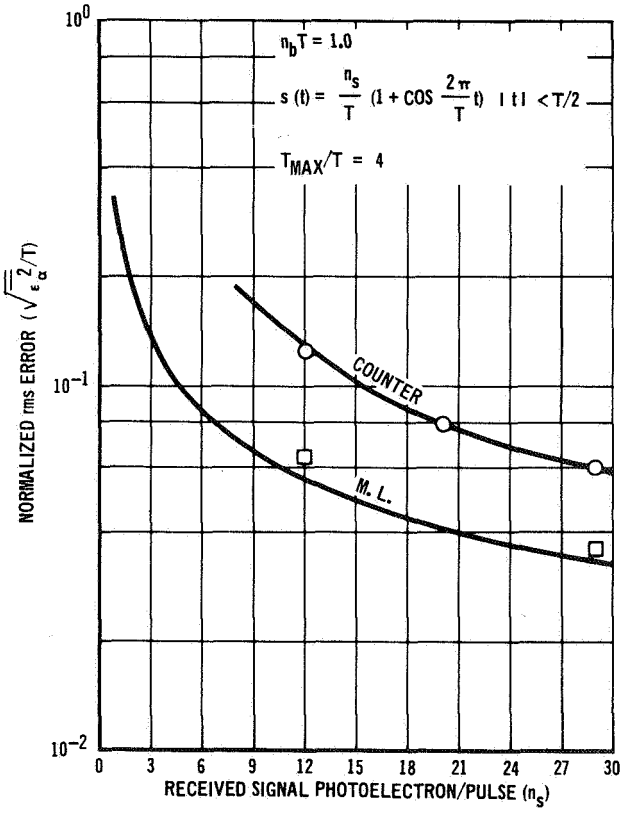

FIGURE 6 VALIDATION BY SIMULATION

the analytical results to within the expected error of the simulation.

WEIGHTED COUNTER SIMULATION

An intuitive design of a pulse arrival time estimator might use a weighted photoelectron counter with the weighting function matched to the received pulse shape. Instead of simply integrating the output of the optical detector over the previous pulse width, the weighted counter includes a weighting function, w(t) in the integration. Thus the output of the weighted counter is given by $\int_{t-T}^{t} x(t')\, w(t' - t + T/2)dt'$, where x(t) is the sequence of impulses from the optical detector. This is equivalent to replacing the "sliding window" integrator with a filter. The output of the weighted counter is applied to a threshold detector. This design comes about either by analogy with the matched filter result from Gaussian detection theory or by mdoifying the ML estimator by replacing the maximum detector with a threshold detector.

Performance of this estimator is difficult to evaluate analytically because the instantaneous distribution of the counter output is a complex shot noise process. Figure (7) compares the rms estimation error of two weighted counters with the "sliding window" counter. One counter uses the weighting function log $[S(t) + n_b]$ while the other uses S(t). Use of S(t) as a weighting function appears to be superior to use of log $[S(t) + n_b]$ and roughly 20% superior in rms error to the "finite window" counter. Thus, using a "matched" filter rather than the "sliding window" integrators (i.e. a filter with a square impulse response) before the threshold offers some performance improvement but is not as good as the ML estimator.

Comparison of the previous results indicate, but definitely does not prove, that the use of a maximum detector rather than a simple threshold provides significant performance gains. Some of the difference between the ML estimator and the "sliding window" counter can be eliminated by replacing the integrator with a carefully designed filter but the magnitude of the improvement is limited.

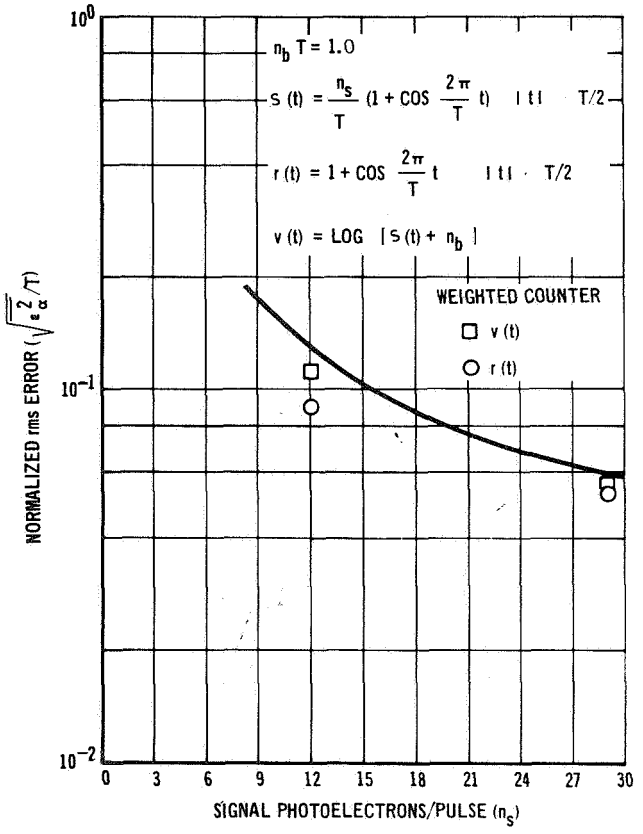

FIGURE 7

One way to approximate a maximum detector is to use an adaptive threshold or equivalently an instantaneous AGC. One solution to this problem is to delay the estimation of α by at least T_{max}. This allows an estimate of the total energy in the pulse which is then used to normalize the received signal before thresholding. This system is shown in Figure 8. Figure 9 shows the performance of this system using both a "sliding window" and weighted counter (weighting function is S(t))with AGC. Note that the weighted counter with AGC is as good as the ML estimator for this case. The main difficulty with this approach is the realization of wideband ideal delay lines.

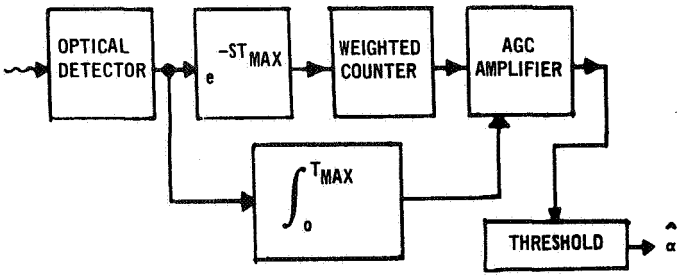

FIGURE 8 ADAPTIVE THRESHOLD TECHNIQUE

SUMMARY

The timing resolution of various sub-optimum estimators were compared with the resolution of the ML estimator using both analytical and simulation techniques. For typical signal and background parameters the ML estimator is approximately a factor of 2 superior in timing resolution to a simple "sliding window" integrator followed by a threshold detector. It appears that most of this difference is due to the use of a maximum rather than a threshold detector. This difference can be made up by using an adaptive threshold detector.

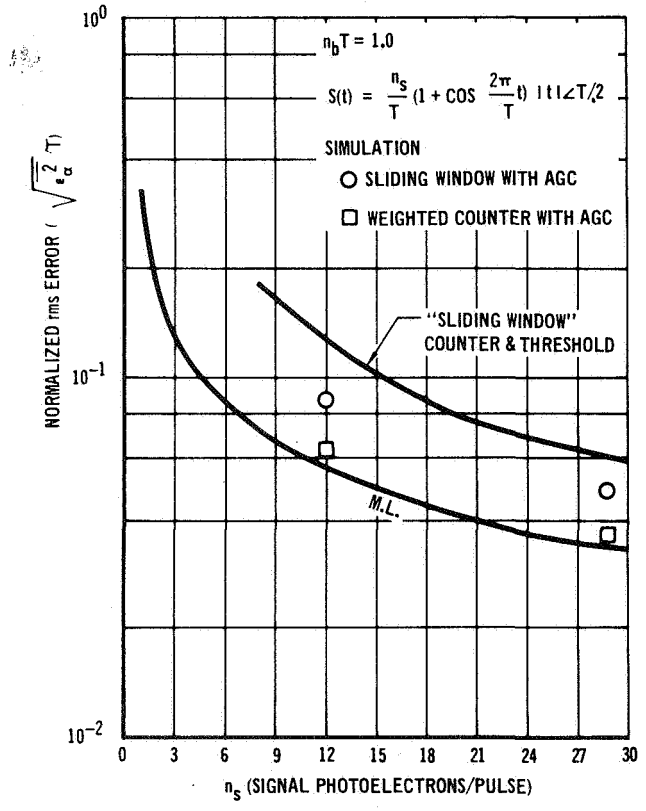

FIGURE 9 ADAPTIVE THRESHOLD SYSTEM PERFORMANCE

APPENDIX A

Let S(t, a) be a function of time and the random vector process $\underline{a}$. It is desired to find P (t) where P (t) is defined to be the probability that the first τ for which equation (37) holds is less than t.

$$S(\tau, \underline{a}) \geq L \tag{37}$$

P(t) can now be determined by the same reasoning as that used for a two state Markov process with one absorbing state.

$$P(t+\Delta) = \text{Prob}\{\text{no crossing before time } t\} \cdot \text{Prob}\{\text{crossing in the interval } (t, t+\Delta) \mid \text{no crossing before time } t\} + \text{Prob}\{\text{first crossing occurs before time } t\} \tag{38}$$

$$\text{Prob}\{\text{first crossing before time } t\} = P(t) \tag{39}$$

$$\text{Prob}\{\text{no crossing before time } t\} = 1 - P(t) \tag{40}$$

$$P(t+\Delta) = [1-P(t)]\,\text{Prob}\{\text{crossing in the interval } (t,t+\Delta) \mid \text{no crossing before time } t\} + P(t) \tag{41}$$

Thus dividing equation (41) by Δ and taking the limit as $\Delta \to 0$ equation (42) is obtained.

$$\lim_{\Delta\to 0} \frac{P(t+\Delta) - P(t)}{\Delta} = [1-P(t)] \lim_{\Delta\to 0} \frac{\text{Prob}\{\text{crossing in the inverval } (t, t+\Delta) \mid \text{no crossing before time } t\}}{\Delta} \tag{42}$$

$$\frac{dP}{dt} = [1-P(t)]\,a(t) \tag{43}$$

where $a(t) = \lim_{\Delta\to 0} \frac{1}{\Delta} \text{Prob}\{\text{crossing in the interval } (t,t+\Delta) \mid \text{no crossing before time } t\}$

Thus,

$$P(t) = 1 - (1-P_0)\exp\left[-\int_0^t a(t')dt'\right] \tag{44}$$

where $P(0) = P_0$.

Equation (44) is a formal solution to the first level crossing problem. The remaining problem is the determination of the transition probability a(t).

$$\text{Let} \quad S(t+\Delta, \underline{a}) - S(t, \underline{a}) = \Delta S \tag{45}$$

If S(t, $\underline{a}$) is assumed to be mathematically well behaved, then in the limit as $\Delta \to 0$, S(t, $\underline{a}$) can have only one zero crossing in the interval (t, t + Δ).

$$a(t) = \lim_{\Delta\to 0} \frac{1}{\Delta} \int_{-\infty}^{\infty} \text{Prob}\{\Delta S > L-X \mid S(t,\underline{a}) = X,\ S(t', \underline{a}) < L,\ 0 \leq t' \leq t\}\ \text{Prob}\{S(t, \underline{a}) = X \mid S(t', \underline{a}) < L,\ 0 \leq t' \leq t\}\, dX \tag{46}$$

Assuming S(t, $\underline{a}$) is a suitable smooth function, ΔS can be determined from equation (47).

$$\Delta S = \frac{dS(t,\underline{a})}{dt}\Delta t + \sum_{i=1}^{n} \frac{dS(t,\underline{a})}{da_i}\Delta a_i \tag{47}$$

If S (t, $\underline{a}$) is not a continuous function of t, P (t) must be updated at each discontinuity using the laws of conditional probabilities. Equation (47) shows that the distribution of ΔS can be found if the joint distribution of the Δa_i is known.

For many cases of practical interest $\underline{a}$ or S(t, $\underline{a}$) is represented as a vector Markov process. When S(t, $\underline{a}$) is a vector Markov process,

$$\text{Prob}\{\Delta S > L-X \mid S(t, \underline{a}) = X,\ S(t', \underline{a}) < L,\ 0 \leq t' \leq t\} = \text{Prob}\{\Delta S > L-X \mid S(t, \underline{a}) = X\} \tag{48}$$

Note that the right side of equation (48) can usually be evaluated without difficulty. Using the Markov assumption, Prob $\{S(t, \underline{a}) = X \mid S(\tau, \underline{a}) < L, 0 \leq \tau \leq t\}$ can be determined from,

$$\text{Prob}\{S(t,\underline{a}) = X \mid S(t',\underline{a}) < L, 0 \leq t' \leq t\} = \frac{P_s(x,t)}{\int_0^L P_s(y,t)\,dy} \quad (49)$$

where $P_S(y,t)$ is the solution to the diffusion equation for $S(t, \underline{a})$ with an absorbing boundary at $S(t, \underline{a}) = L$.

Using the idea of an absorbing boundary, several authors [6, 7] have considered the special case where $S(t, \underline{a})$ is a process with independent increments since the first crossing density can then be determined directly by solving a Fokker-Planck equation. For this case the derivative of $S(t, \underline{a})$ with respect to time exists almost nowhere and it can be argued intuitively

$$\lim_{\substack{X \to L \\ X \leq L}} \text{Prob}\{S(t,\underline{a}) = X \mid S(t',\underline{a}) < L, 0 \leq t' \leq t\} = \lim_{\substack{X \to L \\ X \leq L}} P_s(X, t) = 0$$

Unfortunately, the zero boundary condition comes directly from nonphysical attributes of independent increment processes (for instance, an infinite number of level crossings in zero time). There appears to be no general technique for evaluating the boundary condition for Prob $\{S(t, \underline{a}) = X \mid S(t', \underline{a}) < L, 0 \leq t' \leq t\}$ at $X = L$ for physically realizeable processes. Yang and Shinozuka [8] have suggested a way around the unknown boundary value problem by formulating the solution in terms of the Kolmogorov backward equation rather than the forward (Fokker-Planck) equation.

Perhaps the most valuable attribute of this whole approach is not that it leads to exact solutions of previously intractable problems (which it usually does not), but that it expresses the first crossing distribution in terms of quantities that can often be accurately approximated.

APPROXIMATION FOR THE CONDITIONAL DENSITY

The conditional density of ΔS can often be exactly determined, however general solutions for the conditional density of $S(t, \underline{a})$ are not known. One useful approximation is given by equation (50).

$$\text{Prob}\{S(t,\underline{a}) = X \mid S(t', \underline{a}) < L, 0 \leq t' \leq t\} \doteq \text{Prob}\{S(t,\underline{a}) = X \mid S(t,\underline{a}) < L\} \quad (50)$$

By definition,

$$\text{Prob}\{S(t,\underline{a}) = X \mid S(t,\underline{a}) < L\} = \begin{cases} 0 & \text{for } X \geq L \\ \dfrac{f(X,t)}{\int_{-\infty}^{L} f(X,t)\,dX} & \text{for } X < L \end{cases} \quad (51)$$

where $f(S,t)$ is the distribution of $S(t, \underline{a})$.

The use of this approximation and this general approach in obtaining closed form expressions for the first crossing density for various types of random processes is discussed in reference [4]. The approximation makes uses of the fact that for many processes of practical interest specifying that the process has not crossed some level in the past does not significantly alter its present distribution.

We now consider the optical pulse detection case where photoelectrons are being emitted from an optical detector according to a Poisson distribution with mean rate $\lambda(\alpha, t)$. A "sliding window" counter, that is a counter which determines the number of photoelectrons received during the previous T seconds, is used to filter the optical detector output. The output of the counter is then applied to a threshold detector which estimates pulse arrival time.

Let $N(t)$ = the number of photoelectrons received in the interval $[t - T, t]$ (i.e., signal and background).

Define,

$$P(t) = \text{Prob}\{N(s) < L, 0 \leq s \leq t\}.$$

Thus $P(t)$ is determined by equation (44) where

$$a(t) = \lim_{\Delta \to 0} \frac{1}{\Delta} \text{Prob}\{N(t+\Delta) \geq L \mid N(t') < L, 0 \leq t' \leq t\}$$

$$= \lim_{\Delta \to 0} \frac{1}{\Delta} \sum_{M=1}^{L-1} \text{Prob}\{N(t+\Delta) \geq L \mid N(t) = M, N(t') < L, 0 \leq t' \leq t\} \cdot \text{Prob}\{N(t) = M \mid N(t') < L, 0 \leq t' \leq t\}$$

$$\text{Prob}\{N(t) = M \mid N(t) < L\} = \frac{\frac{(\bar{n}T)^M}{M!}\exp(-\bar{n}T)}{\sum_{K=0}^{L-1} \frac{(\bar{n}T)^K}{K!}\exp(-\bar{n}T)} \quad \text{for } M < L \quad (52)$$

where $\bar{n}$ is the effective mean rate for the interval $[t - T, t]$.

In the limit as $\Delta \to 0$, $\frac{1}{\Delta}$ Prob $\{N(t+\Delta) \geq L \mid N(t) = M, N(\tau) < L, 0 \leq \tau \leq t\}$ approaches zero unless $M = L - 1$. For $M = L-1$, the probability of a threshold crossing due to one or more counts dropping out and two or more counts occuring in time Δ also goes to zero faster than $\frac{1}{\Delta}$.

$$\lim_{\Delta \to 0} \frac{1}{\Delta} \text{Prob}\{N(t+\Delta) \geq L \mid N(t) = L-1, N(t') < L, 0 \leq t' \leq t\} = n \quad (53)$$

where n is the instantaneous mean rate at time t. For the case where $L = 1$, $a(t)$ can be evaluated exactly since

$$\text{Prob}\{N(t) = M \mid N(\tau) < 1, 0 \leq \tau \leq t\} = \text{Prob}\{N(t) = M \mid N(t) < 1\} = \delta_{M,0} \quad (54)$$

Thus for the case of background alone ($\bar{n} = \bar{n}_b$), the false alarm probability in a time period t is exactly given by

$$P_{fa} = 1 - \exp(-\bar{n}_b t) \quad (55)$$

For the general case

$$a(t) \doteq n(t) \frac{\frac{(\bar{n}T)^{L-1}}{(L-1)!}}{\sum_{K=0}^{L-1} \frac{(\bar{n}T)^K}{K!}} \quad (56)$$

where $n(t) = \lambda(t, \alpha)$ is the instantaneous mean rate at time t. Note that the density of the first crossing time can easily be expressed

$$p(t) = \frac{dP(t)}{dt} = a(t)\exp\left[-\int_0^t a(t')dt'\right] \quad (57)$$

REFERENCES

1) E. Hoversten, D. Snyder, R. Harger and K. Kurimoto, "Direct-Detection Optical Communication Receivers", IEEE Trans. on Communications Vol. COM-22, January 1974.
2) E. Hoversten and D. Snyder, "On the Performance of Pulse Position Modulation in Direct Detection Optical Communication Systems: Mean Square Error and Threshold", International Information Theory Symposium, 1972.
3) I. Bar-David, "Communication Under the Poisson Regime", IEEE Trans. on Information Theory, Vol. IT-15, January 1969.
4) G. Lee and D. Fogle, "A Solution to the First Crossing Problems", International Conference on Communications, 1971.
5) T. Curran and M. Ross, "Optimum Detection Thresholds in Optical Communications," Proc. IEEE , Vol. 53, November 1965.
6) W. Lindsey, "Nonlinear Analysis of Generalized Tracking Systems," Proc. IEEE, Vol. 57, October 1969.
7) A. Viterbi, "Phase-Locked Loop Dynamics in the Presence of Noise by Fokker-Planck Techniques,", Proc. IEEE, Vol. 51 , December 1963.
8) J. N. Yang and M. Shinozuka, "A Note on the First Passage Time Problem," JPL Technical Report 32-1334, October 1968.

APPENDIX F

TARGET SIGNATURE ANALYSIS

1.0 CUBE-CORNER GAIN AND ANTENNA PATTERN

For this study, the LAGEOS type of optical retro-reflector was chosen as the model retro-reflector. The LAGEOS retro-reflector is a 3.8-cm diameter, fused silica cube-corner, with an intentional dihedral angle offset of 1.5 $\pm$0.5 arcsec. This specific design was chosen to optimize the return at 0.6943 μm wavelength for ranging from the ground to a low to medium altitude satellite. Over the broader range of conditions encountered in this study we find the cube-corner is usable but not necessarily optimum.

The cube-corner is modeled as a receiving/transmitting aperture to which an incident phase wave is applied. As the wave passes through the cube-corner, the phase is perturbed, both by systematic effects, such as dihedral angle offsets, and by nonsystematic effects, such as temperature gradients. The amplitude of the wave is also affected. The LAGEOS cube-corners use total internal reflection, which cause a linearly polarized incoming wave to be decomposed into two, nonuniformly[1] distributed, orthogonally polarized reflected waves, and some net energy loss is encountered. For the purposes of this study, both temperature gradient and polarization state transfer effects were ignored.

We define the gain product of an ideal cube-corner retro-reflector as the product of the effective receive aperture antenna gain and the effective transmit aperture antenna gain. At normal incidence, the effective aperture is the face diameter, and the on-axis gain, with respect to isotropic radiators, is simply,

$$G(o) = (\pi D/\lambda)^4 \qquad \text{(F-1)}$$

D = face diameter, m

λ = wavelength, m

[1] R. F. Chang, et al, "Farfield Diffraction Pattern for Corner Reflectors with complex reflection coefficients," Journal of the Optical Society of America, Volume 61, Number 4, April 1971, ps 431-438.

The far-field antenna pattern is then given by,

$$G(\theta) = (\pi D/\lambda)^4 \left[\frac{2\ J_1(\pi\theta D/\lambda)}{(\pi\theta D/\lambda)}\right]^2 \qquad \text{(F-2)}$$

This is the well known $(J_1(x)/x)^2$ pattern from a circular aperture with uniform amplitude and phase distribution within the aperture.

In order to compute the antenna pattern when the effective aperture is noncircular, and the phase is nonuniform, we must resort to numerical techniques. The starting point is the Fraunhoffer approximation to the Fresnel-Kirckhoff integral.[2]

$$\tilde{E}(x_2,y_2,L) = \frac{ie}{\lambda L}^{iKL} - \frac{iK}{2L}(x_2^2 + y_2^2) \iint_{-\infty}^{\infty} \tilde{E}(x_1,y_1,o)\ \exp\left\{\frac{iK}{L}(x_1,x_2 + y_1y_2)\right\}\ dx_1dy_1 \qquad \text{(F-3)}$$

E is the complex spacially dependent "wave function," and x_1, y_1 are dimensions in the plane containing the transmit aperture, x_2, y_2 are dimensions in a parallel plane, spaced a distance L from the aperture plane, which describes the location of the point detector, and K is the wave number, $2\pi/\lambda$. The exponential external to the integral is simply a phase term, and may be dropped from this expression for our purposes.

The power within the aperture is simply,

$$P_A = \iint_{-\infty}^{\infty} \tilde{E}(x_1,y_1,o) \cdot \tilde{E}^*(x_1,y_1,o)\ dx_1dy_1 \qquad \text{(F-4)}$$

When the amplitude is uniform over the aperture, as we have assumed,

$$\tilde{E}(x_1,y_1,o) = E_o \exp\left\{if(x_1,y_1)\right\}, \qquad \text{(F-5)}$$

within the aperture and zero elsewhere

$$P_A = E_o^2\ A$$

where A is the aperture area.

[2] Klein, Miles V.; "OPTICS," John Wiley & Sons, New York (1970), pg 421.

The field from an isotropic radiator with power P_A is,

$$\tilde{E}_I(x_2,y_2,L) = \sqrt{\frac{AE_o^2}{4\pi L^2}} \tag{F-6}$$

The cube-corner receive gain, compared to an isotropic radiator, is $4\pi A/\lambda^2$. Thus, the normalized field at the detector is,

$$\tilde{E}_N(x_2,y_2,L) = \frac{\tilde{E}(x_2,y_2,L)}{\tilde{E}_I(x_2,y_2,L)} \cdot \sqrt{\frac{4\pi A}{\lambda^2}} \tag{F-7}$$

$$\tilde{E}_N(x_2,y_2,L) = \frac{4\pi}{\lambda^2} \iint_A \exp\left\{i\left[f(x_1,y_1) + \frac{K}{L}(x_1x_2 + y_1y_2)\right]\right\} dx_1 dx_2$$

Next, let $\phi_x = x_2/L$ and $\phi_y = y_2/L$

Then,

$$\tilde{E}_N(\phi_x,\phi_y) = \frac{4\pi}{\lambda^2} \iint_A \exp\left\{i\left[f(x_1,y_1) + K(x_1\phi_x + y_1\phi_y)\right]\right\} dx_1 dy_1 \tag{F-8}$$

Equation (F-8) reduces to Equation (F-2) for uniform phase ($f(x_1,y_1)=o$).

In this form, we clearly see that E_N is simply the two-dimensional Fourier transform of $e^{if(x_1,y_1)}$, taken within the aperture. Since we wish to describe the entire far-field pattern over the region of interest, it is most economical, numerically, to use the fast Fourier transform (FFT) technique. This requires representing the function to be transformed as a set of samples,

$$\frac{\tilde{E}(x_1,y_1,o)}{E_o} = \sum_{-\infty}^{\infty}\sum \Delta A\, E_{m,n}\, \delta(x_1 - m\Delta x, y_1 - n\Delta y) \tag{F-9}$$

where

$$E_{m,n} = \exp\left\{if(m,n)\right\}\ ,\ m\Delta x,\ n\Delta y \text{ within the aperture,}$$

$$= 0 \text{ elsewhere,}$$

and

$$\tilde{E}_N(\phi_x,\phi_y) = \frac{4\pi}{\lambda^2}(\Delta x\Delta y)\sum_{-\infty}^{\infty}\sum E_{mn}\exp\left\{iK(m\Delta x\phi_x + n\Delta y\phi_y)\right\} \qquad \text{(F-10)}$$

Then

$$G_N(\phi_x,\phi_y) = E_N(\phi_x,\phi_y)\cdot E_N^*(\phi_x,\phi_y)$$

A short digression on the FFT is in order. The basic purpose is to compute the Fourier transform of a periodic process, represented by a set of samples. There are two significant requirements for reliable application of this technique. First, the sample spacing must satisfy the Nyquist criteria. Second, the sample set must be sufficiently long to provide the desired output resolution.

In spatial terms, a one-dimensional transform, with sample spacing Δx, and a length N_T (samples), results in a sample spacing after transform, of $\Delta\phi = \lambda/N_T\Delta x$.

The domain of the sample set, after the transform, is $\pm\phi_F(\phi_F = \lambda/2\Delta x)$. In this context, ϕ_F can be considered as the folding frequency. If we choose Δx sufficiently small, and N_T sufficiently large, the transformed sample set is a good estimate of the Fourier transform of the nonperiodic process.

The two-dimensional transform process is accomplished by first transforming each row of a sample matrix, S(I,J), and then transforming each column (or conversely). Finally, we note that the sample matrix (MxM) may be smaller than the transform set (N_T), provided only that the transformed sample matrix covers the domain, in transform space, that is of interest.

The output antenna pattern in units of receive/transmit gain product is obtained by processing the transformed sample matrix,

$$G(I\Delta\phi_x,J\Delta\phi_y) = \left(4\pi\Delta x\Delta y/\lambda^2\right)^2\cdot S(I,J)\cdot S^*(I,J) \qquad \text{(F-11)}$$

The next step is to establish the process for obtaining the sample matrix. This would be a trivial operation for an open cube-corner with no dihedral

angle offsets, since the output aperture is simply the input aperture folded successively about each axis, and a ray which intersects the face plane within both the entrance and exit aperture is a valid (nonzero) sample ray. However, for the solid fused silica cube-corner, with dihedral angle offsets, it is necessary to account for both refraction and phase taper.

The technique we employed was to construct a rectangular sampling matrix normal to the input wave direction vector. The intercept of each ray with the face plane was computed, and the ray was refracted into the cube. If the ray was within the entrance aperture, the reflection surface contact sequence and exit coordinates were computed. If after reflection the ray was within the exit aperture, the phase was computed based on the contact sequence and the magnitude of the dihedral angle offset. A complex variable with unit amplitude and the computed phase was then stored in the sample matrix.

After the sample matrix was completed, the two-dimensional FFT was performed, followed by the scaling conversion shown in Equation (F-11). The resultant data matrix was processed by several data presentation subroutines. The subroutine used for most subsequent data processing converted the data from the rectangular sample spacing into the mean gain in annular slots, typically 2.5 μrad wide. For the final production runs, the annular slot gain data was stored in a file for subsequent access by other programs.

The complete data file includes the annular slot mean (and variance) gain data for the nominal cube-corners, at incidence angles from zero to 40° in 5° steps, for both 0.53 μm and 1.06 μm illumination, in 2.5 μrad bins from 2.5 μrad (center) to 72.5 μrad. During execution of this program, 180,000 gain points were generated, which were compressed to 540 values for the mean and variance of the gain product in the annular slots. This program, and two of the data conversion programs used to process the gain data, are presented in Appendix A.

2.0 LAGEOS SIGNATURE DATA

Conceptually, the LAGEOS type of target presents a uniform signature regardless of the direction of the incident radiation, resulting in a target which can be used for ranging purposes both from the ground and from a spacecraft in a high altitude orbit. For this reason, the LAGEOS was chosen as a prototype for the passive low altitude target (LATS).

The LAGEOS configuration, which was used in this study, is shown in Figure F-1. Retro-reflectors are installed in rings (constant latitude), and slightly recessed into the surface. Each retro-reflector is identified by a location vector in polar coordinates, summarized in Table F-1. When illuminated by an impinging laser pulse, with a direction vector $\vec{v}$, each retro-reflector, whose position (in terms of central angle between the retro-reflector location vector and the complement of the pulse direction vector) is less than some critical angle, will contribute to the return pulse. The angle between the first contact point and the retro-reflector location vector is given by Equation (F-12).

$$\alpha = \text{ARCCOS}\Big(\text{COS}(\text{LAT}_P)\ \text{COS}(\text{LAT}_R) + \text{SIN}(\text{LAT}_P)\ \text{SIN}(\text{LAT}_R)\ \text{COS}(\text{LONG}_P - \text{LONG}_T)\Big) \quad \text{(F-12)}$$

This is shown, schematically, in Figure F-2A.

LAGEOS CONFIGURATION

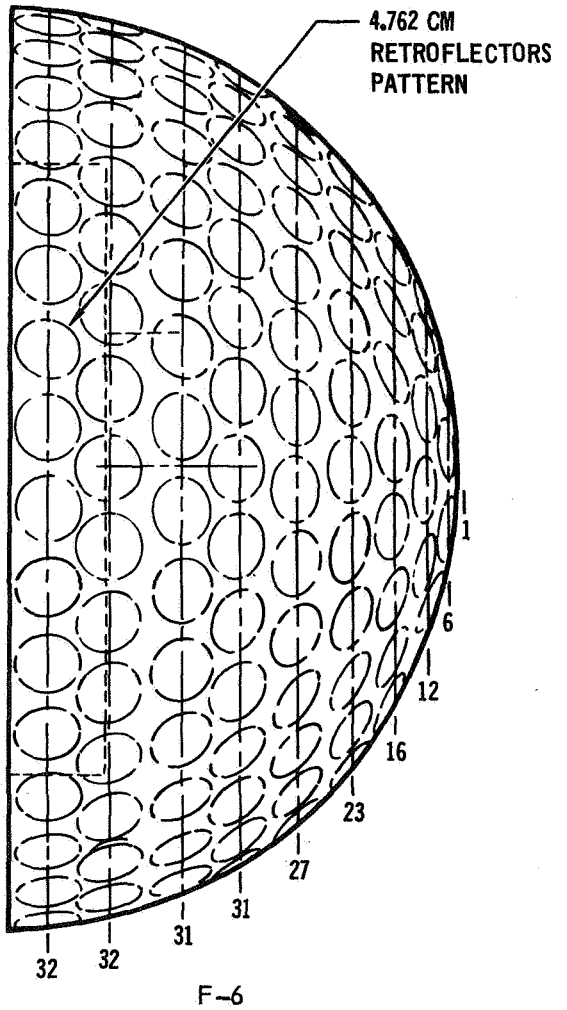

FIGURE F-1

ILLUMINATION GEOMETRY

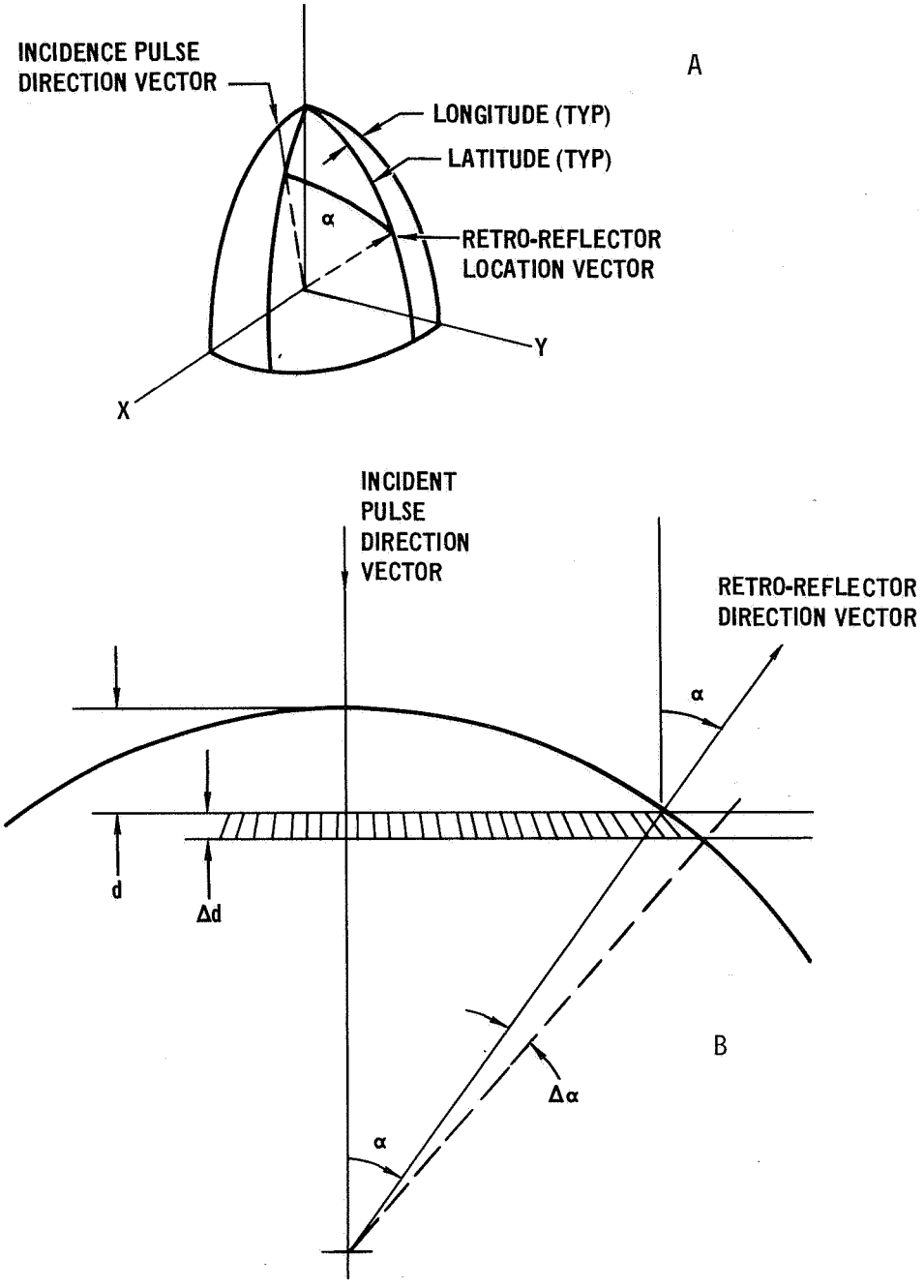

FIGURE F–2

TABLE F-1: LAGEOS RETRO-REFLECTOR LOCATIONS
(UNIFORMLY SPACED WITHIN RINGS)
TYPICAL, EACH HEMISPHERE

RING	NO. OF RETROS	RING LATITUDE (DEGREES)	LONGITUDE OF FIRST RETRO (DEGREES)
1	32	4.87°	5.625°
2	32	13.25°	0°
3	31	22.98°	5.806°
4	31	31.23°	0°
5	27	40.96°	0°
6	23	50.69°	0°
7	18	60.42°	0°
8	12	70.15°	0°
9	6	79.88°	0°
10	1	90°	-

Figure F-2B shows this geometry in the plane containing the two vectors. The pulse reflected from this retro-reflector must travel 2d further than if it were aligned with the pulse vector. Thus, for the nth retro-reflector, there is a characteristic delay time, τ_n.

$$\tau_n = \frac{2d_n}{c} = \frac{2r_s}{c}(1 - \cos \alpha_n) \qquad \text{(F-13)}$$

r_s = radius of the sphere (m)

c = speed of light (2.997925×10^8 m/s)

Now, if the laser pulse has an amplitude time envelope, g(t), g(o)=1, the reflected pulse has a mean amplitude envelope, S(t).

$$S(t) = \sum_{n=1}^{N} g(t - \tau_n)\, a_n \qquad \text{(F-14)}$$

where

a_n is the gain product constant for the n_{th} retroreflector, with an incidence angle, α_n.

The spherical surface area of the annular ring defined by α, $\alpha+\Delta\alpha$, is simply $2\pi r_s(\Delta d)$. Thus, if the spherical surface area is divided into N such rings, we would find $\Delta d = 2\pi r_s/N$. Thus, a LAGEOS type of target with a "uniform" retro-reflector distribution would have one retro-reflector in each annular ring, resulting in a target impulse response consisting of a series of equally spaced impulses ($\Delta t = 8\pi r_s/CN$), whose amplitudes nominally decrease with increasing delay.

Now, if the incident laser pulse is temporarily Gaussian, the incident pulse g(t), is defined by Equation (F-15).

$$g(t) = \exp\left\{-\frac{t^2}{T^2} + jw_c t\right\} \qquad \text{(F-15)}$$

Then, by substitution in Equation F-14 S(t) is given by Equation (F-16)

$$S(t) = \sum_{n=1}^{N} a_n \exp\left\{-\frac{(t-\tau_n)^2}{T^2} + jw_c t - jw_c\tau_n\right\} \qquad \text{(F-16)}$$

The $\exp\{jw_c t\}$ term is simply the laser carrier frequency term. The $jw_c\tau_n = (j\theta_n)$ term is a phase term which is, effectively, a random variable, uniformly distributed in 2π radians. When the return pulse is detected, the detected signal, X(t), is given by Equation (F-17).

$$X(t) = S(t)\,S^*(t) = \sum_{n=1}^{N}\sum_{m=1}^{N} a_n a_m \cos(\theta_n-\theta_m) \exp -\left\{\frac{(t-\tau_n)^2 + (t-\tau_m)^2}{T^2}\right\} \qquad \text{(F-17)}$$

Now, the a_n are random variables whose randomness is principally attributable to angular distribution variations. The θ_n are random variables determined by $\theta_n = (w_c\tau_n) \bmod 2\pi$. Since w_c is very large, θ_n and τ_n are therefore relatively independant. Finally, the τ_n are random variables, where the randomness is attributable to the randomness in the latitude and longitude of the incident

wave direction vector, in terms of the target coordinate system. The expected value of X(t) can be obtained by first taking the expectation with respect to θ_n, then with respect to a_n. This results in Equation (F-18)

$$E\{X(t)\} = \sum_{n=1}^{N} E\{a_n^2\} \exp\left\{-\frac{2(t-\tau_n)^2}{T^2}\right\} \qquad \text{(F-18)}$$

The term, $E\{a_n^2\}$, is simply the mean power gain of the retro-reflector at the incidence angle corresponding to τ_n.

The next step in the process is to determine the relative magnitude of the various contributers to the randomness of X(t). The first step is to integrate X(t) over all time, resulting in Y, the total energy in the pulse.

$$Y = \int_{-\infty}^{\infty} X(t)\, dt = T\sqrt{\frac{\pi}{2}} \sum_{n=1}^{N} \sum_{m=1}^{N} a_n a_m \cos(\theta_n - \theta_m) \exp - \left\{\frac{(\tau_n - \tau_m)^2}{2T^2}\right\} \qquad \text{(F-19)}$$

Then, let,

$$Y' = E\left\{Y \mid a_n, \tau_n\right\} = \frac{T}{2}\sqrt{\frac{\pi}{2}} \sum_{n=1}^{N} a_n^2 \qquad \text{(F-20)}$$

Then,

$$E\{Y'\} = \frac{T}{2}\sqrt{\frac{\pi}{2}} \sum_{n=1}^{N} E\{a_n^2\} \qquad \text{(F-21)}$$

$$E\{Y'^2\} = \frac{\pi T^2}{8} \sum_{n=1}^{N} \left[E\{a_n^4\} + E\{a_n^2\} \sum_{\substack{m=1 \\ m\neq n}}^{N} E\{a_m^2\}\right] \qquad \text{(F-22)}$$

$$\sigma_{Y'}^2 = E\{Y'^2\} - E\{Y'\}^2$$

$$= \frac{\pi T^2}{8} \sum_{n=1}^{N} \left[E\{a_n^4\} - E\{a_n^2\}^2\right] = \frac{\pi T^2}{8} \sum_{n=1}^{N} \sigma_{a_n^2}^2 \qquad \text{(F-23)}$$

Now, if we consider $E\{Y'\}$ as the "signal", and σ^2 as the noise, due to gain variations, the target signature signal-to-noise power ratio (SNR_G) is given by Equation (F-24).

$$SNR_G = \frac{\left[\sum_{m=1}^{N} E\left\{a_n^2\right\}\right]^2}{\sum_{n=1}^{N}\left[E\left\{a_n^4\right\} - E\left\{a_n^2\right\}^2\right]} \qquad \text{(F-24)}$$

Thus, we conclude that the mean, or many pulse, integrated average detected power SNR is dependant only on the gain variation noise, assuming variations in location cause negligible effect on the mean gain. Figure F-3 shows the dependance of SNR_G to point-ahead angle magnitude at both 0.53 μm and 1.06 μm wavelengths. These curves were computed using the data from the cube-corner gain analysis discussed in Section 1.0 of this Appendix, using the program, CONVV, shown in Appendix B. The data shows that the effective target SNR, although dependant on point-ahead angle and wavelength, is on the order of 15 to 20 dB, which is considerably greater than the expected shot-noise signal-to-noise ratio for narrow pulse ranging.

In order to evaluate the effect of the nonuniform distribution of retro-reflectors over the surface of the LAGEOS sphere, we resorted to a simulation. For each time (t), an incident wave direction vector was chosen randomly (over 4π steradians), and $E\{X(t)\ \tau_n\}$ was computed. The variance of $E\{X(t)\ \tau_n\}$ was also computed. This process was repeated on the order of 50 times for each sample time, and the mean and variance of the estimates of the mean gain, due to incident wave direction variations were calculated. The variance of the estimate of the mean gain, due to direction variations, was uniformly small compared to the variance of the gain due to gain variations. These data were generated for a 0.2 ns laser pulsewidth. The results, therefore, allowed us to consider, in all subsequent work, that the LAGEOS was well modeled as having a uniform distribution of retro-reflectors. For a less symmetrical target, this assumption cannot be made, and target signature variations with incident wave direction vector must be considered.

The effect of point-ahead angle and wavelength on $E\{X(t)\}$ as defined by Equation F-18 using the cube-corner gain data, discussed in Section 1, of this Appendix, was evaluated for a temporally Gaussian incident pulse of 0.2 ns width

TARGET SIGNATURE SIGNAL-TO-NOISE RATIO DUE TO GAIN VARIATIONS

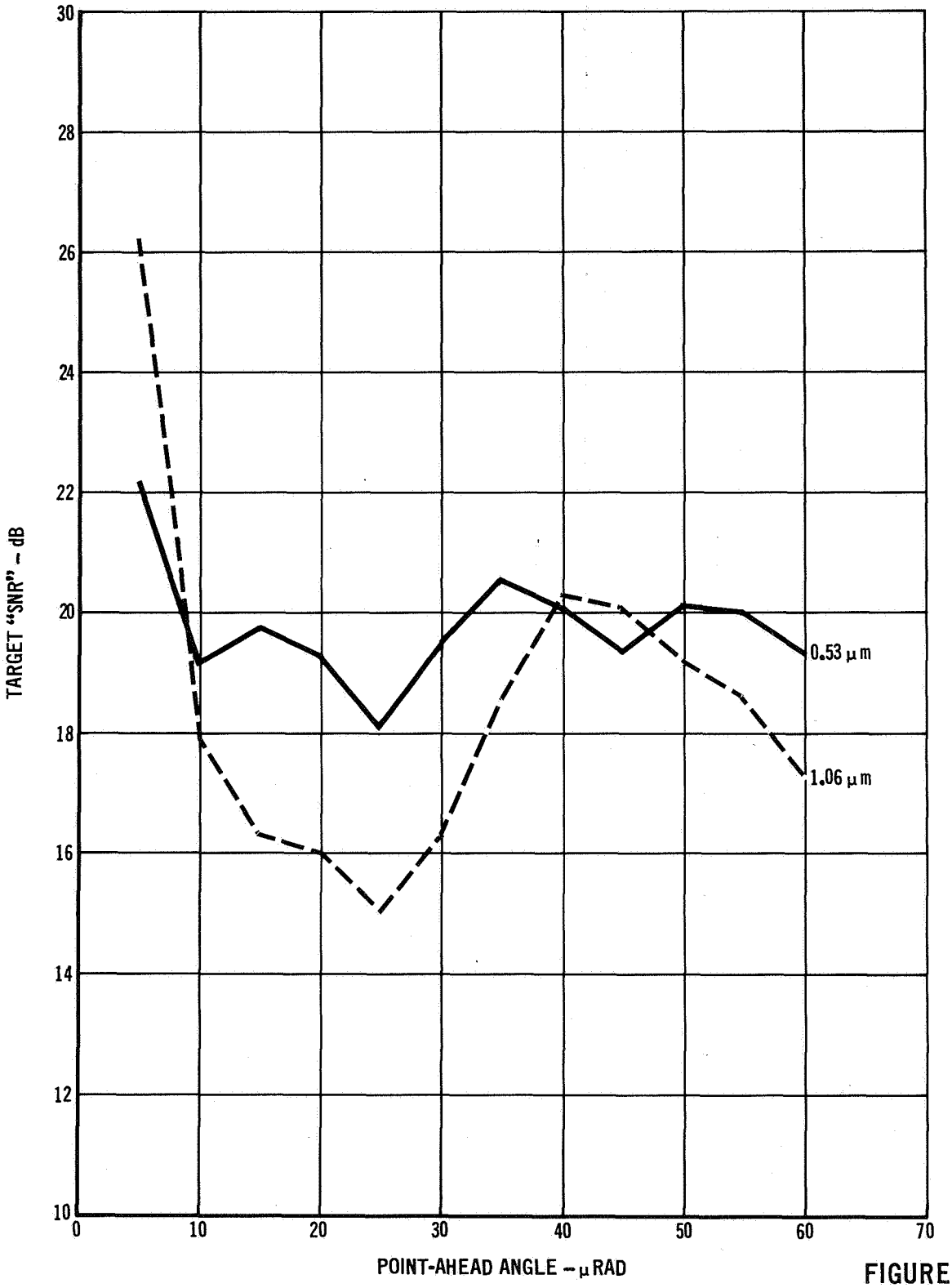

FIGURE F–3

at the e^{-2} power point. This data, and the generating program, are presented in Appendix B. A considerable variation in mean return pulse amplitude, shape, and width was observed.

We can examine the effect of the variation in mean return pulse amplitude, shape, and width on a split gate range tracking loop by considering the function $f(\varepsilon)$.

$$f(\varepsilon) = \int_{\varepsilon}^{\infty} X(t)\, dt - \int_{-\infty}^{\varepsilon} X(t)\, dt \qquad \text{(F-25)}$$

where $x(t)$ is given by Equation (F-17).

With $E\{X(t)\}$ defined as in Equation (F-18), this results in an expected value of $f(\varepsilon)$ given by Equation (F-26).

$$g(\varepsilon) = E\{f(\varepsilon)\} = \frac{T}{2}\sqrt{\pi} \sum_{n=1}^{N} E\left\{a_n^2\right\} \operatorname{erf}\left\{\frac{\tau_n - \varepsilon}{T}\right\} \qquad \text{(F-26)}$$

where,

$$\operatorname{erf}(x) = \frac{2}{\sqrt{\pi}} \int_{0}^{x} e^{-t^2}\, dt$$

If we expand $g(\varepsilon)$ in a Taylor series, and ignore the second and higher ordered terms, we find the ε_0, such that $g(\varepsilon_0) = 0$, is given by Equation (F-27).

$$\varepsilon_0 = \frac{T\sqrt{\pi}}{2}\left[\frac{\sum_{n=1}^{N} E\left\{a_n^2\right\} \operatorname{erf}\left\{\tau_n/T\right\}}{\sum_{n=1}^{N} E\left\{a_n^2\right\} \exp\left\{-\tau_n^2/T^2\right\}}\right] \qquad \text{(F-27)}$$

Equation F-27 is evaluated in Figure F-4 as a function of point-ahead angle, for two laser pulsewidths and at both 0.53 and 1.06 μm wavelengths. The program used to compute this data is shown in Appendix C.

STATIC BIAS – LAGEOS VS POINT-AHEAD

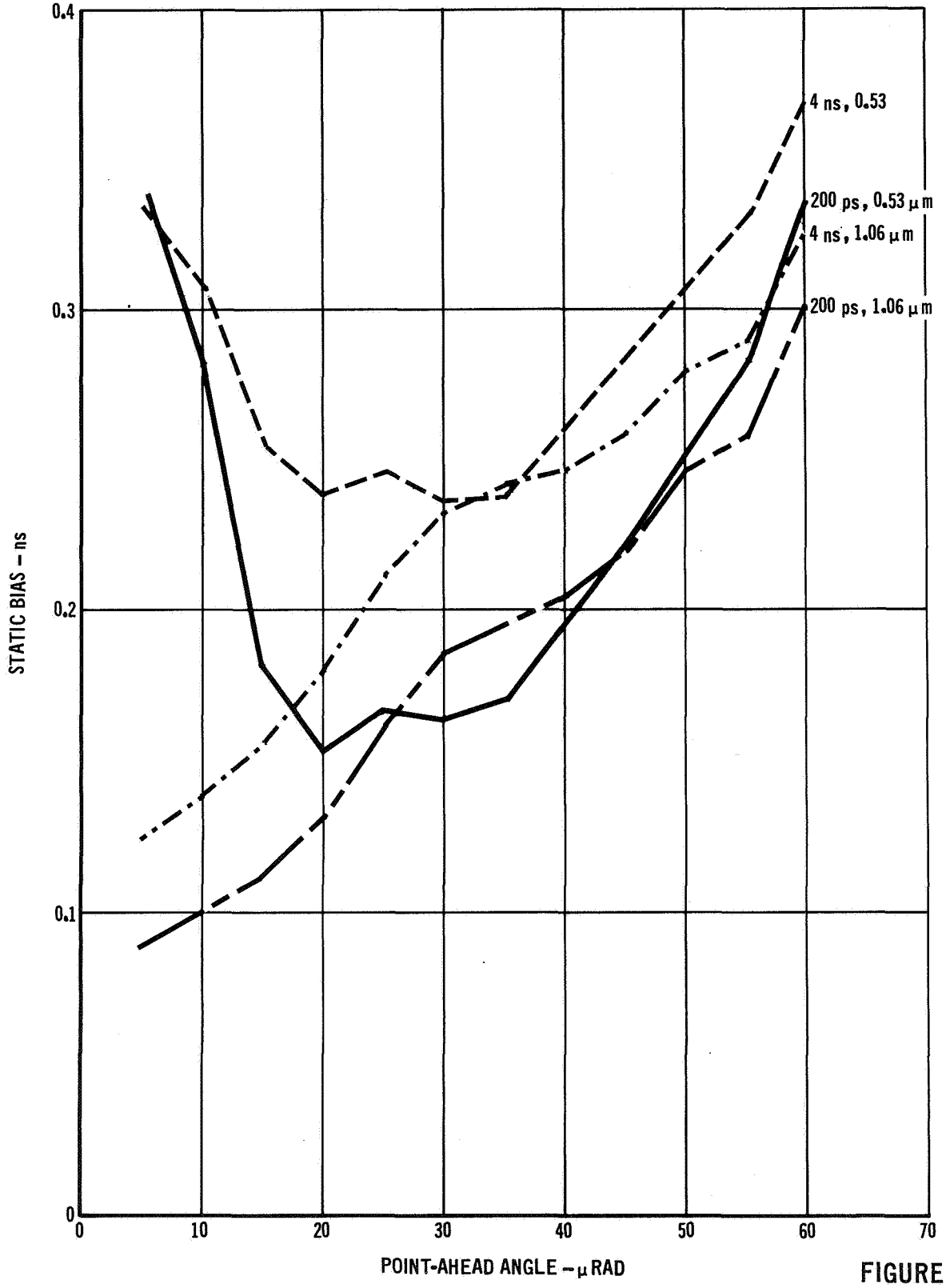

FIGURE F–4

Two approximations of Equation (F-27) can be obtained, for the cases where the pulse is either very long or very short. Where the pulse is very long,

$$\varepsilon_o \simeq \frac{\sum_{n=1}^{N} a_n \tau_n}{\sum_{n=1}^{N} a_n} ; \qquad T >> \tau_N \tag{F-28}$$

When the incident pulse is very short ($T << \tau_N$), and $\tau_n = n\Delta\tau$, ε_o is within the range of values which satisfy Equation (F-29).

$$\sum_{n=1}^{INT(\varepsilon_o/\Delta\tau)} a_n = \sum_{n=1+INT(\varepsilon_o/\Delta\tau)}^{N} a_n \tag{F-29}$$

In addition to computing ε_o, we also computed the two approximations, and found close agreement between ε_o, computed using Equation (F-27), and the approximations, where we compared the 200 ps pulse to the very short pulse approximation and a 4 ns pulse to the very long pulse approximation. The calculated pulse centroids, for the 200 ps pulsewidth, were also shown on the signature curves in Appendix B. We conclude that is the cube-corner response is uniformly close to the "ideal," which was used to compute the mean gains, we can easily compensate for the static bias, since the point-ahead angle is well known in operation.

Note, however, that manufacturing tolerances and thermal gradients cause variations in the far-field response of the individual cube-corner. These variations are most like to significantly affect the location and depth of deep nulls, which are only observed at near normal incidence angles. Thus, we would nominally expect to find manufacturing tolerances and thermal gradients having maximum influence on the leading edge of the pulse. The nominal, near normal incidence angle antenna pattern at 0.53 μm (Appendix A, page A-9) exhibits a significant reduced gain region at small point-ahead angles. This reduced gain is responsible for the significant rise in static bias at small point-ahead angles as shown in Figure F-4. This effect disappears at 1.06 μm, since the aperture is only half the number of wavelengths in diameter.

The effects of thermal gradients on the far field antenna pattern are, of course, a function of the type and direction of the gradient. The axial gradient, i.e., where the temperature within the corner-cube varies linearly

from apex to face, and is constant in planes parallel to the face is a good example. This type of thermal gradient produces a parabolic phase shift in the reflected energy, which may either enhance or combat the phase shift caused by dihedral angle offset. Depending on the direction and magnitude of the gradient, then, the far-field pattern can vary from near diffraction limited performance for zero phase error, to many interference rings within the nominal range of point-ahead angles. Thus, the extremely important leading edge of the return pulse is strongly influenced by local conditions with the target, and we could hypothesize that the static bias could easily very, at small point-ahead angles, between the 80 ps value calculated for 0.53 μm and the 340 ps value calculated for 1.06 μm. Gradients of 1 to 2°C are sufficient to cause this magnitude of effect. This should be much less severe at larger point-ahead angles. Note that for ranging between two spacecraft, small point-ahead angles are encountered only for nearly coplanar spacecraft, and even then, only for short periods. For a HATRS/LATS link, with coplanar spacecraft at 22000 km and 1000 km altitudes, respectively, the point-ahead angle is less than 15 μrad for about 36% of a viewing opportunity, roughly centered between acquisition (at horizon) and closest approach. This effect should be virtually unobservable from the ground, since the point-ahead angle nominally remains large over a viewing opportunity. Finally, we note that the potential variation in static bias is relatively unaffected by laser pulsewidth.

3.0 COHERENT INTERFERENCE EFFECTS

In the previous section, the LAGEOS signature was computed, assuming noncoherent (power) summing of the returns from the individual retro-reflectors. In this section, we address the more general situation, and determine the statistics of the processes as fully as possible. Figure F-6 shows the detection process in block diagram form. Previously, we noted that the return pulse, S(t), was simply the convolution of the laser pulse with the impulse response of the LAGEOS. Since these processes are linear, the order is immaterial, and is shown in Figure F-5 to emphasize the contribution of laser pulsewidth on the overall process. The responses are summarized below.

$$h_L(t) = \sum_{n=1}^{N} a_n e^{j\theta_n} \delta(t-\tau_n) \qquad \text{(F-30)}$$

$$h_p(t) = e^{-t^2/T^2} \tag{F-31}$$

$$S(t) = h_L(t) * h_p(t) = \sum_{n=1}^{N} a_n \, e^{j\theta_n - \frac{(t-\tau_n)^2}{T^2}} \tag{F-32}$$

$$X(t) = S(t) \cdot S^*(t) = \sum_{n=1}^{N} \sum_{m=1}^{N} a_n a_m \cos(\theta_n - \theta_m) e^{-\frac{(t-\tau_n)^2}{T^2} - \frac{(t-\tau_m)^2}{T^2}} \tag{F-33}$$

MODEL DETECTION PROCESS

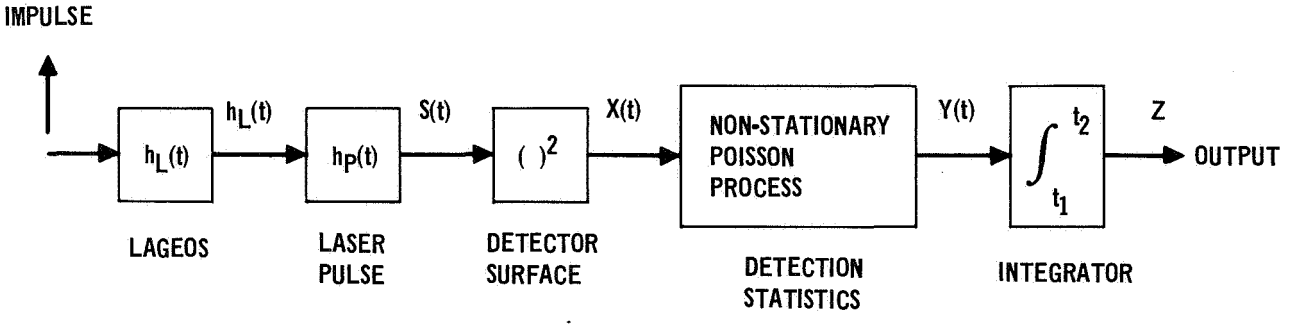

FIGURE F-5

Equations (F-30) through (F-33) describe the processes through the detection block. Note that a_n and θ_n are random variables. Y(t) can be described as a non-stationary Poisson process, whose mean rate varies in a random manner. Equation (F-32) is the same as Equation (F-16) with the carrier frequency term dropped, and Equation (F-33) is the same as Equation (F-17). We would like to determine the statistics of the output of a perfect integrator, Z, on a pulse by pulse basis.

When the laser pulse is narrow compared to the mean temporal spacing between individual impulse responses of the LAGEOS retro-reflectors, the phase terms drop out, and power summing is exactly correct. Then, the probability distribution of Z can be determined by repeated convolutions of the probability distribution of Zn, n = 1,2 ···, N, where Z_n is the incremental increase in Z due to the nth impulse.

Thus, we write, $Pr\{Z_n = K\ C_n\} = (C_n)^K/K!e^{-c_n}$ where c_n is a factor which relates the retro-reflector gain, a_n^2, to detected photoelectrons. Then,

$$Pr\left\{Z_n = K\right\} = \int_0^\infty Pr\left\{Z_n = K \,\middle|\, C_n\right\} f_{C_n}(C_n)\, dC_n$$

Since we will be convolving a number of these individual functions, it is convenient to work in the transform domain, i.e., to compute the characteristic function, $\phi_Z(w)$.

$$\phi_{Z_n}(w) = \sum_{K=0}^{\infty} e^{iwK} Pr\left\{Z_n = K\right\}$$

$$\phi_{Z_n}(w) = \int_0^\infty \exp\left\{C_n(e^{iw} - 1)\right\} f_C(C_n)\, dC_N \qquad \text{(F-34)}$$

In order to proceed to the solution, we need to assume a model for the probability distribution of C. One simple model is the exponential distribution, which has equal mean and root variance, which is a reasonable match to the cube-corner gain statistics. Thus, assuming $f_C(C) = \frac{1}{m} e^{-c/m}$, results in Equation (F-35).

$$\phi_{Z_n}(w) = \left[m_n(e^{iw} - 1) - 1\right]^{-1} \qquad \text{(F-35)}$$

(This is the characteristic function of the Geometric distribution.) Then, Z has a characteristic function which is the product of the characteristic function of each term.

$$\phi_Z(w) = \prod_{n=1}^{N} \left[m_n(e^{iw} - 1) - 1\right]^{-1} \qquad \text{(F-36)}$$

Then, solving for the mean and variance of Z, we find

$$\psi_Z(w) = \ln \phi_Z(w) = -\sum_{n=1}^{N} \ln\left[m_n(e^{iw} - 1) - 1\right]$$

$$\psi_Z'(w) = \frac{d\psi_Z(w)}{dw} = -\sum_{n=1}^{N} \frac{im_n e^{iw}}{m_n(e^{iw} - 1) - 1}$$

$$\psi_Z'(o) = i\eta_Z = i \sum_{n=1}^{N} m_n$$

$$\eta_Z = \sum_{n=1}^{N} m_n \tag{F-37}$$

$$\psi_Z''(w) = - \sum_{n=1}^{N} \frac{m_n(m_n + 1)\, e^{iw}}{\left[m_n(e^{iw} - 1) - 1\right]^2} \tag{F-38}$$

$$\psi_Z''(o) = -\sigma_Z^2$$

$$\sigma_Z^2 = \sum_{n=1}^{N} (m_n^2 + m_n) \tag{F-39}$$

Thus, if the m_n are small ($<<1$), the distribution will retain a Poisson type of characteristic; if they are large, the distribution will tend toward the exponential distribution.

Other distribution models for $f_c(C)$ will alter these results somewhat, however we expect the small m_n cases to retain the Poisson characteristic virtually independant of the actual probability distribution of cube-corner gain.

For the long laser pulse case, the results are similar. In this case, $T>>N\Delta\tau$ thus, equation F-33 reduces to,

$$X(t) \simeq e^{-2t^2/T^2} \sum_{n=1}^{N} \sum_{K=1}^{N} a_n a_K \cos(\theta_n - \theta_K),$$

which can be written as

$$X(t) \simeq e^{-2t^2/T^2} \left[\left(\sum_{n=1}^{N} a_n \cos\theta_n\right)^2 + \left(\sum_{n=1}^{N} a_n \sin\theta_n\right)^2\right].$$

Thus, $X(t)$ is the product of a non-time-dependent random variable and the non-random pulse amplitude time function.

The statistics of the random variable can be deduced readily. Let

$$A = \sum_{n=1}^{N} a_n \cos\theta_n, \qquad B = \sum_{n=1}^{N} a_n \sin\theta_n.$$

A and B are then orthogonal random variables with zero-mean and equal variances. By invoking the Central limit theorem, we hypothesize that A and B tend to normal random variables, thus the sum of A^2+B^2 will have an exponential distribution.

Then, the statistics of the output of the integrator (Z) can be deduced from,

$$\Pr\{Z=K\} = \int_0^\infty \Pr\{Z=K|s\}\ f_c(s)\ ds$$

$$\Pr\{Z=K\} = \int_0^\infty \left(\frac{s^K}{K!}e^{-s}\right)\frac{1}{m}\ e^{-s/m}\ dc$$

$$= \frac{1}{m\cdot K!}\int_0^\infty s^K\ e^{-s(1+1/m)}\ ds$$

$$\Pr\{Z=K\} = \frac{1}{m}\left(\frac{m}{1+m}\right)^{K+1} = \left(\frac{1}{1+m}\right)\left(\frac{m}{1+m}\right)^K .$$

Hence, Z has a geometric distribution, with $n_Z=m$, $\sigma_Z^2=m+m^2$.

For the case where the pulse is larger than the cube-corner spacing but shorter than the overall impulse response of the target, the preceding approximations cannot be relied upon. A simulation was conducted to determine the pulse shape variations that could be expected for the intermediate pulse width condition. Figure F-6 shows the mean pulse shape and six return pulses obtained in successive trials, where the optical phase terms in equation F-33 were chosen randomly for each pulse. A laser pulsewidth of 0.15 ns (FWHM) was used.

As a first order approximation, then, we can divide the return signal into several segments, each of which is essentially uncorrelated with the others. This results in the probability distribution of Z determined by convolving the probability distributions of the individual segments.

Thus, we can see that independant of the pulsewidth, the mean value of Z is, $Z = \sum_{n=1}^{N} m_n$. The variance of Z differs, however, for differing laser pulsewidths. This is shown in the next three equations.

$$\sigma_Z^2 \simeq \sum_{n=1}^{N} m_n + \sum_{n=1}^{N} m_n^2 , \qquad T<\Delta\tau \qquad \text{(F-40)}$$

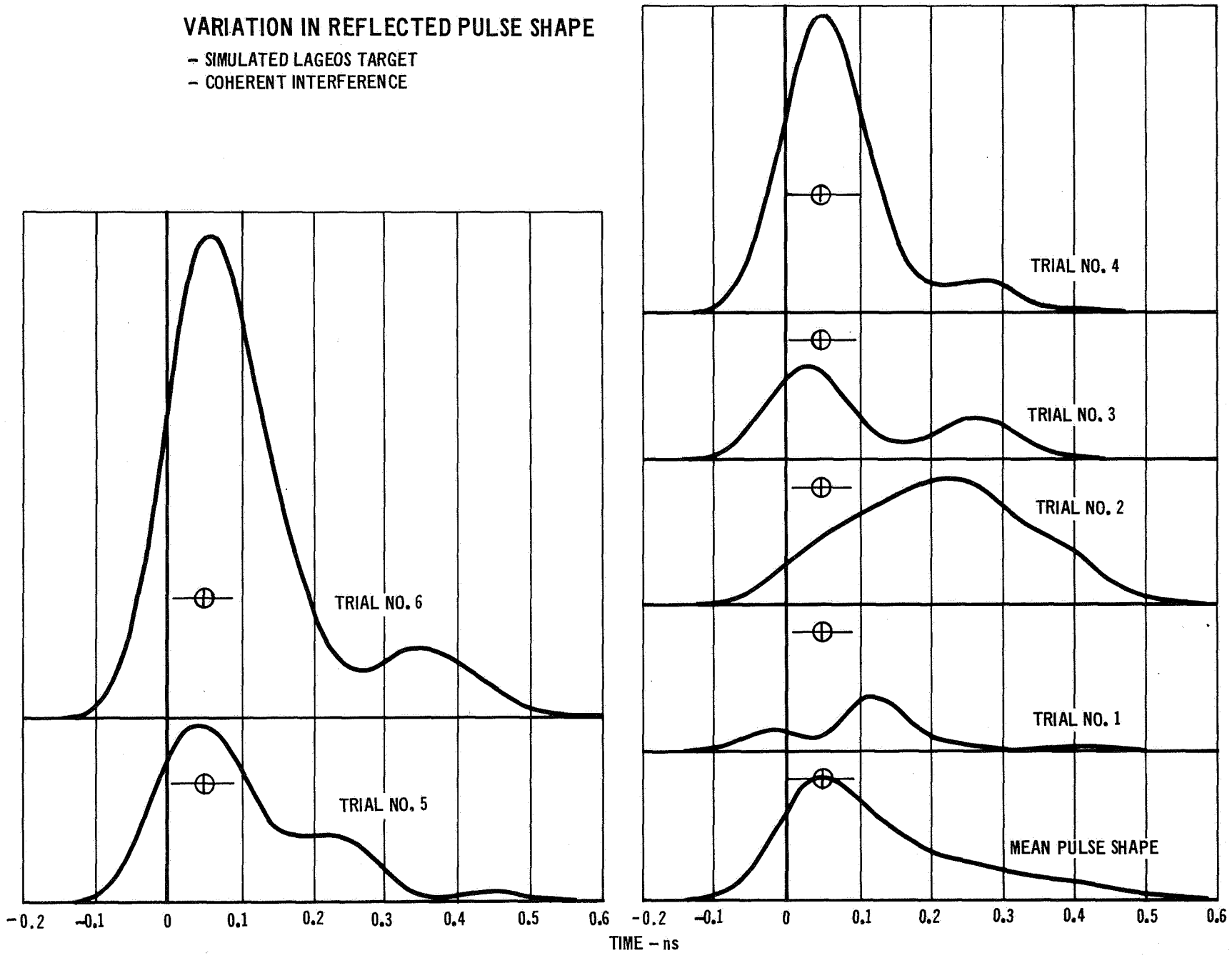
VARIATION IN REFLECTED PULSE SHAPE
- SIMULATED LAGEOS TARGET
- COHERENT INTERFERENCE
TRIAL NO. 4
TRIAL NO. 3
TRIAL NO. 2
TRIAL NO. 1
MEAN PULSE SHAPE
TRIAL NO. 6
TRIAL NO. 5
-0.2
-0.1
0
0.1
0.2
0.3
0.4
0.5
0.6
TIME - ns

FIGURE F-6

$$\sigma_Z^2 \simeq \sum_{n=1}^{N} m_n + \left(\sum_{n=1}^{n_1} m_n\right)^2 + \left(\sum_{n=n_1+1}^{n_2} m_n\right)^2 + \cdots + \left(\sum_{n=n_x+1}^{N} m_n\right)^2, \quad \Delta\tau<T<N\Delta\tau \qquad \text{(F-41)}$$

$$\sigma_Z^2 \simeq \sum_{n=1}^{N} m_n + \left(\sum_{n=1}^{N} m_n\right)^2, \qquad T>N\Delta\tau \qquad \text{(F-42)}$$

In conclusion, we see that as the pulsewidth increases from very small to very large, the mean value of the integrator output is unchanged, assuming equal energy per pulse, but the variance increases with the pulsewidth in the transition region. Thus, assuming that the mean detected signal has an exponential distribution is a conservative estimate with the degree of conservatism decreasing as the pulsewidth increases to values larger than the maximum target delay.

If the target were a planar array of retro-reflectors at near normal incidence, the coefficients (a_n) would be the same, i.e., the randomness is significantly reduced. For large numbers of retro-reflectors, the orthogonality argument is still potent, and the probability distribution of Z should tend toward exponential. This was verified by simulation, and Figure F-7 shows the cumulative probability distribution for four planar arrays, containing 4, 9, 25, and 36 retro-reflectors. All four cases represent the histogram results of 1000 trials, and confirm the reasonableness of the exponential distribution model. Thus, for all subsequent work, we elected to use the exponential distribution as the limiting case, regardless of target geometry or laser pulsewidth, when the target is composed of several individual retro-reflectors.

4.0 GROUND TARGETS

Ground targets may be single retro-reflectors or arrays of retro-reflectros. Both types of targets were considered during the study. The basic problem is obtaining enough signal return to satisfy the ranging function. Since the ground targets do not exist, at this time, a modest amount of latitude in selecting cube-corner characteristics is assumed, i.e., we can tailor the cube-corner physical characteristics to optimize the return.

The major factor in determining the fundamental limits on the achievable cube-corner gain is the restrictions which must be imposed on the far-field

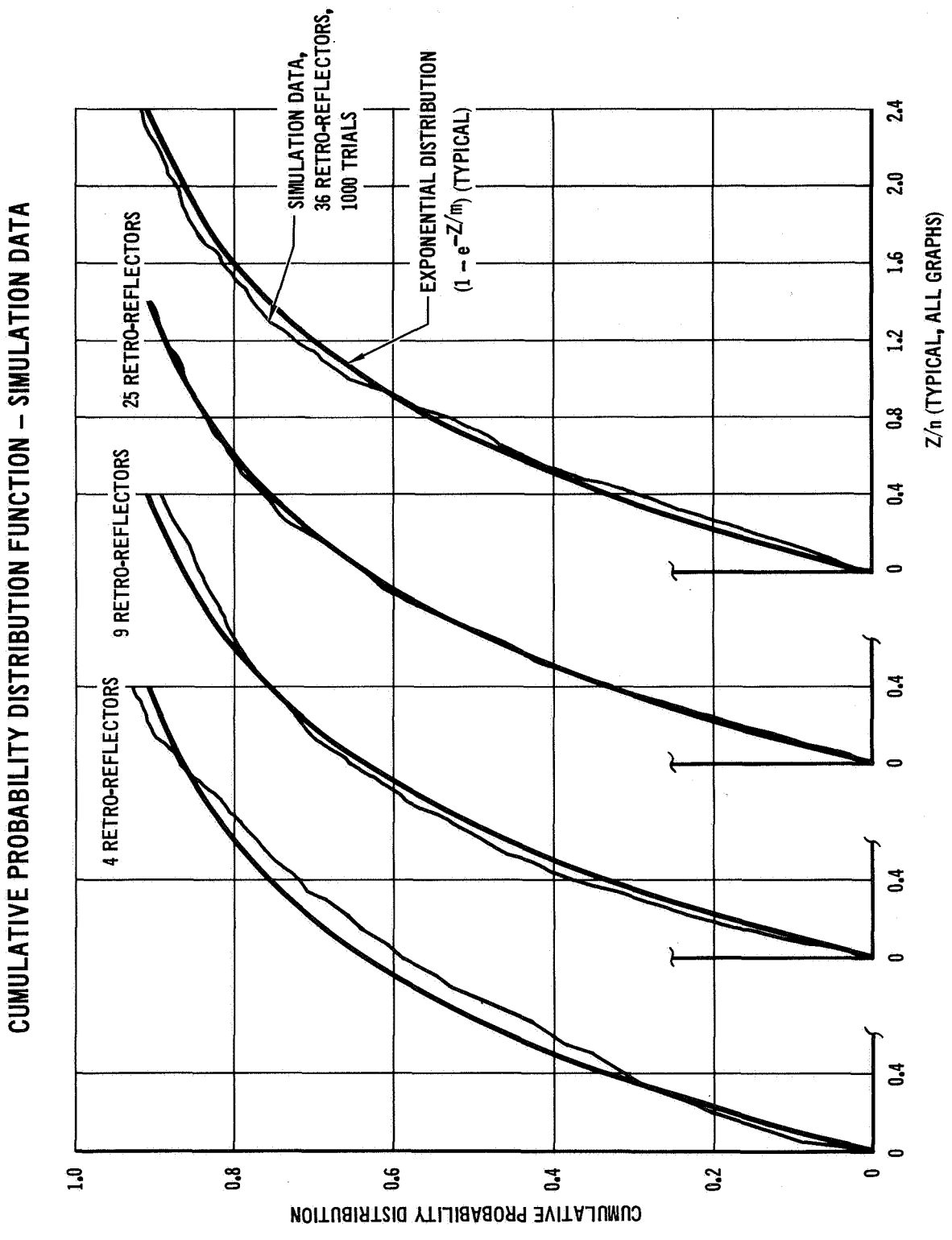
CUMULATIVE PROBABILITY DISTRIBUTION FUNCTION – SIMULATION DATA
CUMULATIVE PROBABILITY DISTRIBUTION
1.0
0.8
0.6
0.4
0.2
0
4 RETRO-REFLECTORS
9 RETRO-REFLECTORS
25 RETRO-REFLECTORS
SIMULATION DATA, 36 RETRO-REFLECTORS, 1000 TRIALS
EXPONENTIAL DISTRIBUTION $(1 - e^{-Z/m})$ (TYPICAL)
0
0.4
0.8
1.2
1.6
2.0
2.4
Z/n (TYPICAL, ALL GRAPHS)

FIGURE F–7

antenna pattern, due to velocity aberration (point-ahead angle) effects. When viewed from the ground, the maximum point-ahead angle occurs when the host spacecraft passes directly overhead. Assuming a circular orbit, the spacecraft tangential velocity component is the orbital velocity at this point, and ranges from approximately 3.75 to 7.73 km/s for altitudes of 22000 km to 300 km, respectively. The maximum point-ahead angle ($2V_T/C$) is therefore between 25 and 51.5 μrad, assuming negligible effect from Earth rotations ($V_{Tg} \leq 0.074$ km/sec, $PA_G < 0.5$ μrad). The minimum point-ahead angle occurs at minimum elevation angle, when the spacecraft orbit plane passes through the ground site. The variation in point-ahead angle with elevation angle under these conditions is,

$$PA = \frac{2V_s}{C}\sqrt{1 - \left(\frac{r_e \cos E}{r_s}\right)^2} \qquad \text{(F-43)}$$

where V_s is the spacecraft orbital velocity

$C = 3 \times 10^5$ km/s

r_e = earth radius ≃ 6378.16 km

r_s = S/C radius = $r_e + h_s$

E = elevation angle

For the high altitude S/C, h_s = 22000 km, V_s = 3.75 km/sec, and the point-ahead angle varies only slightly with elevation angle (from ∿ 24.4 to 25.0). For the low altitude spacecraft, h_s = 300 km, V_s = 7.73 km/sec, the point-ahead angle varies considerably with elevation angle, as shown in Figure F-8. For a minimum usable elevation angle of 30°, the PA varies from 29 μrad to 51.5 μrad.

For the low altitude S/C-ground link, when the target latitude is comparable to the orbit inclination, the angular orientation of the tangential velocity vector may be in almost any direction, thus we require the "optimum" cube-corner transmit antenna pattern to be circularly symmetric, with nearly uniform gain in the annular ring between ∿35 and 55 μrad. The gain product for this coverage is, therefore,

$$G = \frac{4(\pi D/\lambda)^2}{\left(\phi_2^2 - \phi_1^2\right)} \qquad \text{(F-44)}$$

POINT-AHEAD ANGLE VARIATION FOR 300 KM ALTITUDE S/C – GROUND TARGET

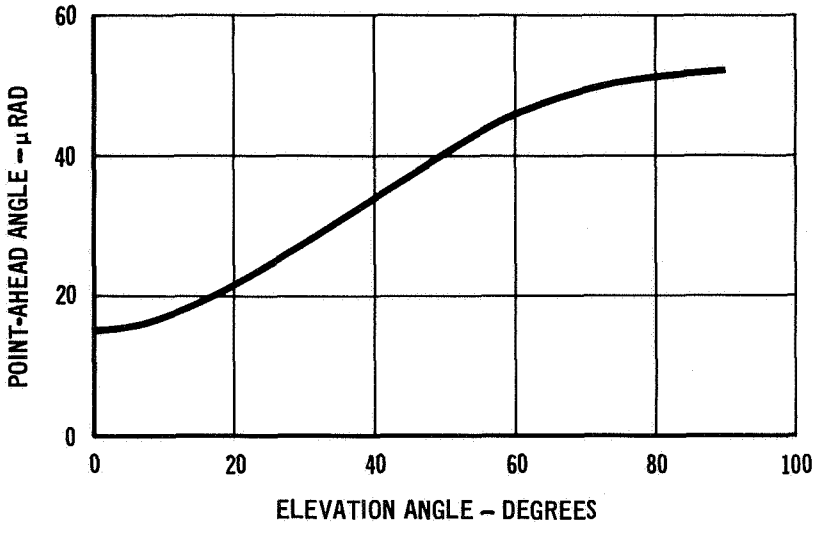

FIGURE F–8

Evaluating equation F-44 results in,

$$G_{DB} = 227.676 + 20 \log (D) \qquad \text{(F-45)}$$

where

D = face diameter (m)

and

$\lambda = 0.53\ \mu m$

Table 2 summarizes the gain product for several cube-corner sizes.

FACE DIAMETER (cm)	GAIN PRODUCT (dB)
3.8	199.3
5.0	201.7
10.0	207.7

For the high altitude S/C ground link, the point-ahead angle range is much smaller, permitting substantially larger net gain products. Further, since the high altitude spacecraft orbit is near polar inclination, the range of tangential velocity vector orientations for most target latitudes is substan-

tially reduced, permitting some additional freedom in shaping the cube-corner transmit antenna pattern.

The next step in this process is to determine which cube-corner characteristics can be used to optimize the far-field pattern. One possible alternative is to grind the face to provide a lens effect, i.e., a physical radius of curvature which provides a parabolic phase shift in the return wave front. For relatively modest values of phase shift, this process should provide an otherwise undistorted wavefront.

At normal incidence, for a circular aperture, the far-field pattern of the cube-corner with a parabolic phase shift is shown in Appendix G to be,

$$\tilde{E}_N(\phi) = i \frac{(Kr)^2}{Z} \sum_{n=1}^{\infty} \left(\frac{2iZ}{Kr\phi}\right)^n J_n(Kr\phi)\, e^{iZ} \qquad \text{(F-46)}$$

$$= i \frac{(Kr)^2}{Z} \sum_{J=0}^{\infty} \frac{\left(-\frac{i(Kr\phi/2)^2}{Z}\right)^J}{J!} \left[1 - e_J(-iZ)\, e^{iZ}\right] \qquad \text{(F-47)}$$

where

$$e_J(Z) = \sum_{n=0}^{J} \frac{Z^n}{n!}$$

The second form is obtained by expanding the Bessel functions in series form and rearranging the terms. This expression is convenient for numerical evaluation. The gain is $G(\phi) = \tilde{E}_n(\phi) \cdot E_n^*(\phi)$.

Figure F-9 shows the gain, vs point ahead angle (ϕ) computed from equation F-47 for a 10-cm diameter cube-corner, at normal incidence, as the parabolic phase shift, measured at the edge of the aperture, is increased from $\pi/2$ to 13 $\pi/2$ in steps of π radians. The shaded portions of the curves denote the regions where the gain product is greater than 200 dB. In the nominal region of interest, the shading is deeper. The shift of energy from the center out to 50 μrad is clearly evident. The ripples in the gain curves result from the physical size of the aperture and exhibit a period of ∿6.5 μrad, which is the nominal period of the diffraction pattern for the uniform phase front case.

PARABOLIC PHASE TAPER BROADENS CUBE-CORNER ANTENNA PATTERN

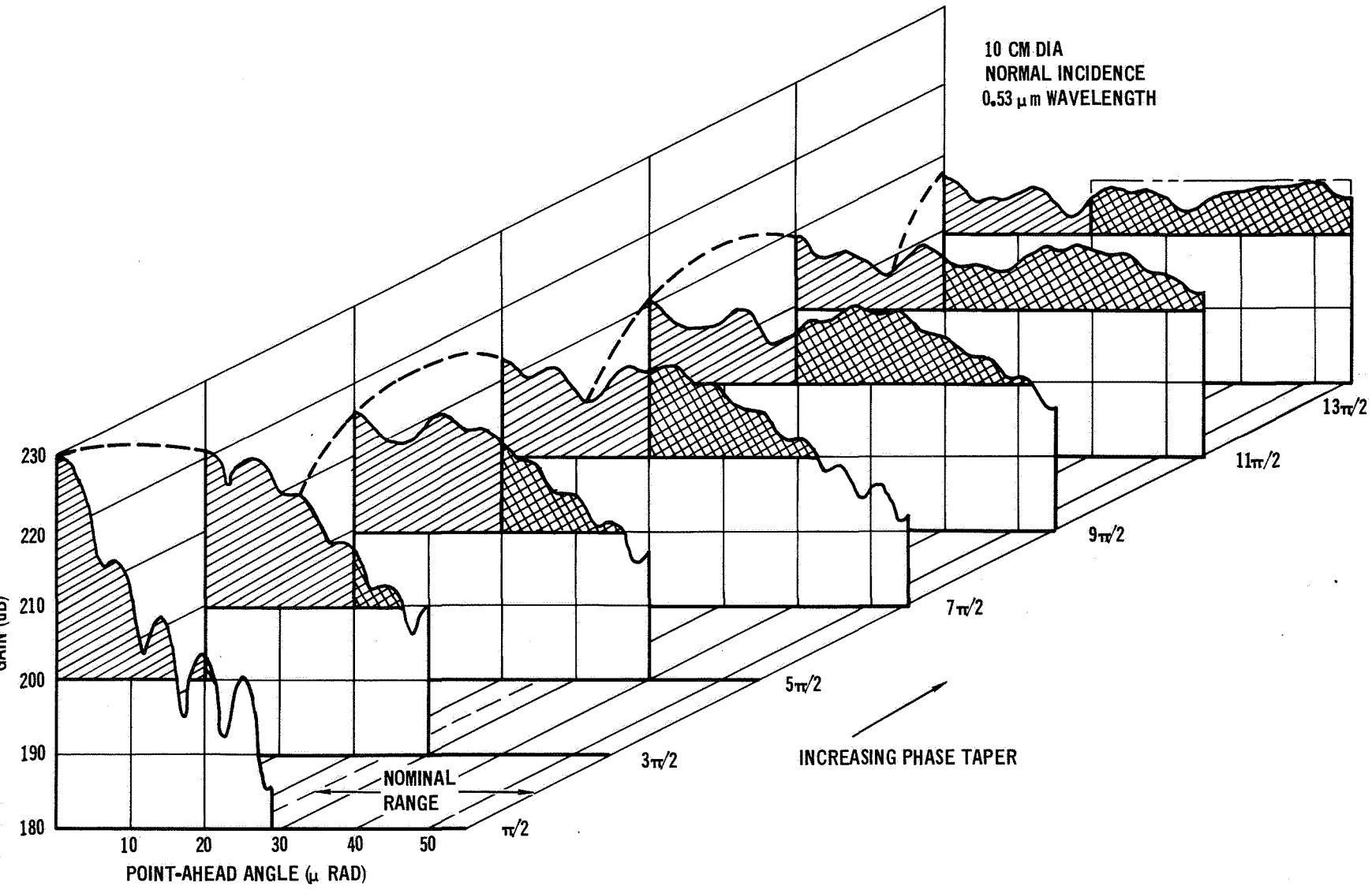

FIGURE F-9

Figure F-10 shows the gain product vs point ahead angle for a 5 cm diameter cube-corner. In this case, the region above 194 dB gain product is shaded. We note, when comparing this figure with the preceding figure (for a 10-cm diameter cube-corner), that analagous performance characteristics are obtained with approximately one-half the phase shift at the edge.

CUBE CORNER ANTENNA PATTERN VARIATION WITH PARABOLIC PHASE TAPER

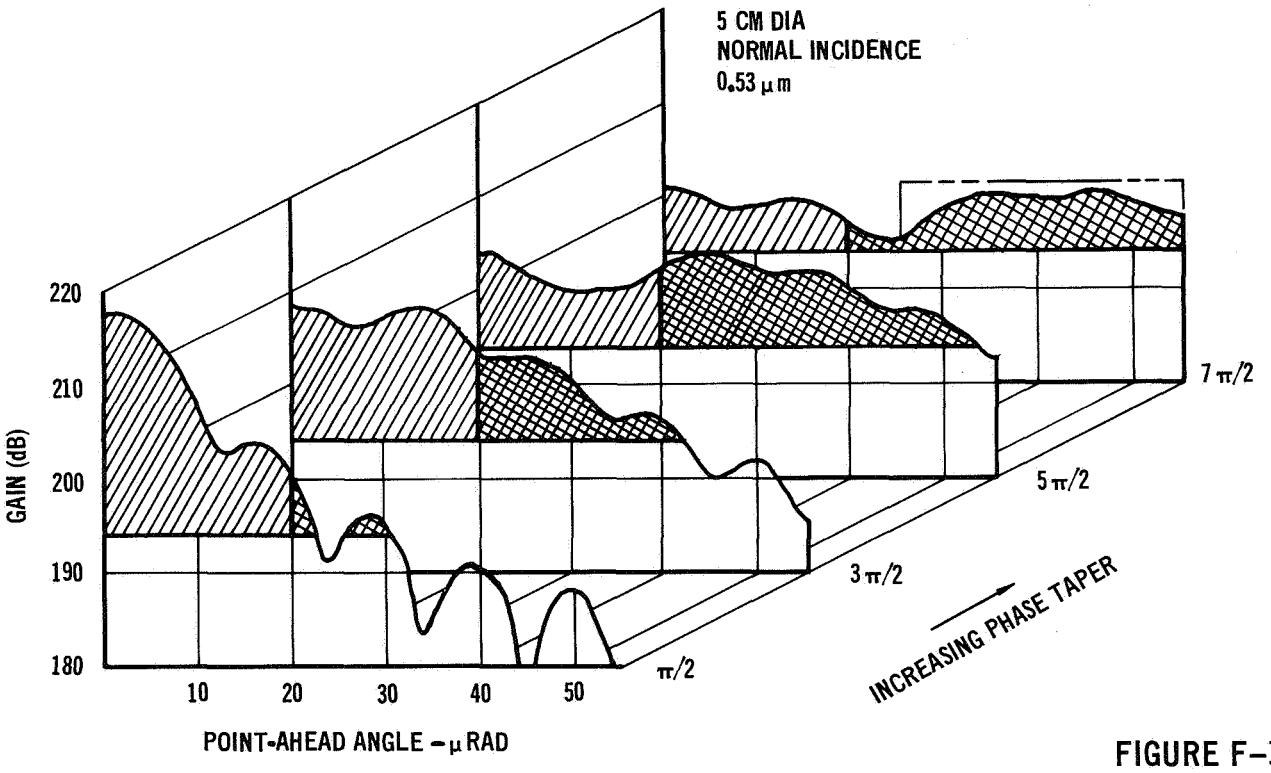

FIGURE F-10

Thus, based on these two figures, we conclude that the desired cube-corner pattern characteristics, for normal incidence, can probably be achieved for any reasonably sized device, and that the net gain-product in the region of interest increases essentially in proportion to the cube-corner face area.

Also shown in Figures F-9 and F-10 are the gains (dashed lines on the last curve), for the low altitude S/C computed from equation F-44. The computed gain produced is within 3 dB of this gain over most of the region of interest.

At nonnormal incidence angles, the effect of a parabolic phase shift is less clear. The changes in gain at nonnormal incidence angles results from two distinct effects. First, as the incidence angle increases, a "cos (θ)" scaling

term begins to be effective. This scaling term, for an otherwise unperturbed aperture shape, results in a relatively minor beam spread.

For a cube-corner, however, as the incidence angle increases, the effective aperture decreases rather significantly. The basic concept is that the path thru the cube-corner can be shown as a straight line, which is analagous to folding the cube-corner about the three reflecting planes, in the ray contact sequence. Then, the exit aperture is in a plane parallel to the entrance aperture, and spaced a distance of $D\sqrt{2} \tan \theta_{DF}$. Thus, the projection of the entrance and exit apertures shows an offset as a function of incidence angle. When the aperture face has a large radius of curvature, resulting in a small parabolic phase shift, the net phase shift is the sum of the excess phase at the entrance and exit points. The resulting phase shift is also a paraboloid of revolution, whose center is exactly half-way between the two centers. Thus, the dashed lines in Figure F-11, represent lines of constant phase.

FACE-PLANE PROJECTION – 15^0 INCIDENCE ANGLE

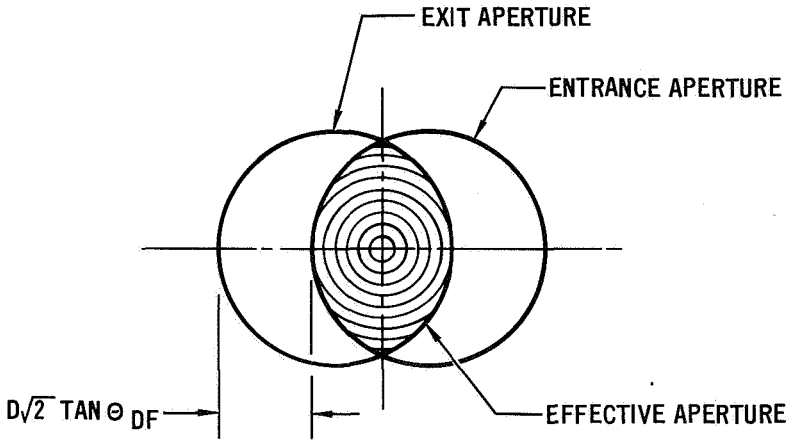

FIGURE F–11

Since the paraboloid of revolution is unchanged, the defocussing effect is also unchanged. Thus, as the incidence angle increases, the first effect to be observed is simply the area decrease, and the transmit beamwidth is virtually unaffected. However, as the incidence angle continues to increase, the nominal diffraction limited beamwidth of the cube-corner increases, so that the effective beamwidth begins to increase, resulting in an increasing steeper rate of reduction of gain.

We find that an approximate gain law vs incidence angle is $G \propto \overline{10}^{\theta/25}$, where θ is the incidence angle in degrees, is a quite reasonable approximation in the region of interest, and seems to hold fairly well provided the beam is spoiled at normal incidence angles.

Thus, we can now project the expected performance capability for optimized cube-corner retro-reflectors which are used singly or in arrays for ground targets. Equation (F-48) presents this projection for the low altitude S/C target configuration.

$$G_{DB} \simeq 225 + 20 \log D - \theta/2.5 \qquad \text{(F-48)}$$

D = diameter (m)

θ = incidence angle, degrees

For the HATRS/ground link, the target is assumed to consist of a planar array of cube-corners, in a 4 x 4 arrangement, which is used only for local elevation angles of 60° or above. The individual cube-corners are 6-cm diameter, and spoiled to maximize the return at 25 μrad point-ahead. The expected gain for each cube-corner is ∿200 dB at 30° incidence angle (60° elevation), yielding a mean array gain of ∿212 dB. At 60° elevation angle, the physical dimensions of the array result in a significant amount of pulse spreading. Alternatively, the array could be mechanically gimballed to reduce the incidence angle. Several techniques seem reasonable for this purpose, and could be used in conjunction with environmental protection devices to reduce periodic maintenance requirements.

In any event, it is reasonable to assume a ground target gain product of 210 dB for use by the HATRS radar, which results in comparable link margins for the HATRS/ground and the HATRS/LATS links. For the Shuttle or Spacelab experiment, however, the target viewing opportunity is rather short, and it would be preferable to choose a ground target configuration which resulted in a single cube-corner response, to facilitate dual frequency (1.06 μm and 0.53 μm) ranging for atmospheric delay evaluation.

Thus, for reasonably sized cube-corners, the maximum usable mean target gain product is considerably less, more on the order of 192 to 196 dB at 0.53 μm, and 186 to 190 dB at 1.06 μm wavelength, for incidence angles up to 30°. Environmental protection is desirable, although possibly not required during a Shuttle mission assuming favorable locations and weather conditions.

APPENDIX G

FAR FIELD RADIATION PATTERN
TRUNCATED GAUSSIAN APERTURE

1. INTRODUCTION. This appendix presents a solution of the integral describing the far field radiation pattern of a finite aperture illuminated with a Gaussian intensity distribution.

2. ANALYSIS. The far field radiation pattern of circularly symmetric plane radiation from a finite circular aperture is described by,[G1]

$$I = \left[\left(1 + \cos(\theta)\right)A(L)\int_0^a f(r)J_0(Kr\sin\theta)\,rdr\right]^2 \qquad \text{(G-1)}$$

where

θ is the angle from the optical axis
a is the aperture radius
K is the wave number $(2\pi/\lambda)$
A(L) is a propagation constant
J_0 is the zero order Bessel function

and

f(r) is the electric field distribution in the aperture

For small angles, and neglecting unimportant constants, this reduces to,

$$I_1 = \left[\int_0^a f(r)J_0(K\theta r)\,rdr\right]^2 \qquad \text{(G-2)}$$

A Gaussian intensity distribution in the aperture is described by,

$$f(r) = \exp\{-r^2/R^2\} \qquad \text{(G-3)}$$

where R is the radius of the e^{-2} power point of the intensity distribution. Substituting equation (G-3) into equation (G-2) results in,

$$I_1^{\frac{1}{2}} = \int_0^a e^{-\frac{r^2}{R^2}} J_0(K\theta r)rdr \qquad \text{(G-4)}$$

Next, we substitute $t = r^2$, resulting in,

$$I_{\frac{1}{2}} = \frac{1}{2} \int_0^{a^2} e^{-\frac{t}{R^2}} J_0(K\theta\sqrt{t})dt \qquad \text{(G-5)}$$

Now, the Laplace transform of $J_0(2\sqrt{bt})$ is,(G2)

$$L\{J_0(2\sqrt{bt})\} = \frac{1}{S} e^{-\frac{b}{S}} \qquad \text{(G-6)}$$

Hence,(G3)

$$L\{e^{-ct} J_0(2\sqrt{bt})\} = \frac{1}{(S+C)} e^{-\frac{b}{(S+C)}} \qquad \text{(G-7)}$$

Therefore,(G-4)

$$L\{\int_0^t e^{-ct} J_0(2\sqrt{bt})dt\} = \frac{1}{S(S+C)} e^{-\frac{b}{(S+C)}} \qquad \text{(G-8)}$$

$$L\{e^{+ct} \int_0^t e^{-ct} J_0(2\sqrt{bt})dt\} = \frac{1}{S(S-c)} e^{-\frac{b}{S}} \qquad \text{(G-9)}$$

$$= \sum_{i=0}^{\infty} \frac{c^i}{S^{2+i}} e^{-\frac{b}{S}} \qquad \text{(G-10)}$$

Hence,(G5)

$$e^{ct} \int_0^t e^{-ct} Jo(2\sqrt{bt})dt = \sum_{i=0}^{\infty} c^i \left(\frac{t}{b}\right)^{\frac{1+i}{2}} J_{1+i}(2\sqrt{bt}) \qquad \text{(G-11)}$$

Then, let,

$2\sqrt{b} = K\theta$

$C = 1/R^2$

$t = a^2$

We find, therefore,

$$I_1^{\frac{1}{2}} = \frac{1}{2} R^2 \sum_{i=1}^{\infty} (2a/K\theta R^2)^i \, J_i(K\theta a) e^{-\frac{a^2}{R^2}} \tag{G-12}$$

Next, we find,

$$\lim_{\theta \to 0} I_1^{\frac{1}{2}} = \frac{1}{2} R^2 \, e^{-\frac{a^2}{R^2}} \sum_{i=1}^{\infty} \frac{\left(\frac{a^2}{R^2}\right)^i}{i!} = \frac{1}{2} R^2 \left(1 - e^{-\frac{a^2}{R^2}}\right) \tag{G-13}$$

This is the result obtained by solving equation (G-2) with $\theta=0$. In order to establish the limit of $I_1^{1/2}$ as $a \to \infty$, we use the identity,[G6]

$$e^{\frac{1}{2} Z(t-\frac{1}{t})} = \sum_{n=-\infty}^{\infty} t^n \, J_n(Z) \tag{G-14}$$

Thus,

$$\sum_{i=1}^{\infty} (2a/K\theta R^2)^i \, J_i(K\theta a) e^{-\frac{a^2}{R^2}} = e^{-\left(\frac{K\theta R}{2}\right)^2} - \sum_{n=0}^{\infty} \left(\frac{K\theta R^2}{2a}\right)^n J_n(K\theta a) e^{-\frac{a^2}{R^2}}$$

Whence,

$$\lim_{a \to \infty} I_1^{\frac{1}{2}} = \frac{1}{2} R^2 \, e^{-\left(\frac{K\theta R}{2}\right)^2} \tag{G-15}$$

This is the expected Gaussian intensity far field pattern for a nontruncated Gaussian plane radiation.

Last, we note that,

$$\lim_{R \to \infty} I_1^{\frac{1}{2}} = a^2 \left(\frac{J_1(K\theta a)}{K\theta a}\right) \tag{G-16}$$

Thus, as $R \to \infty$, the aperture illumination becomes uniform, and the expected $(J_1(x)/x)^2$ intensity pattern is obtained. Note that Equation (G-12) also applies when a defocus condition is postulated. In this application we simply replace $\frac{1}{R^2}$ with the complex quantity,

$$\gamma = \frac{1 + j^{x2}}{R^2}$$

REFERENCES

G1 Buck, A. L., "The Radiation Pattern of a Truncated Gaussian Aperture Distribution", Proceedings of the IEEE, March 1967, page 448

G2 Abramowitz and Stegun, "Handbook of Mathematical Functions", Dover Publications, New York, 5th printing, Page 1026, 29.3.75

G3 Op. Cit., Page 1021, 29.2.12

G4 Op. Cit., Page 1020, 29.2.6

G5 Op. Cit., Page 1026, 29.3.80

G6 Op. Cit., Page 361, 9.1.41